Micro and Macro Mechanical Assessment of Small and Intermediate Strain Properties of Granular Material

Dissertation

as a requirement of the degree of
Doktor-Ingenieur (Dr.-Ing.)

at the Faculty of
Civil and Environmental Engineering
Ruhr-Universität Bochum

submitted by
Meisam Goudarzy
from Isfahan, Iran

Reviewers
Prof. Dr.-Ing. habil. Tom Schanz
Prof. Dr. Carlos Santamarina
Prof. Dr.-Ing. habil. Theodoros Triantafyllidis

Bochum, November 2015

This work is dedicated to my beloved parents

Abstract

The goal of this research is to explore the influence of fines content and stress induced anisotropy on the small and intermediate strain properties (G_{max}, $G(\gamma)$ and $\eta(\gamma)$) of granular materials from microscopic to macroscopic level. Accordingly, the work is divided into two parts: in the first part the influence of fines content is examined and in the second part the influence of stress-induced anisotropy is assessed.

(1) The resonant column tests were conducted on clean Hostun Sand to detect the influence of mean effective stress, p', and void ratio, e, on G_{max}, $G(\gamma)$ and $\eta(\gamma)$. Then, the effect of fines on the maximum shear modulus, G_{max}, $G(\gamma)$ and damping ratio, $\eta(\gamma)$, was investigated with a systematic increase in fines content, f_c, up to 40%. The experimental results revealed that G_{max} decreased with an increase in e and f_c. Furthermore, the experimental results showed that damping ratio increased with an increase in f_c up to f_c of 20% and it then decreased with further increase in fines content.

Micro CT scans demonstrated that sand with fines develops two different micro-structures: "fines-in-sand" and "sand-in-fines". For "fines-in-sand", fine particles are partially active in the sand force structure and for "sand-in-fines", sand particles float in fine particles. The void ratio, e, does not capture the force structure or fabric of the sample and only represents the density of the sample. The equivalent granular void ratio, e^*, is a parameter for the density and fabric of the sample in transition soils.

Analyses conducted in this study revealed that e^* in comparison with e provides a unique relationship between G_{max}, $f(p')$ and $f(e^*)$ in space, where the fitting parameters of Hardin´s relationship are the same as clean sand. This unique relationship can be used to predict the small and intermediate strain properties of granular materials containing fines based on test results for the clean host material.

(2) The resonant column device was modified for applying the additional vertical stress inside the samples for the anisotropic stress state tests. Simulation using FEM and piezoelectric elements were employed for the calibration and validation of the modified device. Then a series of stress induced anisotropic tests were conducted on Hostun Sand specimens for various stress paths (sp): isotropic loading, sp I (σ_3 = constant), sp II (p' = constant), sp III (K= constant.), where σ_1 and σ_3 are the principal stresses, $p' = (\sigma_1 + 2\sigma_3)/3)$ and $K = \sigma_3/\sigma_1$. Experimental results revealed that the impact of stress induced anisotropy on the small and intermediate strain properties of dry Hostun Sand depends on the adopted stress path. In sp I, the effect of the stress ratio on G_{max} was significant but the influ-

ence of the stress ratio on $G(\gamma)/G_{max}$ and $\eta(\gamma)$ was not significant. The experimental results reveal a significant influence of stress induced anisotropy on G_{max}, $G(\gamma)/G_{max}$ and $\eta(\gamma)$ for sp II and III. The empirical relationships were written as a function of stress components to predict the small and intermediate strain properties of granular material subjected to stress induced anisotropy for different stress paths.

DEM analyses were also conducted on a granular packing to determine the effect of stress induced anisotropy on the contact properties for various stress paths from the microscopic point of view. The micro-mechanical observations showed that the variations in normal contact force in the grain-to-grain contacts and coordination numbers were the main micro-mechanical properties which had a significant effect on the values of G_{max} and G/G_{max} for different stress paths.

Zusammenfassung

In dieser Arbeit wird der Einfluss des Feinkornanteils und der spannungsinduzierten Anisotropie auf die Steifigkeit und das Dämpfungsverhalten von granularen Materialien bei kleinen und mittleren Dehnungszuständen auf makroskopischer und mikroskopischer Ebene betrachtet. Ziel ist es für die unterschiedlichen Ausgangs- und Randbedingungen (Feinkornanteil und anisotroper Spannungszustand) Ansätze zu entwickeln, die maßgebenden Steifigkeiten (Steifigkeit bei kleinen Dehnungen G_{max}, Steifigkeit als Funktion der Dehnung, $G(\gamma)$, und die zutreffende Dämpfung, γ), aus möglichst wenig Versuchen zu bestimmen. Entsprechend gliedert sich die Arbeit in zwei Teile. Im ersten Teil (1) wird der Einfluss des Fein-kornanteils betrachtet, im zweiten (2) der Einfluss der spannungsinduzierten Anisotropie.

Zu (1) werden zunächst Resonant Column (RC) Versuche an Huston Sand durchgeführt, wobei der Einfluss des Spannungszustandes und der Porenzahl auf G_{max}, $G(\gamma)$ und $\eta(\gamma)$ erfasst wird. Anschließend wird mit dieser Versuchstechnik der Einfluss des Feinkornanteils f_c in Huston Sand auf G_{max}, $G(\gamma)$ und $\eta(\gamma)$ systematisch in einem Bereich von $f_c =$ 0 bis $f_c = 40$ % untersucht.

Die Versuche zeigen, dass G_{max} mit zunehmender Porenzahl und zunehmenden Feinkornanteil kleiner wird. Die Dämpfung, $\eta(\gamma)$, steigt zunächst mit zunehmendem Feinkorngehalt bis $f_c = 20$ % an. Bei größerem fc nimmt sie wieder ab. Im Mikro-CT konnte nachgewiesen werden, dass sich auf mikroskopischer Ebene zwei unterschiedliche Strukturen in Abhängigkeit des Feinkornanteils ausbilden, "Feines im Sand", wenn die feinen Partikel an der Lastabtragung zwischen den Körnern nur begrenzt partizipieren, und "Sand im Feinen", wenn die Sandkörner im Feinanteil schwimmen. Die Zustandsgröße Porenzahl e kann diese Übergänge nicht abbilden, wogegen die äquivalente Porenzahl e^* eine konsistente Zustandsgröße darstellt. Mit deren Einführung ergibt sich die Beziehung $G_{max}/Ap_a(\frac{p'}{p_a})^n$ vs $f(e^*)$, worin die Parameter A und n unabhängig vom Feinkornanteil sind und am Sand ohne Feinkornanteil ermittelt werden können. Damit können G_{max}, $G(\gamma)$ und $\eta(\gamma)$ für einen Sand mit unterschiedlichem Feinkornanteil allein auf Basis von Versuchen am reinen Sand bestimmt werden.

Zu (2) wurde das vorhandene RC-Gerät zunächst um eine Belastungseinrichtung zum Aufbringen zusätzlicher Vertikalspannungen und damit anisotroper Spannungszustände auf die Probe erweitert. Dazu wurde das Systemverhalten durch numerische Berechnungen

abgebildet und das Gerät nach dem Umbau unter anderem durch Vergleichsmessungen mit Piezoelementen kalibriert und die Funktion validiert. Anschließend wurde das Verhalten von Huston Sand unter vier Spannungspfaden (sp) ermittelt: isotrope Belastung, sp I ($\sigma_3 = \text{const.}$), sp II ($p = \text{const}$), sp III ($K = \text{const.}$) mit σ_1 und σ_3 Hauptspannungen, $p = (\sigma_1 + 2\sigma_3)/3$), $K = \sigma_3/\sigma_1$. Die Abhängigkeit der Eigenschaften des Sandes bei kleinen Dehnungen vom Spannungspfad wurde dabei deutlich. Unter sp I ist die ist der Einfluss des Spannungsverhältnisses auf G_{max} ausgeprägt aber auf $G(\gamma)$ und die Dämpfung, $\eta(\gamma)$, nicht. Bei sp II und sp III wirkt sich die Anisotropie auf alle drei Parameter, G_{max}, $G(\gamma)$ und $\eta(\gamma)$ aus. Bekannte empirische Beziehungen werden verwendet, um die Spannungspfadabhängigkeit von G_{max}, $G(\gamma)$ und $\eta(\gamma)$ zu erfassen und ein Bestimmen dieser Parameter zu ermöglichen. Um die gefundenen Abhängigkeiten physikalisch zu erklären, wird das Spannungs-Verformungsverhaltens granularer Materialien bei kleinen Dehnungen numerisch mit der Methode der DEM abgebildet. Dieses erlaubt die Lastabtragung zwischen den Körnern auf der Mikrostrukturebene zu bewerten. Aus den Ergebnissen wird die Abhängigkeit zwischen der anisotropen Belastung, den Veränderungen in den Normalkräften in den Korn-zu Korn-Kontakten sowie der Koordinationszahl und den Veränderungen von G_{max}, $G(\gamma)$ und $\eta(\gamma)$ bei den verschiedenen Spannungspfaden deutlich.

Vorwort des Herausgebers

Die vorliegende Promotion von Herrn Meisam Goudarzy ist im Bereich der Grundlagenforschung in der Bodenmechanik angesiedelt. Herr Goudarzy beschäftigt sich sowohl experimentell, als auch numerisch mit den Eigenschaften von granularen Materialien bei kleinen Dehnungsamplituden. Im Vordergrund stehen dabei die maximale (Schub-) Steifigkeit und deren Entwicklung mit zunehmender Schubverzerrung. Außerdem untersucht Herr Goudarzy die Änderung der Dämpfung mit der Schubverzerrungsamplitude. Derartige Studien an granularen Materialien haben mittlerweile eine über dreißigjährige Tradition in der Bodenmechanik. Neuartig an Herrn Goudarzys Untersuchung ist die Berücksichtigung des Feinkornanteils an einem reinen Sand über einen weiten Bereich dieses Anteils. Auch hier gibt es zwar in der Literatur bereits Untersuchungen, jedoch ist die Studie von Herrn Goudarzy in der Hinsicht originär, dass sowohl unterhalb des sog. Schwellenwerts als auch oberhalb des Schwellenwerts umfangreiche Verhältnisse des Feinkornanteils für den gleichen Sand untersucht wurden. Ein zweiter herausragender Beitrag von Herrn Goudarzy ist es, eine der ganz wenigen Studien in der Fachliteratur zu dokumentieren, die den Einfluss der belastungsinduzierten Anisotropie auf die genannten Stoffeigenschaften untersuchen. Auf Grund der gerätespezifisch schwierigen Herausforderung im Resonant Column Gerät (RC) sind derartige Studien, welche die Aufbringung eines anisotropen Spannungszustandes vor Untersuchung der Probe erfordern, nur im geringen Umfang dokumentiert. In dieser Arbeit wird (nach unserer Kenntnis erstmals) der eigentlich im RC-Gerät isotrope Spannungszustand durch die Aufbringung einer zusätzlichen Vertikalspannung anisotrop erweitert. Die notwendigen Gerätemodifikationen wurden umfangreich verifiziert und kalibriert. Herr Goudarzy setzt mit seiner Arbeit erfolgreich eine Bochumer Forschungstradition auf dem allgemeinen Gebiet der Bodendynamik fort, die vor bereits mehreren Jahrzehnten durch Prof. Jessberger begründet wurde.

Univ. Prof. Dr.-Ing. habil. Tom Schanz
Bochum, November 2015

Acknowledgements

All praises and thanks be to God for giving me strength and courage to achieve one of the challenging tasks of my life. This PhD thesis is a result of three years of research work carried out at the Chair of Foundation Engineering, Soil and Rock Mechanics, Ruhr-Universität Bochum. I would like to thank first and foremost my supervisor, Professor Tom Schanz, who gave me the opportunity to start my PhD and provided his continues support over all these years. My sincere gratitude goes to Dr.Diethard König, who helped me during my research and for his comments and suggestions throughout these years. The greatest thanks go to Professor Santamarina at the university of Georgia Tech. for his scientific discussions and his suggestions. I would also like to appreciate Dr. Magnanimo at the university of Twente for her contribution in discrete element simulations and the numerous scientific discussions and the assistance. Sincerest thanks go to Dr.Rahman at the university of South Australia for the scientific discussions and his comments. Also, I am extremely grateful to Professor Triantafyllidis, for accepting to be a reviewer of this research and his comprehensive comments and discussions.
I would like to appreciate Prof.Mukunoki at the university of Kumamoto, Japan, for providing the Micro-CT images on adopted sand mixtures in this study. My gratitude should also be extended to institute of information and communication technology, Bulgarian Academy of Sciences, for providing the Micro-CT images on adopted glass bead mixtures for this study.
My gratitude should also be extended to all my current and former colleagues, laboratory staffs (Mr. Skubisch, Mr. Mosinski and Mr. Blazytko), and to all parties who indirectly assisted me during my period of stay in Bochum.
I would like to appreciate from Wille company in Götingen-Germany, because, the technical aspects of the experimental work presented here would not have been possible without their technical support.

Last but not least, I wish to thank my parents, who taught me to strive more for worthwhile things and they supported me immensely.

Bochum, November 2015
Meisam Goudarzy

Contents

List of Figures

List of Tables

Nomenclature

A Constant fitting parameter in Hardin's relation

a A factor which is a function of rotational frequency and shear wave velocity

A_1, A_2 The cross section area of loading bar

B Constant fitting parameter of Hardin's relation with coordination number function

b Fraction of active fines in sand force structure

C Cycle of analysis in DEM simulation

c_1, c_2 Constant fitting parameters of damping ratio function

CN Coordination number

$CN_{coarse-coarse}$ Coarse-coarse coordination number

C_{uc}, C_{uf} Uniformity coefficient of coarse and fine mixture

D, d Size of coarse and fine particles

D_{10} Size of sand at 10% finer

d_{50} Size of fine at 50% finer

e Void ratio

e_0 Initial void ratio

E_{max} Maximum Young's modulus

e_{max}, e_{min} Maximum and minimum void ratio

e^* Equivalent granular void ratio

F Generated vertical load by double acting pressure device

f_c Fines content

F_N Normal contact force between two particles

f_r Resonant frequency

$Frac$ Fraction factor in DEM simulation

F_T Shear contact force between two particles

f_{thr} Threshold fines content

F_v Corrected vertical load on top of the actuator

f_1, f_2 The value of frequency when the amplitude of excitation is equal to 0.707 time of maximum amplitude

G_{max} Maximum shear modulus

G_s Specific gravity

G_p Shear modulus of particles

G_1, G_2 Shear stiffness of particles

G_γ Shear modulus respect to shear strain

J Mass moment of inertia of sample

J_L Mass moment of inertia of bottom part

J_{mass} Mass moment of inertia of extra mass

J_0 Mass moment of inertia of top part

k Constant fitting factor

K_N Normal stiffness between two particles

K_T Tangential stiffness between two particles

L Height of sample

l Distance between center of two particles

L_1, L_2 Constant parameters related to the particle properties

m Factors related to the effect of coarse in fines mixture

M_{max} Maximum P-wave modulus

m_1, m_3 Stress exponents in reference shear strain function

N_c Number of contacts

$N_{c,coarse-coarse}$ Number of contacts between coarse particles

$N_{b,coarse}$ Number of coarse particles

n Exponent of mean effective stresses of Hardin's relation

n_{cn} Exponent of coordination number function

N_B Number of particles

N_0 Number of particles with zero contacts

N_1 Number of particles with one contacts

n_1, n_2, n_3 Exponent of stress components of Roesler's relation

P, P_0 Applied pressures in double acting cell pressure for applying vertical stress in the Bochum RC device

p' Mean effective stress

p_a Atmospheric pressure

p_{kk1}, p_{kk2} Peak to peak amplitude of signals from the resonant column

Q Amplitude of oscillation for two particles model

R Particle radius

s Contact area between loading bar and actuator

t Diameter of aluminium sample

v_s Shear wave velocity

W Total energy

x, y Fitting parameters of void ratio function

z_1, z_2 The peak to peak amplitude of recorded signals from accelerometer

α Hertz contact area between two particles

β Fitting parameters of Hardin's hyperbolic curve

γ Amplitude of shear strain

γ_{dmin} and γ_{dmax} Minimum and maximum dry density

γ_r Reference shear strain

γ_{et} The maximum shear strain that the shear stiffness has the maximum value

γ_{r1} Reference shear strain at p'=100 kPa

δ Sliding of particles with oscillation

Δt Time step

Δ_v Deviation of obtained frequency of aluminium sample from experimental

ΔW Dissipation of energy

Δ_1, Δ_2 Deviation of obtained frequency of aluminium sample during anisotropic loading from FEM simulation

$\dot{\epsilon}$ Rate of boundary motion in DEM simulation

ζ Exponent of contact forces

η Damping ratio

η_{min} Minimum damping ratio

κ Exponent of mean effective stress in Stokoe´s relationship

θ Volumetric water content

λ, n_b Fitting parameters of b function

μ friction coefficient between two particles

μ_i Initial friction coefficient in DEM simulation

μ_f Final friction coefficient in DEM simulation

ν Poisson's ratio of particles

ρ Density of sample

$\sigma_1, \sigma_2, \sigma_3$ Stress components of Roesler's relation

σ_3 Confining pressure inside the resonant column cell

τ_{max} Peak shear strength

τ_r Shear strength at reference shear strain

ϕ Friction angle

Ω Exponent of normal contact force in normal contact stiffness relationship

ω Rotational frequency

1 Introduction

1.1 Introduction

Experimental and analytical studies in the last few decades show that the mechanical properties of geo-materials strongly depend on the amplitude of deformation or vibration generated by dynamic events, e.g. earthquake, traffic, machine foundations. For example, during an earthquake, compression and shear waves propagate through the soil mass from the bedrock to the designed structures. The goal is to find the effect of waves on the stability of structures located on the soil mass. The structures are usually safe against compression waves because of the weight of the structure. Therefore, the shear component of seismic waves is usually the most critical component because of the susceptibility of structures to horizontal motions and ground settlement during vibration (Darendeli 2001). Thus, to evaluate the stability of structures, it is important to assess the response of soil to the shear wave (vertical propagation and horizontal polarization) which is generated by earthquake or vibration of bedrock (Figure 1.1). Different parameters (e.g. depth or distance of vibration source, soil properties and duration of vibration) make significant effects on response of structure or ground motion during a vibration. Among these parameters, soil properties can make significant effects on soil-structure interaction during wave propagation (Darendeli 2001). Shear modulus, G, and material damping, η, are soil properties which have a significant effect on ground motion during vibration (Seed et al. 1986). These properties are used to determine the velocities and decay of stress waves propagating through the geomaterials.

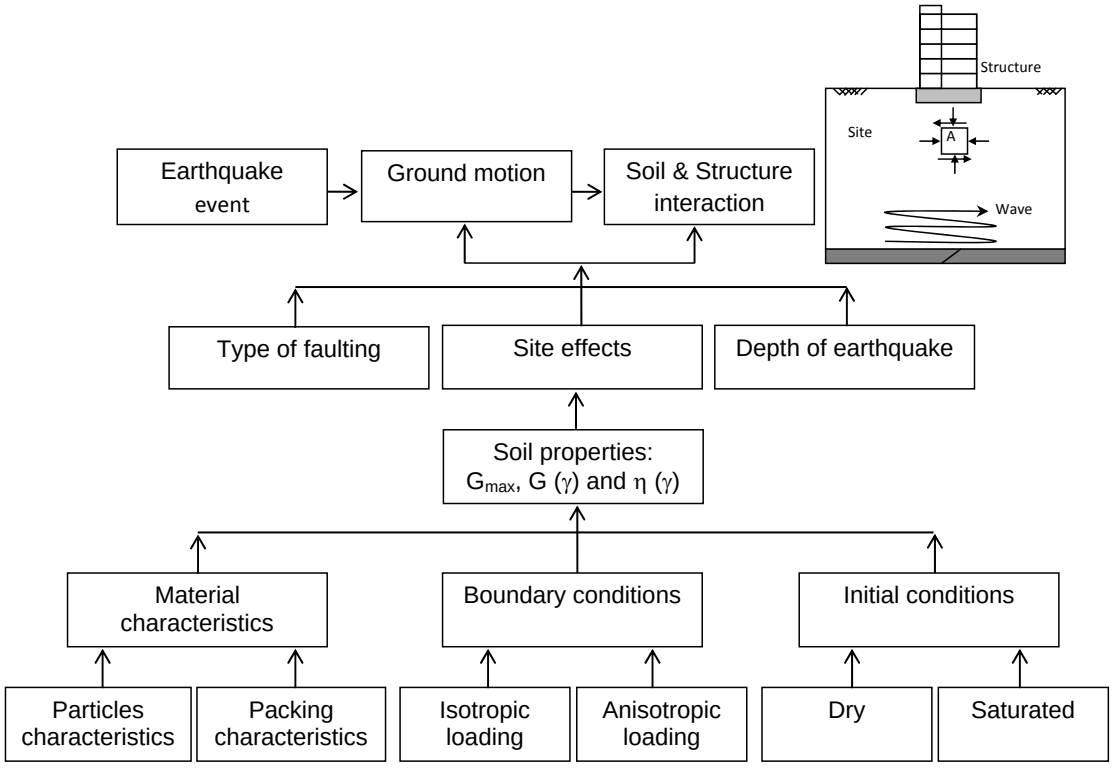

Figure 1.1: Sketch of shear wave propagation in soil deposit and factors influencing ground motion

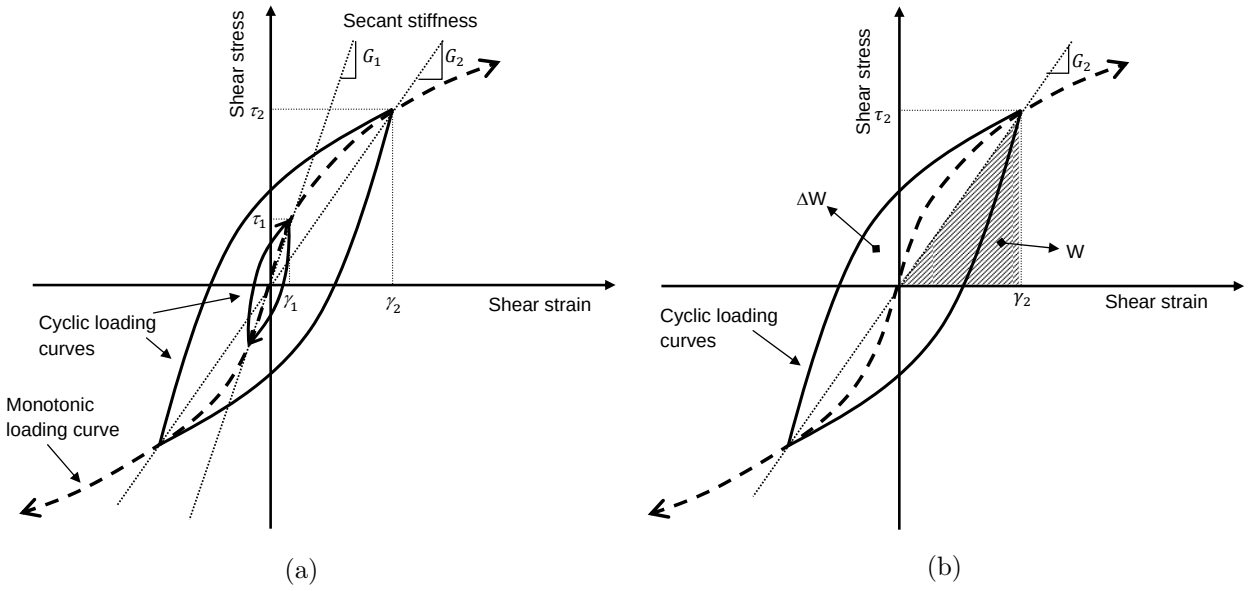

Figure 1.2: Schematic sketch of shear stress versus shear strain: (a) monotonic and cyclic loading (Mitchell & Soga 2005); (b) damping ratio, $\eta = \frac{\Delta W}{2\pi W}$ (Ishihara 1996)

Furthermore, settlement of soils is one of the challenging problems in the soil-structure interaction problems during earthquake or ground shaking. Differential settlement may cause distress in the structures founded in the soil mass during earthquake (Ghayoomi et al. 2010). The primary factor controlling settlement in dry sands is cyclic shear strain amplitude during earthquake shaking which is a function of shear modulus at any given depth in a soil deposit (e.g. Tokimatsu & Seed 1987). The settlement behavior of soils during earthquake may differ from those predicted by models based on the isotropic stress conditions (e.g. Tokimatsu & Seed 1987), which can lead to an inefficient or unsafe design. Therefore, to perform an accurate dynamic analysis the shear stiffness and damping ratio must be determined accurately. Shear modulus, G, represents the shear stiffness of soil elements. Shear modulus can be defined as the gradient of τ-γ curve (Ishihara 1996). Regarding this curve, shear modulus of soils changes with strain amplitude (Figure 1.2a). In soil elements subjected to cyclic loading, generated hysteresis loop (Figure 1.2b) represents the effect of shear strain on shear stress (Ishihara 1996). In this case, damping of material is defined as dissipated energy, ΔW, at a cycle of loading over the total energy, W (Ishihara 1996). Dissipated energy over the loading cycle is represented by the white area in Figure 1.2b (hysteresis loop) and total energy is represented by triangular area (hatched area).

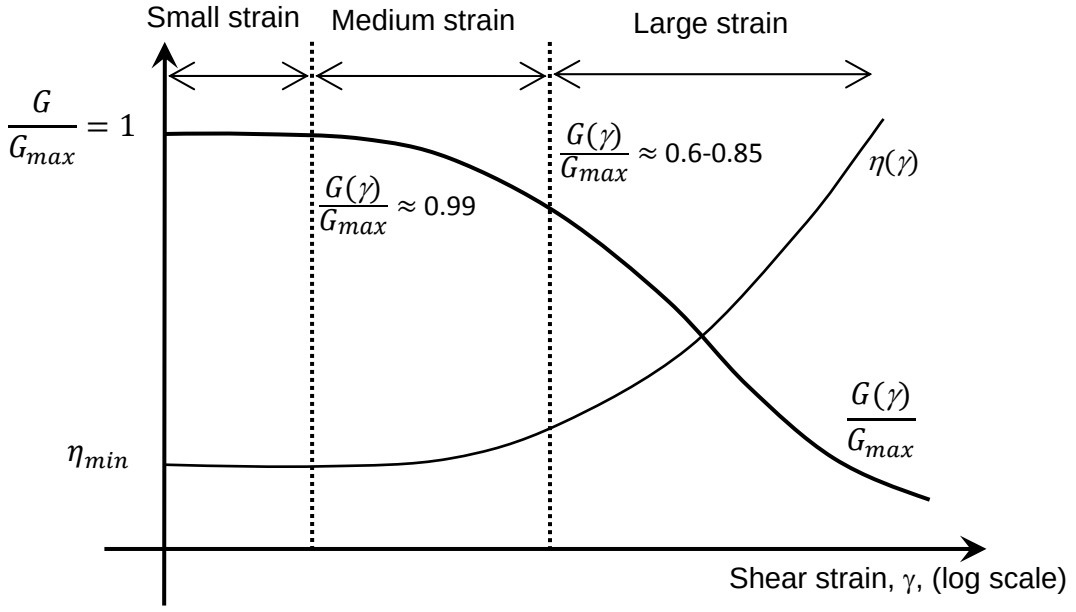

Figure 1.3: Characteristics of shear modulus and damping ratio of soils at different strain levels (Wang & Santamarina 2007)

Shear stiffness and damping ratio are significantly affected by amplitude of shear strain which is important in deposited soils because the stiffness and damping in each layer is related to the amplitude of shear strain in that layer. Figure 1.3 shows a schematic shape of damping and modulus ratio versus amplitude of shear strain in logarithmic scale. This figure shows that the shear modulus decreases with an increase in the amplitude of shear strain and damping ratio increases with an increase in the amplitude of shear strain. The previous studies using resonant column and torsional shear device, e.g. Hardin & Drnevich (1972*b*), Drnevich (1978), Seed et al. (1986) and Wichtmann & Triantafyllidis (2013), confirm that shear modulus at small strain region has the maximum value which is called maximum shear modulus, G_{max}. At this region soil behavior is linear and soil behave nonlinear with further increase in the amplitude of shear strain (Figure 1.3). Material damping ratio at small strain region has the minimum value which is called minimum damping ratio, η_{min} and it increases with further increase in the amplitude of shear strain. In analyzing the response of soil elements when these elements are subjected to small deformations or vibrations, elastic parameters (G_{max} and η_{min}) are applicable for analyzing the response of soils. By increasing the amplitude of deformations, shear modulus, G, and damping ratio, η, will be different in comparison with the initial values. The mechanical properties of soils at medium strain region (Figure 1.3) is so-called intermediate strain properties in the current research work. Small and intermediate strain properties (G_{max}, $G(\gamma)$, $\eta(\gamma)$) of geo-materials are key parameters to analyze the mechanical response of soil elements subjected to small deformation or vibration (Benz 2007). To perform an accurate analysis, especially in deposited soils, stiffness and damping ratio in soil elements must be determined at different level of deformation or vibration accurately. For an example, equivalent linear procedure proposed by Schnable et al. (1972) and developed by Idriss & Sun (1992) is one of the concepts that is applicable to account the nonlinearity of soils using an iterative procedure to obtain values of modulus and damping.

The small and intermediate strain stiffness of soils can be measured using laboratory tests on undisturbed or disturbed soil samples, including: piezoelectric elements (e.g. Jovicic & Coop 1988, Sadek 2006 and Wang & Mok 2008), torsional shear test (e.g. Tatsuoka et al. 1978, Stokoe et al. 1999*a*) and resonant column device (e.g. Hardin & Drnevich 1972*b*, Drnevich 1978 and Wichtmann & Triantafyllidis 2013) or in the field from in-situ tests including: seismic piezo-cone sounding (e.g. Schneider & Mayne 1999 and Stokoe et al. 1999*a*). In-situ geo-physical tests are also available to measure the wave velocity and consequently, stiffness in different soil layers (e.g. Figure 1.4 from Schneider & Mayne 1999).

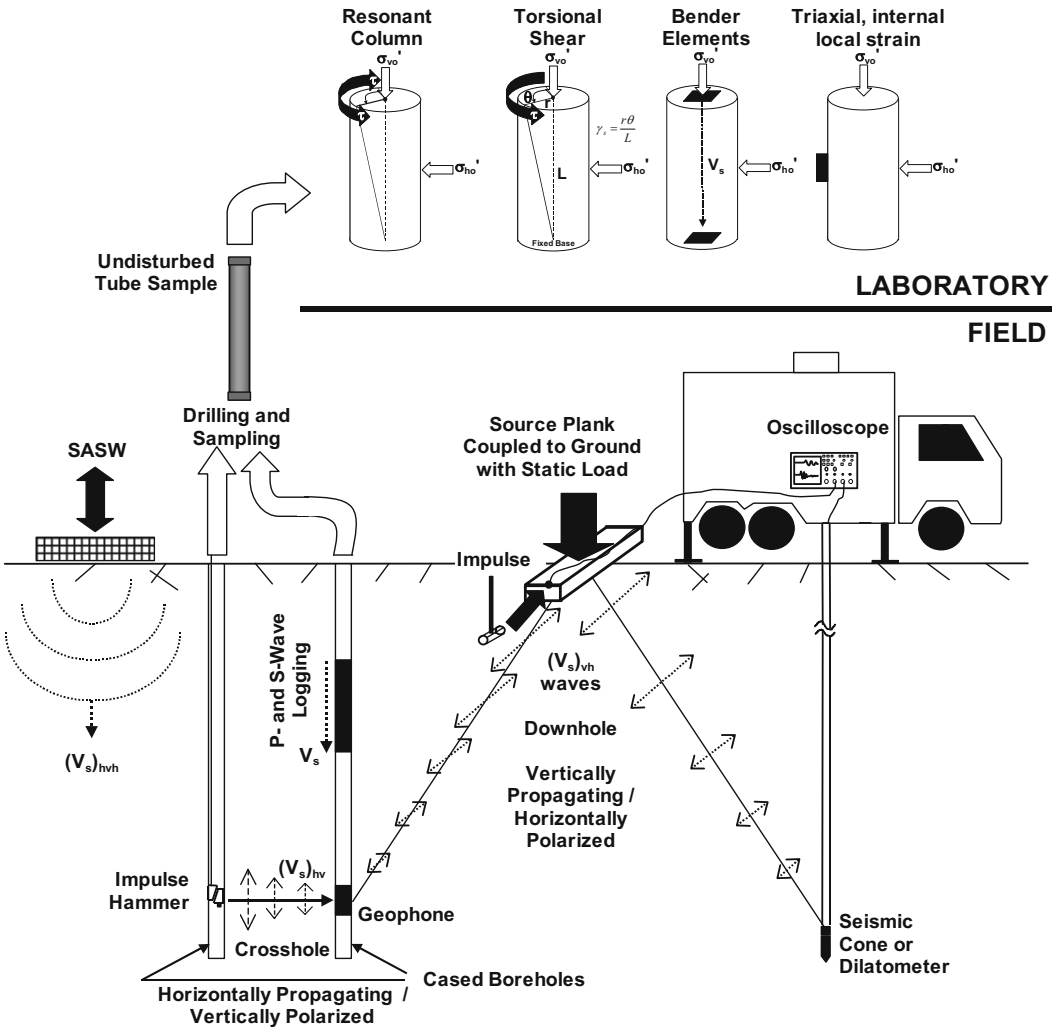

Figure 1.4: Field and laboratory methods to determine shear wave velocity (Schneider & Mayne 1999)

1.2 Background and objective of this study

In the last few decades, a number of cyclic and dynamic laboratory measurements have been conducted for determining the stress-strain properties of granular arrays and natural sands at small to intermediate strain regions. The small and intermediate strain properties includ: i) maximum shear modulus at small strains, G_{max}; ii) the variation of shear modulus with shear strain, $G(\gamma)$; iii) the variation of damping ratio with strain, η; and, iv) the reference shear strain, γ_r.

The effect of various parameters on the small and intermediate strain properties of geo-

materials have been studied in previous works. However, by reviewing the literature, systematic studies on the effect of fines content and stress induced anisotropy are rare and the following gaps can be highlighted.

Part 1: there are soils with the same host sand but with different amount of fines along the geological profile, e.g. Christchurch, New Zealand (Green & Cubrinovski 2010) and Ahmedabad, India (Raju et al. 2004) where both sites severely liquefied during earthquakes. The influence of fine particles on sand force structure, from micro-structure point of view, was presented by Mitchell (1976) and then simplified by Thevanayagam (1998) for other mechanical responses of transition soils. In transition soils, the concept of threshold fines content (f_{thr}) is important for separating "fines-in-sand" and "sand-in-fines" models (Rahman & Lo 2008). Depending on the interaction between fine and sand particles, Thevanayagam (1998) suggested an "equivalent" void ratio, e^* instead of e as an appropriate density index (the concept of e^* is discussed later). Thevanayagam (1999) and Rahman et al. (2012) used the concept of equivalent void ratio for limited published data sets to predict maximum shear modulus in transition soils. However, collected data sets were originally not designed for the evaluation of e^* to capture the effect of f_c on G_{max} and the maximum f_c was only 20%. Thus, a suitable approach for capturing the effect of a wide range of f_c on G_{max}, $G(\gamma)$ and $\eta(\gamma)$ is still a topic of research interest. Furthermore, the effect of f_c on the fabric of soil must be explained through the microscopic observations.

Part 2: from the literature, numerous experimental studies have been done by resonant column device to evaluate the influence of various parameters on the small strain properties of geo-materials but, these studies were restricted to the isotropic stress state. As we know, in soil-structure interaction problems, most of the times we are dealing with soil elements subjected to anisotropic loading. The small and intermediate strain properties of soil elements may be different than the observed results at the laboratory under the isotropic stress state.

Studies on the effect of stress induced anisotropy can be divided into two main groups:1- studies on the small strain properties (G_{max} and η_{min}) and, 2- studies on intermediate strain properties of granular materials ($G(\gamma)$ and $\eta(\gamma)$).

By reviewing the literature (Chapter 2), numerous experimental studies were conducted by piezoelectric elements for evaluating the effect of induced anisotropy on G_{max} (small strain properties) of granular materials, although some of them (e.g. Hardin & Black 1966, Tatsuoka et al. 1979, Yu & Richart 1984, Santamarina & Cascante 1996) used the resonant column device and they concluded that at stress ratio less than two, the effect of stress induced anisotropy on G_{max} is not significant but their studies were restricted to dense samples. Therefore, the effect of density of sample on the maximum shear modulus

must be assessed for different stress paths.
Regarding the literature, studies on the effect of induced anisotropy on intermediate strain properties of granular material are rare, and we can refer to the performed study by Tatsuoka et al. (1979) using a torsional shear device. He studied the effect of stress induced anisotropy on damping ratio and shear modulus for one stress path (confining pressure constant and vertical pressure variable) and reported that the impact of stress ratio on damping is not significant. But, their study was restricted to the stress path with constant confining pressure, however, soil elements may be subjected to more complicated stress conditions in comparison with the stress conditions applied in the existing studies up to now. Therefore, the second goal of this study is to find the effect of stress induced anisotropy, for different stress paths, and density of sample on the small and especially intermediate strain properties of sand. The experimental results are used to present a model for prediction the modulus degradation and damping ratio in the soil samples subjected to stress induced anisotropy for different stress paths.
Experimental methods to measure the small strain stiffness do not cause fabric changes (Santamarina & Aloufi 1999). Therefore, contact parameters, contact forces and contact numbers, will control the response of granular packing at macroscopic level. At microscopic point of view, properties of the particles, interaction laws at the contact level, as well as the distribution of contact- and force-networks, i.e. the micro-structure of the sample, can induce modifications to the shear stiffness of the packing, as measured in experiments. In this work the discrete element method (DEM) is used to study the behavior of the force/contact network during axisymmetric compression with different stress ratio. The orientation of contacts and distribution of forces and also their evolution during the various deformation paths will be discussed. Final goal is to link the modulus in granular materials to the orientation of the normal and tangential force network. Finally, the influence of stress ratio and force network on the maximum shear modulus, modulus degradation and damping is carefully discussed and findings are compared with laboratory results from the resonant column device.
Therefore, the goals of the study are to answer the following questions:

- What is the effect of fines content,"fines-in-sand" and "sand-in-fines", on small and intermediate strain properties of sand samples?
- Is it possible to predict the small strain properties of host sand containing fines content with concept of equivalent granular void ratio?
- What is the effect of stress induced anisotropy for various stress paths on small and intermediate strain properties of sand?

- Is it possible to predict the small and intermediate strain properties of sand subjected to stress induced anisotropy?
- How small strain stiffness is affected by fines content and stress induced anisotropy from the microscopic point of view?

1.3 General concept of the study

Experimental and analytical methods are adopted to find and discuss the effect of fines content and stress induced anisotropy on the small and intermediate strain properties of granular materials. Resonant column device and piezoelectric elements are used for the experimental study. Afterward, Micro-CT scanning and DEM simulation are employed to analyze the experimental results from the microscopic point of view. Finally, the experimental results are used to modify and develop the empirical relationships for predicting the small and intermediate strain properties of granular materials containing fines content and subjected to stress induced anisotropy for different stress paths (Figure 1.5).

Fines content:

Resonant column and piezoelectric element tests will be conducted on the mixture containing wide range of fines content. Two mixtures will be used for this section: i) angular sand mixed with quartz powder ii) highly rounded glass particles mixed with rounded fines glass beads. Micro-CT scanning will be used to discuss the observed experimental results from microscopic point of view. Afterward, the conceptual frame work developed by Thevanayagam (1998) will be assessed to predict the small strain properties of sand in fine and fine in sand mixtures.

Stress induced anisotropy:

Bochum resonant column device will be modified to perform the test on the samples subjected to the stress induced anisotropy for different stress paths. The method of modification and adopted numerical and experimental methods for validation and calibration of modified resonant column device will be discussed in this thesis. Afterward, a series of stress induced anisotropic tests will be conducted on spherical glass particles and angular sand. DEM simulations, using TRUBAL code, will be calibrated with the experimental results on glass bead samples. This analysis will be used to discuses the observed experimental results from microscopic point of view. Then, resonant column tests on sand samples will be used to develop an empirical relation to predict the intermediate strain properties of granular materials. Due to the limitation of device, maximum applied shear strain was about 3×10^{-4} and maximum applied stress ratio was 3.00.

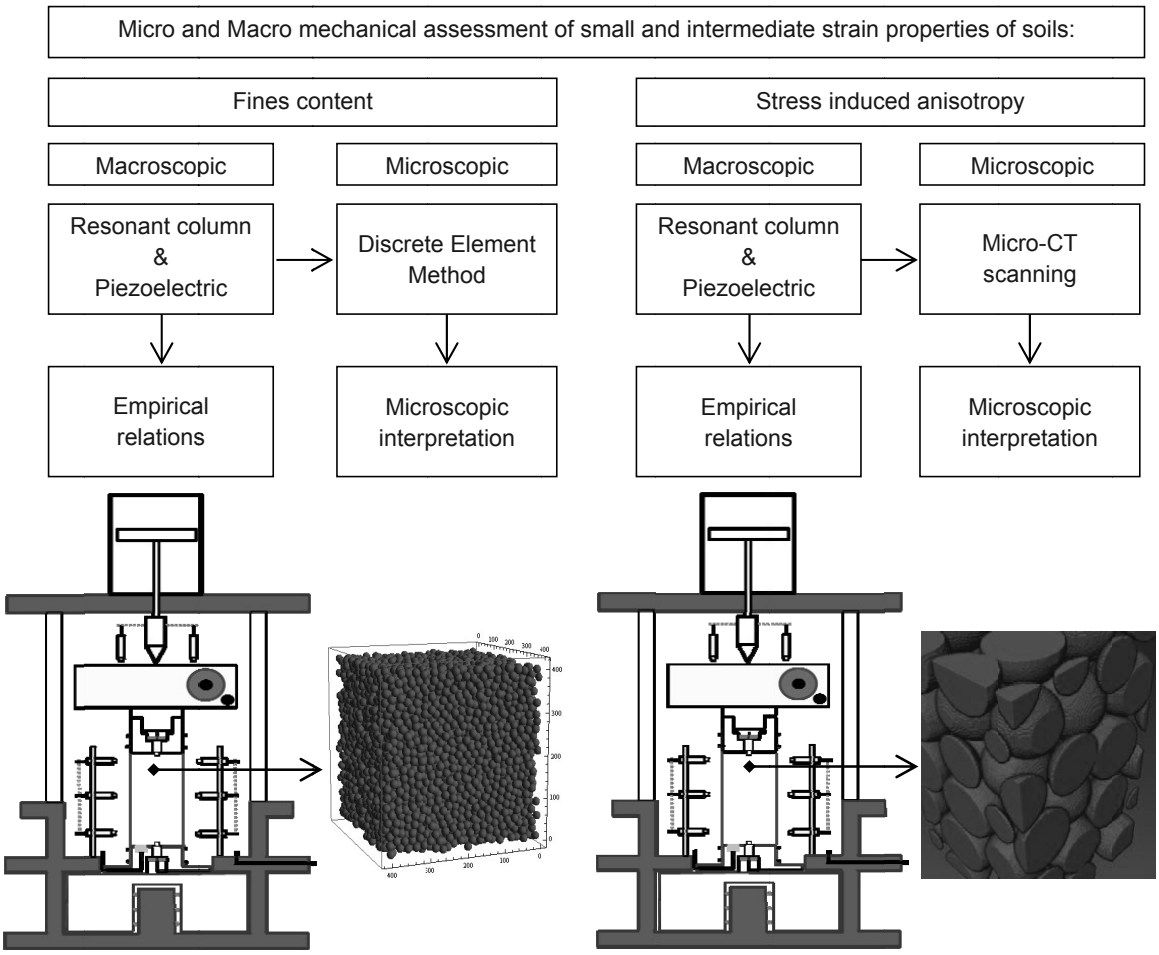

Figure 1.5: Flowchart of experimental work in the current study

1.4 Organization of the dissertation

The thesis consists of seven chapters, of which the content can be briefly described as follows:

Chapter 1: Presents an introduction on this research work.

Chapter 2: Presents a brief literature review on the small strain response of geo-materials, effects of initial conditions, effects of boundary conditions and material properties. This chapter will highlight the performed works on the small strain stiffness, regarding the objective and scope of this research work.

Chapter 3: The experimental program will be discussed in this chapter. This chapter will highlight the adopted procedure and limitations of adopted procedure for approaching to the objective. Calibration, validation and limitation of adopted experimental apparatus (Bochum resonant column device) will be discussed in this chapter.

Chapter 4: Presents the observed experimental results on impact of fine particles on small strain properties of granular materials. Equivalent void ratio concept will be used to discuss the observed experimental results. Furthermore, observed experimental results will be discussed from the microscopic point of view.

Chapter 5: Discrete Element Method, DEM, will be introduced and calibrated in this chapter. Calibrated model will be used to explain the effect of stress induced anisotropy from micro-mechanic point of view.

The experimental results on the effect of stress induced anisotropy on the small strain properties of granular materials will be presented in this chapter. Empirical relations will be modified to predict the maximum shear modulus and damping of sands subjected to anisotropic loading.

Chapter 6: Draws conclusions, gives recommendations, and suggests further areas of study.

2 Literature review

2.1 Introduction

In the past few decades, a number of experimental studies have been conducted for determining the stress-strain properties of granular packings and natural sands at small to intermediate strain regions. The small and intermediate strain properties have included: i) maximum shear modulus at small strains, G_{max}; ii) the variation of shear modulus with shear strain, $G(\gamma)$; iii) the variation of damping ratio with strain, $\eta(\gamma)$; and, iv) the reference shear strain, γ_r. Important experimental results have been presented by Hardin & Richart (1963), Hardin & Black (1966), Hardin & Drnevich (1972*b*), Afifi & Richart (1973), Iwasaki & Tatsuoka (1977), Drnevich (1978), Kokusho (1980), Avramidis & Saxena (1990), Ishibashi et al. (1991), Ashmawy & Drnevich (1994), Jamiolkowski et al. (1995), Cascante & Santamarina (1996), Lo Presti et al. (1997), Chien & Oh (1998), Fioravante (2000), Darendeli (2001), Cascante et al. (2005), Chang et al. (2006), Wichtmann & Triantafyllidis (2009), Clayton (2011) and Wichtmann & Triantafyllidis (2013). The published results indicate that the small and intermediate strain properties of soils are affected by various parameters, e.g. strain amplitude, stress conditions, void ratio, number of loading cycles, degree of saturation, the over-consolidation ratio (OCR), loading frequency, aging, soil gradation, soil structure, and so on. Among these parameters, the mean effective stress, void ratio and shear strain amplitude are the predominant ones.
The effects of some important parameters, including; particle characteristics, void ratio, confining pressure, fines content, sample preparation and stress induced anisotropy, on the small and intermediate strain properties of geo-materials are presented in this chapter. The effects are discussed from the micro-mechanics point of view (at particle contact level), which has a strong connection to particle and contact characteristics. The gaps in our current understanding on the effects of fines content and stress induced anisotropy will be highlighted in this chapter.

2.2 Particle characteristics

Particle characteristics include particle size, particle shape, and mineral composition of particles. From a microscopic point of view, Skinner (1969) performed a series of shear box tests and showed that the coefficient of friction between two spherical glass ballotini increases with an increase in the particle size. From a macroscopic point of view, in spherical arrays, Patel et al. (2008) conducted tests using bender elements and reported that the size dependence of the small strain stiffness is not in line with the results presented for sand samples (Figure 2.1a). However, it appears to be consistent with the results presented by Bartake & Singh (2007), who performed BE tests on three dry sands with similar gradation and found G_{max} increased as the mean particle size of the sand decreased. Gu & Yang (2013), conducted a series of RC and BE tests on glass beads with different particle sizes and concluded that the maximum shear modulus is affected slightly by particle size and G_{max} decreased with increasing particle size in glass bead samples. From the micro-mechanic perspective, Gu & Yang (2013) concluded that the maximum shear modulus is independent of sphere radius.

Hardin & Drnevich (1972a) concluded from the results of resonant column tests that the influence of particle size on maximum shear modulus can be explained through the effect of particle size on void ratio. Ishihara (1996) summarized the published data points as in Figure 2.2 to show the impact of particle size. He concluded that G_{max} decreases with decreasing particle size in the soil samples. Hardin & Kalinski (2005), based on experimental results from the resonant column test, concluded that the value of G_{max} for relatively clean uniform and graded gravels increases with particle size and they defined the particle size function ($f(D)$) to capture the impact of particle size.

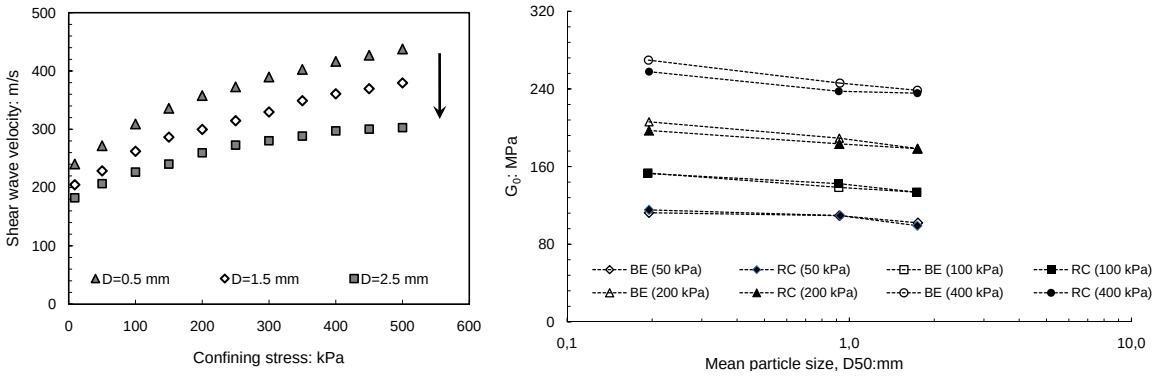

(a) (b)

Figure 2.1: The effect of particle size on: (a) shear wave velocity (Patel et al. 2008); (b) maximum shear modulus (Gu & Yang 2013)

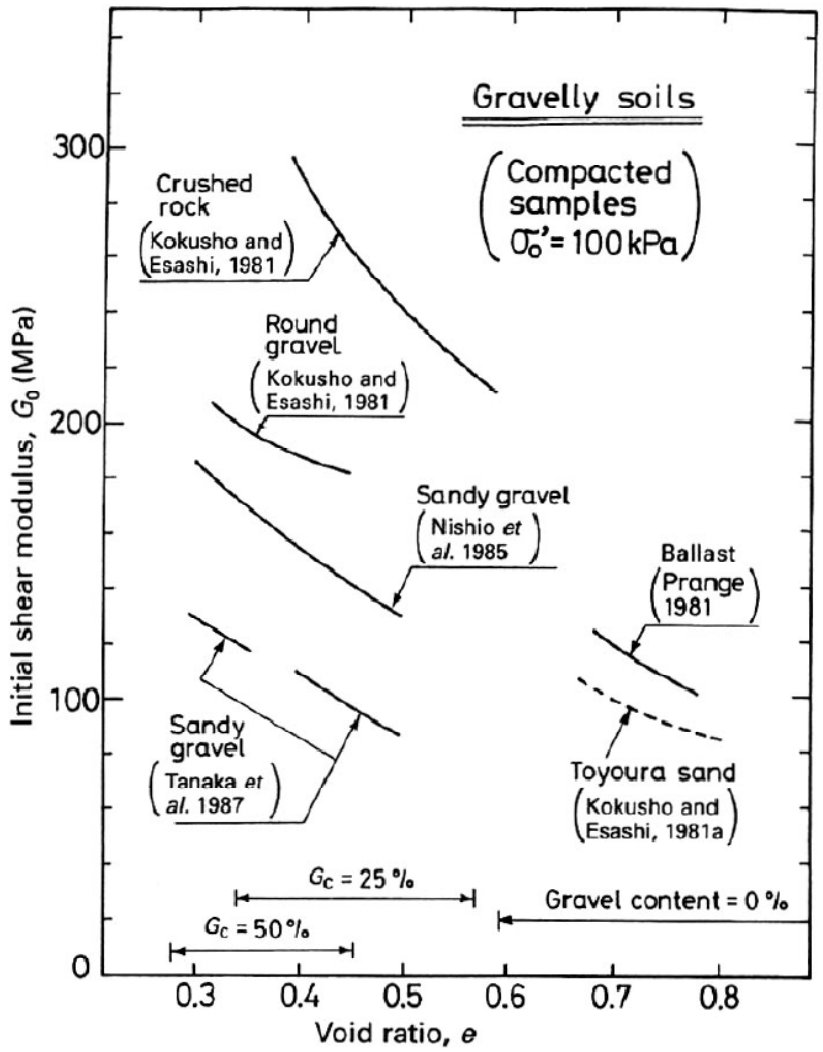

Figure 2.2: The effect of particle size on maximum shear modulus (Ishihara 1996)

The mineral composition of particles is the primary parameter governing many properties of particles. For example, mineral composition controls the specific gravity (Terzaghi et al. 1996) and the particle elastic constants, i.e. Young's modulus, shear modulus, and Poisson´s ratio (Mitchell & Soga 2005). Furthermore, the elastic constants influence contact properties, such as contact area, contact pressure, and consequently, contact stiffness (Hertz 1882). Mineral composition is also a key parameter influencing particle surface properties such as water adsorption/absorption, and electro-chemical bonding, especially for fine particles such as clay (Mitchell & Soga 2005). Many researchers (e.g. Koerner 1970, Procter & Barton 1974) have suggested that the particle mineral composition significantly influences the inter-particle friction coefficient.

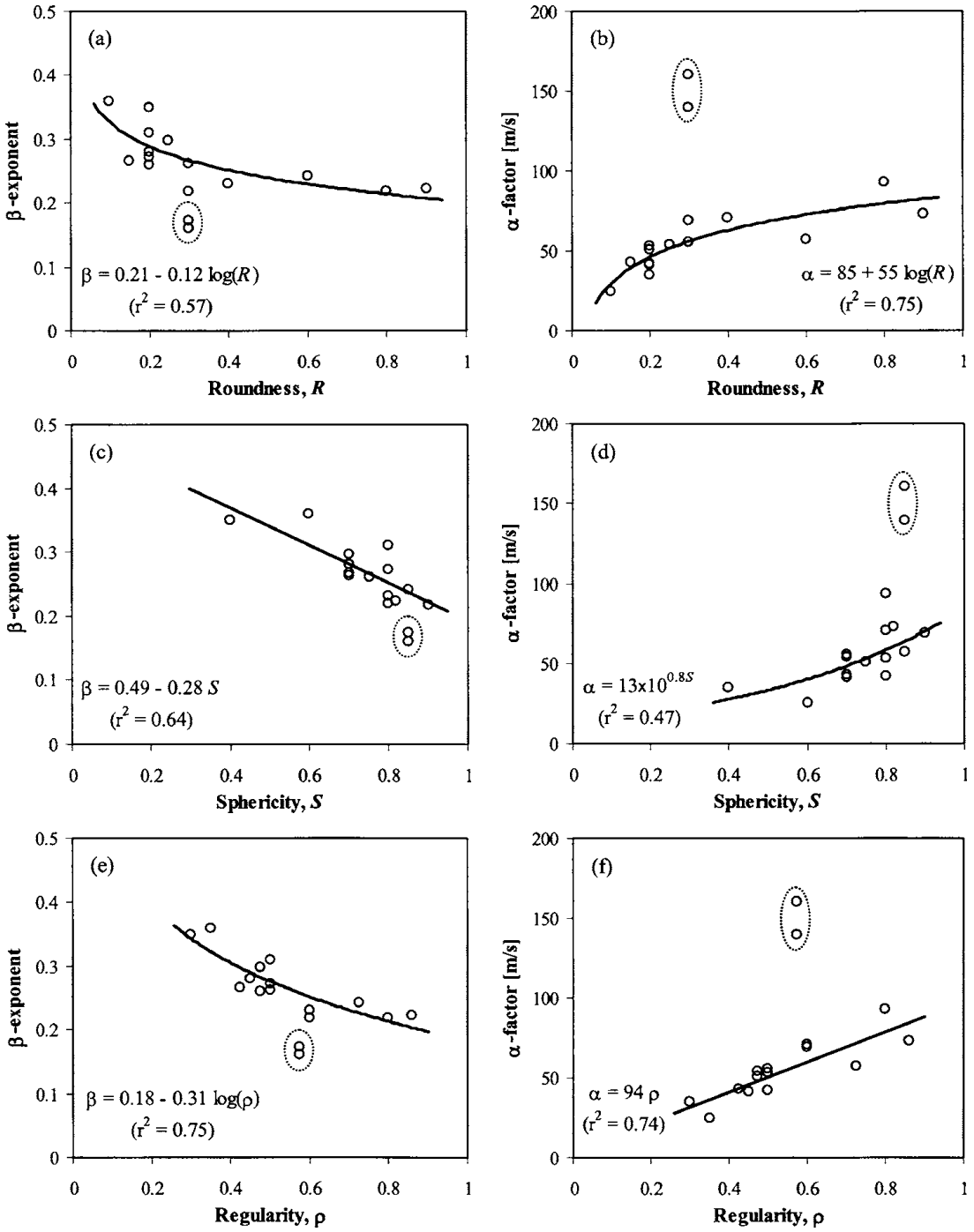

Figure 2.3: The effect of particle shape on constant parameters of shear wave velocity, $V_s = \alpha(\sigma_0)^\beta$, (Cho et al. 2006)

Particle shape is an inherent soil characteristic that plays a major role in the mechanical behaviour of soils (Mitchell & Soga 2005). Barrett (1980) suggested that particle shape

includes three independent properties, particle form, particle roundness, and surface texture or particle roughness. Koerner (1970), Miura et al. (1997), Cho et al. (2006) and Reddy (2008) have shown that the void ratio range, $e_{max} - e_{min}$, is a function of particle form and particle roundness/angularity. Bowden & Tabor (1950) have suggested that particle roughness strongly influences inter-particle friction. It is recognized that particle shape controls the fabric of soils, e.g. particle and contact orientations and type of contacts (Mitchell & Soga 2005).
Cho et al. (2006) mounted piezoelectric elements in an oedometer device and studied the influence of particle shapes on shear wave velocity and they reported that the increase in the particle irregularity (angularity and/or eccentricity) leads to a decrease in stiffness (Figure 2.3). Shin & Santamarina (2013) studied the influence of particle shape on the mechanical behaviour of soils. They measured wave velocity in mixtures containing rounded Ottawa 20-30 sand and angular blasting sand using bender elements installed in the oedometer cell. From the experimental results, they reported that G_{max} increased by increasing the mass fraction of angular particles.
Yang & Wei 2012 performed a series of undrained triaxial tests on the mixtures containing angular and rounded coarse and fine particles. They concluded that the behaviour of mixtures strongly depends on the shape of coarse and fine particles.

2.3 Void ratio

Void ratio is a packing characteristic and has a significant effect on the maximum shear modulus. From a micro-mechanics point of view, the effect of void ratio can be explained through the number of contacts (Figure 2.4). As can be seen in Figure 2.4, the number of contacts decreases significantly with an increase in the void ratio. The effect of void ratio on the maximum shear modulus can be explained through the coordination number, CN, from the micro-mechanic points of view (Section 5.2). It has been shown that CN strongly depends on the void ratio, e.g. Smith et al. (1929), Field (1963), Oda (1972), Oda (1977), Yanagisawa (1983) and so on.
At a macroscopic level, experimental evidence confirms that the value of G_{max} decreases with an increasing void ratio (Figure 2.5). The impact of void ratio on maximum shear modulus is captured through void ratio function ($f(e)$) which was developed by Hardin & Drnevich (1972*b*). Other researchers in the past few decades, in relation to their experimental results, have proposed various void ratio functions which are summarized in

Table 2.1. In contrast, the curves $G(\gamma)$ and $\eta(\gamma)$ are rather independent of soil density or void ratio (e.g. Tatsuoka et al. 1978, Kokusho 1980, Wichtmann & Triantafyllidis 2013).

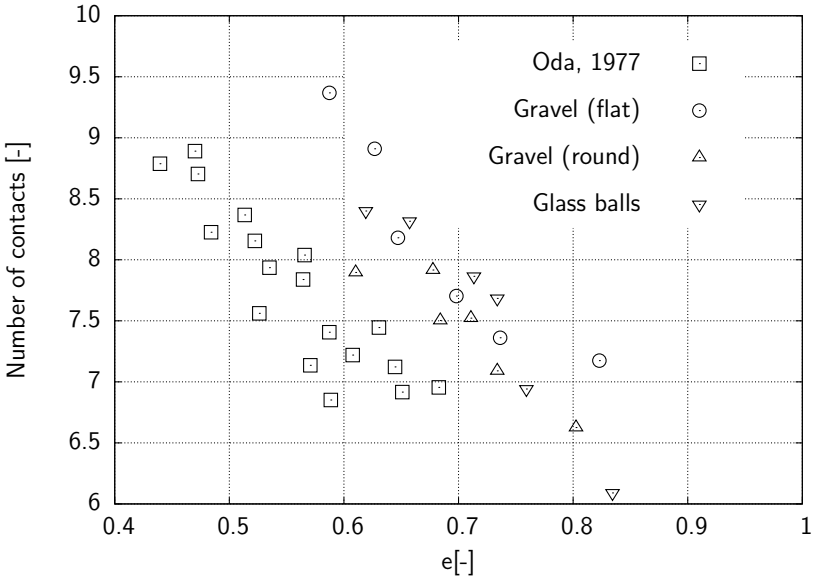

Figure 2.4: Contact number versus void ratio, modified after Yanagisawa (1983)

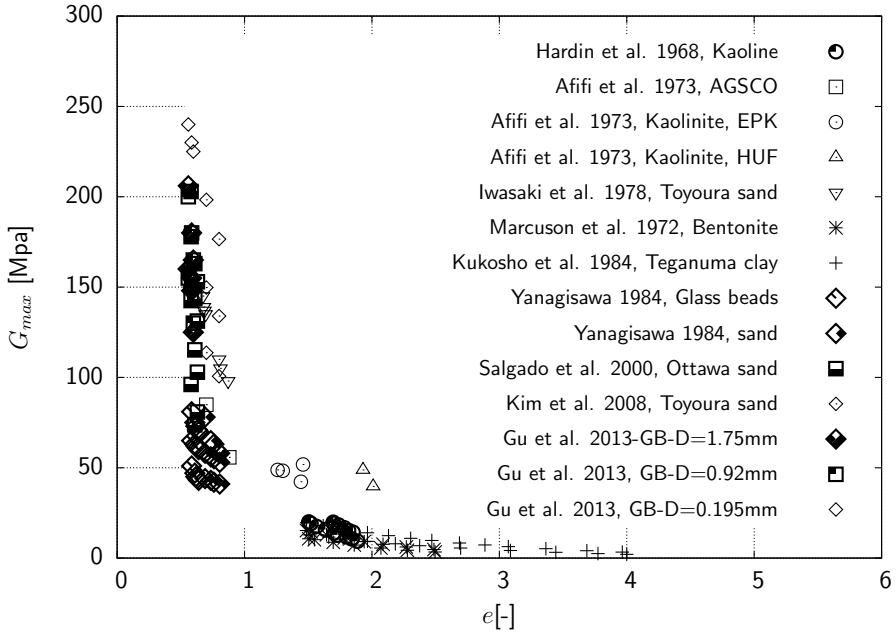

Figure 2.5: Maximum shear modulus versus void ratio from published experimental results, modified after Bui (2009)

Table 2.1: Some of the main void ratio functions from the literature, modified after Bui (2009)

Soil	e	$f(e)$	n	Ref.
Ottawa sand	-	$\frac{(2.174-e)^2}{1+e}$	0.5	Hardin & Black (1966)
Crusged Quartz	-	$\frac{(2.973-e)^2}{1+e}$	0.5	Hardin & Black (1966)
Kaolinite		$\frac{(2.97-e)^2}{1+e}$	0.5	Hardin & Drnevich (1972b)
Bentonite	1.5-2.5	$\frac{(4.4-e)^2}{1+e}$	0.5	Marcuson & Whals (1972)
Teganuma Clay	1.5-4	$\frac{(7.32-e)^2}{1+e}$	0.45	Kokusho et al. (1982)
Quiou sand	0.9-1.1	$e^{-1.3}$	0.62	Lo Presti et al. (1997)
Toyoura sand	0.81-0.95	$e^{-1.3}$		Lo Presti et al. (1997)
Ticino sand	0.81-0.95	$\frac{(2.27-e)^2}{1+e}$	0.43	Lo Presti et al. (1993)
reconstituted clay	-	$(1+e)^{-2.4}$	0.5	Shibuya et al. (1997)
Kenya carbonate sand	0.81	$e^{-0.8}$	0.516	Fioravante (2000)
Quartz sand	0.4-0.85	$\frac{(1.8-e)^2}{1+e}$	0.42	Wichtmann & Triantafyllidis (2009)
Glass beads	0.58-0.65	$e^{-3.98}$	0.403	Goudarzy et al. (2014)

2.4 Confining pressure

Stiffness of granular materials depends on the micro-structural properties, mainly, particle and contact properties. However, for a given material, particle properties may remain the same and contact properties will have the major contribution to the variation in packing stiffness. According to the Hertz-Mindlin's theory, the normal and tangential stiffness are function of contact forces and the elastic properties of a particle (Johnson 1985 and Yimsiri & Soga 2002).

$$K_T = L_2 K_N \big[1 - \frac{F_T}{F_N \tan\phi}\big]^{\zeta} \tag{2.1}$$

Where K_N is the normal stiffness ($K_N = L_1 F_N^{\Omega}$), L_1 and L_2 are related to the particle properties, ζ and Ω are material constants (ζ=Ω=1/3, Yimsiri & Soga 2002), F_N and F_T are normal and tangential forces at contact points, and ϕ is the friction angle between two particles.

The effect of confining pressure on the distribution of contact forces have also been studied in recent decades (e.g. Petrakis et al. 1988, Rothenburg & Bathurst 1989, Ng & Petrakis 1996, Wang & Mok 2008).

Several authors (e.g. Gassmann 1951, White & Sengbush 1953, Brandt 1955) calculated

the influence of isotropic confining pressure on wave velocity for various arrays of smooth and rough spheres. Also, they concluded that both velocities increase proportionally to $\sigma_0^{1/6}$. Based on Hertz's theory, Duffy & Mindlin (1957) and Duffy (1959) theoretically concluded that the tangential stiffness of sphere packing is proportional to the cubic root of effective stress ($\sigma^{1/3}$). For regular packing, Petrakis & Dobry (1987), and for random packing of sphere, Walton (1987) and Liao et al. (2000) have shown that the exponent of isotropic pressure is equal to 1/3.

At a macroscopic level, it is well-known that G is related to σ^n; the exponent n can be used as an indicator of the type of contact which can be a value from 1/3 for spherical contacts to 1/2 for cone to plane contacts (Cascante & Santamarina 1996). Experimental works conducted by many researchers with various soils show that G_{max} increases in an exponential manner with mean effective stress. A summary of determined values for stress exponent, n, is presented in Table 2.1. This table shows the exponent n in practice varies from 0.4 to 0.62 and the value of 0.5 was proposed by many researchers.

From a microscopic point of view, dissipation of energy between two particles (Figure 2.6a) subjected to the sinusoidal oscillation is written as Equation 2.2 (Johnson 1985).

$$\Delta W = \frac{9\mu^2 F_N^2}{10R}\left(\frac{2-\nu_1}{G_1}+\frac{2-\nu_2}{G_2}\right)\left[1-\left(1-\frac{Q}{\mu F_N}\right)^{5/3}-\frac{5Q}{6\mu F_N}\left[1-\left(1-\frac{Q}{\mu F_N}\right)^{2/3}\right]\right] \quad (2.2)$$

When the amplitude of oscillation is too small ($\mu F_N >> Q$), the Equation 2.2 is summarized to Equation 2.3 (Johnson 1985).

$$\Delta W = \frac{1}{36R\mu F_N}\left(\frac{2-\nu_1}{G_1}+\frac{2-\nu_2}{G_2}\right)Q^3 \quad (2.3)$$

where, G_1 and G_2 are shear stiffness of particles, ν_1 and ν_2 are Poisson's ratio of particles, μ is the friction coefficient between particles, F_N is the normal contact force between particles, Q is the amplitude of oscillation, R is the particle radius. Damping ratio is defined as dissipated energy (ΔW) at one cycle of loading over the total energy (W), $\eta = \frac{\Delta W}{2\pi W}$, (Ishihara 1996). For two particles with the same properties, total energy (W) is the area of the hatched part in Figure 2.6b, $W = (Q \times \delta)/2$. Equation 2.3 was used to determine the dissipated energy between two particles subjected to a low amplitude of oscillation. Then damping between two particles, with the same properties, subjected to oscillation, can be determined using Equation 2.4 (Bui 2009).

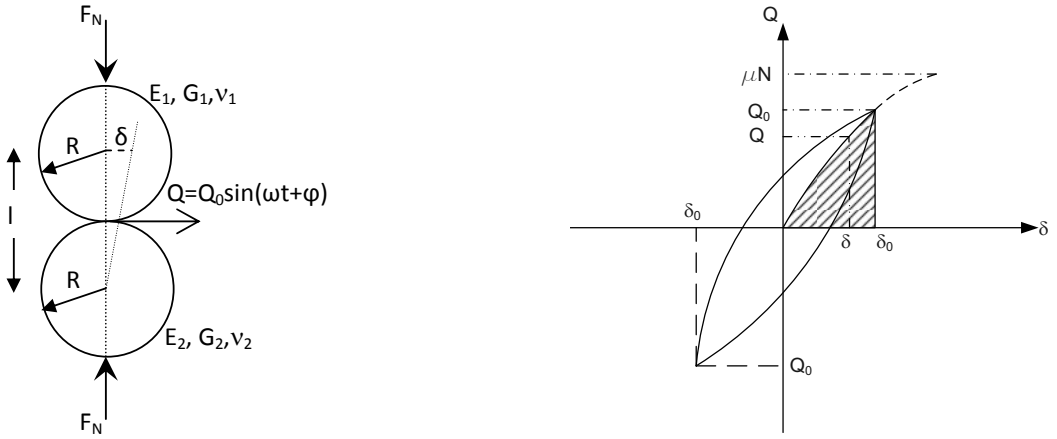

(a) (b)

Figure 2.6: Dissipation of energy between two particles subjected to oscillation: (a) particles subjected to oscillation (b) hysteresis loop (Johnson 1985)

$$\eta = \frac{8Q^2 l}{18\pi\mu^2 F_N^2 \left[1 - \left(1 - \frac{Q}{\mu F_N}\right)^{2/3}\right]} \tag{2.4}$$

The relative tangential displacement of the two particles (Figure 2.6a) is found by Equation 2.5 (Johnson 1985).

$$\delta = \frac{3\mu F_N}{16a}\left(\frac{2-\nu_1}{G_1} + \frac{2-\nu_2}{G_2}\right)\left[1 - \left(1 - \frac{Q}{\mu F_N}\right)^{2/3}\right] \tag{2.5}$$

where, a is the Hertz contact area. With regard to Figure 2.6a, shear strain for two particles with the same properties is equal to $\gamma = \delta/l$. Thus, from Equation 2.5 the value of γ can be determined by Equation 2.6 (Bui 2009).

$$\gamma = \frac{3\mu F_N}{8al}\left(\frac{2-\nu}{G}\right)\left[1 - \left(1 - \frac{Q}{\mu F_N}\right)^{2/3}\right] \tag{2.6}$$

From the presented relations at a microscopic level, it can be concluded that particle characteristics, contact force and amplitude of oscillation are factors influencing the damping ratio in the small strain region.

Experimental works confirm that damping ratio is significantly affected by mean effective stress at macroscopic level (e.g. Tatsuoka et al. 1978, Kokusho 1980 and Wichtmann & Triantafyllidis 2013). The experimental results show that damping ratio decreases with an increase in the mean effective stress.

2.5 Empirical relationships

Research efforts, since 1960's, have advanced our understanding of the factors and how they affect G_{max}, $G(\gamma)$ and $\eta(\gamma)$ which has led to the development of various prediction models which are applicable to the computer programs for site response analysis. Earlier studies recognized that G_{max}, $G(\gamma)$ and $\eta(\gamma)$ for soils depend on the packing density and mean effective stress (Hardin & Black 1966, Hardin & Drnevich 1972*b*, Drnevich 1978, Tatsuoka et al. 1978, Seed et al. 1984). From the experimental results using the resonant column device, Hardin & Black (1966) proposed one of the most widely used empirical relationship that considers the effect of density through void ratio (e) and p' to predict G_{max} of a soil. This relationship is referred as Hardin's relation which is represented by the following general form (Equation 2.7):

$$G_{max} = Ap_a(\frac{p'}{p_a})^n f(e) \tag{2.7}$$

where, A is a material constant which depends on soil type, p_a is atmospheric pressure (100 kPa), p' is mean effective stress, n is an exponent and $f(e)$ is the void ratio function. Seed et al. (1984) also proposed a relationship between G_{max} and p' as G_{max}=218.8 $K_{2,max}(p')^{0.5}$ (in SI unit), where $K_{2,max}$ may be a function of e. Although the above relationships were adequate to predict G_{max} for a particular soil, the evaluation of their relative performance with a large data set is rare. Also, the effect of particle shape, size and their distribution for different type of soils were not considered in the above relationships. Recent studies show that particle size and their distribution have a significant effect on G_{max} (Darendeli 2001, Menq 2003, Hardin & Kalinski 2005, Wichtmann & Triantafyllidis 2009, Wichtmann & Triantafyllidis 2013 and Wichtmann & Triantafyllidis 2014). Wichtmann & Triantafyllidis (2009) studied the effect of grain size distribution on small and intermediate strain properties of sand samples using the Bochum resonant column device. They suggested a correlation for fitting parameters of Hardin's relation to C_u and d_{50}. Hardin & Kalinski (2005) studied the influence of particle size and reported that G_{max} increased with particles size for uniform graded gravelly sands and Hardin's relation can be a function of particle size, $f(D)$.

Empirical relationships were also developed by Hardin & Black (1966) and Roesler (1979) to predict the maximum shear modulus (G_{max}) in the samples subjected to stress induced anisotropic conditions. Hardin & Black (1966) believed that shear stress has an insignificant effect on shear modulus, and thus concluded that Equation 2.8 can be used to predict the maximum shear modulus with sufficient accuracy.

$$G_{max} = Af(e)p_a^{(1-n)}(\frac{\sigma_1 + \sigma_3}{2})^n \tag{2.8}$$

where, A is the dimensionless coefficient, $f(e)$ is a void ratio function, n is the empirical stress exponent and p_a is atmospheric pressure. Roesler (1979) performed experimental studies on cubic soil samples to evaluate the effects of stress components on shear wave velocity under anisotropic loading. Roesler (1979) modified general Hardin's relation based on the stress components (Equation 2.9).

$$G_{max} = Af(e)p_a\left(\frac{\sigma_1}{p_a}\right)^{n_1}\left(\frac{\sigma_2}{p_a}\right)^{n_2}\left(\frac{\sigma_3}{p_a}\right)^{n_3} \tag{2.9}$$

where, n_1 and n_3 are the empirical stress exponents for vertical and horizontal stress respectively; σ_2 is horizontal stress (out of plan stress) and p_a is atmospheric pressure. Based on the studies conducted by Bellotti et al. (1996) and Sadek et al. (2007), n_2 is approximately zero. Thus, Roesler's relation can be applied for cylindrical samples in a resonant column device. A Summary of determined values for stress exponents of sample subjected to stress induced anisotropic tests is presented in Table 2.2.

After Roesler (1979), Yu & Richart (1984) studied the effects of the stress ratio on the maximum shear modulus (G_{max}) of soils subjected to a stress ratio of more than two. From the observed experimental results, they proposed a reduction factor for Roesler's and Hardin's relationships.

Empirical relationships were also developed and modified to predict the modulus degradation and damping of granular materials.

Table 2.2: The obtained fitting parameters for relationships 2.8, 2.9 from previous works, (Modified after Wang & Mok 2008)

		Isotropic	Anisotropic		
Test Method	Material	n	n_1	n_3	Researcher
Cubical sample	Fine sand	0.512	0.298	0.214	Roesler (1979)
Resonant column	Ottawa sand	-	0.25	0.28	Yu & Richart (1984)
	Brazil sand	-	0.24	0.28	
Cylindrical chamber	Ticino sand	0.54	0.24	0.30	Lo Presti & O'Neill (1991)
Resonat column	Barco sand	0.54	0.20	0.34	Santamarina & Cascante (1996)
Triaxial	Ticino sand	0.44	0.272	0.168	Fioravante (2000)
specimen	Kenya sand	0.52	0.244	0.272	
True triaxial box	Toyoura sand	0.483	0.27	0.27	Wang & Mok (2008)

Hardin & Drnevich (1972*a*) proposed a well known empirical relationship (Equation 2.10) to predict the backbone curve in nonlinear behavior of soil elements. Hardin's relation is based on two main parts: maximum shear modulus and reference shear strain.

$$\frac{G}{G_{max}} = \frac{1}{1 + \frac{\gamma}{\gamma_r}} \tag{2.10}$$

where G_{max} is the maximum shear modulus, γ is shear strain and γ_r is the reference shear strain. while γ_r determined at $G/G_{max} = 0.5$ would be the most objective way, the stiffness curves obtained from the resonant column tests were in the range of G/G_{max} of 0.68 to 1.0 for clean sand, which would not give a reliable γ_r. However, γ_r can be estimated from Equation 2.11:

$$\gamma_r = \frac{\tau_r}{G} \tag{2.11}$$

where, τ_r is the shear stress corresponding to γ_r at G/G_{max} equal to 0.5.
Also, Hardin & Drnevich (1972*a*) proposed Equation 2.12 to predict the modulus degradation.

$$\frac{G}{G_{max}} = \frac{1}{1 + \frac{\gamma}{\gamma_r}[1 + \beta \exp(-\frac{\gamma}{\gamma_r})]} \tag{2.12}$$

where α and b are fitting curve parameters and γ_r is the reference shear strain.
The value of reference shear strain is defined as (Hardin & Drnevich 1972*a*):

$$\gamma_r = \frac{\tau_{max}}{G_{max}} \tag{2.13}$$

where, τ_{max} is the peak shear strength which is determined by Equation 2.14 and G_{max} is the maximum shear modulus (Hardin & Drnevich 1972*a*).

$$\tau_{max} = \sigma_v \left[\left(\left(\frac{1 + (\frac{\sigma_3}{\sigma_1})}{2} \right) sin\phi \right)^2 - \left(\frac{1 - (\frac{\sigma_3}{\sigma_1})}{2} \right)^2 \right]^{1/2} \tag{2.14}$$

where, ϕ is the friction angle, σ_3 and σ_1 are the confining pressure and the vertical stress respectively. Tatsuoka et al. (1979) showed that Equation 2.13 and Equation 2.14 are not valid for determining the reference shear strain in samples subjected to stress induced anisotropy.
The dependency of γ_r on the confining pressure can be described as (Stokoe et al. 1999*b*):

$$\gamma_r = \gamma_{r1} \left(\frac{p'}{p_a} \right)^{\kappa} \tag{2.15}$$

where, γ_{r1} is the reference shear strain when the confining pressure is equal to 100 kPa, p_a is the atmospheric pressure (assumed 100 kPa) and κ is the stress exponent.

Additionally, in the cases that there is not information about the shear strength of materials, the normalization of γ can be done by $\sqrt{\frac{p'}{p_a}}$ instead of γ_r which is valid for soil elements subjected to isotropic loading (Hardin & Kalinski 2005).
Furthermore, damping can be written as a function of modulus degradation (Zhang et al. 2005).

$$\eta - \eta_{min} = c_1(\frac{G}{G_{max}})^2 - c_2\frac{G}{G_{max}} + (c_2 - c_1) \tag{2.16}$$

where c_1 and c_2 are constant parameters and η_{min} is the minimum damping at small strain region. Following a review of the literature we can see that a systematic study is essential to evaluate the effects of stress ratio and stress path on modulus degradation and damping in granular materials. Furthermore, the empirical relationships must be assessed to predict the modulus degradation and reference strain (γ_r) in soil elements subjected to anisotropic loading.

2.6 Fines content

Previous studies have been mainly confined to either clean sands or gravel. Systematic studies on transition soils (i.e. clean sand mixed with fine particle, $d \leq$0.075mm) containing a wide range of fines content are rare, although transition soils are not uncommon. A recent example of such transition soil is the many liquefied sites in Christchurch, New Zealand, due to the Darfield earthquake (2010) where clean sand has almost the same grain size distribution but is mixed with different percentage of fines content, f_c (Green & Cubrinovski 2010).
The effect of fine particles on sand force structure, from a micro-structure point of view, was presented by Mitchell (1976) and then simplified by Thevanayagam (1998) for other mechanical responses of transition soils. When fine particles are sufficiently smaller than sand particles, all fine particles do not contribute in sand force structure when loaded. Thus, by neglecting some fine particles in sand force structure, Thevanayagam (1998) suggested an "equivalent void ratio", e^*, instead of e as an appropriate density index (the concept of e^* is discussed later). Thevanayagam & Liang (2001) assumed secant modulus at axial strain of 0.0005 from a triaxial test as G_{max} for Foundary Sand with up to 25% non-plastic f_c (fines with PI=0), and reported that the effect of f_c can be captured by replacing e by e^* in Equation 2.7. However, the process of obtaining e^*, during that time, was essentially a back analysis process which limits the applicability of Hardin's relation (Equation 2.7). Rahman et al. (2012) estimated e^* from soil grading properties and used

this in Hardin's relation to capture the effect of fines for collected data sets. They reported that e^* in Equation 2.7 can capture the effect of non-plastic fines. However, collected data sets were not designed for the evaluation of e^* to capture the effect of f_c on G_{max} and the maximum f_c covered was only 20%. Thus, a suitable approach for capturing the effect of non-plastic f_c on G_{max} is still a topic of research interest.

From a macroscopic point of view, a systematic study on the effect of fine particles on G_{max} was first presented by Iwasaki & Tatsuoka (1977). Two clean sands, Iruma Z1 and Iruma W, were mixed with a different percentage of non-plastic f_c and resonant column tests were conducted to assess the effect of fines content (Figure 2.7). With regard to the experimental results, Iwasaki & Tatsuoka (1977) concluded that the value of G_{max}, obtained from resonant column test, decreased with an increase in f_c (Figure 2.7). Based on the bender element tests, Salgado et al. (2000) also reported that G_{max} for Ottawa sand decreased with an increase in non-plastic f_c. Tao et al. (2004) performed cyclic torsional shear tests on thin hollow cylindrical samples to evaluate the effect of fines content on the stress-strain behaviour of sands obtained from the San Fernando dam. From the experimental results, they observed that G_{max} decreased with an increase in the non-plastic f_c up to 28% and then G_{max} increased with f_c of more than 28% (Figure 2.7). Chien & Oh (2002) conducted a series of resonant column test on Yun-Ling sand. They observed that G_{max} increased with f_c up to f_c of 20% and then it decreased with further increase of f_c. Carraro et al. (2009) performed a series of tests with sands containing fines content using bender elements installed in the triaxial device. They reported that the effect of non-plastic f_c on G_{max} is more than plastic f_c and there was a general trend of decreasing G_{max} with non-plastic f_c. Wichtmann et al. (2015) performed a series of RC tests on a sand containing limited amount of fines content ($f_c < 20\%$). They found that G_{max} decreases and damping ratio increases with an increase in fines content but their study was limited to the fines content of less than 20%.

Some efforts have been observed to capture the effects of non-plastic f_c within the framework of Hardin's relationship (Equation 2.7). Salgado et al. (2000) suggested that constant parameters, A and n, in Hardin's relationship might be affected by f_c. Iwasaki & Tatsuoka (1977) reported that parameter A was affected by f_c while other parameters remain constant. Therefore, They proposed a reduction factor for Hardin's relationship.

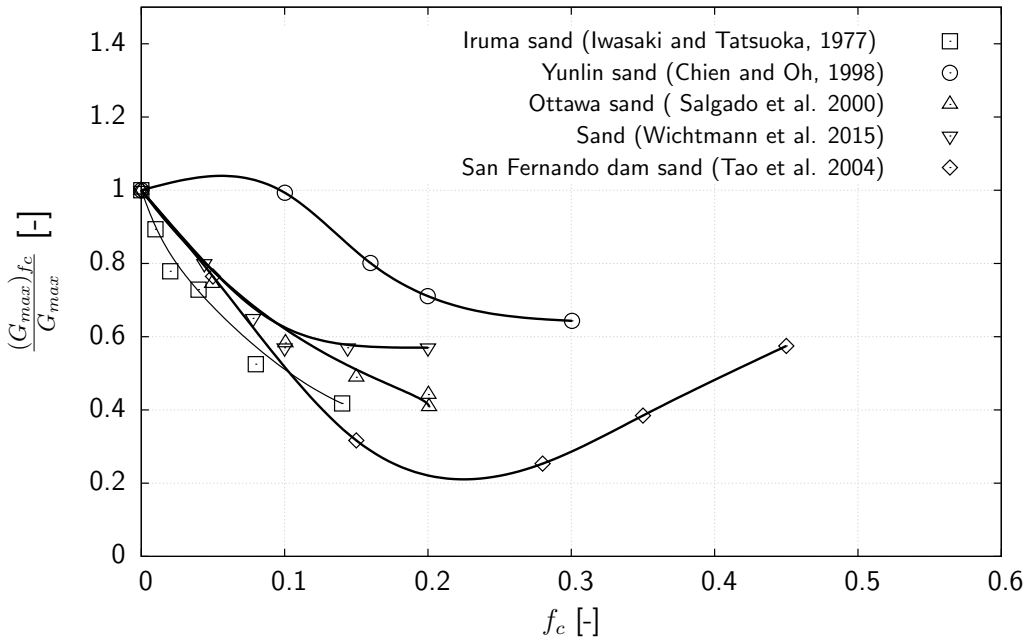

Figure 2.7: The effect of fines content on maximum shear modulus, G_{max}

However, the variation of reduction factor with f_c are different for different host sands with fines (Figure 2.7). Wichtmann et al. (2015) correlated the fitting parameters of Hardin's relationship to f_c.

In this research the resonant column test will be conducted on clean Hostun Sand as well as on clean Hostun Sand containing non-plastic fines, to find the effect of wide range of fines content on small and intermediate strain properties of granular materials. Furthermore, the relative performance of Hardin's formulation (Equation 2.7) with the concept of the equivalent granular void ratio, e^*, will be discussed.

2.7 Sample preparation and fabric

Granular materials consist of discrete particles and voids between particles. Therefore, the response of such a discrete medium highly depends on the particle characteristics, e.g. stiffness, shape and angularity, contact characteristics and the arrangement of particles and contacts in assembly. Practically, soil structures, natural or man-made, are influenced by the generation procedure and gravitational field which induce an anisotropic fabric. During the deposition of soil particles, particles tend to be oriented in some preferred directions, initial inherent anisotropy in the soil structure, which eventually affects the

engineering properties of granular soils. The term fabric refers to the arrangement of particles, particle groups and pore spaces in a soil (Mitchell & Soga 2005). It is reasonable to assume that different sample preparation methods produce different soil fabrics and the macroscopic behaviour of granular material (i.e. stiffness and anisotropy) strongly depends on the fabric of granular assemblies (Oda 1972). Oda (1972) studied the effect of initial fabric, with different sample preparation, on the shear strength of two materials: 1- elongated particles and 2- spherical particles. They did triaxial tests on the prepared samples and observed that the effect of sample preparation on the peak stress ratio of the sample containing spherical particles was not obvious, however, a significant effect was observed for samples containing elongated particles which was due to the contact and particle orientation. Mahmood & Mitchell (1974) performed tests using direct shear test to show the effect of fabric on the shear strength of fine granular materials. They showed that grain arrangement and pore size distributions are different when samples are deposited in different ways. Tatsuoka et al. (1986) studied the effect of sample preparation on the cyclic undrained stress-strain behaviour of sand using triaxial and torsional shear tests. They prepared samples using four methods: air-pluviation, wet-tamping, wet-vibration and water-vibration. They reported that the cyclic undrained torsional shear strengths and cyclic undrained triaxial strengths were strongly affected by sample preparation methods. Vaid et al. (1999) performed a series of triaxial and direct shear tests on the Fraser River sand samples provided with different sample preparation. Samples were prepared by moist tamping, air pluviation, and water pluviation. From their experimental observations, they concluded that the sample preparation has a significant influence on the static undrained behavior of Fraser River sand. Wang & Mok (2008) performed a series of tests on Toyoura sand and rice particles using true triaxial device. From experimental observations, they concluded that the fabric-induced stiffness anisotropy increases with an increase in the aspect ratios of particles, which is the length ratio between the major and minor axes. Ezaoui & Di Benedetto (2009) studied the effect of sample preparation on the maximum moduli of Hostun sand using piezoelectric elements that were installed in the triaxial device. They prepared samples using three methods: i) pluviation method, ii) vibration method and iii) tamping method. They reported that the samples prepared by pluviation and vibration had a higher stiffness in the horizontal direction, whereas samples prepared by tamping induced higher stiffness in the vertical direction.

Juneja & Raghunandan (2011) conducted a series of consolidated drained (CD) and consolidated undrained (CU) triaxial compression tests on sand samples prepared using pluviation and tamping techniques, under both dry and moist conditions. They reported that the stress-strain behaviour of samples prepared with various methods showed con-

siderable difference in peak stress and dilation.
DEM simulations also indicate that initial anisotropic conditions have a great influence on the strength and deformation of granular assemblies (Ng 2004, Magnanimo et al. 2008, Azéma et al. 2009 and Hosseininia 2012).
Therefore, particle alignment has a significant effect on the mechanical properties of granular assemblies. This causes a significant difference in the magnitude of contact forces for the two directions. As a result, the anisotropy in contact area and contact force causes anisotropic effects on G_{max}. The effect of sample preparation on the coordination number and the stiffness of granular assembly will be discussed using DEM simulations in this study.

2.8 Stress induced anisotropy

It is well-known that the stiffness of geo-materials depends on the state of stress in the soil elements. Hardin & Black (1966) studied the influence of the stress ratio on the maximum shear modulus of dry sand using a resonant column device. From experimental studies, Hardin & Black (1966) concluded that the shear modulus is independent of the deviatoric component of the initial stress state. Also, they concluded that Hardin's relationship with sufficient accuracy can be used to predict the maximum shear modulus of soil elements subjected to anisotropic loading. Drnevich (1978) studied the influence of initial shear stress on the maximum shear modulus and damping of dry Ottawa Sand with the RC device and reported that the impact of initial shear stress on the maximum shear modulus is small. Also, they concluded that damping increases with the initial shear stress but the increase in damping is not significant. Tatsuoka et al. (1979) performed a series of cyclic torsional tests to evaluate the impact of static stress conditions on the small strain properties of Toyoura Sand using a torsional shear device. From their experimental results they concluded that the impact of extension loading on the maximum shear modulus is more remarkable than compression loading and they also concluded that the impact of the stress ratio and initial shear stress on the damping ratio is not significant. Yu & Richart (1984) studied the impact of the stress ratio on the maximum shear modulus of Brazil Sand and Ottawa Sand using a resonant column device. Yu & Richart (1984) concluded that G_{max} can be affected by shear stress at a stress ratio of more than two.
After these studies, Isenhower et al. (1987) modified Stokoe resonant column device to perform stress induced anisotropic tests. Santamarina & Cascante (1996) studied the effect of stress induced anisotropy on shear wave velocity in Barco Sand with the modified

Stokoe resonant column device. However, their study was restricted to a stress ratio of less than two. Santamarina & Cascante (1996) reported that wave velocity will increase with an increase in the stress ratio but the effect of stress ratio on η_{min} is not significant. All of the previous works to evaluate the effect of stress induced anisotropy on the maximum shear modulus were conducted on dense samples.

By reviewing the literature, systematic studies on the effect of stress induced anisotropy on the intermediate strain properties of granular material are rare, and we can refer to the study by Tatsuoka et al. (1979). They studied the effect of induced anisotropy on damping ratio and shear modulus on one stress path with a dense sample and reported that the impact of stress ratio on damping is not significant. However, their study was restricted to the stress path with a constant confining pressure on a dense sample. However, soil elements can be subjected to more complicated stress conditions in comparison with the stress conditions applied in the existing studies on intermediate strain properties up to now. Therefore, a major objective of this research work is to find the effect of stress induced anisotropy for different stress paths and density of sample on the small, and especially intermediate strain properties of sand. The resonant column device at Ruhr Universität Bochum was modified for performing such studies.

2.9 Summary

- The small strain properties of geomaterials can be explained by stress-strain hysteresis loops. Maximum shear modulus, G_{max}, shear modulus as a function of shear strain, $G(\gamma)$ and damping ratio, η, are the main parameters which control the response of the soil elements subjected to vibration. They are also the key parameters in soil-structure interaction problems with small deformations under rapid and repetitive loads.

- The effect of f_c on G_{max} and $\eta(\gamma)$ must be evaluated with a systematic increase of f_c. Application of the equivalent granular void ratio to predict the small strain stiffness of granular material must be studied. The data sets collected from the literature were limited to the maximum 20% f_c. Thus, a suitable approach for capturing the effect of a wide range of f_c on G_{max} and $\eta(\gamma)$, beyond threshold fines content, is still a topic of research interest.

- Studies on the effect of stress induced anisotropy on the small and intermediate strain properties can be divided into two main groups: 1-studies on the small strain properties (G_{max}), and 2- studies on intermediate strain properties ($G(\gamma)$ and $\eta(\gamma)$).
  Concerning 1: As is apparent from the literature review, numerous experimental studies have been conducted by piezoelectric elements for evaluating the effect of induced anisotropy on G_{max} (small strain properties) of granular materials, but some of them (e.g. Hardin & Black 1966, Tatsuoka et al. 1979, Yu & Richart 1984 and Santamarina & Cascante 1996) used the resonant column device and they concluded that at a stress ratio of less than two, the effect of stress induced anisotropy on G_{max} is not significant but these studies were restricted to dense samples.
  Concerning 2: From the literature review we can see that studies on the effect of induced anisotropy on the intermediate strain properties of granular material are rare, and we can refer to the study by Tatsuoka et al. (1979). They studied the effect of induced anisotropy on damping ratio and shear modulus for one stress path (confining pressure constant and vertical pressure variable) on dense samples and reported that the impact of the stress ratio on damping is not significant. However, soil elements can be subjected to more complicated stress conditions in comparison to the stress conditions applied in the studies conducted on intermediate strain properties up to now. Therefore, additional studies are essential to assess the effect of stress induced anisotropy for different stress paths on the small, and especially

intermediate strain properties of sand. Furthermore, the empirical relations must be developed to predict $G(\gamma)$ of soil samples subjected to stress induced anisotropy for different stress paths.

3 Material and experimental program

3.1 Introduction

The adopted experimental program to assess the influence of fines content and stress induced anisotropy on the small and intermediate strain properties of granular materials will be presented in this chapter. This chapter has three main objective: Firstly, the physical and mechanical properties of adopted materials are discussed. Hostun sand and glass beads are introduced as host and main materials used in this study. Also, two mixtures, Hostun Sand containing quartz powder and glass beads containing fine glass beads, are introduced as a mixture to study the effect of fines content. Secondly, the apparatus used for the experimental study is introduced. Before performing tests, calibration and validation of the apparatus are essential. Therefore, the numerical, theoretical and experimental procedures for the calibration and validation of the apparatus are discussed. The effect of vertical load on the dynamic behaviour of the system (resonant column device) will be examined with the numerical modeling of the device. Finally, the experimental procedure for performing the isotropic and stress induced anisotropic tests will be presented.

3.2 Materials

Two types of materials were used in this research: 1) Hostun Sand; and 2) glass beads. Both of the materials were adopted as host materials for studying the effect of fines and stress induced anisotropy on small and intermediate strain properties. The physical properties of these materials are presented in the following sections.

3.2.1 Hostun Sand

The main experimental program for this study was conducted on Hostun Sand which has been used in the previous studies (Flavigny et al. 1990, Schanz & Vermeer 1996 and Sadek 2006). The color of Hostun Sand ranges between gray-white and rosy-beige, while its chemical components consist of a large amount of siliceous, $SiO2 > 98\%$, (Amat 2007). Hostun Sand is a quartz sand with grain sizes ranging from 0.1 mm to 1.0 mm. Figure 3.1a shows the microscopic image of particles. The grain shape varies from angular to sub-angular. According to the USCS classification, the material is a poorly-graded medium sand SP (Lins 2009). The values of the maximum and minimum void ratios, e_{max} and e_{min}, of Hostun Sand were measured using DIN 16126 and the results are summarized in Table 3.1.

A particle size distribution analysis was carried out using DIN 18123 standard. Figure 3.1b shows the particle size distribution of Hostun Sand.

The stress-strain behaviour of Hostun Sand was essential for the discussion of the observed experimental results using the resonant column device. Hence, triaxial tests were conducted at the confining pressure of 200 kPa, σ_3=200 kPa, on dense ($Dr = 90\%$) and loose ($Dr = 35\%$) samples. The initial conditions in triaxial tests were the same as the conditions for the samples in resonant column tests. The stress-strain curve and volumetric changes of dense and loose Hostun Sand are presented in Figure 3.2a and Figure 3.2b.

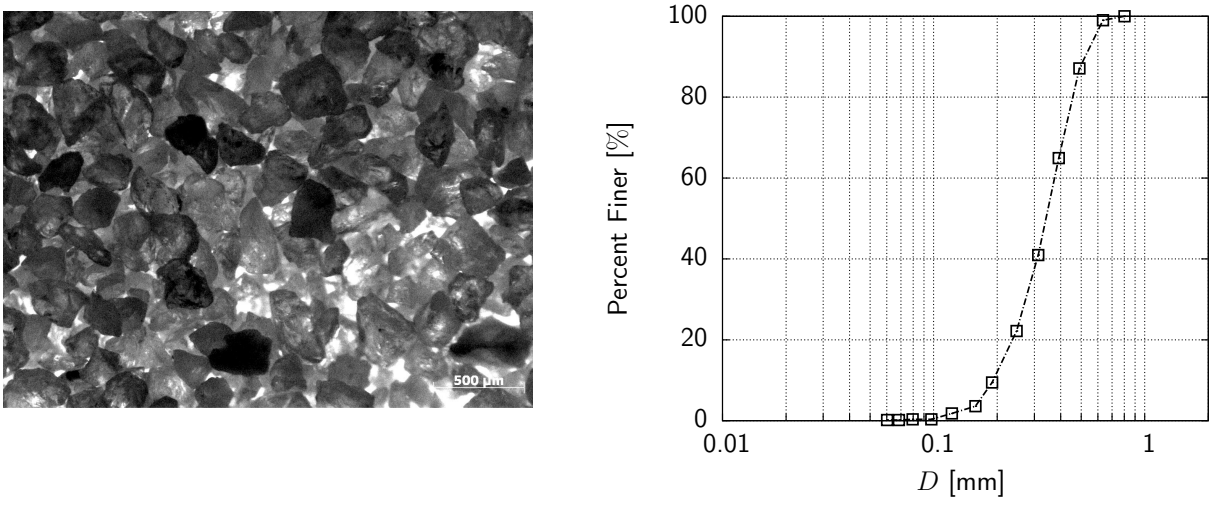

(a) (b)

Figure 3.1: Particle characteristics of Hostun Sand: (a) shape of particles; (b) grain size distribution

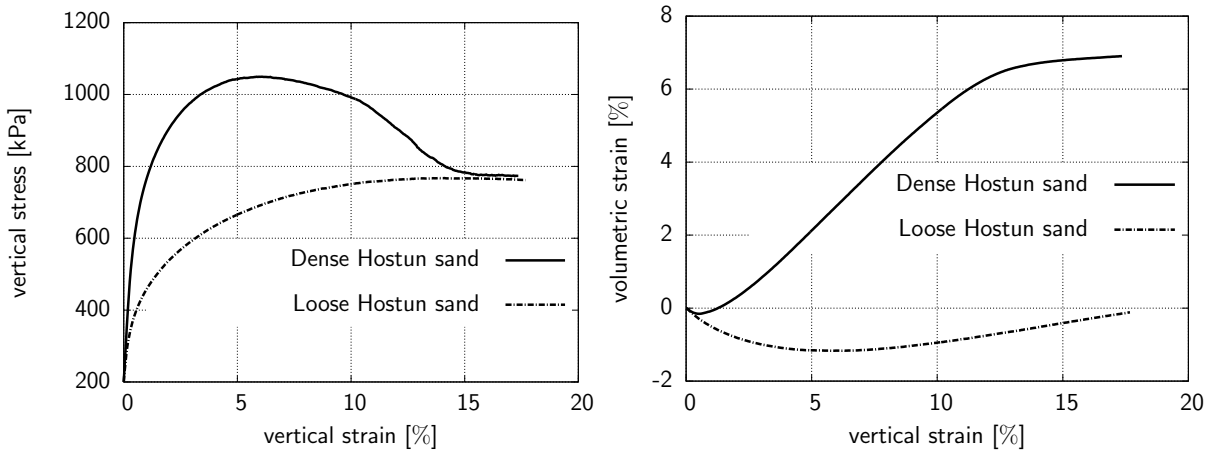

(a) (b)

Figure 3.2: Triaxial behaviour of dry Hostun Sand at the confining pressure of 200 kPa, σ_3=200 kPa,: (a) vertical stress versus vertical strain for loose and dense samples; (b) volumetric strain versus vertical strain for loose and dense samples

These figures show the well-known behaviour of dense and loose sand by increasing the vertical strain. Figure 3.2a shows the samples reach the critical state zone at vertical strain of more than 15%. Also, the results in Figure 3.2b show that the dense sample dilated at the vertical strain by more than 1.5% and the loose sample compacted with an increase in the vertical strain.

3.2.2 Glass beads

Spherical glass particles with a diameter of 1.25 mm were used as the second host material for studying the effect of fine particles and stress induced anisotropy on small and intermediate strain properties. The SEM photographs, scanning electron microscope, of glass beads are shown in Figure 3.3. The stress-strain behaviour of the adopted glass beads were essential for the calibration and validation of the prepared model in DEM simulation and the stress-strain results were also essential for interpretation of the test results from the resonant column test. Discrete element simulations and resonant column tests were conducted on the dense glass bead samples. Therefore, triaxial tests were conducted on the dense glass bead packing (Dr = 88%) at the confining pressure of 200 kPa, σ_3=200 kPa, for calibration of the DEM model. Figure 3.4 shows the behaviour of the dense glass bead packing obtained from the triaxial test. Figure 3.4a demonstrates that the vertical stress in the dense sample reached the maximum value at a vertical strain of less than

2% and dilation occured at a vertical strain of more than 0.6% (Figure 3.4b). The other physical properties of the adopted glass particles are summarized in Table 3.2.

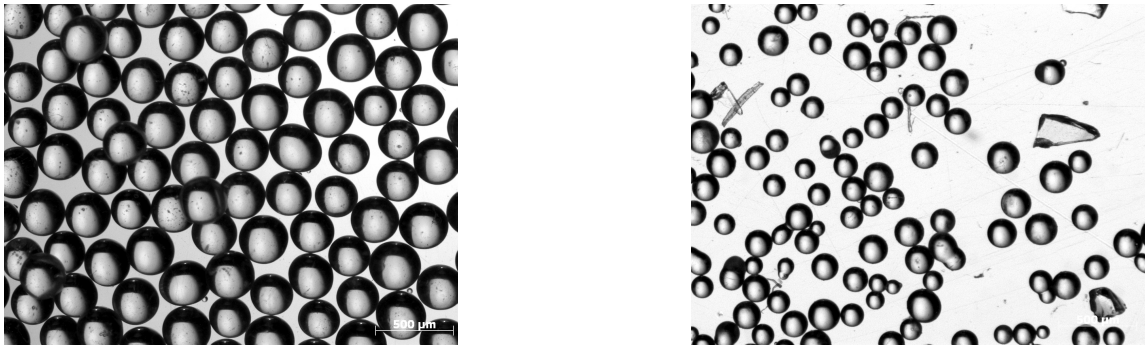

(a) (b)

Figure 3.3: Particle characteristics of glass beads: (a) coarse particles, D=1.25 mm; (b) fine particles, d=0.125 mm

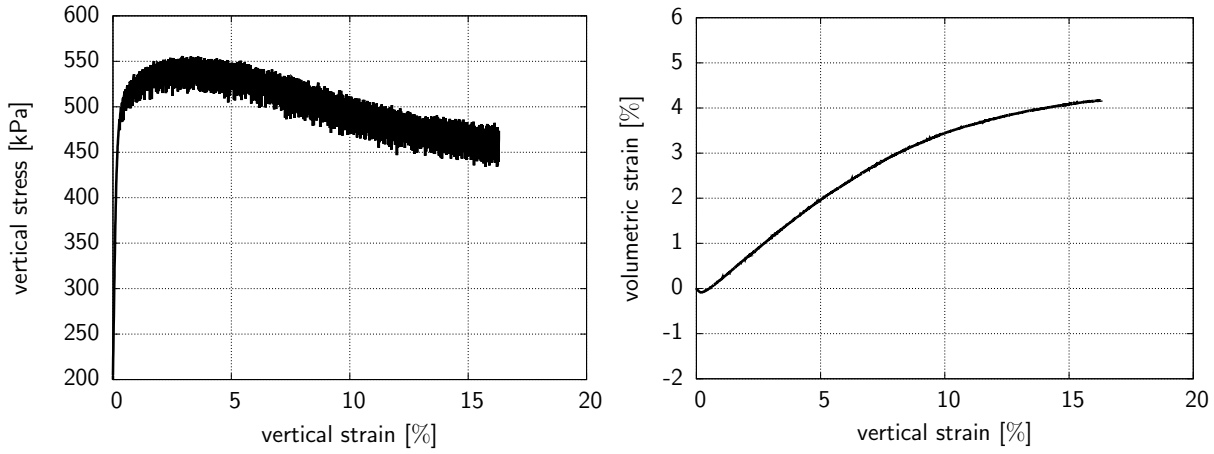

(a) (b)

Figure 3.4: Triaxial behaviour of dry dense glass beads (Dr = 88%) at the confining pressure of 200 kPa, σ_3=200 kPa,: (a) vertical stress versus vertical strain; (b) volumetric strain versus vertical strain

3.3 Mixtures

Two types of mixture were used in this study: 1) Hostun Sand mixed with fine quartz powder 2) glass beads mixed with glass fines particles which are discussed in this section.

3.3.1 Hostun Sand and quartz powder

Hostun Sand was washed to separate the particles with a diameter of less than 0.075 mm, so-called clean Hostun Sand. Clean Hostun Sand was mixed with 0, 5, 10, 20, 30 and 40 gravimetric percentages of non-plastic fines. The adopted non-plastic fines were a commercial quartz powder (M500), composed of 99% SiO_2, from the Euro-quartz company. Before performing tests with the prepared mixtures, the maximum and minimum void ratio of the mixtures must be determined. There is no applicable ASTM procedure to determine the maximum and minimum void ratios of soils with 15% or more fines content (Tao et al. 2004) which is due to the segregation of particles during pluviation. However, the ASTM standard has been used to detemine the maximum and minimum void ratio for coarse materials containing more than 15% fines in previous works (e.g. Tao et al. 2004). In this research, the procedure adopted to determine the variation of e_{max} and e_{min} with the systematic increase of fines content was the same as the procedure presented in DIN 18126. Regarding this standard, the value of e_{max} was determined by placing the standard funnel at the bottom of the standard mold. Then, the funnel was raised slowly without dropping the particles which reduces particles segregation. To determine the value of e_{min} the sample, from the e_{max} test, was devided into five equal layers. After placing each layer inside the mold, the mold was tapped uniformly with a standard hammer. The variation of e_{max} and e_{min} for Hostun Sand with different percentages of f_c and the other physical properties of the mixtures are summarized in Table 3.1.

Table 3.1: The physical properties of Hostun Sand-quartz powder mixtures

Soil	e_{max} [-]	e_{min} [-]	γ_{dmin} $[\frac{g}{cm^3}]$	γ_{dmax} $[\frac{g}{cm^3}]$	G_s [-]	D_{50} [mm]	D_{10} [mm]
Clean Hostun sand	1.023	0.671	1.310	1.586	2.65	0.385	0.211
CHS+5%f_c	1.097	0.642	1.264	1.614	2.65	0.380	0.172
CHS+10%f_c	1.219	0.635	1.194	1.624	2.65	0.379	0.082
CHS+20%f_c	1.501	0.624	1.072	1.630	2.65	0.337	0.004
CHS+30%f_c	1.739	0.682	0.968	1.575	2.65	0.324	0.003
CHS+40%f_c	1.925	0.791	0.906	1.479	2.65	0.266	0.002

Table 3.2: The physical properties of glass bead-glass bead mixtures

f_c [%]	e_{max} [-]	e_{min} [-]	γ_{dmin} $[\frac{g}{cm^3}]$	γ_{dmax} $[\frac{g}{cm^3}]$	G_s [-]
0	0.6851	0.5616	1.4836	1.5908	2.50
10	0.5706	0.4356	1.5817	1.7414	2.50
20	0.47	0.3399	1.667	1.8659	2.50
30	0.3849	0.2698	1.7423	1.9369	2.50
40	0.3973	0.2767	1.734	1.9336	2.50
50	0.4225	0.3064	1.7224	1.9284	2.50

The test results show the e_{min} decreased up to fines content of 20% and then increased with further increases of f_c. The f_c, that is the boundary between the "fines-in-sand" and "sand-in-fines" micro-structure, is called the threshold fines content, f_{thr} (Rahman & Lo 2008). Regarding the e_{min} analysis, the value of f_{thr} is the fines content that e_{min} starts to increase with further increases in fines content (Naeini & Baziar 2004 and Zuo & Baudet 2015). From Table 3.1, the value f_{thr} should be in between 20% and 30% for Hostun Sand mixed with quartz powder which was assumed to be 25% for this study.

3.3.2 Glass bead mixtures

Coarse glass beads (D=1.25 mm) were mixed with 0, 10, 20, 30, 40 and 50 gravimetric percentages of spherical fine glass beads (d=0.125 mm, Figure 3.3b). The values of e_{max} and e_{min} was determined for all of the mixtures, the procedure was the same as the adopted procedure for the Hostun Sand mixtures. The variations of e_{max} and e_{min} for the glass bead mixtures are summarized in Table 3.2. The results show that the value of e_{min} decreased up to 31% f_c and then increased with a further increase of f_c.

3.4 Sample preparation

Dry funnel deposition and the air pluviation method are two common methods for sample preparation. In the air pluviation method, dry sands are pluviated through a diffuser from a constant height and thus may not be suitable for sand with more than 15% f_c, due to particle segregation. In the dry deposition method, the specimens were prepared

by placing the funnel at the bottom of the mold. Then the material were placed inside the funnel and the funnel was raised slowly which reduced particle segregation. The mold was tapped in a symmetrical pattern to achieve a dense specimen. This technique was commonly used for testing silty sands by Ishihara (1993), Lade & Yamamuro (1997), Yamamuro & Lade (1997) and Monkul & Yamamuro (2011). Therefore, the dry deposition method, which gives the most uniform specimen compared to pluviation for mixtures, was used for the sample preparation in this study.

3.5 Apparatus

3.5.1 Description of equipment

Resonant column and piezoelectric elements are two common laboratory devices for measuring the small and intermediate strain properties of geo-materials. The piezoelectric elements are mounted in the different laboratory devices to measure the maximum shear modulus at a low amplitude of vibration (e.g. Jovicic & Coop 1988, Kuwano et al. 2000, Kuwano & Jardine 2004 and Wang & Mok 2008). These elements are also applicable when determining the modulus reduction curves and damping ratio of soils (e.g. Karl et al. 2008, Choo et al. 2013) although it is not a standard procedure.
Besides the piezoelectric elements, the resonant column device is one of the standard methods (ASTM D-4015) for measuring small and intermediate strain properties. The resonant column technique is based on the oscillation of the cylindrical sample on one of its vibration modes, flexural mode (Cascante et al. 1998), normal mode (Saxena & Reddy 1989) and torsional mode (a common type of resonant column), to determine the resonant frequency of a sample.
The torsional resonant column device is the common type of resonant column. The torsional resonant column device was initially adopted by Iida (1937), a Japanese researcher, to evaluate the influence of water content on wave velocity (Figure 3.5a). This device was developed in the last few decades, e.g. Hardin & Black (1966), Hardin & Drnevich (1972*b*), Hardin & Drnevich (1972*a*), Drnevich (1978) and Stokoe et al. (1999*a*), for studying the small strain properties of soils (Figure 3.5b). The torsional resonant column device is divided into two groups, free-free and fix-free resonant column devices which are appropriate for determining the mechanical properties of soils with a wide range of strain, from a very small strain to medium strain (Figure 1.3).

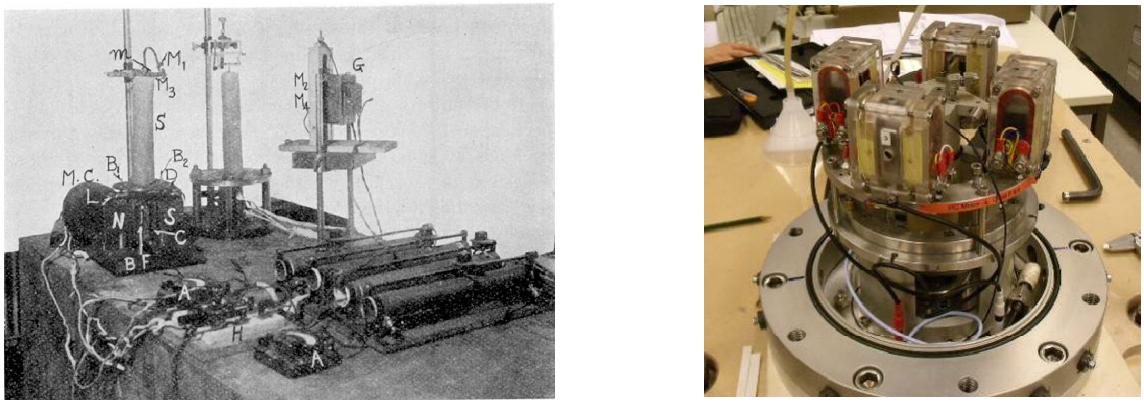

(a) (b)

Figure 3.5: The resonant column device: (a) by Iida (1937); (b) the common type, Stokoe resonant column (Bai 2011)

In free-free resonant column device, the actuator is mounted on the top or bottom of the sample whereas the other end is free in rotation. In the fix-free resonant column device, one side of the sample is constrained against rotation and the other side is free in rotation (Drnevich resonant column and Stokoe resonant column). The resonant column device at Ruhr-Universität Bochum (Figure 3.6) was designed so that the polar mass moment of inertia in bottom part (J_0) is about 17.2 times the polar mass moment of inertia in the top part (J_L), ($J_0/J_L = 17.2$). Thus, this device can be categorized in a free-free resonant column device group and relationships must be developed based on the free-free boundary conditions. Regarding the boundary conditions of the Bochum resonant column device, the Equation 3.1 and Equation 3.2 are applicable for determining the maximum shear modulus of materials (Richart et al. 1970 and Wichtmann et al. 2001).

$$atan(a) - \frac{J^2}{J_0 J_L}\frac{tan(a)}{a} = \frac{J}{J_0} + \frac{J}{J_L} \tag{3.1}$$

$$G = \left(\frac{2\pi L f_r}{a}\right)^2 \rho \tag{3.2}$$

where, a is $\omega L/v_s$, ω is the rotational frequency, v_s is the wave velocity, J_0 and J_L are the polar mass moment of inertia for the bottom and top parts of the resonant column, J is the polar mass moment of inertia for the sample, ρ is the density of the sample, f_r, is the resonant frequency and L is the height of the sample. By assuming the infinite value for J_0 in Equation 3.1, the relationship will be the same as the proposed relationship for the fix-free resonant column device. The top part of the Bochum resonant column device (Figure 3.7a) includes two mini-shakers for applying a rotational excitation at the top

of the sample. Two transducers (accelerometers) were mounted on the mini-shakers and the actuator were used for monitoring the signals (Pkk_1 and Pkk_2, Figure 3.7a) using oscilloscope device. Phase difference between the signals received from the mini-shakers and displacement transducers (Pkk_1 and Pkk_2) must be $\pi/2$ at the resonant frequency.

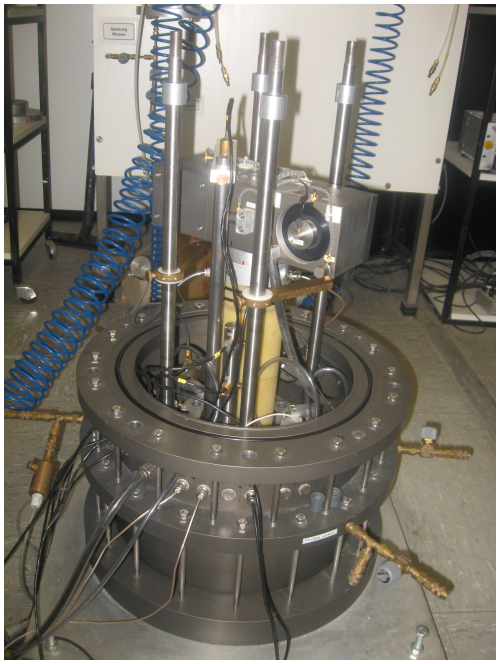

Figure 3.6: The torsional resonant column device at Ruhr Universität Bochum

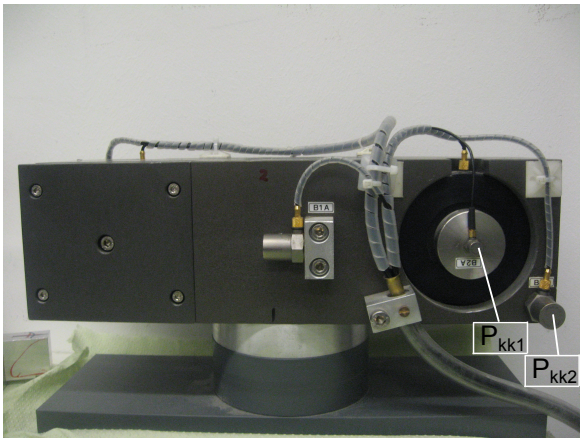

(a)

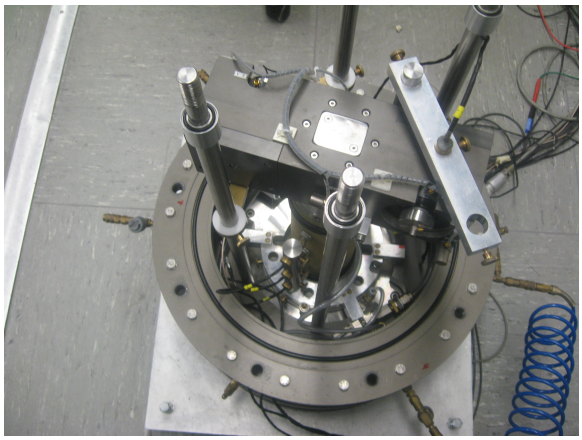

(b)

Figure 3.7: The Bochum resonant column device: (a) the actuator or top part of the Bochum resonant column device; (b) top view of assembled device

According to Equation 3.1 and Equation 3.2, three constant values (J_L, J_0 and J) are key parameters for determining G_{max} with the resonant column device. To increase the accuracy of the results, these values must be determined accurately.
The bottom part of the Bochum resonant column device and the sample have a cylindrical shape with a given density and dimensions, thus the polar mass moment of inertia (J_0 and J) of these parts can be determined using geometric relations. The top part of the Bochum resonant column device (Figure 3.7a) has a complex shape, including electrical equipment, cables and holes, thus the polar mass moment of inertia for this part (J_L) can not be determined accurately with geometric methods. Hence, experimental methods must be used to determine the value of J_L. By a simple experimental procedure the value of J_L can be calculated. With this method, the shear modulus of the aluminum sample (G) was assumed to be a value between 24 and 27 GPa, and then, the resonant frequency of the aluminum sample is measured using the resonant column device. Hence, the parameter a can be determined by substituting the shear modulus and the measured resonant frequency in Equation 3.2. The mass moment of inertia for the top part (J_L) can be calculated by substituting the determined values for a, J and J_0 in Equation 3.1. In this study, the stiffness of aluminum (G) was an unknown value, thus G was assumed to be 25 GPa. Therefore, this experimental method includes an error because of the stiffness of the aluminum sample. Another experimental method, which is independent of the shear modulus (G) of the aluminum sample, was used to determine the value of J_L with a high degree of accuracy. The experimental method developed by Tatsuoka & Silver (1980) for the fix-free resonant column device was employed for determining the value of J_L in the free-free resonant column device. In this experimental method, an extra mass with given density and geometry was used to determine the value of J_L. The extra mass was placed on the top of the actuator and the resonant column tests were conducted for both of the conditions (with and without extra mass). By rewriting Equation 3.1 and Equation 3.2, three unknown values: a, b and J_L were defined.

$$a\tan(a) - \frac{J^2}{J_0 J_L}\frac{\tan(a)}{a} = \frac{J}{J_0} + \frac{J}{J_L} \tag{3.3}$$

$$b\tan(b) - \frac{J^2}{J_0(J_L + J_{mass})}\frac{\tan(b)}{b} = \frac{J}{J_0} + \frac{J}{(J_L + J_{mass})} \tag{3.4}$$

$$\frac{a}{b} = \frac{f_{r1}}{f_{r2}} \tag{3.5}$$

where, f_{r1} is the resonant frequency of the aluminum sample without the extra mass and f_{r2} is the resonant frequency of the aluminum sample with the extra mass. According to the dimension of the sample (2 cm in diameter and 30 cm in height), the mass moment

of inertia of the sample (J) was about $1.2723E-5$ kg.m^2. Also, the value of J_0 could be determined by the geometric method and was 1.171415 kg.m^2. The resonant frequency of the aluminum sample without the extra mass was determined by a resonant column test which was 22.82 Hz (f_{r1}). The extra mass with a given mass moment of inertia (J_{mass}=0.0148 kg.m^2) was placed on the top of the actuator and the resonant frequency of the aluminum sample was measured (f_{r2}) which was 20.71 Hz. By substituting the measured resonant frequencies in Equation 3.5, the value of b will be equal to $ka = 0.9075a$. Therefore, Equation 3.3, Equation 3.4 and Equation 3.5 were reduced to Equation 3.6 and Equation 3.7 with two unknown parameters (a and J_L).

$$F(a, J_L) = a\tan(a) - \frac{J^2}{J_0 J_L}\frac{\tan(a)}{a} - \frac{J}{J_0} - \frac{J}{J_L} = 0 \tag{3.6}$$

$$G(a, J_L) = ka\tan(ka) - \frac{J^2}{J_0(J_L + J_{mass})}\frac{\tan(ka)}{ka} - \frac{J}{J_0} - \frac{J}{(J_L + J_{mass})} = 0 \tag{3.7}$$

where, k, J, J_0 and J_{mass} are equal to 0.9075, $1.2723E-5$ kg.m^2, 1.171415 kg.m^2 and 0.0148 kg.m^2 respectively. From the performed calculations, J_L is equal to 0.0647 kg.m^2. The value of J_L was also calculated with the geometric method and its value with geometric relations was about 0.0659 kg.m^2 but the J_L from the experimental method was used in all of the tests with the resonant column device on the soil samples.

3.5.2 Mode of vibration

Two types of rotational modes may be achieved during the test with the free-free resonant column: 1- actual rotational mode; and 2- spurious rotational mode (defined by Avramidis & Saxena 1990). The actual rotational mode is achieved when there is an phase difference between the top and bottom of the sample during the rotational excitation of the sample. The other one, spurious or fake mode, is achieved when the top and bottom of the sample have the same rotational phase during the RC test to avoid this mode of vibration mass moment of inertia of free side (J_0 in Bochum RC) must be increased or samples with less stiffness must be used. The rotational mode of vibration must be distinguished during isotropic and anisotropic tests with the resonant column device. Two accelerometers were installed on the rotatable bottom part of the resonant column device, Acc.2, (Figure 3.8a) to determine the type of rotational mode, actual or spurious. The received signals from the accelerometers, Acc.1 and Acc.2, were monitored and compared with each other during the resonant column test.

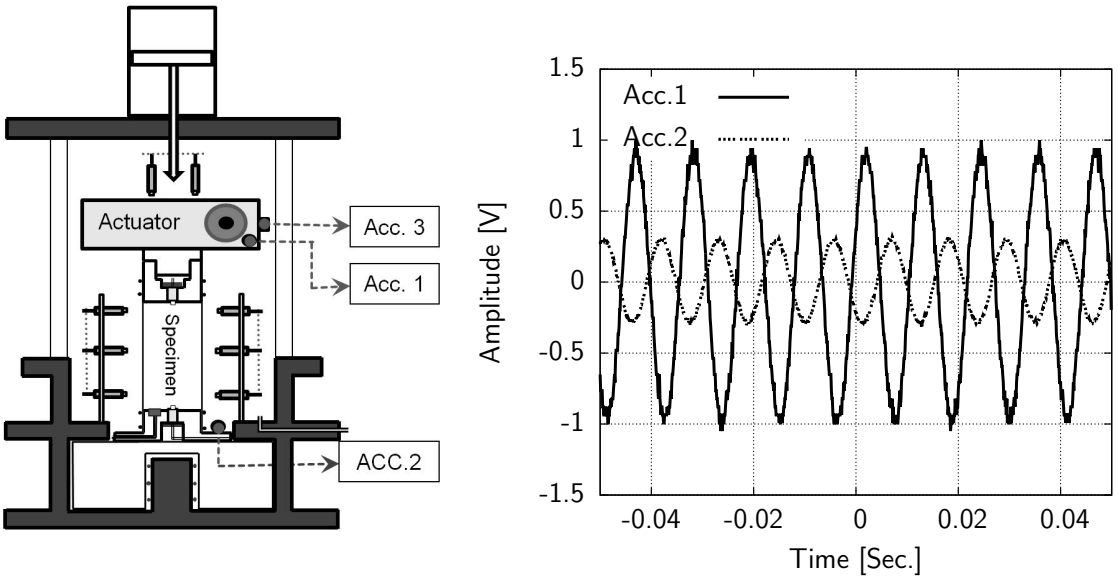

(a) (b)

Figure 3.8: Rotational mode of vibration in the Bochum resonant column: (a) schematic sketch of the RC device; (b) received signals from top and bottom of the sample

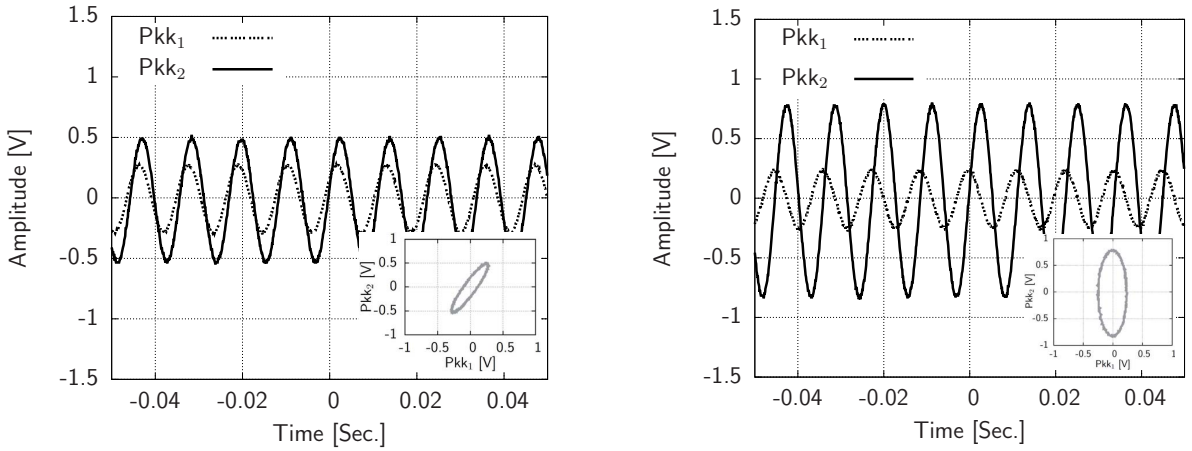

(a) (b)

Figure 3.9: Frequency of rotational vibration: (a) frequency of actual vibration; (b) resonant frequency of actual vibration

Due to the shape of actuator, additional mode of vibration cloud be achieved during tests with the Bochum resonant column device which is called flexural or bending mode of vibration. This mode of vibration was monitored using Acc.3 which was mounted in one side of the actuator (Figure 3.8a). The received signals from Acc.3 showed that the amplitude of signals were not significant in comparison with the applied torsional vibration. This means that the flexural mode of vibration can be ignored during tests using the

Bochum resonant column device.
Figure 3.8b shows an example of the signals received from Acc.1 and Acc.2. Figure 3.8b shows an example of the applied signals at the top of the sample in comparison with the received signals from the bottom of the sample. As can be seen in this figure, when the peak value of the signals applied to the top of the sample (Acc.1) was $0.97v$, the peak amplitude of the signals received from the bottom was about $0.38v$ which means the bottom of the sample is free in rotation. Furthermore, Figure 3.8b shows a π phase difference between the received signals which is due to the direction of the installed accelerometers at the top and bottom of the RC (both of them are in the same direction).
The obtained results show that the bottom and top of the sample rotate at different phases. The resonant frequency will be determined for the actual rotational mode of excitation. This frequency is achieved when the phase difference between Pkk_1 and Pkk_2 signals is $\pi/2$ (Figure 3.9b). For ease of determining the resonant frequency, Pkk_2 was drawn versus Pkk1 (Figure 3.9a) on the oscilloscope device. Then the frequency of the applied signal was changed to get the resonant frequency; at the resonant frequency the generated ellipse shape must be vertical (Figure 3.9b).

3.5.3 Modification and calibration of apparatus

3.5.3.1 Loading system

The actuator of the Bochum resonant column device is the cubic part which includes the electrical equipment (Figure 3.6). To apply additional vertical stress inside of the sample, the actuator was loaded in a vertical direction using a double acting pressure cylinder added by APS Wille Geotechnik GmbH, Götingen, (Figure 3.10). The load of the cylinder was transferred with a loading bar, a hardened steel tip, to the hardened steel plate which was mounted at the central axis of the actuator and sample (Figure 3.10). Firstly, the relationship between pressure p and the generated force in the loading bar, F, must be determined. The calibrated load cell was used to determine the value of F with systematic increase of p in double acting pressure cylinder.
Figure 3.11 shows the relationship between the applied pressure, p, and F in the loading bar. In this calibration, p_0 was assumed to be constant and equal to 50 kpa. The value of p_0 was applied to improve the motion of the loading bar during the unloading process. Then, the effect of cell pressure (σ_3) on the value of F must be calculated (Figure 3.10b). As can be seen in Figure 3.10b, cell pressure has both a negative and positive effect on the magnitude of F in the loading bar which must be assessed.

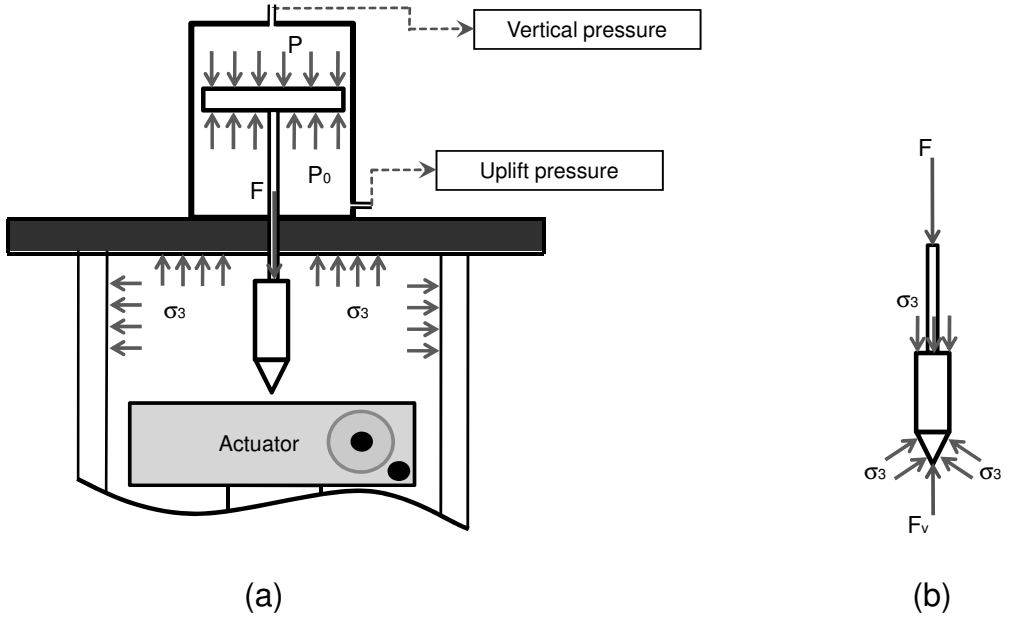

Figure 3.10: Instrumentation for applying vertical load: (a) schematic sketch of double acting pressure device and loading bar; (b) the effect of cell pressure on loading bar

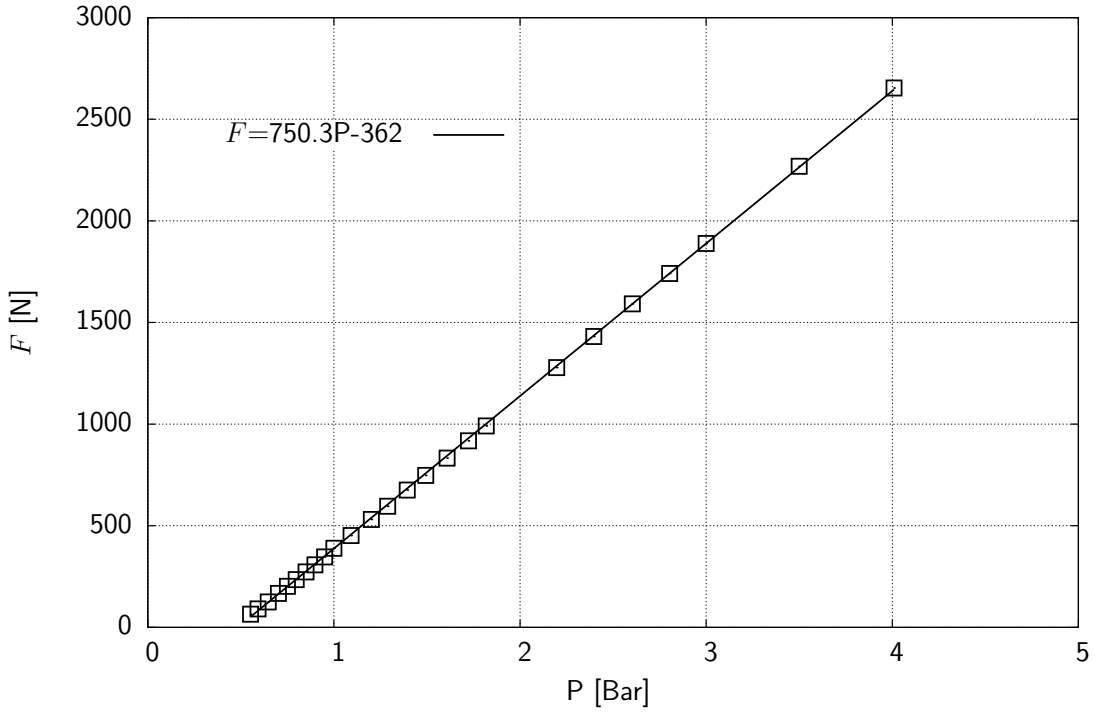

Figure 3.11: Calibration of double acting pressure cylinder, p_0=50 kPa

The effect of cell pressure on the vertical load, F, was calculated by writing the equilibrium relationship in a vertical direction (Equation 3.8).

$$F_v = F + A_1(\sigma_3) - A_2(\sigma_3) \tag{3.8}$$

Where, A_1 and A_2 are equal to 2.155 cm^2 and 5.02 cm^2 respectively. From the equilibrium relation, the value of F_v was a function of cell pressure.
Finally, the influence of the loading equipment on the dynamic behaviour of the system (bottom mass, sample and actuator) and its interaction with the actuator must be assessed. Therefore, the finite element method, ABAQUS software, and experimental methods, using aluminum samples, were used for this assessment.

3.5.3.2 The effect of the loading bar

Damping ratio in aluminum specimens is approximately zero (Zemanek & Rudnick 1961). Therefore, the resonant frequency of aluminum samples is approximately equal to the natural frequency which allows modeling of the resonant column device with the aluminum sample in ABAQUS software. This type of analysis was helpful to evaluate the effect of loading and interaction between the loading bar and the actuator on the natural frequency of the aluminum sample and the dynamic behaviour of system. A numerical model was developed to analyze the behavior of the RC device without a vertical loading system. After validation of the model, the numerical model was extended to analyze the influence of the vertical loading system on the behaviour of the RC device. In the numerical model, the RC device was idealized into three main parts: actuator, sample and bottom part. The geometries of these parts were modeled the same as the real device (Figure 3.12). All of the connections, e.g. connections between the actuator and the top of the sample, and the bottom part of the device and sample, were assumed to be rigid connections. Material properties of the modeled parts were the same as the real device in the laboratory (the actuator and the sample was made of aluminum and the rotatable bottom part was made of steel). The top part of the modeled device was free for displacement or rotation but the bottom part of the system was constrained against displacement and it was free in rotation only, the same as the boundary conditions of the device in the laboratory.
For validation of the model, the frequency analyses were conducted to determine the natural frequency of the aluminum samples with a diameter of 2, 4 and 6 cm and 30 cm height. Two types of rotational frequencies were achieved from the numerical model, actual and spurious frequency (Figure 3.12a and Figure 3.12b). As is apparent from Figure 3.12a, the top and bottom of the model have the same colour. This means the

top and bottom of the model have the same rotational phase. In this case the rotational frequency is the so-called spurious frequency. However, Figure 3.12a shows the actual mode of vibration and this frequency is used to determine the shear stiffness. Therefore, the obtained actual frequencies from the numerical model for aluminum samples were extracted and presented in Tables 3.3 and 3.4. Table 3.3 shows the measured frequencies of aluminum samples without vertical loading which was calculated with different methods. The results confirm a good agreement between frequencies calculated by the numerical model and measured values using the resonant column device (Table 3.3).

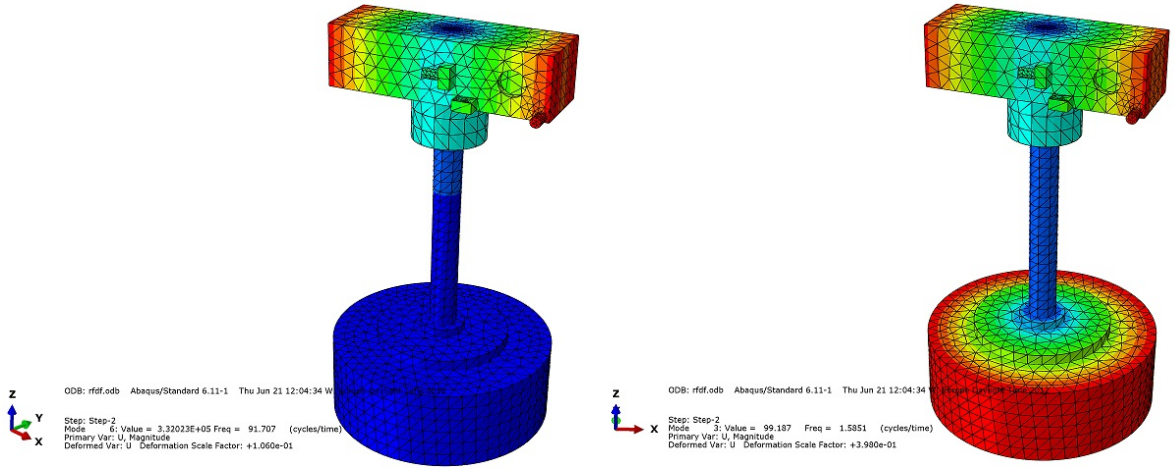

(a) (b)

Figure 3.12: The obtained rotational frequencies for aluminum sample No.4 from numerical analysis: (a) actual mode of vibration; (b) spurious mode of vibration

Table 3.3: The measured resonant frequencies for the aluminum samples with various methods, without vertical load

Specimen	RC test	Theory Equations 3.1 and 3.2	Modeled in ABAQUS
t [cm]	fr [Hz]	fr [Hz]	fr [Hz]
2	22.82	23.43	23.371
4	92.41	93.45	91.707
6	182.95	209.86	198.523

Table 3.4: The measured resonant frequency for the aluminum sample using the numerical method, with vertical load

Specimen t [cm]	Diameter of contact area s [cm]	Vertical F_v [N]	Modeled in ABAQUS f_r [Hz]	Effect of loading bar Δ_1 [%]
4	1	0	133.45	45.52%
		4000	139.23	51.82%
4	0.2	0	91.791	0.31%
		4000	92.078	0.40%
4	0.1	0	91.713	0.045%
		4000	91.754	0.05%

After validation of the numerical model, the effect of the vertical load on the dynamic behaviour of system was considered. For approaching to this aim, additional modification was applied to the prepared numerical model to evaluate the effect of the loading bar. A rigid cylindrical element was defined as a loading bar in the FEM model. The loading bar, in FEM model, was constrained in all of the directions but it was free in the vertical displacement. One step was defined before the frequency analysis step to develop the effect of the vertical load on the obtained frequency from the modeled device. The mechanical changes like loading and friction interaction between the loading bar and the actuator were defined in this step of analysis and their effects were observed during frequency analysis in the second step. The effect of two main variables on the response of the system during loading were studied: 1- the effect of the diameter of connection, s, between the loading bar and the actuator (s was equal to 1, 0.2 and 0.1 cm); and 2- the effect of the vertical load, F_v, which was equal to 0 and 4000 N. In all of the analyses the fiction coefficient between the loading bar and the actuator was assigned as a smooth steel-steel friction coefficient (assumed 0.3). The results of the FEM analysis are summarized in Table 3.4. For ease of discussion, the frequency of aluminum sample ($t = 4cm$) without the vertical load (Table 3.3) was assumed to be a reference value. Table 3.4 shows that the frequency of the aluminum sample increases by 45.52% with increase in the diameter of connection, s, to 1cm which is due to the friction between the loading bar and actuator. By increasing the vertical load from 0 to 4000 N, the frequency increased by 51.82% which is due to the increase in the friction and, consequently, the generated resistance moment between the loading bar and the actuator. Table 3.4 shows that by decreasing the connection area from 1 to 0.1 cm the natural frequency of the aluminum sample increases by 0.045% in comparsion with the reference value and by increasing the vertical load from 0 to 4000 N,

the natural frequency increases by 0.05%. This means the effect of the loading bar and the vertical load on the response of the device decreases with an decrease in the resistance moment in the connection area. The variations of Δ_1 in Table 3.4 show that the effect of the vertical load on the dynamic behaviour of the device decreases with a decrease in the connection area (s) and generated resistence moment. Therefore, the rotational frequency of the aluminum sample was affected by the generated resistance moment at contact point which was due to the frictional interaction between the loading bar and actuator. This resistance moment can be reduced by minimizing the contact area and decreasing the friction between the loading bar and actuator. According to this argument, the effect of point loading (loaded on central axis of device) on the rotational mechanism of device can be neglected. For decrease the friction in the connection area, the diameter of the connection area between the loading bar and the top cap of the resonant column device was decreased to less than 1 mm and also a smooth steel plate with a high stiffness and the minimum friction coefficient was added to the top of the actuator.

3.5.4 Validation of modified apparatus

3.5.4.1 Validation with the aluminum sample

Aluminum samples with diameters of 2, 4 and 6 cm and 30 cm in height (defined as samples No.2, No.4 and No.6) were used to control the compliance (defined by Clayton et al. 2009) of the resonant column device. Three methods were used to determine the resonant frequency of the aluminum samples. In method one, the aluminum samples were mounted in the resonant column device and the resonant frequency of the aluminum samples and, consequently, the stiffness of the samples were determined. In the second method, so-called theoretical method, the stiffness of aluminum samples was assumed 25 GPa and the resonant frequency of the samples was determined using Equation 3.1 and Equation 3.2. In the third method, the finite element model was used to determine the frequency of the samples (as discussed above). The calculated resonant frequencies for the aluminum samples with these methods are summarized in Table 3.3. As can be seen in Table 3.3, error of the device for sample No.2, in comparison with the theoretical method, is more than error of the device for aluminum sample No.4. This difference is due to the compliance of the sample, because the stem of sample No.2 in comparison with its length is so thin, therefore rotational signals may be affected by flexural signals during tests with this sample. As can be seen in Table 3.3, a significant error was obtained for sample No.6, which was due to the type of rotational mode. Sample No.6 was too stiff and thus the top

and bottom of the sample rotated in the same phase. In this situation, a spurious mode was measured instead of the actual mode.
Aluminum sample No.4 was chosen for the calibration and validation of the device for induced anisotropic tests. Aluminum sample No.4 was installed in the resonant column device and vertical load was increased from 0 to 3000 N. A small increment (0.88%) was observed in the obtained frequency for the aluminum sample (Table 3.5). The observed increment may be due to the compliance of the aluminum sample and connections.

3.5.4.2 Validation with soil sample

Piezoelectric elements (shear plates) were installed in the top and bottom caps of the modified resonant column device (Figure 3.6). A series of resonant column and piezoelectric element tests were conducted on dry samples subjected to isotropic and stress induced anisotropic loading.

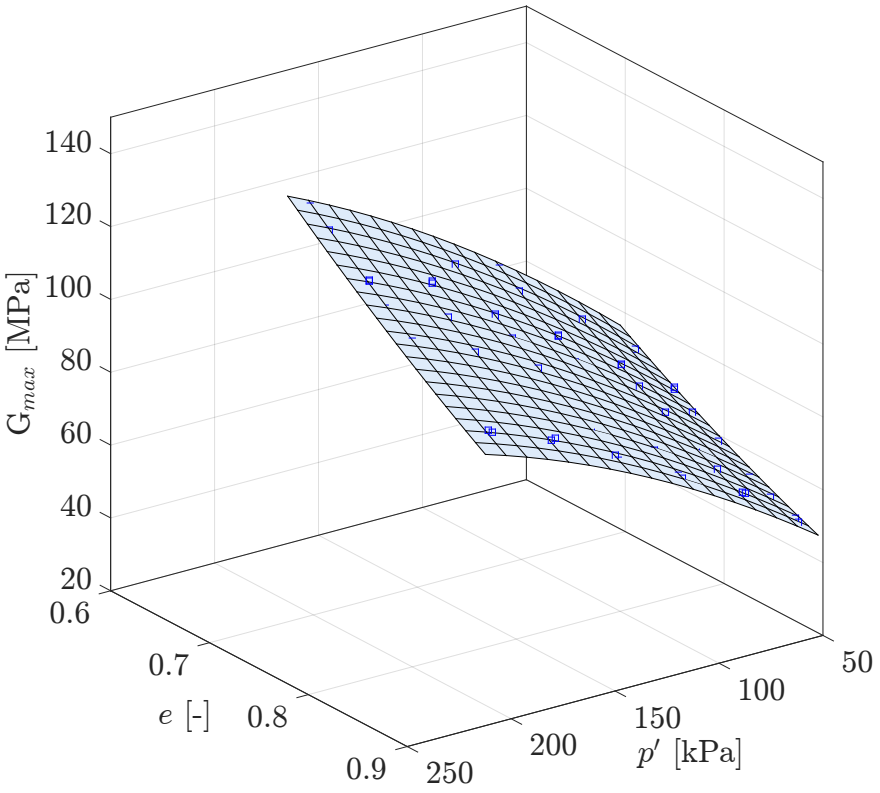

Figure 3.13: The effect of void ratio and confining pressure on maximum shear modulus

Figure 3.13 shows a decrease in maximum shear modulus with an increase in void ratio and a decrease in confining pressure for dry Hostun Sand subjected to isotropic confining pressure. The increase in stiffness with an increase in the confining pressure is due to the increase in the normal contact forces at contact points (will be discussed in Chapter 5). Four stress paths were defined (Figure 3.14a) to perform the stress induced anisotropic tests on dry Hostun Sand. In this experimental program shear plates (SP) were mounted in the top and bottom caps of the resonant column device and stress induced anisotropic tests were conducted with both of the devices simultaneously. The measured maximum shear modulus with both of the methods are compared with each other in this section.

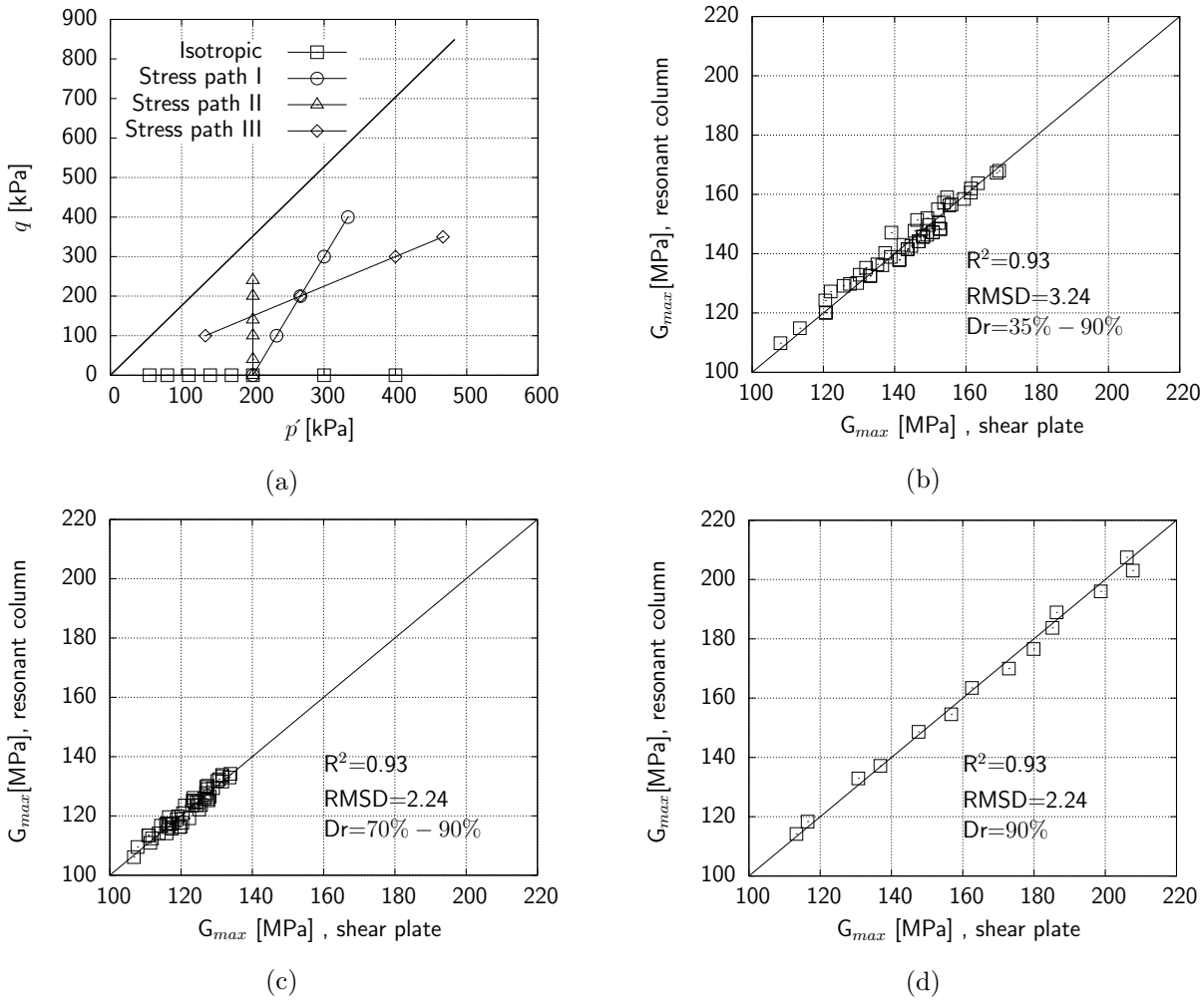

Figure 3.14: The experimental results using the resonant column device and shear plate elements: (a) stress paths; (b) stress path: I, Dr=35%−90%; (c) stress path: II, Dr=50%−90%; (d) stress path: III, Dr=70% − 90%

Two statistical measures of Root-Mean-Square-Deviation (RMSD) and R^2 were used to estimate the scatter of measured results by the resonant column in comparison with SP. For stress path I, vertical pressure was increased and confining pressure was kept constant at 200 kPa during RC tests. The measured maximum shear modulus (G_{max}) with RC and SP tests for this stress path is presented in Figure 3.14b.
This figure confirms a good agreement between the obtained results with the modified resonant column device and bender elements at this stress path. For stress path II, $p' = \frac{\sigma_1+2\sigma_3}{3}$ was kept constant at 200 kPa during RC tests and $q = \sigma_1 - \sigma_3$ was increased. The values of G_{max} for dry Hostun Sand with relative density of $70\% - 90\%$ for this stress path are presented in Figure 3.14c. Figure 3.14c shows a good agreement between the obtained results with the modified resonant column device and shear plate elements at this stress path. For the third stress path (stress paths III), the constant stress ratio was used to compare and contrast the obtained experimental results (K=$\frac{\sigma_3}{\sigma_1}$=0.5). As is clear in Figure 3.14d, the obtained results from the modified resonant column device are consistent with the obtained results from shear plate elements.
Sadek et al. (2007) conducted a comprehensive series of stress induced anisotropic tests on Hostun Sand with a relative density of 65% using cubical cell apparatus designed at Bristol. The results obtained by Sadek (2006) and the results from the modified resonant column device on the same stress path are presented in Figure 3.15.

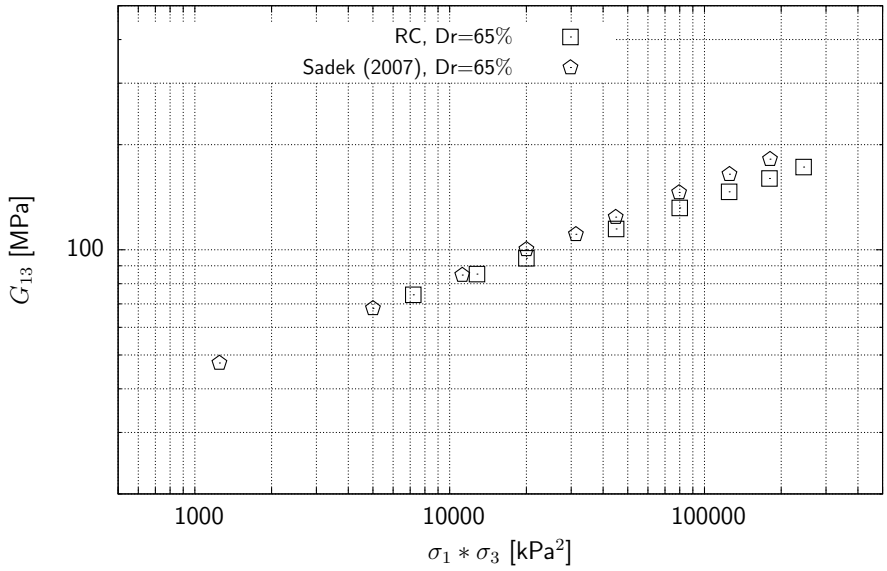

Figure 3.15: Maximum shear modulus for Hostun Sand, obtained by the cubical cell apparatus, Sadek (2006) and the modified resonant column

As can be seen in this figure, there is a good agreement between the results from the modified resonant column device and the results presented by Sadek (2006), although the device and the test methods are quite different in both of the experimental studies.

3.5.5 Calibration for damping

The objective of this section is to validate the adopted method, the energy method, for determining the damping ratio in the soil samples and to assess the effect of vertical load on the equipment damping. Energy method was used to measure the damping of soils with the Bochum resonant column device (Wichtmann et al. 2001, Wichtmann & Triantafyllidis 2013, Wichtmann et al. 2015). In the energy method, the damping ratio is determined from the hysteresis loop as the ratio of the dissipated energy in one cycle of loading (ΔW) over the 4π times of the total energy (W). However, the device and the method of calculation of damping must be calibrated before performing a test with the device.

Aluminum sample No.4 was used to determine the equipment damping. The measured damping for aluminum sample No.4 with the energy method is presented in Figure 3.17. According to this figure, the damping in a very small strain region is more than the measured damping in a small strain region. Therefore, two additional methods, free vibration decay curves and the bandwidth method, were used to determine the damping ratio in the aluminum sample and to compare the results with the energy method.

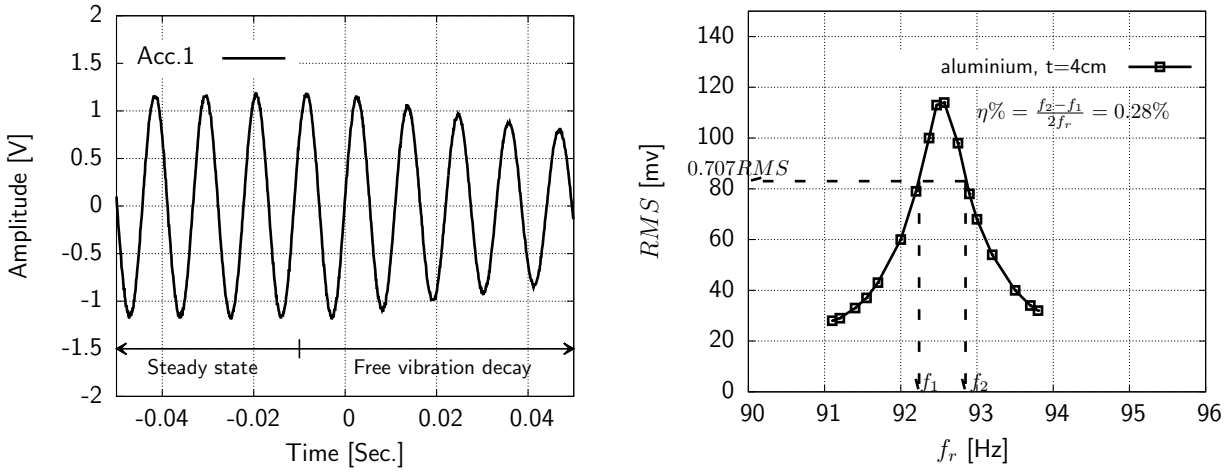

(a) (b)

Figure 3.16: Measurement of damping ratio: (a) free vibration decay curve; (b) band width method

In the free vibration decay curve, after taking resonant frequency, the input power of device was disconnected and the signal received from the accelerometer (Acc.1) was recorded. The recorded signal was used to determine the damping ratio. The logarithmic decrement of, Z, is calculated from the recorded decay curve (Stokoe et al. 1999*a*):

$$Z = ln(\frac{z_1}{z_2}) \tag{3.9}$$

where, z_1 and z_2 are the amplitude of two cycles (Figure 3.16a). Material damping ratio is calculated from the the value of Z (Stokoe et al. 1999*a*).

$$\eta = \left[\frac{Z^2}{(4\pi^2 + Z^2)}\right]^{1/2} \tag{3.10}$$

In the second method, the bandwidth method or half-power method, the variation in RMS in respect to frequency was recorded. The recorded data were used to determine the resonant frequency and damping ratio at the desired shear strain amplitude. Resonant frequency and half-power frequencies (f_1 and f_2) are the main variables to calculate the damping ratio with this method. The frequencies f_1 and f_2 are two points, where the amplitude of excitation is equal to $1/\sqrt{2}$ of maximum amplitude (Figure 3.16b). In material with a small damping ratio, damping ratio can be estimated from the following relationship (details can be found in: Das 1993 and Stokoe et al. 1999*a*):

$$\eta = \frac{f_2 - f_1}{2f_r} \tag{3.11}$$

The measured damping with these methods for aluminum sample No.4 is summarized in Figure 3.17. This figure shows the impact of noise on damping at a very small strain region with the bandwidth method is less than that for the other methods which may be due to the effects of near field conditions on accelerometers. According to the observed results, two calibration lines can be defined as equipment damping in the Bochum resonant column device (Figure 3.17). The first line relates to the very small strain regions. In this region amplitude of deformations is so small (oscillation with low amplitude) that the results were affected by noise or near field conditions. The other line, which is approximately constant at the small strain region, is related to the equipment damping which is due to the connections and quality of the sample.

The equipment damping was measured under anisotropic loading by increasing the vertical load. Table 3.5 shows damping decreases with an initial increase in the vertical load at top of the sample. Connections between the aluminum sample and the device may be fitted to each other better by increasing the vertical load, therefore, the initial decrease in the damping may be due to the compliance of connections and the sample.

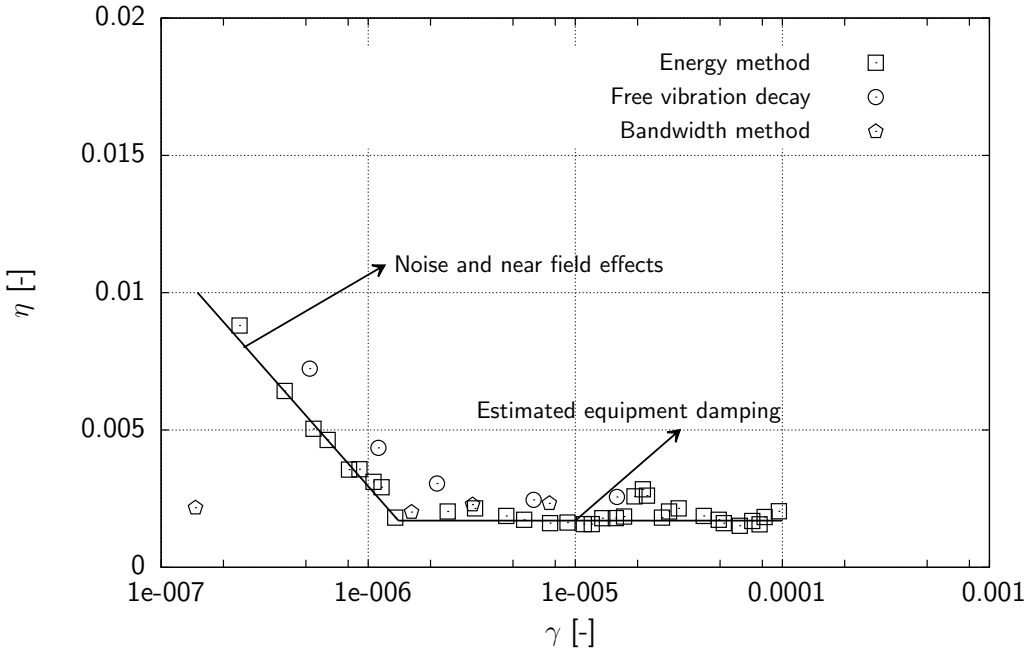

Figure 3.17: Equipment damping with aluminum sample, t=4cm

Table 3.5: The measured resonant frequency for aluminum sample under anisotropic loading

Specimen t [cm]	Contact size s [cm]	Vertical load F_v [N]	RC test f_r [Hz]	Effects of loading bar Δ_v [%]	damping ratio at $\gamma \approx 10^{-5}$
4	0.1	0	92.41	-	0.00205
4	0.1	500	92.83	0.45%	0.00184
4	0.1	1000	93.11	0.76%	0.00163
4	0.1	2000	93.19	0.84%	0.00158
4	0.1	3000	93.22	0.88%	0.00161

3.6 Experimental procedure

3.6.1 Isotropic tests

Figure 3.18 shows the steps for assembly of the Bochum resonant column device. Firstly, specimens with 10 cm in diameter and 20 cm in height were prepared by the dry funnel deposition method for mixtures and clean coarse materials. Afterward, the top cap was

mounted at the top of the sample. Then, the maximum vacuum of 55 kPa was applied through the top and bottom caps to stabilize the sample before assembling the resonant column device. The sample dimensions were measured accurately and then the sample was transfered to the RC device and the other parts of the device were assembled. Afterwards, the vacuum was reduced and the confining pressure was increased slowly step by step. The specimens were consolidated to the desired isotropic pressure of $\sigma_1 = \sigma_3$=55, 80, 110, 140, 170 and 200 kPa before performing resonant column test.

3.6.2 Anisotropic tests

Specimens with 10 cm in diameter and 20 cm in height were prepared by the dry pluviation method. The maximum vacuum of 55 kPa was applied through the top and the bottom caps to stabilize the sample. Then the vacuum was reduced and the confining pressure was increased slowly step by step. For stress induced anisotropic tests with a constant confining pressure, the confining pressure was increased up to desired value (σ_3=200 kPa), then the vertical pressure was increased using the double acting cylinder (Figure 3.10) slowly to: 250, 300, 350, 400, 500, 550 and 600 kPa. After consolidation of ´the samples at the desired stress state, resonant column tests were conducted on the sample. Then the pressure was released and the device was prepared for the new sample to perform a resonant column test for the next stress ratio. To perform the test with constant p' the confining pressure was decreased and the vertical pressure was increased slowly (Table 3.6). For the stress path with constant stress ratio, confining pressure was increased to the desired isotropic pressure (55, 100, 200 and 300 kPa) and then the vertical stress was increased up to a stress ratio equal to two.
After consolidation of the sample at the desired stress conditions, the amplitude of excitation was increased to get the resonant frequency, and consequently, the stiffness and damping ratio at different amplitudes of excitation.

Table 3.6: The measured resonant frequency for aluminum sample using the resonant column device

No.	stress path	confining pressure, σ_3, [kPa]	vertical pressure, σ_1, [kPa]
1	Isotropic	σ_3	σ_3
2	Constant σ_3	σ_3	σ_3+$\Delta\sigma$
3	Constant p'	σ_3-$\Delta\sigma''$	σ_3+2$\Delta\sigma''$
4	Constant $K = \sigma_3/\sigma_1$	σ_3	σ_3+σ_3

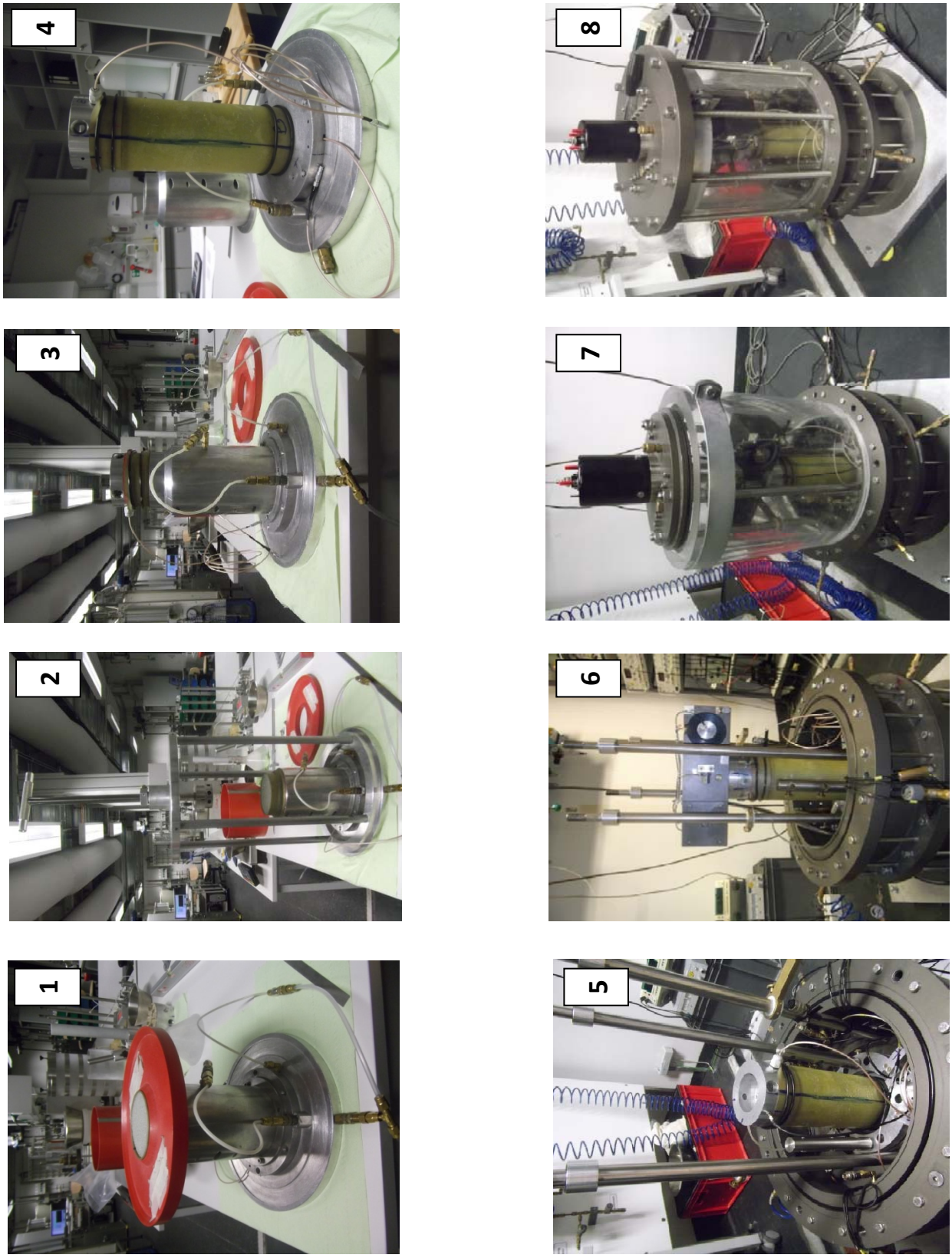

Figure 3.18: Steps of assembly of the Bochum resonant column apparatus

3.7 Summary

The experimental program of this research was discussed in this chapter. The physical and mechanical properties of adopted materials, Hostun Sand and glass beads, were discussed in the required detail for the interpretation of the experimental results in later chapters of this thesis. The resonant column device is an accurate device but the accuracy of the results depends on the calibration of the device (Drnevich 1978). Therefore, the adopted numerical, theoretical and experimental procedures for the calibration and validation of the apparatus were discussed in this chapter. According to the analysis with ABAQUS software and experimental tests performed with aluminum samples: 1- two rotational frequencies can be detected with the free-free resonant column device, one of them is the actual rotational mode of the sample, 2- the effect of the vertical load on the dynamic behaviour of the system (resonant column device) can be ignored by minimizing the resistance moment produced at the connection area, between the loading bar and the actuator. The experimental results measured with the resonant column device were consistent with the results from the piezoelectric elements for the same sample and various stress paths. Therefore, the results showed that this device has been modified and validated successfully.

4 Effect of fines content

4.1 Introduction

Mechanical properties of geo-materials, e.g. stiffness and damping, are significantly related to the amplitude of deformations or vibrations. The small strain properties of materials can be affected by parameters which are related to the particle properties, structure of packing and boundary conditions. The structure of packing is one of the important parameters which have a significant influence on the stiffness of materials (e.g. Hardin & Drnevich 1972*b*, Drnevich 1978, Tatsuoka et al. 1978, Darendeli 2001, Hardin & Kalinski 2005 and Wichtmann & Triantafyllidis 2013). the structure of packing may be affected by the existence of fine particles in granular packing. The influence of fine particles on the fabric of samples is explained from a microscopic level and also empirical relationships can be modified based on the micro and macroscopic observations which is helpful to estimate the small strain stiffness of mixtures. Thevanayagam (1999) used the concept of equivalent void ratio for limited published datasets to predict maximum shear modulus and reported that the effect of f_c can be captured by replacing e by e^* in Equation 2.7 but their data were too limited to draw conclusions. Rahman et al. (2012) estimated e^* from soil grading properties and used it in Equation 2.7 to capture the effect of fines for collected data sets. They reported that e^* in Equation 2.7 can capture the effect of non-plastic fines. However, collected data sets were not designed for the evaluation of e^* to capture the effect of f_c on G_{max} and the maximum f_c covered was only 20%. Thus, a suitable approach for capturing the effect of a wide range of non-plastic f_c on small and intermediate strain properties is still a topic of research interest.

Soil elements have a nonlinear behaviour when they subjected to a different amplitude of deformation or vibration. The lower and upper curves for modulus ratio and damping ratio curves, proposed by Seed et al. (1984), are shown in Figure 4.1a and Figure 4.1b.

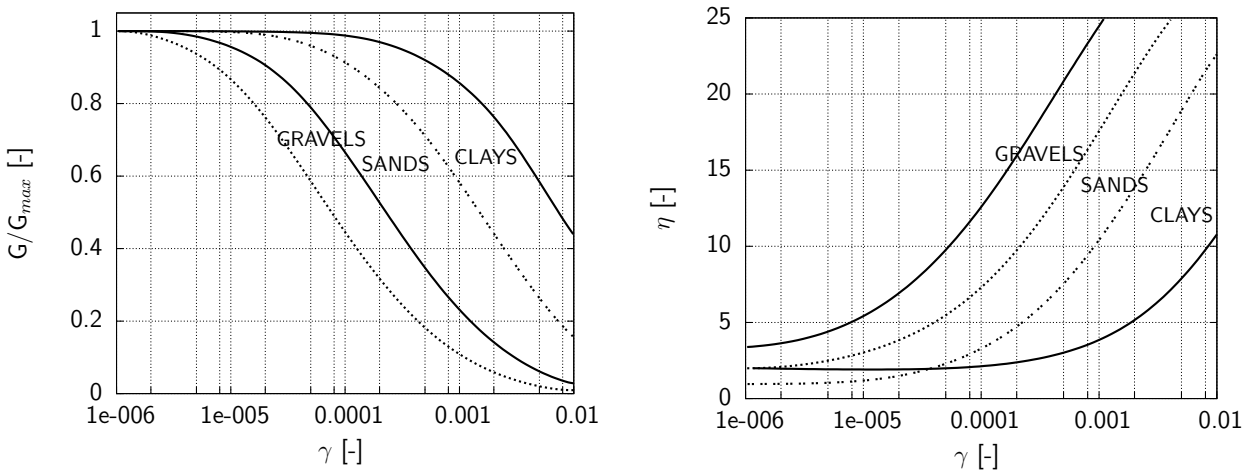

(a) (b)

Figure 4.1: Small strain stiffness and damping in materials, modified after Darendeli (2001): (a) modulus ratio versus shear strain; (b) material damping ratio versus shear strain

From Figure 4.1a and Figure 4.1b, it can be seen that damping and modulus degradation are significantly affected by material properties, (e.g. Iwasaki & Tatsuoka 1977, Ishibashi & Zhang 1993, Darendeli 2001 and Wichtmann & Triantafyllidis 2013). Ishibashi & Zhang (1993) studied the influence of the plastic index (PI) on the nonlinear behaviour of soils using the resonant column device and concluded that the modulus ratio increases and the damping ratio decreases by increasing PI. Darendeli (2001) and Wichtmann & Triantafyllidis (2013) studied the influence of grain size distribution on the modulus degradation curve and damping. However, studies on the modulus degradation and damping ratio in granular material containing a wide range of fines content are rare. Hence, discussions on the effect of fine particles on the intermediate strain properties of granular packing containing a wide ranges of fines content are also considered in this chapter. The effect of fines on the observed experimental results will be discussed from the microscopic point of view.

Therefore, resonant column and compression wave velocity tests were conducted on the mixtures (Section 3.3) containing a wide range of fines content to evaluate the effects of fine particles on small strain properties at a macro level. Afterward, the observed results were explained through the concept of equivalent void ratio, e^*, developed by Thevanayagam (1998).

This chapter has four major objectives: (i) present the results from resonant column and piezoelectric element test on mixtures, covering a wide range of f_c, e and p'; (ii) present

a micro-mechanic analysis, Micro-CT scan, to assess the effect of f_c on elastic properties; (iii) evaluate the relative performance of Hardin's formulation for the mixtures; (iv) predict the maximum moduli of mixtures with Hardin's empirical relation (Equation 2.7) and calculate fitting parameters for coarse particles.

4.2 Test results on sand mixtures

4.2.1 Test results on G_{max}

The influence of p' and e on G_{max} of clean Hostun Sand and sand containing fines content is presented in Figure 4.2. Test data show distinctive and separate trends of G_{max} - e relation for different p' and G_{max}. These figures show G_{max} increases with increasing p' irrespective of f_c. Figure 4.2 shows the effect of void ratio on maximum shear modulus for all of the mixtures. This figure shows that the value of maximum shear modulus decreases with an increase in the void ratio. For instance, the value of G_{max} for dense clean Hostun Sand (Dr=90%) is 73 MPa at the confining pressure of 55 kPa but, this value increases to 145 MPa at confining pressure of 200 kPa. Also, the value of G_{max} for Hostun Sand with relative density of 90% is 145 MPa at the confining pressure of 200 kPa and decreases to 94 MPa for loose sample with relative density of 35% at the confining pressure of 200 kPa. These results confirm the dependency of G_{max} on the confining pressure and density of sample which is also true for all of the mixtures (Figure 4.2). Figure 4.3 shows the effect of fines content on maximum shear modulus. This figure shows that the maximum shear modulus decreases with an increase in the fines content. As can be seen in Figure 4.3, the highest value for maximum shear modulus was obtained for clean Hostun Sand for all of the applied confining pressures. For instance, according to Figure 4.3f at p'=200kPa and e=0.72, the value of G_{max} for clean Hostun Sand is about 128 MPa. This value decreases to 84 MPa for clean Hostun Sand containing 30% f_c.

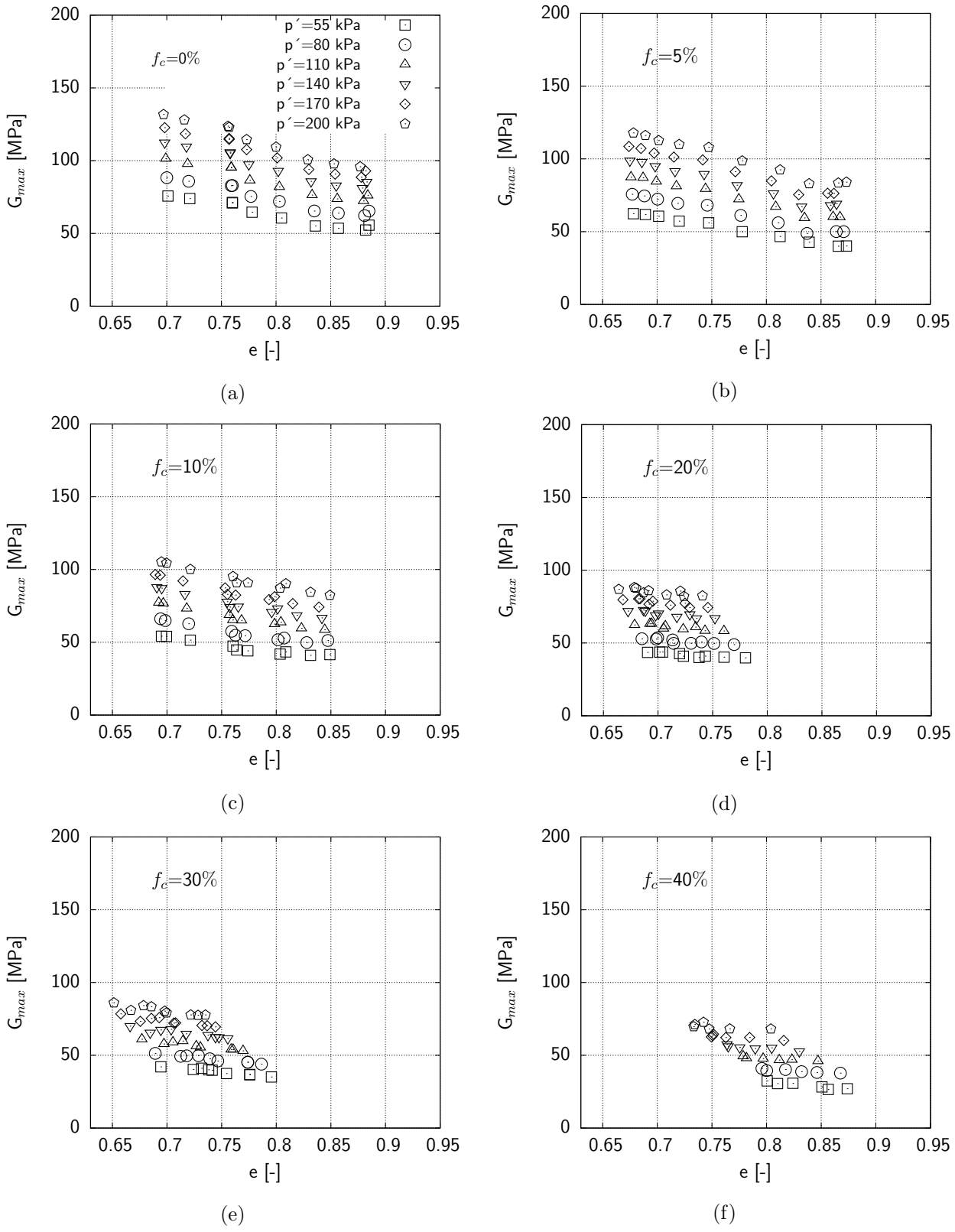

Figure 4.2: The effect of confining pressure and void ratio on the maximum shear modulus of mixtures: (a) f_c=0%; (b) f_c=5%; (c) f_c=10%; (d) f_c=20%; (e) f_c=30%; (f) f_c=40%

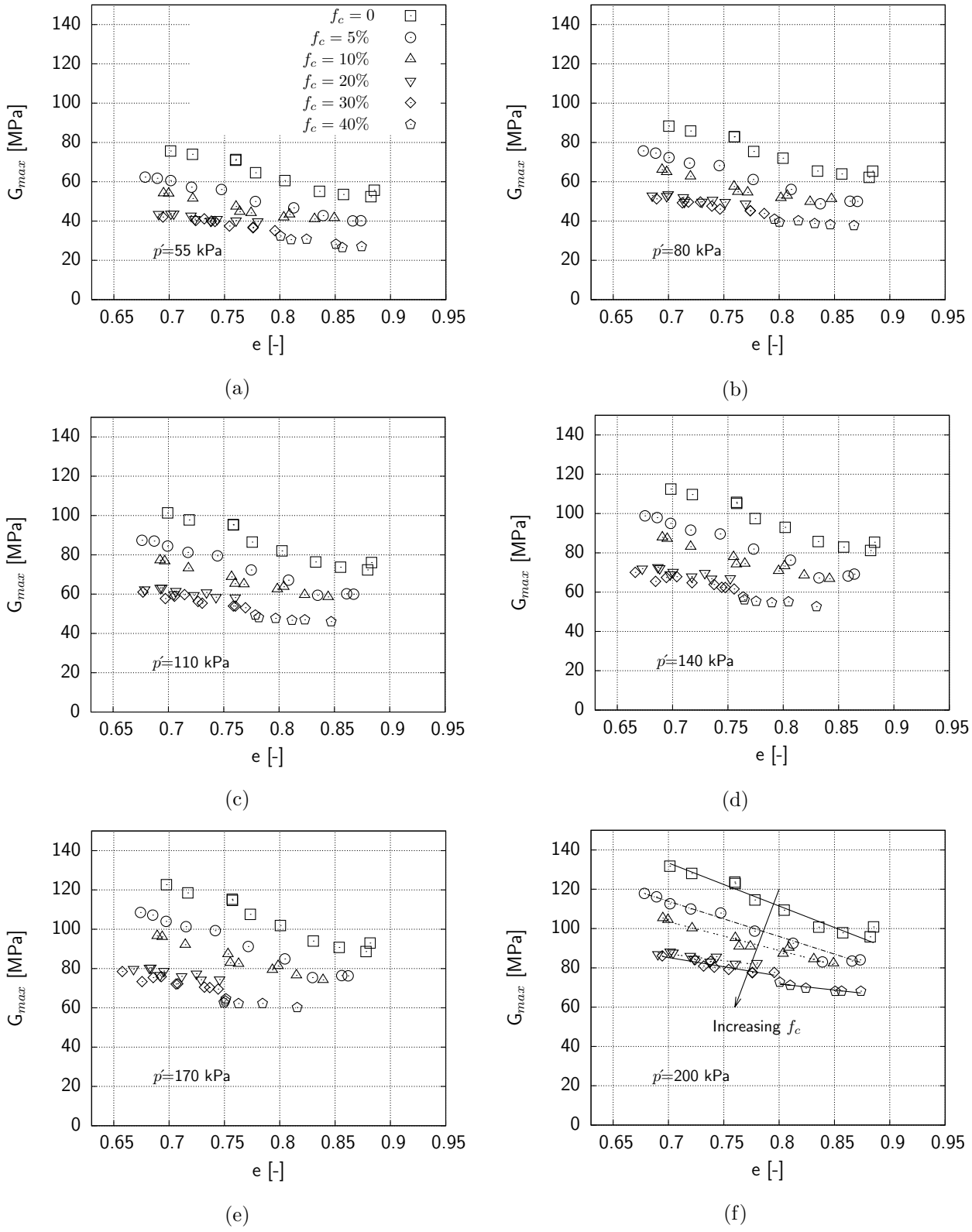

Figure 4.3: The effect of fines content on the maximum shear modulus for the various confining pressures: (a) p'=55 kPa; (b) p'=80; kPa (c) p'=110 kPa; (d) p'=140 kPa; (e) p'=170 kPa; (f) p'=200 kPa

4.2.2 Test results on $G(\gamma)$ and $\eta(\gamma)$

Resonant column tests were conducted to evaluate the effect of shear strain amplitude and fines content on intermediate strain properties ($G(\gamma)$ and $\eta(\gamma)$) of mixtures. Figure 4.4 shows, as an example, the effect of isotropic loading on the modulus degradation and damping curves of clean Hostun Sand. Figure 4.4a shows that shear modulus is constant and equal to the maximum shear modulus up to a shear strain amplitude of 5E-6. Also, this figure shows modulus ratio increases with an increase in the confining pressure. The effect of the confining pressure on the damping ratio is shown in Figure 4.4b. As it can be seen in this figure, the damping ratio decreases with an increase in the confining pressure. Figure 4.5 shows the effect of fines content on modulus and damping ratio curves, in comparison with clean Hostun Sand, for samples with a relative density of 75%-77%. The general trend shows the G/G_{max}-$log\gamma$ shifts to the lower stiffness with an increase in the fines content up to fines content of 20% and then, G/G_{max} increases for mixtures with a higher amount of fines content (Figure 4.5a). Experimental test data show that damping ratio curves have also been affected by fines content (Figure 4.5b). This figure shows the damping ratio decreases with an increase in the fines content up to fines content of 20% and it then decreases with further increases in the fines content.

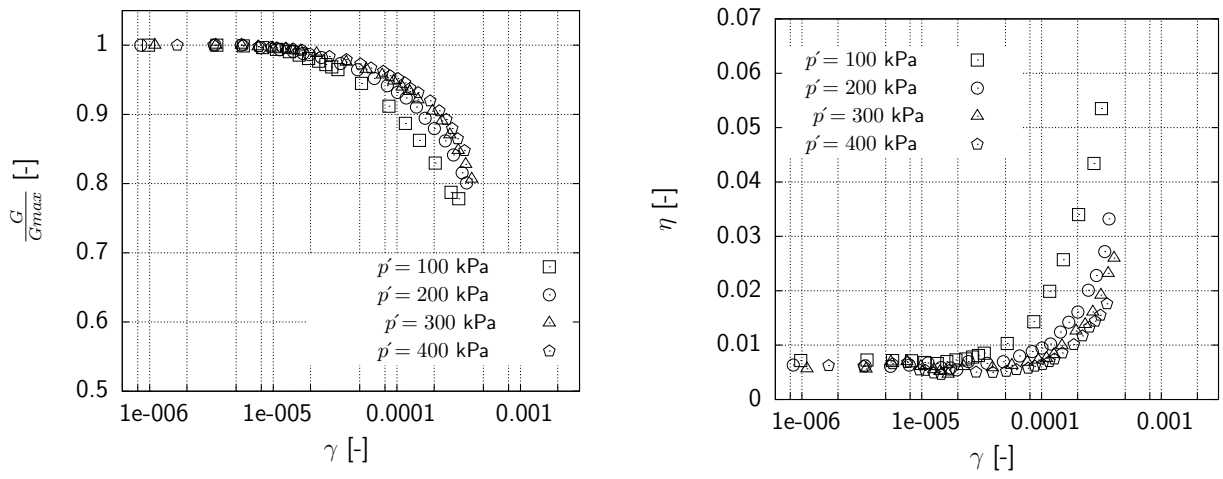

(a) (b)

Figure 4.4: The effect of p' on intermediate strain properties of clean Hostun Sand Dr=38% for isotropic loading: (a) G/G_{max}; (b) damping ratio (η)

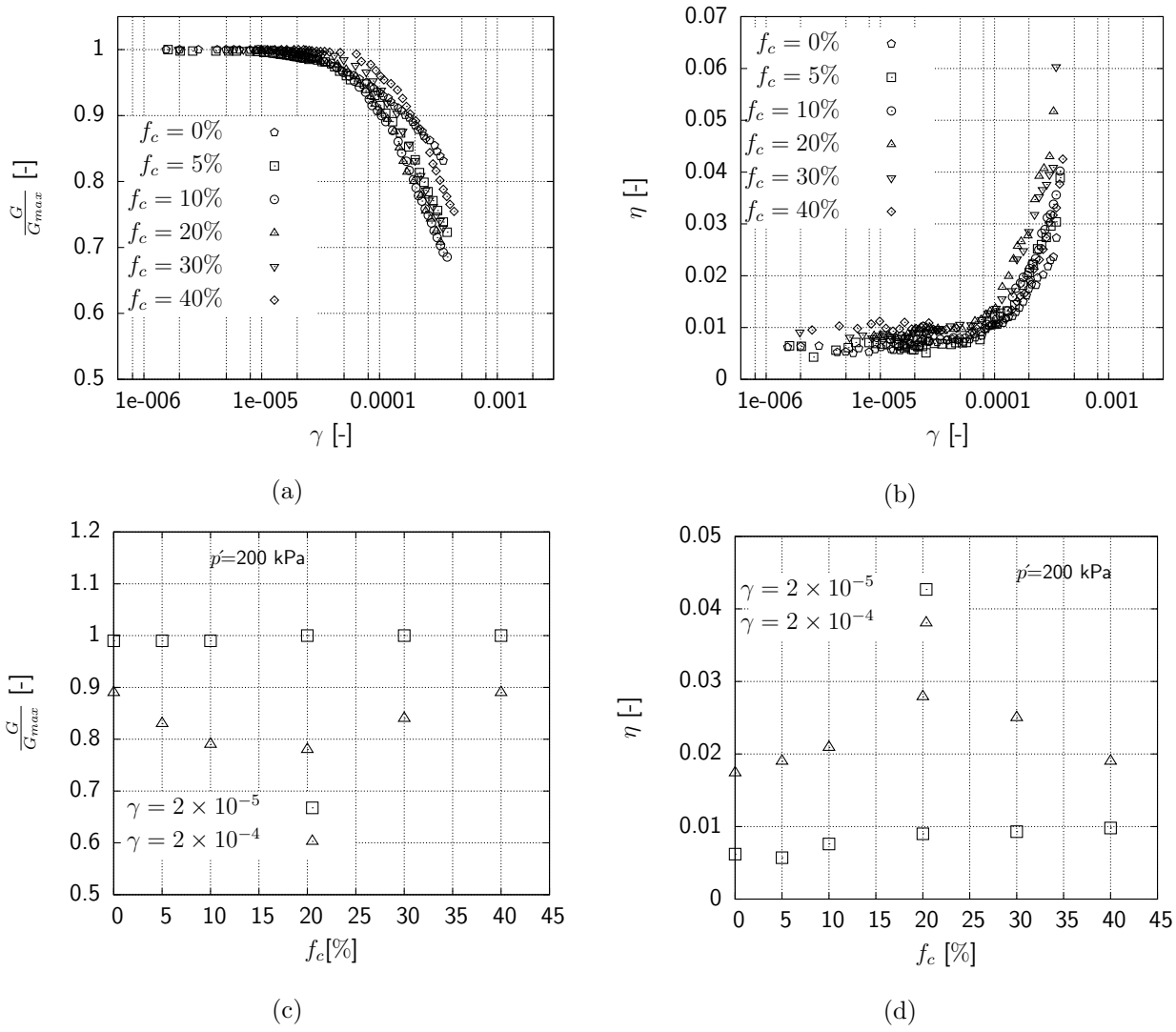

Figure 4.5: Small and intermediate strain stiffness and damping of mixtures, Dr=80%-90%: (a) modulus degradation curves; (b) damping curves; (c) the effect of fines content on G/G_{max}; (d) the effect of fines content on $\eta(\gamma)$

The test data shows that the value of η_{min} increases with an increase in the fines content. Damping and the modulus ratio at small and intermediate strain amplitude, 2E-4 and 2E-5, are presented in Figure 4.5d and Figure 4.5c with respect to fines content (quartz powder). These figures show the dependence of damping and the modulus ratio to fines content which is more significant in the intermediate strain region.

The test data in Figure 4.6 reveal that the shear modulus (G) is significantly affected by the density of the sample. This figure also shows that the shear modulus is constant and equal to the maximum shear modulus up to a shear strain less than the elastic threshold value, γ_{et} (Stokoe et al. 1999*b*), which is a value between 5E-6 for clean Hostun Sand to

1.5E-5 for clean Hostun Sand containing 40% fines content. The value of γ_{et} increases significantly with an increase in the fines content. The general relation between G/G_{max} and $log\gamma$ curves for the mixtures at the mean effective stress of 200 kPa is presented in Figure 4.7. This figure shows that the effect of density of sample on G/G_{max} is not significant for all of the mixtures. Figure 4.8 shows the effect of void ratio on damping ratio curves. The presented experimental results show the insignificant effect of relative density on the damping ratio and G/G_{max} of clean Hostun Sand and mixtures which is in line with the experimental results presented by Kokusho (1980), Iwasaki et al. (1978) and Wichtmann & Triantafyllidis (2013). This figure reveals that γ_{et} decreases slightly with an increase in the fines content up to $20\% f_c$, and it then increases significantly with an increase in the f_c. The test data show that the damping ratio increases with an increase in the fines content up to f_c of 20% and then decreases with further increases in the fines content.

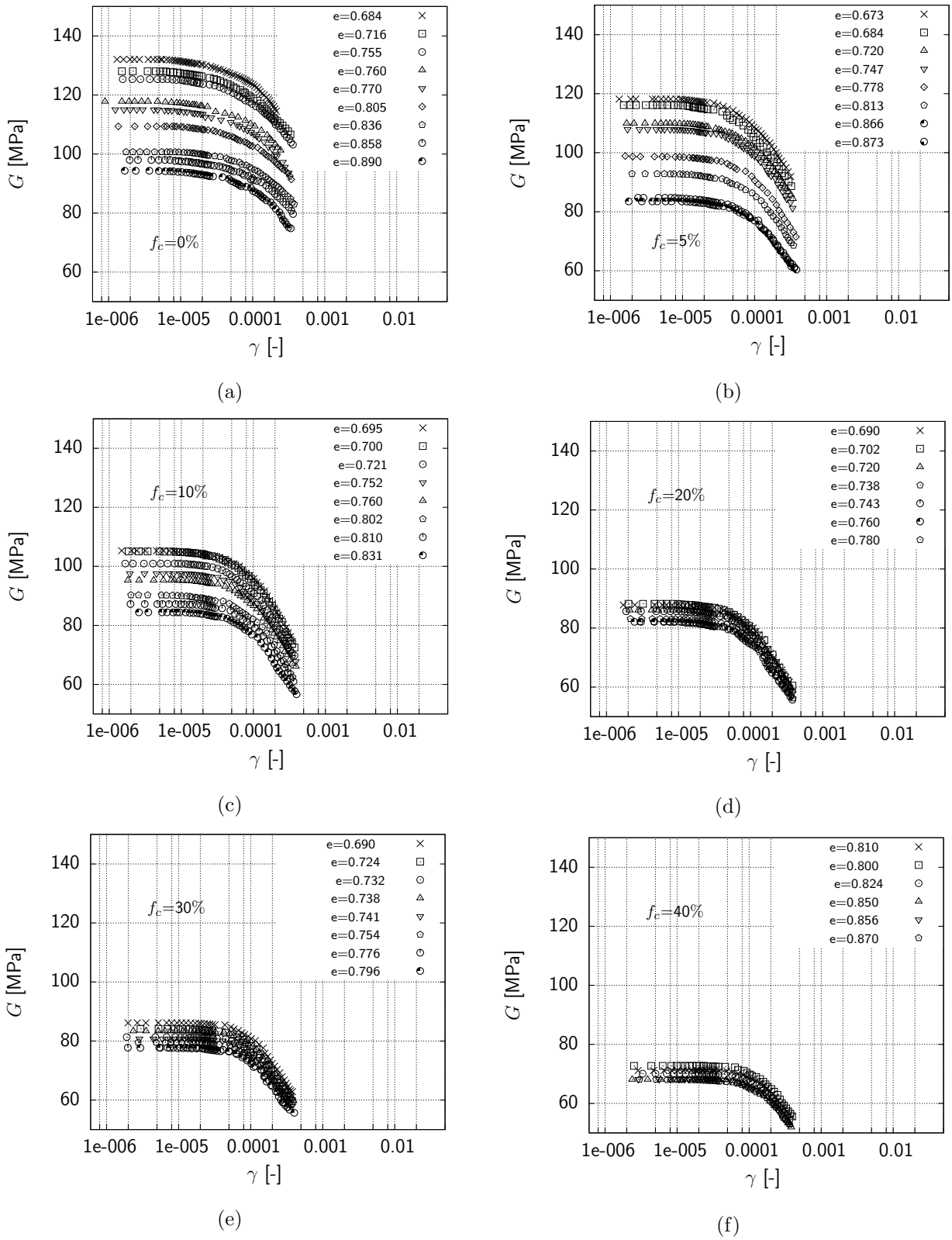

Figure 4.6: Shear modulus versus shear strain, p'=200 kPa: (a) f_c=0; (b) f_c=5%; (c) f_c=10%; (d) f_c=20%; (e) f_c=30%; (f) f_c=40%

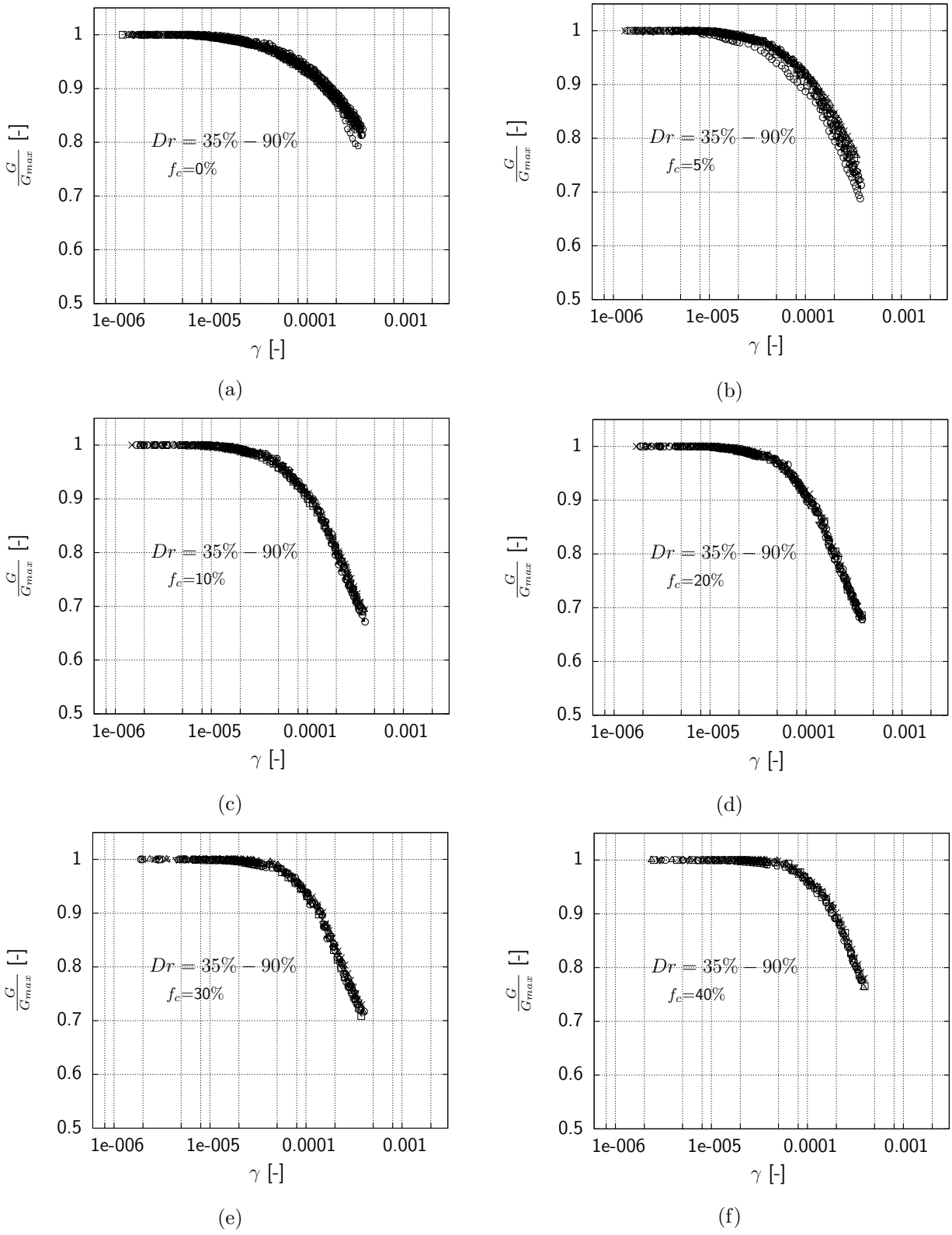

Figure 4.7: Modulus ratio (G/G_{max}) versus shear strain, p'=200 kPa: (a) f_c=0; (b) f_c=5%; (c) f_c=10%; (d) f_c=20%; (e) f_c=30%; (f) f_c=40%

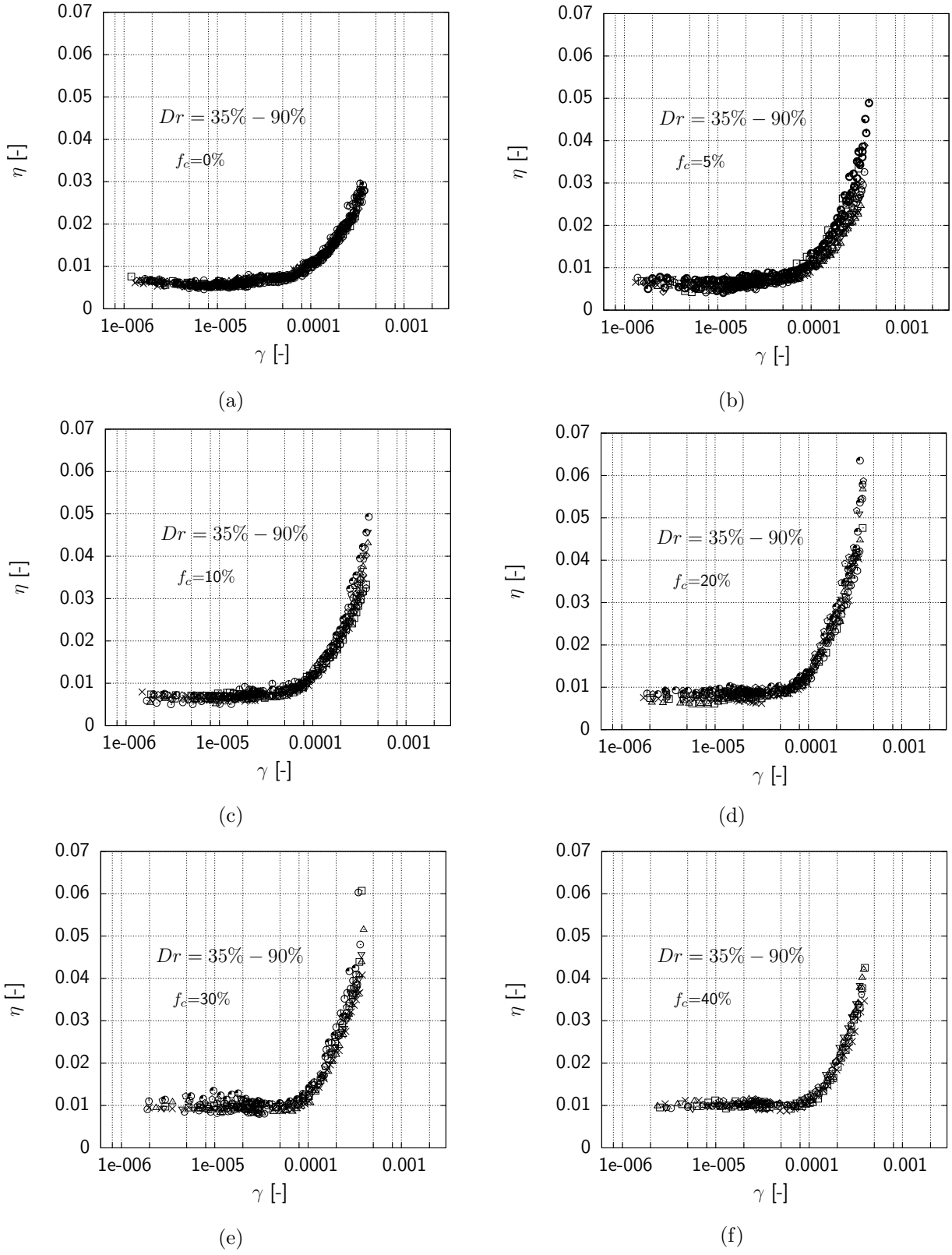

Figure 4.8: Damping ratio versus shear strain, p'=200 kPa: (a) f_c=0; (b) f_c=5%; (c) f_c=10%; (d) f_c=20%; (e) f_c=30%; (f) f_c=40%

4.3 Test results for glass bead mixtures

Resonant column tests and compression element tests were conducted on coarse glass beads and mixtures to assess the effect of fines content on stiffness (Goudarzy et al. 2014). Resonant column and compression element tests were carried out at isotropic pressures of 50, 100, 150 and 200 kPa. After increasing the isotropic pressure to the target isotropic pressure, a rest period of at least 1 hour was applied to allow for creep of the sample. The structure of adopted samples was susceptible to significant volume change and collapse during the loading which was due to the interaction between the highly rounded fine and coarse particles (Yang & Wei 2012). The results for samples without collapse are presented in this section. The maximum shear modulus was determined by the resonant frequency measured using the resonant column device. In the compression wave velocity test a sinusoidal wave with a frequency of 10 kHz was transmitted by the compression elements which were mounted in the top and bottom caps of the sample. The first arrival or deflection method was adopted to detect travel time, t_p (e.g. Yamashita et al. 2005). Therefore, the compression wave velocity (v_p) is equal to the length of the sample at the time of the compression element test over the travel time. Therefore, the values of G_{max} and M_{max} were measured using the experimental results and the value of Young's modulus, E_{max}, was calculated using Equation 4.1 (Birch 1961 and Mavok et al. 2009).

$$E = \frac{G(3M - 4G)}{M - G} \tag{4.1}$$

where M is the p-wave modulus, G is the shear modulus and E is Young's modulus. The experimental results show the increasing and decreasing of the maximum elastic moduli, G_{max}, M_{max} and E_{max}, with increase in the mean effective stress and void ratio respectively (Figure 4.9). As an example, Figure 4.9a shows the effect of p' on the maximum shear modulus, G_{max}. As can be seen in this Figure, G_{max} increases with an increase in p' and decreases significantly with an increase in e. Also, the results demonstrate the dependence of maximum elastic moduli to fine particles (e.g. Figure 4.9b, Figure 4.9c and Figure 4.9d). Test data show that the value of the maximum elastic moduli decreases with an increase in the fines content up to 30% fines content and then it increase with further increasing of fines content which will be explained from the microscopic point of view in the following sections.

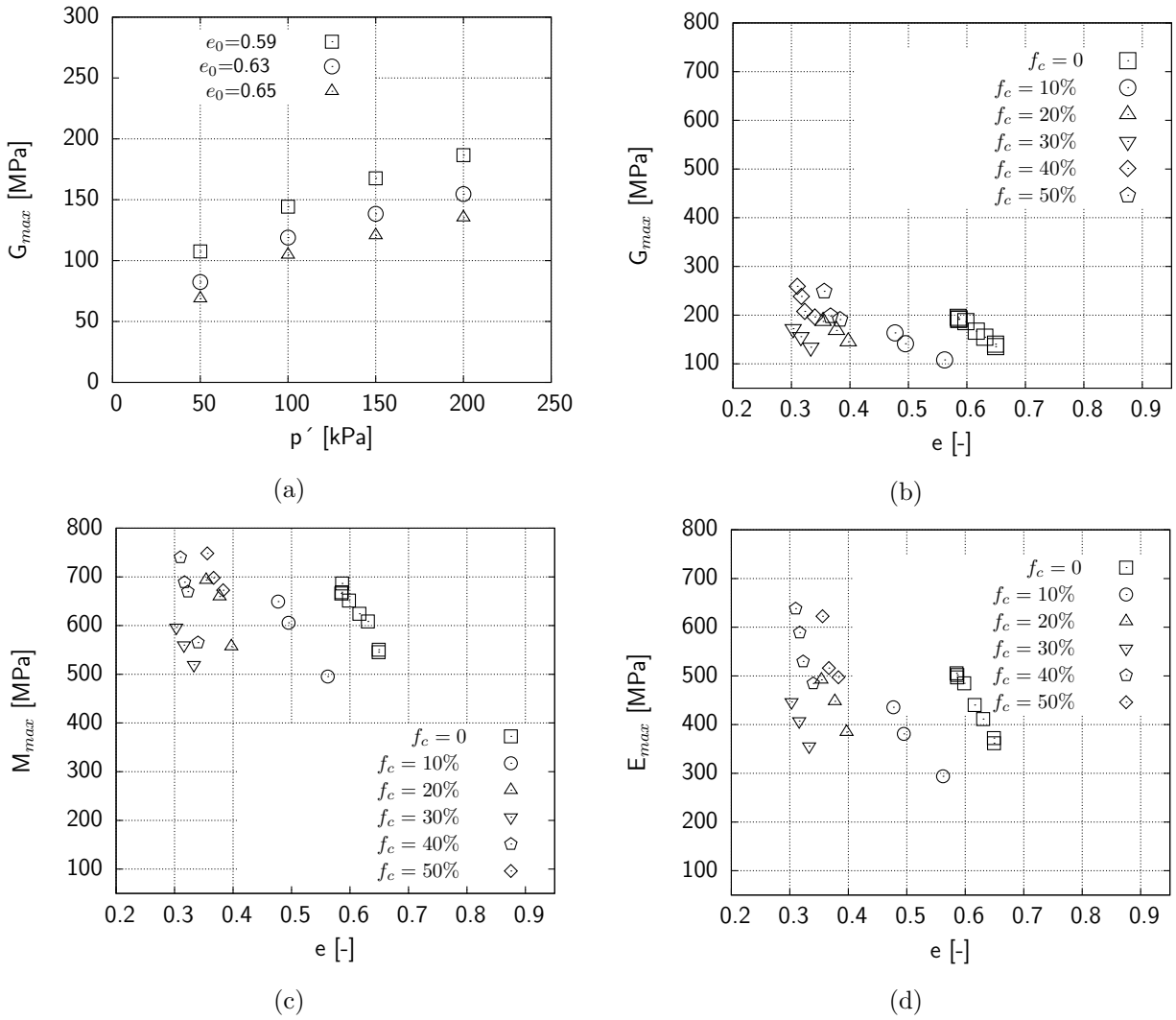

Figure 4.9: (a) the effect of void ratio and p' on G_{max} of coarse glass beads; (b) G_{max} vs e for the mixtures at p'=200 kPa; (c) M_{max} vs e for the mixtures at p'=200 kPa; (d) E_{max} vs e for the mixtures at p'=200 kPa;

4.4 Interpretation based on the micro-structure

The conceptual model developed by Thevanayagam (1998) is used to explain the influence of fine particles on the mechanical response of coarse particles at microscopic and macroscopic scales. Figure 4.10 shows the effect of fine particles on force chains and consequently the stiffness of mixtures. Based on the amount of fines content and the situation of fine particles in the mixture, five cases can be distinguished. In case i: in this case, fines content is zero and coarse particles make up the packing structure.

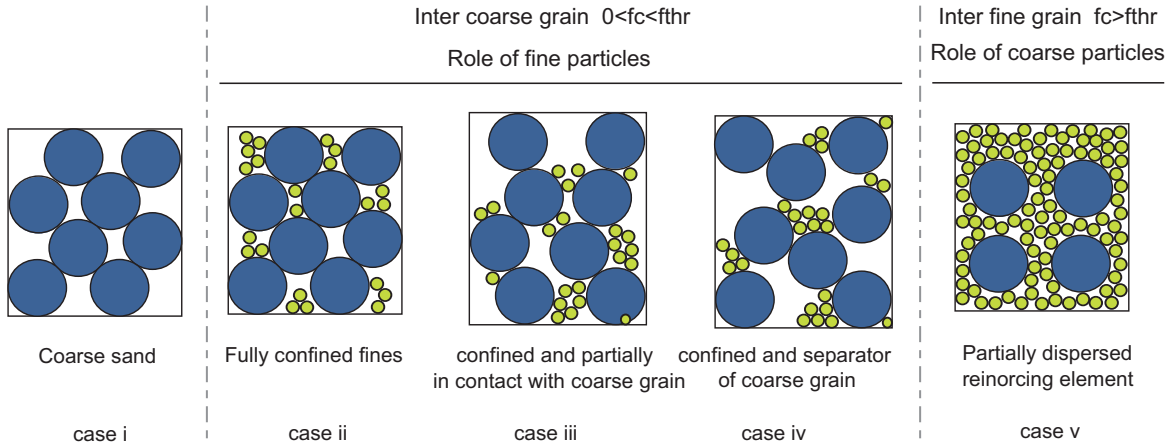

Figure 4.10: Active and inactive contacts in fines in coarse and coarse in fines mixtures, modified after Thevanayagam (2007)

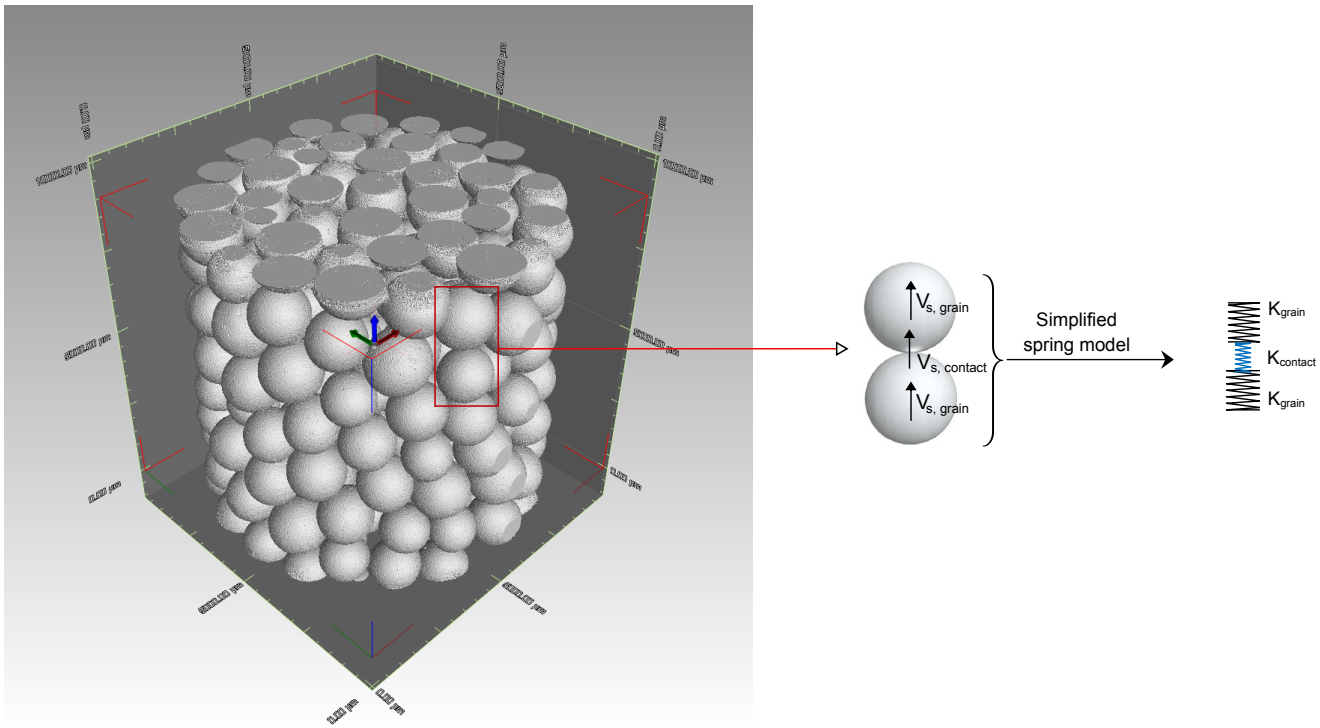

Figure 4.11: Sketch of interaction between two particles, V_s is shear wave velocity

By increasing the fines content, fines are placed in the coarse matrix. Due to the particle size ratio, fine particles can be accommodated in the void spaces and fines are confined by coarse particles (case ii), therefore they do not increase the amount of inter-particle

contacts and so do not contribute in the force chains of granular structure. However, some times, due to the sample preparation methods or material properties, fine particles are accommodated between two coarse particles (case iii and case iv). In this situation, fines separate two coarse particles from each other and due to the interaction between fine and coarse particles; stiffness of packing will be significantly affected. For ease of discussion, Figure 4.11 is used to explain the effect of particle size or interaction between particles on shear stiffness. From literature (e.g. Duffy & Mindlin 1957, Petrakis & Dobry 1987, Walton 1987, Chang & Liao 1994, Bui 2009 and Otsubo et al. 2015), grain stiffness and contact stiffness are two main characteristics which can make a significant effect on shear wave velocity and shear stiffness in granular packings. In the packing containing the same particle characteristics, shear wave velocity and shear stiffness are strongly affected by contact properties or contact stiffness ($K_{contact}$, Figure 4.11). Contact stiffness ($K_{contact}$) between smooth spheres is determined using Hertzian theory (Section 2.4). Hertzian theory reveals that normal contact force, contact radius and contact friction increases proportionally to grain diameter (Johnson 1985). Therefore, the observed decreasing in stiffness for mixtures containing fines (case iii and case iv) could be explained through the weak contact between fine and coarse particles in comparison with a contact between coarse and coarse particles.

By further increasing the fines content, fine particles will be dominant in the response of granular packing (case v); in this case, coarse particles will act like reinforced elements inside fine particles packing. Therefore, displacement and sliding of fines controlled by coarse particles, and the stiffness of packing depends on the characteristics of the fine particles. Thevanayagam (1998) proposed parameters b and m to determine the influences of fine particles at microscopic level (Section 4.5). As long as fines content are less than a certain value (threshold fine content, f_{thr}), parameter b will measure the active contacts (case iii and case iv) and for fines content greater than the threshold value parameter m will evaluate the interaction between coarse and fine particles (case iv).

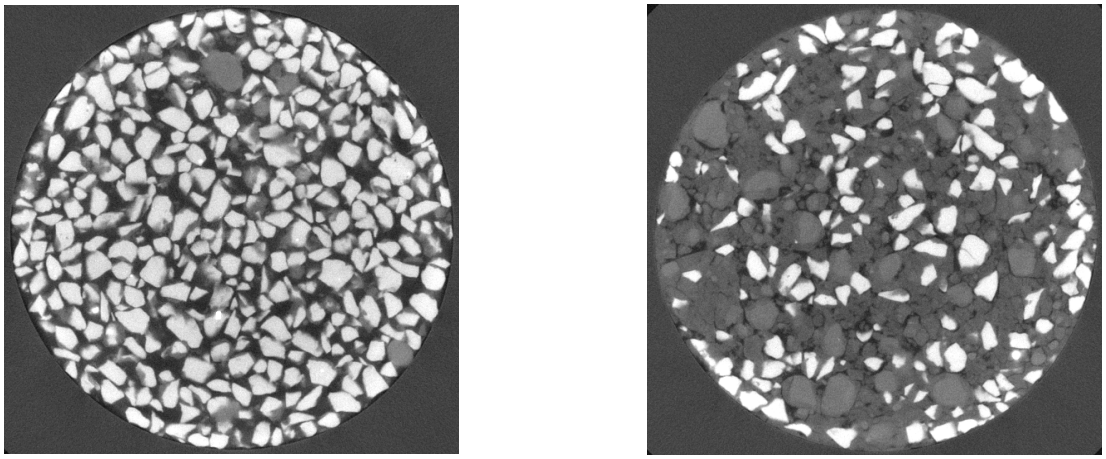

(a) (b)

Figure 4.12: Micro-CT scan image of clean Hostun Sand with: (a) 10% quartz powder; (b) 50% quartz powder, (gray portions: quartz powder, white portions: Hostun Sand)

To evaluate the effect of f_c on the micro-structure of Hostun Sand with f_c, Micro-CT scans on loose and dense specimens were carried out at Kumamoto University. The size of specimens was 40mm in height and 7mm in diameter and was prepared by the same dry deposition method. Figure 4.12a and Figure 4.12b show the Micro-CT images of the cross sections of specimens for sand with 10% and 50% f_c for relative densities of 92% and 85% respectively. The white portions are sand particles and the grey zones are fines, i.e. quartz powders. It is apparent from Figure 4.12a that 10% f_c merely coated some of the coarse particles. A fraction of f_c were located between coarse particles and the remaining fraction of fines were placed in void spaces between the sand particles. However, some coarse particles were still in direct contact. This confirms that the micro-structure for sand with 10% fines is still dominated by sand structure, although some fines are active in contact. The Micro-CT scan for clean Hostun Sand mixed with 50% f_c is presented in Figure 4.12b. It is evident that the shapes of sand particles are lost and they are floating on gray zones, i.e. in f_c. Thus, the stiffness of the specimen would be dominated by f_c. This micro-structure was also explained as "sand-in-fines".
Micro-CT scanning was also done on the glass bead mixtures. The imaging method (Micro-CT scan) was done on samples with 1 cm in diameter and 2 cm in height prepared by tamping methods, the same as the method used for preparing the glass bead mixtures in the resonant column tests. It is worthwhile to mention that the goal of such scanning was to find the effect of sample preparation on the position of fines particle. Figure 4.13 is an example of Micro CT scans of adopted mixtures (30 and 50 percentage of fines content).

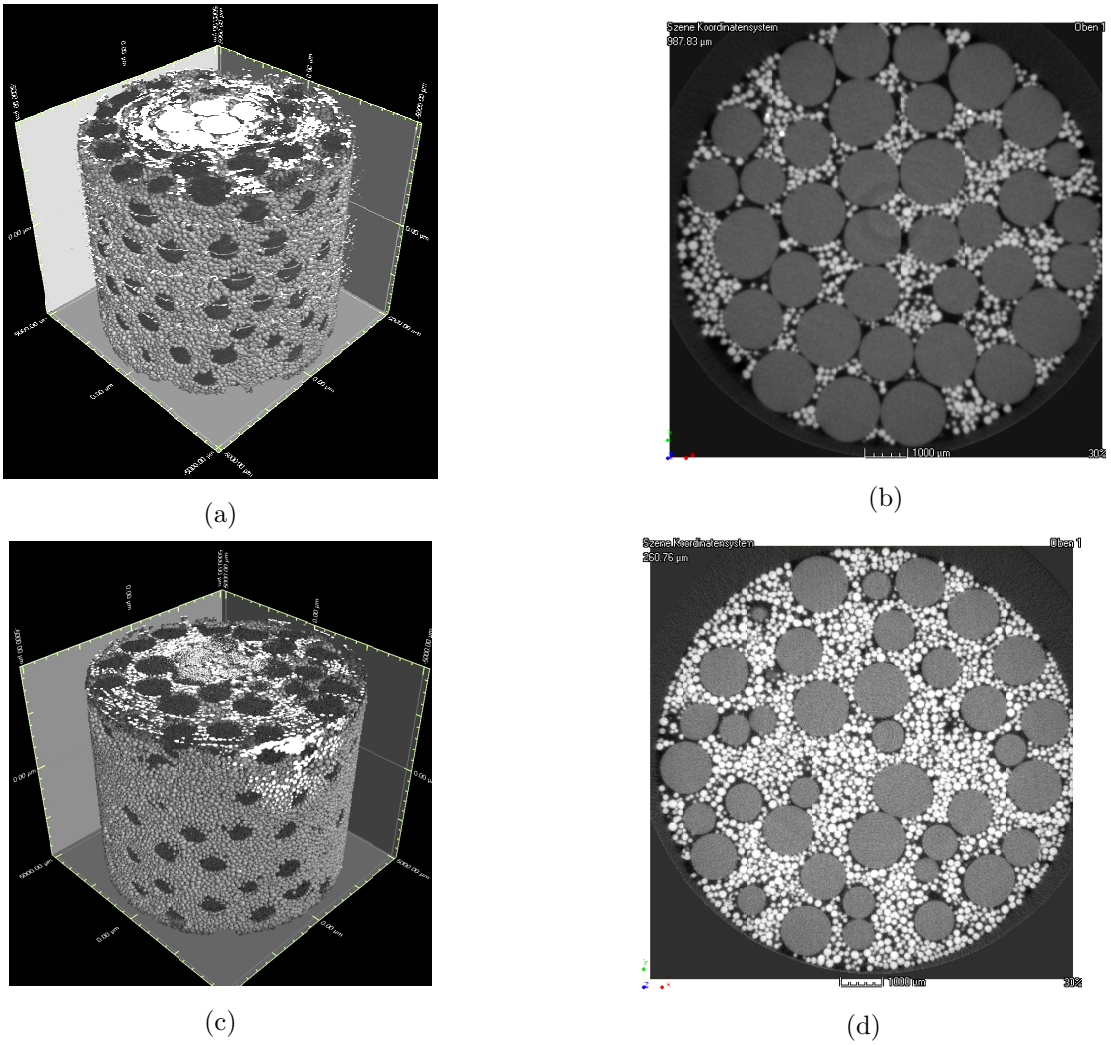

(a) (b) (c) (d)

Figure 4.13: Micro CT scan images: (a) f_c=30%, 3D image; (b) f_c=30%, 2D section; (c) f_c=50%, 3D image; (d) f_c=50%, 2D section, (the Micro-CT scans on the glass bead mixtures were done at SmartLab, Institute of Information and Communication Technology, Bulgarian Academy of Sciences.)

AVISO software was used to count the number of coarse particles and contacts between two coarse particles. For decreasing the time of analysis, two elements, containing 40 coarse particles, were chosen from the samples with 0 and 20 percentage fines content (Figure 4.14a and Figure 4.14b). Analyses of samples show that the number of contacts between coarse particles decreased with an increase in the fines content. For example, the number of contacts in the specimen containing 40 coarse particles and 0% fines content was 77 which decreased to 42 for the specimen containing 43 coarse particles and 20% fines content (specimens with the same number of coarse particles). For ease of discussion, the term of coarse-coarse coordination number, $CN_{coarse-coarse} = \frac{2N_{c,coarse-coarse}}{N_{b,coarse}}$

(Shire et al. 2014) is used for comparing the results. In this relationship, $N_{c,coarse-coarse}$ is the number of contacts between coarse particles and $N_{b,coarse}$ is the number of coarse particles. Therefore, in the sample containing $0\% f_c$, the value $CN_{coarse-coarse}$ was equal to 3.83 and for sample containing 20% f_c, $CN_{coarse-coarse}$ was 1.95 which shows the decreasing of $CN_{coarse-coarse}$ with an increase in fines content. This means, due to the sample preparation some of the fines were placed between the coarse particles. Therefore, for fines content less than threshold value ($f_c < f_{thr}$), micro CT images show that some of the fine particles have been located between coarse particles. Therefore, fines particles participate in force chains and their contribution must be taken into account.
Therefore, stiffness of packing is affected by fines content less than threshold value, the same as the observed experimental results. However, for fines content greater than threshold value ($f_c > f_{thr}$), fine particles will be dominant on coarse particles, therefore, coarse particles act like a reinforced element inside fine materials (Figure 4.13d and Figure 4.13c). This confirms the model of "fines-in-sand" by Thevanayagam et al. (2002) that some fine particles are active in sand force structures and others are inactive. Thus, for the same void/solid ratio, i.e. same e, the effective particle contact decreases with an increase in f_c and, therefore, their stiffness would be less than for clean sand for the same e. This is also consistent with experimental observation as noted above. However, this also means that for the same e, sand with fines does not represent the same force structure as clean sand, and thus the concept of "equivalent" void ratio for sand with f_c emerged.

(a) (b)

Figure 4.14: Analysis of Micro-CT images: (a) clean coarse glass beads; (b) clean coarse glass beads containing 20% fine particles

4.5 Concept of equivalent granular void ratio, e^*

The concept of "equivalent" void ratio was first presented by Mitchell (1976) who considered fines as void in force structure. For the "fines-in-sand" micro-structural model, Thevanayagam et al. (2002) recognized the active contribution of a fraction of fines particles in sand force structure and proposed Equation 4.2.

$$e^* = \frac{e + (1-b)f_c}{1-(1-b)f_c} \tag{4.2}$$

where, e^* is the equivalent granular void ratio and b is the fraction of fines that are active in the sand force structure. In recent years, interest has been growing in the use of the equivalent void ratio to characterize the behaviour of sand-fines mixtures. The key step in doing that is the determination of factor b in Equation 4.2. Most studies have employed the best fit approach to obtain the b value. The value of b varies from 0 to 1. b=0 means fines are inactive (i.e. void) in the sand force structure which is a very common assumption for very low f_c. However, for higher f_c, $b \neq 0$ which means b is a function of f_c. From the mathematical attributes of binary packings, Rahman et al. (2008) developed a semi-empirical relation to predict the parameter b.

$$b = \left[1 - exp\Big[-\lambda\frac{(f_c/f_{thr})^{n_b}}{k}\Big]\right]\Big(r(f_c/f_{thr})\Big)^r \tag{4.3}$$

where $r = (D_{10}/d_{50})^{-1}$, D_{10} = size of sand at 10% finer, d_{50} = size of fine at 50% finer, $k = (1-r^{0.25})$, λ and n_b are the fitting parameters which depend on the soil properties. f_{thr} = threshold fine content which separates "fines-in-sand" from the "sand-in-fines" micro-structure. In this study, f_{thr} was estimated from the e_{min} versus f_c curve. Furthermore, the experimental results from damping ratio and modulus ratio curves revealed that the behaviour of mixtures changed with fines more than 30%. Regarding these evidence, f_{thr} was between 20% to 30% which was assumed to be 25% in this study. It is noted that b can be obtained from back analysis (Thevanayagam et al. 2002; Ni et al. 2005), however to take advantage of the prediction of b, the above approach is used in this study.

For the "sand-in-fines" micro-structure when $f_c \geq f_{thr}$, Thevanayagam (1998) proposed Equation 4.4 to determine e^*.

$$e^* = \frac{e}{f_c + \frac{1-f_c}{R_d^m}} \tag{4.4}$$

Where, m is a fitting parameter that evaluates the influence of coarse particles inside the fine particle matrix and R_d is size ratio, $\frac{D_{50}}{d_{50}}$ (Ni et al. 2005).

It is worthwhile to mention that the current study does not intend to establish e^* concept

which was done earlier (Thevanayagam 1998; Rahman et al. 2008), but offers a simple and unified methodology to predict G_{max} irrespective of f_c which may trigger significant research interest along this line for this challenging problem.

4.6 Empirical relationships for Hostun Sand mixtures

4.6.1 Empirical relationships to predict G_{max}

Various prediction models have been developed in the last few decades which are applicable to computer programs for geo-material response analysis. Hardin & Black (1966) were, arguably, the first to propose one of the most widely used empirical relationship, which considers the effect of density through the void ratio, e, and p' to predict G_{max} of a soil. This relationship is referred to as Hardin's relation which is represented by the following general form (Equation 4.5):

$$G_{max} = kf(e) \rightarrow G_{max} = Af(p)f(e) \rightarrow G_{max} = Ap_a(\frac{p'}{p_a})^n f(e) \tag{4.5}$$

where, A is a material constant which depends on the soil type, p_a is the atmospheric pressure (100 kPa), p' is the mean effective stress, n is an exponent and $f(e)$ is the void ratio function. Two common functional forms for $f(e)$, Equation 4.6 (Hardin & Black 1966) and Equation 4.7 (Jamiolkowski et al. 1995), are usually found in the literature (Table 2.1).

$$f(e) = \frac{(x-e)^2}{1+e} \tag{4.6}$$

$$f(e) = e^{-y} \tag{4.7}$$

where, x depends on the angularity of soils (e.g. x=2.97 for angular sands and 2.17 for rounded sands). Note, x is a limiting void ratio in Equation 4.6; for example, if e is assumed as a value equal to 2.17, for rounded sands $f(e)$ will be equal to zero and consequently, G_{max} will be 0. Therefore, to avoid this limitation, x can be considered as a fitting parameter which may depend on the angularity of soils. y in Equation 4.7 is also a fitting constant. Apart from Hardin and Jamiolkowski's functional forms of $f(e)$, Seed's model has $K_{2,max}$ parameter (Seed et al. 1984). Seed et al. (1984) proposed a relationship between G_{max} and p' as G_{max}=218.8 $K_{2,max}(p')^{0.5}$ (in SI unit); where, $K_{2,max}$ may be a function of e. $K_{2,max}$ versus e for different f_c is presented in Figure 4.15; where $K_{2,max}$ decreased with f_c. The results show that the value of $K_{2,max}$ not only depends on the density of materials but also depends on the fines content. Therefore, $K_{2,max}$, in Seed's relationship, must be correlated with the fines content.

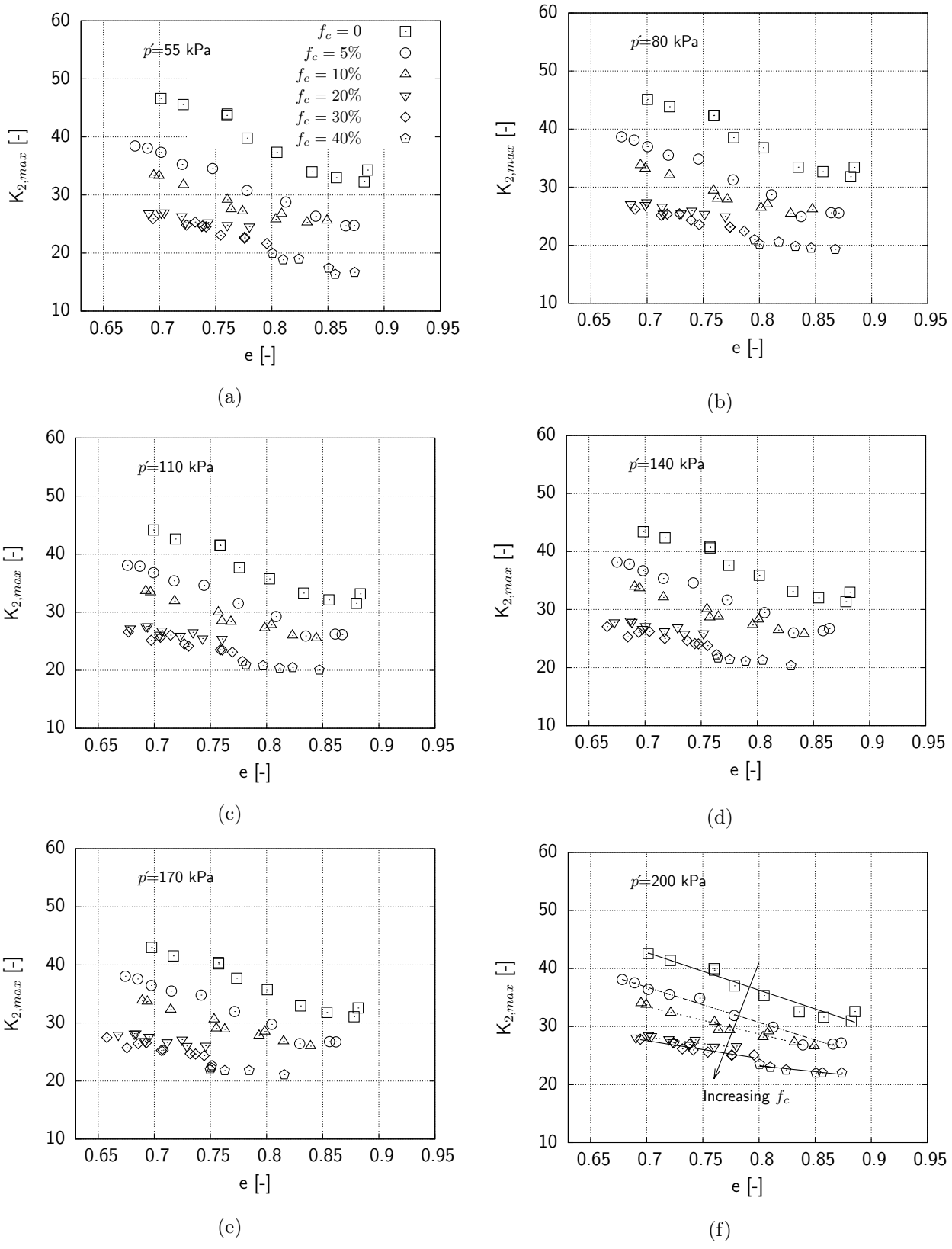

Figure 4.15: The effect of fines content on K_{2max} for the various confining pressures: (a) p'=55 kPa; (b) p'=80 kPa; (c) p'=110 kPa; (d) p'=140 kPa; (e) p'=170 kPa; (f) p'=200 kPa

4.6.2 Inspection of Hardin's relationship

To predict the maximum shear modulus of mixtures, the fitting parameters of Hardin's relation must be determined for all of the mixtures. As a first step, the constant fitting parameters of void ratio functions, x and y, must be determined accurately. The values of x and y were determined by fitting the curve $k.f(e)$ to the test data in G_{max} versus e curves. Figure 4.16 shows an example of the fitted curves to G_{max} versus e for clean Hostun Sand. The trend lines are plotted in this figure as a form of $kf(e)$, where $f(e)$ is the void ratio function (e.g. Equation 4.6 and Equation 4.7) and k is the remaining part of Equation 4.5 which depends on p' and the adopted $f(e)$. By preforming this calibration analysis, the constant values of x and y were determined. The solid lines in Figure 4.16 are related to Hardin's void ratio function, Equation 4.6, and the dashed lines are related to Jamiolkowski's void ratio function, Equation 4.7. Afterwards, G_{max} was normalized with respect to the void ratio function. Figure 4.17a and Figure 4.17b show an example of the normalized G_{max}-p'/p_a for clean Hostun Sand for both of the void ratio functions. These curves are useful to find the value of the parameter A and exponent of pressure function, n, in Hardin's relation (Equation 4.5). The values of the fitting parameters in Hardin's relation for clean Hostun Sand are summarized in Table 4.1.

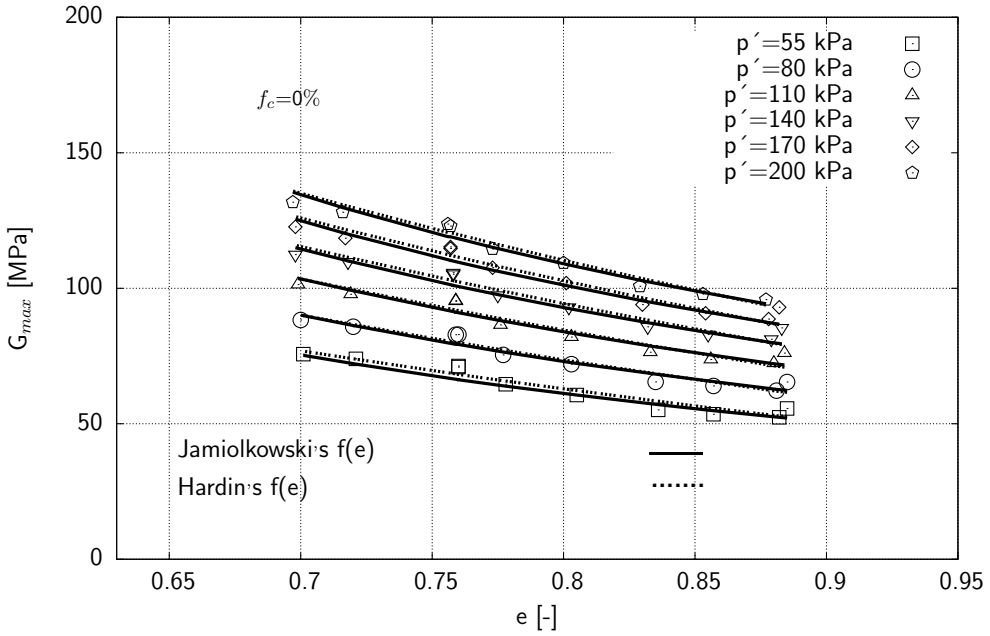

Figure 4.16: G_{max} versus e to determine the constant fitting parameters of the void ratio function for clean Hostun Sand

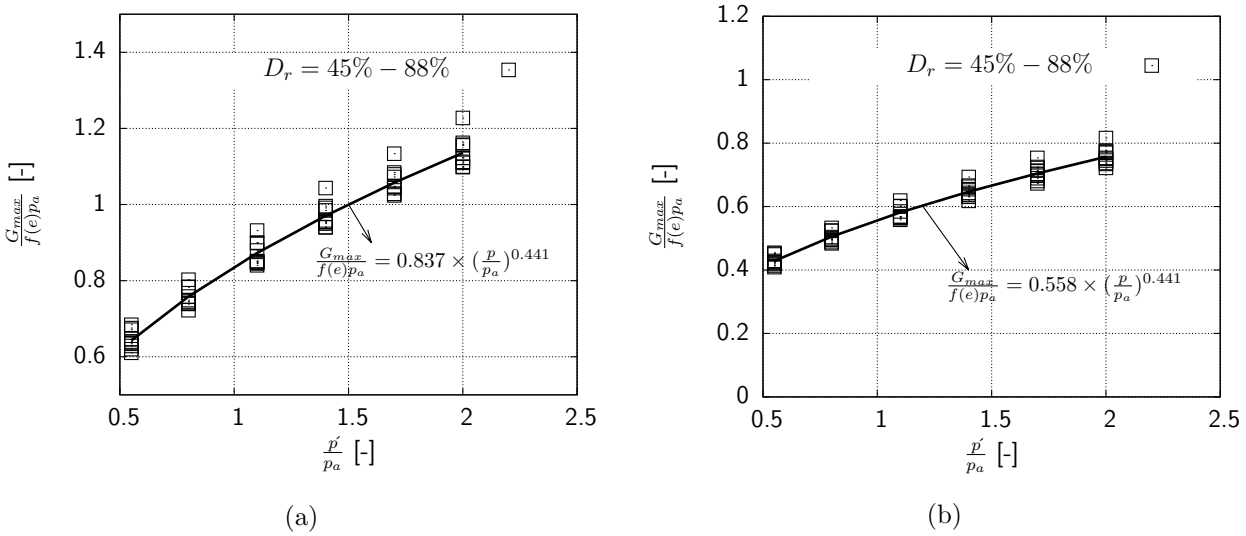

Figure 4.17: The fitting parameters of Hardin's relation to determine G_{max} of clean Hostun Sand: (a) Hardin's void ratio function; (b) Jamiolkowski's void ratio function

Table 4.1: Summary of fitting parameters for Hardin's relation

Hardin's void ratio function					
Dr [%]	x	n	A	R^2	RMSD
40 %- 90%	$x = 2.1232$	$n = 0.441$	$A = 0.837$	R^2 =0.981	2.83
Jamiolkowski's void ratio function					
Dr [%]	y	n	A	R^2	RMSD
40 %- 90%	$y = 1.6631$	$n = 0.441$	$A = 0.558$	R^2= 0.978	2.97

Two statistical measures of Root-Mean-Square-Deviation (RMSD) and R^2 were used to estimate the scatter of the results in Table 4.1. The RMSD and R^2 for Hardin's $f(e)$ were 2.83 and 0.981 and for Jamiolkowski's $f(e)$ were 2.97 and 0.978 respectively. Therefore, the results for both $f(e)$ showed a good agreement between the observed and predicted results.

The same analyses were performed on the other mixtures to determine the fitting parameters of Hardin's relation. Figure 4.18a shows an example of fitted kf(e) curves to the test data for mixture containing 30% fines content to find the constant value of x in the void ratio fuction (Equation 4.6). Figures 4.18b, 4.18c and 4.18d show the effect of fines content on the constant fitting parameters of clean Hostun Sand mixed with quartz powder. As can be seen in Figure 4.18, the fitting parameters of Hardin's relation and the void

ratio function (Equation 4.5 and Equation 4.6) are affected by fines content significantly. Therefore, for the prediction of the maximum shear modulus, using Hardin's relation, the fitting parameters must be determined for all of the mixtures which is beyond the scope of our study. In this chapter, instead of calculating the fitting parameters of Equation 4.5, Equation 4.6 and Equation 4.7 for mixtures, the concept of the equivalent void ratio, e^*, will be used to estimate the value of G_{max} for all of the mixtures.

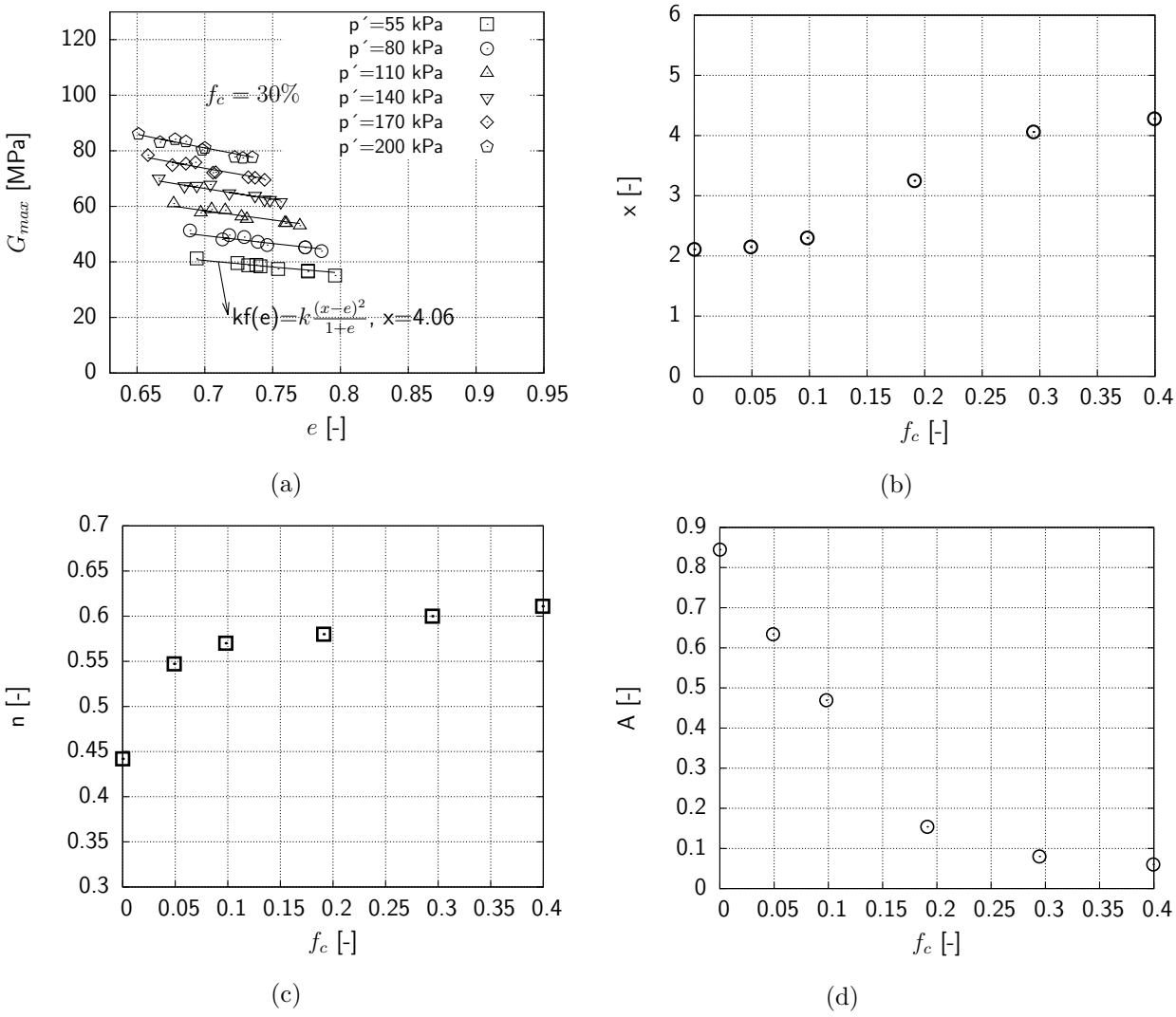

Figure 4.18: (a) G_{max} versus e to determine the value of x in Equation 4.7; (b) the effect of f_c on the value of x in Equation 4.7; (c) the effect of f_c on the stress exponent, n, in Equation 4.5; (d) the effect of f_c on the constant value of A in Equation 4.5

4.6.3 e^* in Hardin's relationship

4.6.3.1 Hardin's relationship for mixtures

Micro-structural studies suggest that the transition soil's behaviour is controlled by sand structure for $f_c < f_{thr}$ and fine structure for $f_c > f_{thr}$, so Hardin's relationship for clean Hostun Sand should capture the effect of f_c through e^*. Thus, Hardin's relation was established first for clean Hostun sand for both functional forms of $f(e)$. The fitting parameters, A, n and x or y for Hardin's relation, are presented in Table 4.1.
According to the micro-structural analysis, the effect of f_c on G_{max} can be captured with e^* while the other parameters remain the same as determined values for clean Hostun Sand. This means that substitution of e^* for e in Equation 4.5 for clean sand should capture the effect of f_c. Thus, the equation Equation 4.5 becomes:

$$G = kf(e^*) \rightarrow G = Af(p)f(e^*) \rightarrow G_{max} = Ap_a(\frac{p}{p_a})^n f(e^*) \tag{4.8}$$

where, A and n are parameters for clean Hostun Sand. Other parameters, x and y in Equation 4.6 and Equation 4.7, also remain the same as determined values for clean Hostun Sand. The accuracy of the predicted results depends on the micro-structural parameter b, i.e. λ, n_b and m in the e^* relationship.

4.6.3.2 Calibration of parameters

Giving consideration to a large number of data sets, Rahman et al. (2008) proposed λ and n_b are equal to 0.3 and 1, respectively, which capture many characteristic responses of undrained soil behaviours through e^* (e.g. Rahman et al. 2008, Rahman & Lo 2012 and Rahman & Lo 2014). However, Rahman et al. (2008) suggested that these parameters may vary for different type of soils. The other micro-structural parameters for Hostun Sand containing fines are available from grading properties. For $f_c > f_{thr}$, m is needed for Equation 4.4. m was determined by back analysis of the test data which were 0.11 and 0.14 for Hostun Sand containing 30 and 40 percent fine content respectively. Ni et al. (2005) showed that m can be a function of $\frac{C_{uc}C_{uf}^2}{R_d}$ where, C_{uc} and C_{uf} are the uniformity coefficient of coarse and fines respectively. The relationship between m and $\frac{C_{uc}C_{uf}^2}{R_d}$ was also approximated by a linear relationship (Figure 4.19) for the mixtures used in this study. According to the grain size distribution of Hostun Sand and quartz powder, the value of $\frac{C_{uc}C_{uf}^2}{R_d}$ for the adopted materials was about 0.32. Thus, $m = 0.12$ was obtained from the linear relation for Hostun Sand for $f_c > f_{thr}$.

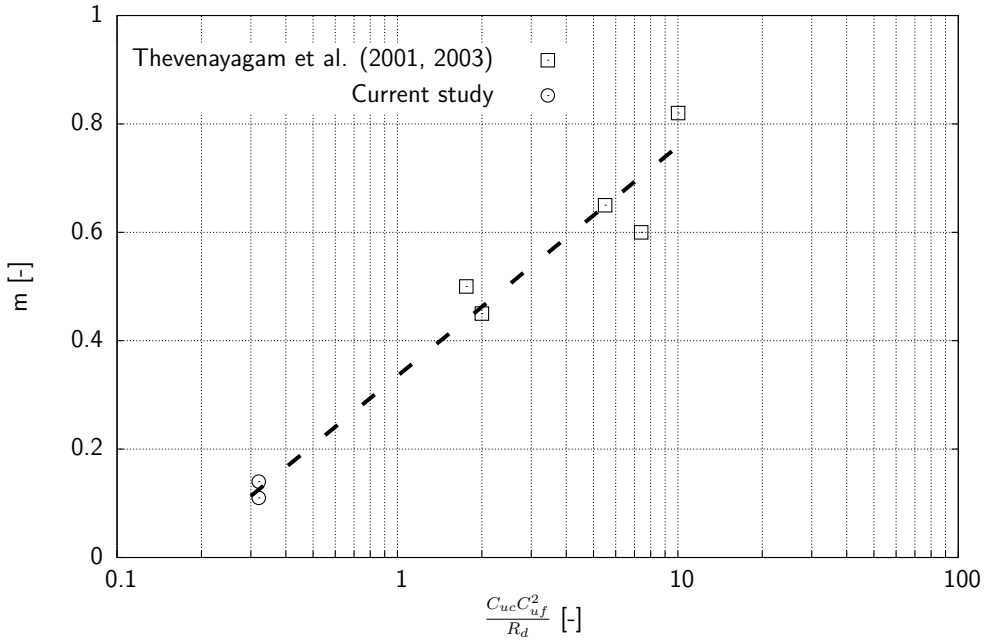

Figure 4.19: Parameter m versus $\frac{C_{uc}C_{uf}^2}{R_d}$, modified after Ni et al. (2005)

Five different calibrations were performed to evaluate the influence of parameters b and m on the accuracy of the predicted G_{max} for clean Hostun Sand containing different percentages of fines content. Parameter b is related to the fitting parameters of λ, therefore, calibrations were performed on the constant fitting parameter of λ. Table 4.2 presents a summary of the calibrations performed in this chapter to find the accuracy of the predicted results using Equations 4.2 and 4.4.

- **Calibration I**

In this calibration, "fines-in-sand" micro-structure is assumed for all f_c and the fitting parameters, as proposed by Rahman et al. (2008) (i.e. λ=0.30 and n_b=1.0), were used to predict G_{max} for f_c=0-40%, despite f_{thr} = 25%. Figure 4.20a and Figure 4.20b show G_{max} vs e^* for the observed results at p' of 55kPa and 200kPa (only the lower and upper range of p' were plotted for clarity).
The results, in comparison to Figure 4.3f, show that the influence of f_c can be captured by the concept of e^*. The dashed lines represent the fitted curves for Hardin's $f(e)$ and the solid lines are the fitted curves for Jamiolkowski's $f(e)$. All other fitting parameters are the same as clean Hostun Sand (Table 4.1). However, the measured G_{max} for f_c<30% are close to both the fitting lines, but deviation was observed for f_c>30%.

Table 4.2: Summary of calibrations performed on parameters λ and m for Jamiolkowski's $f(e)$

	variable			
Calibration	$f_c < f_{thr}$	$f_c > f_{thr}$	R^2	RMSD
Calibration I	Eq. 4.3, λ=0.3	Eq. 4.3, λ=0.3	0.86	8.92
Calibration II	Eq. 4.3, λ=0.3	Eq.4.4, m from Fig. 4.19	0.97	3.58
Calibration III	Eq. 4.3, λ=back analysis	Eq.4.4, m from Fig. 4.19	0.98	3.15
Calibration IV	Eq. 4.3, λ=0.3	Eq.4.4, m=back analysis	0.98	3.23
Calibration V	Eq. 4.3, λ=back analysis	Eq.4.4, m=back analysis	0.98	2.71

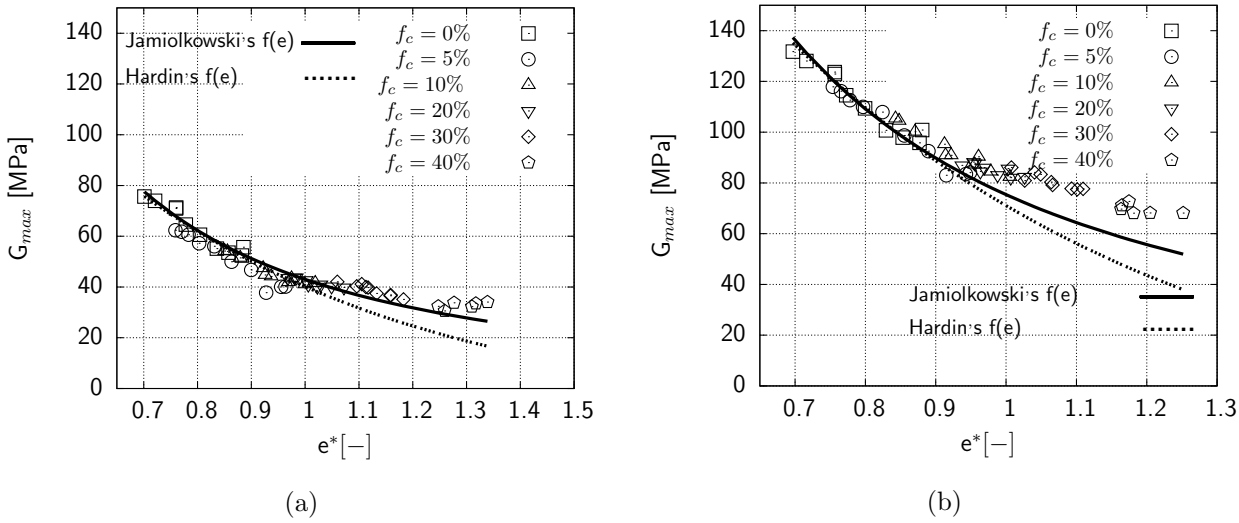

Figure 4.20: G_{max} versus e^* for calibration I: (a) p'=55 kPa; (b) p'=200 kPa

Figure 4.20 also shows all data points and the scatter of the predicted and measured G_{max}. This figure shows that the scatter of data is not acceptable for f_c>30%. The overall R^2 and RMSD for all data points were 0.86 and 8.92 for Hardin's $f(e)$. However, overall R^2 and RMSD were 0.95 and 4.65 for test data with f_c<30%. These results confirm that the "fines-in-sand" model, i.e. Equation 4.2, is suitable for f_c<f_{thr} and it is not applicable for f_c>f_{thr} .

- **Calibration II**

In this calibration, Equation 4.2 and Equation 4.3, with the fitting parameters proposed by Rahman et al. 2008 (i.e. λ=0.30 and n_b=1.0), were used to predict G_{max} of clean Hostun Sand containing up to 20% f_c. Thus, only grading parameters, i.e. D_{10} and d_{50}, were required to calculate e^*.

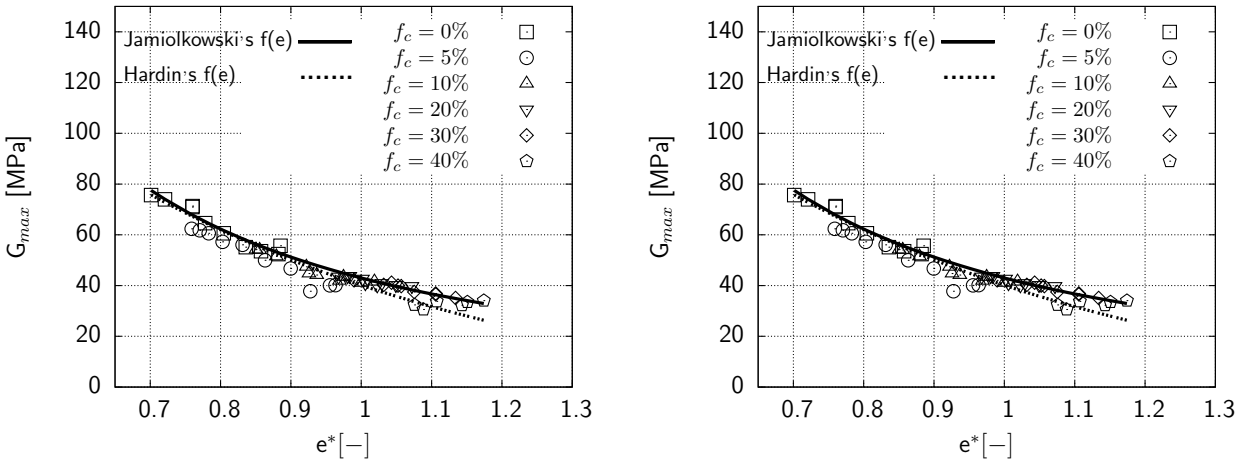

Figure 4.21: G_{max} versus e^* for calibration II: (a) p'=55 kPa; (b) p'=200 kPa

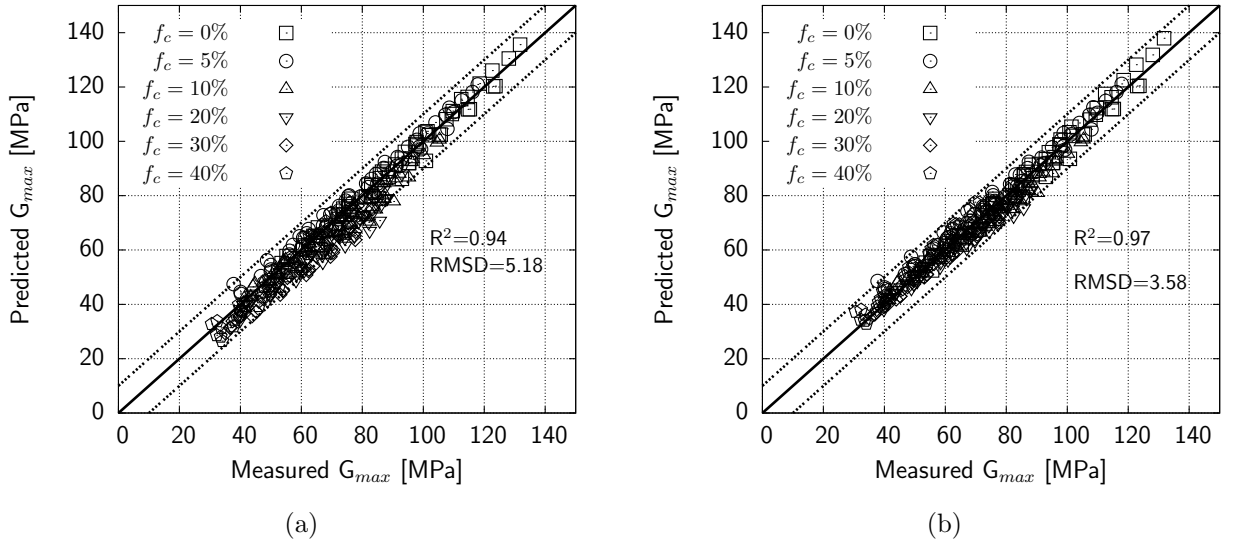

Figure 4.22: Measured G_{max} versus predicted G_{max} for calibration II: (a) Hardin's $f(e)$; (b) Jamiolkowski's $f(e)$

Equation 4.4 was employed to predict G_{max} of clean Hostun Sand with $f_c \geq 30\%$. The grading properties, i.e. D_{50}, d_{50} and m=0.12 from the linear relationship in Figure 4.19, were required to calculate e^*. Therefore, this calibration was not dependent on back analysis which requires test data as a prerequisite. Figure 4.21a and Figure 4.21b show G_{max} versus e^*, at the confining pressure of 55 and 200kPa. The deviation of the measured G_{max} and fitted curves for both $f(e)$ reduced significantly, particularly after $f_c \geq 30\%$. The functional form of Hardin's $f(e)$ and Jamiolkowski's $f(e)$ for clean Hostun Sand are

presented with dotted and solid lines respectively. The data at higher e^* and lower G_{max} show a relatively higher scatter than at lower e^* and higher G_{max}.
Hardin's relation also shows a slight deviation toward a higher e^* and lower G_{max} which may be attributed to the inherent variability of G_{max} toward that end. Therefore, to have an objective comparison, G_{max} was predicted for f_c with Hardin's relation with the same constant parameters as determined for clean Hostun Sand and e replaced by e^*.
The predicted versus measured G_{max} for Hardin's $f(e)$ and Jamiolkowski's $f(e)$, for all of f_c, are shown in Figure 4.22a and Figure 4.22b respectively. Figure 4.22a and Figure 4.22b show a good agreement between the predicted and measured G_{max} for all data points. The values of R^2 and RMSD of predicted results are summarized in Appendix A (Table A.1 and Table A.2) for Hardin's and Jamiolkowski's $f(e)$ respectively. The overall R^2 and RMSD were 0.94 and 5.18 for Hardin's f(e) and 0.97 and 3.58 for Jamiolkowski's $f(e)$ respectively. It is wothwhile to mention that the fitting parameters of Hardin's and Jamiolkowski's void ratios are the same as determined values for clean Hostun sand. It is noted that Jamiolkowski's $f(e)$ with an inverse power function of e gave better prediction than Hardin's $f(e)$ for a large data set with a wide range of f_c and the RMSD of 3.58 is used as a reference value to evaluate the performance of other calibrations.
The fitting parameters for this calibration were obtained from soil grading properties. Also, constant parameters in Hardin's relation (Equation 4.5) are the same as the determined values for clean Hostun Sand (Table 4.1). Therefore, this calibration was not dependent on the back analysis of the test data. Thus, the RSMD of this calibration for Jamiolkowski's $f(e)$, 3.58, was used as a reference value to evaluate the accuracy of other calibrations. The reduction of RMSD for Jamiolkowski's $f(e)$ from calibration I to calibration II is about 23% of 4.65.

- **Calibration III**

In this calibration, Equation 4.3 was used to determine the value of parameter b for clean Hostun Sand containing 0 to 20% f_c. However, the value of parameter λ in Equation 4.3 was determined by back analysis of test data to get the maximum R^2. m=0.12, as in Figure 4.19, was used to find e^* with Equation 4.4 for clean Hostun Sand with 30-40% fines content. G_{max} vs e^* is presented for p'=55 and 200 kPa in Figure 4.23a and Figure 4.23b. The predicted vs measured G_{max} for all data points are shown in Figure 4.24a and Figure 4.24b, and their R^2 and RMSD are summarized in Appendix A (Table A.1 and Table A.2) for Hardin's and Jamiolkowski's $f(e)$ respectively. The overall R^2 and RMSD for all data points were 0.96 and 4.29 for Hardin's $f(e)$ and 0.98 and 3.15 for Jamiolkowski's $f(e)$ respectively.

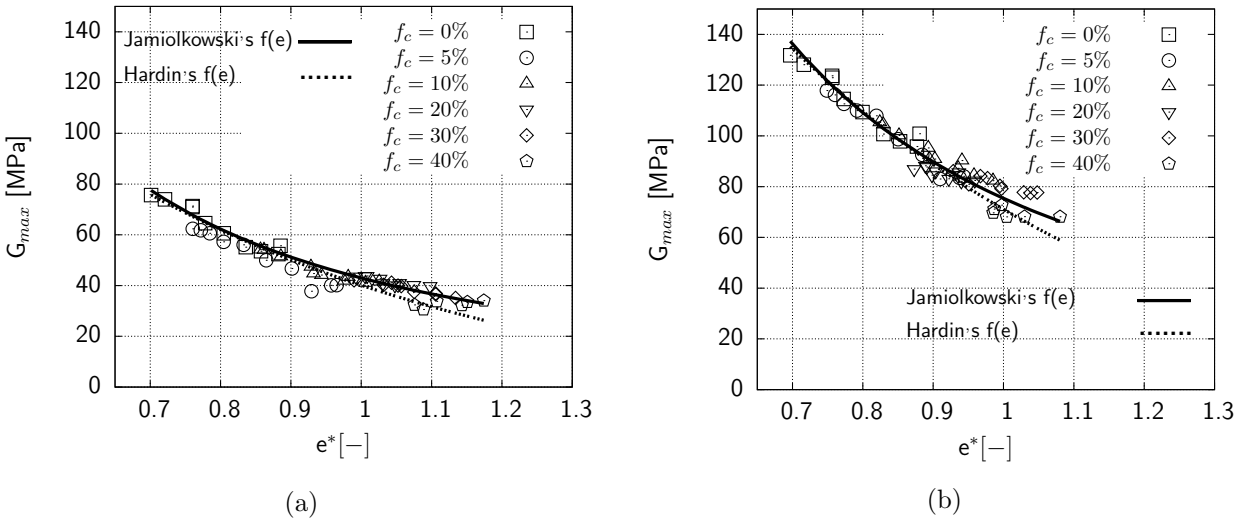

Figure 4.23: G_{max} versus e^* for calibration III: (a) p'=55 kPa; (b) p'=200 kPa

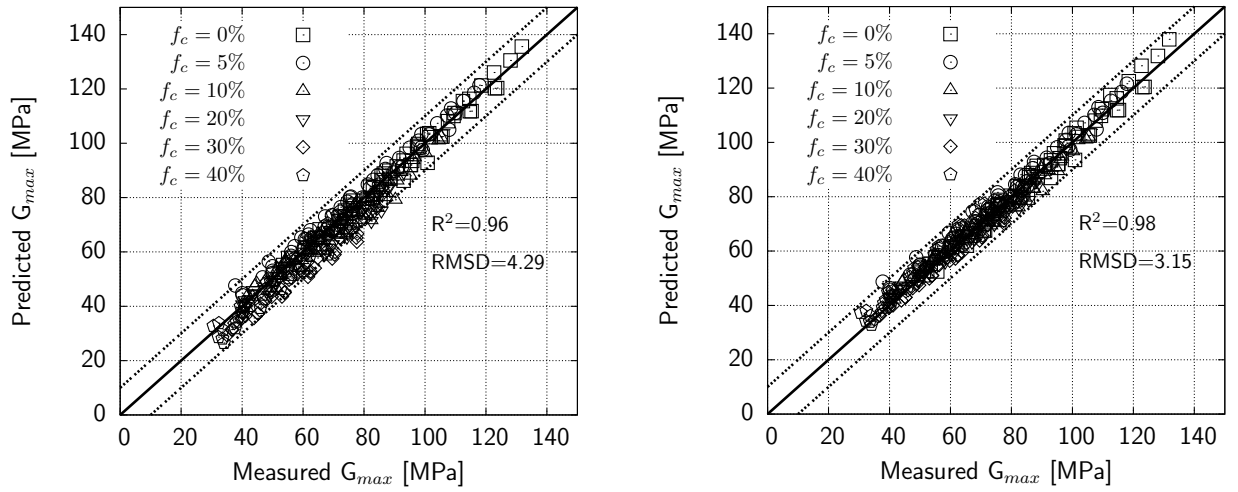

Figure 4.24: Measured G_{max} versus predicted G_{max} for calibration III: (a) Hardin's $f(e)$; (b) Jamiolkowski's $f(e)$

Again, Jamiolkowski's $f(e)$ gives better prediction than Hardin's $f(e)$. The reduction of RMSD for Jamiolkowski's $f(e)$ is only about 12% of 3.58 obtained from calibration II, although a large fraction of data points used in the back analysis to get the value of λ in Equation 4.3.

- **Calibration IV**

In this calibration for $f_c < f_{thr}$, λ=0.30 as proposed by Rahman et al. 2008 was used in Equation 4.3. However, for $f_c > f_{thr}$, m was determined by back analysis for the maximum R^2. m for 30% and 40% f_c, denoted as m_{30} and m_{40}, were variable for different p'.

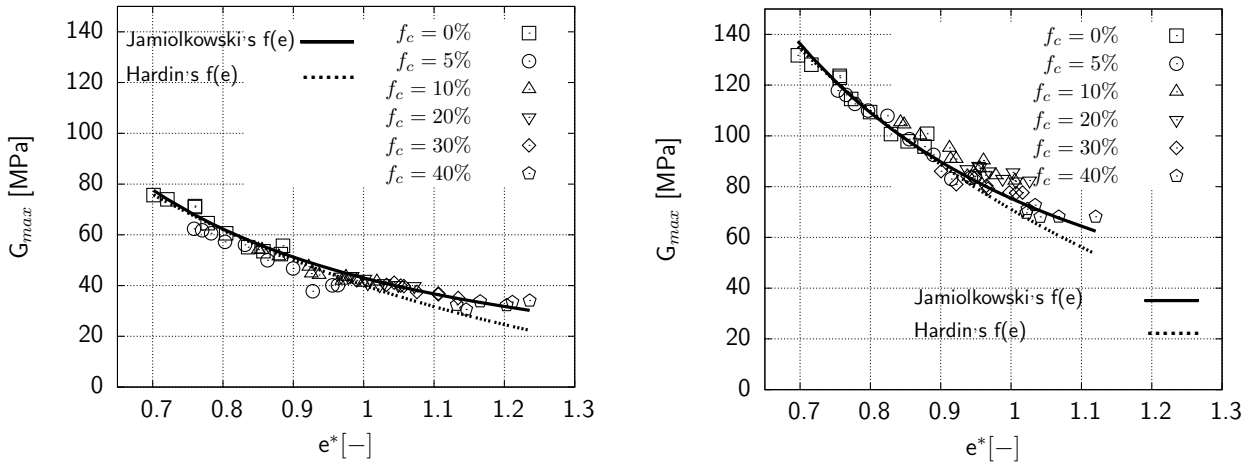

(a) (b)

Figure 4.25: G_{max} versus e^* for calibration IV: (a) p'=55 kPa; (b) p'=200 kPa

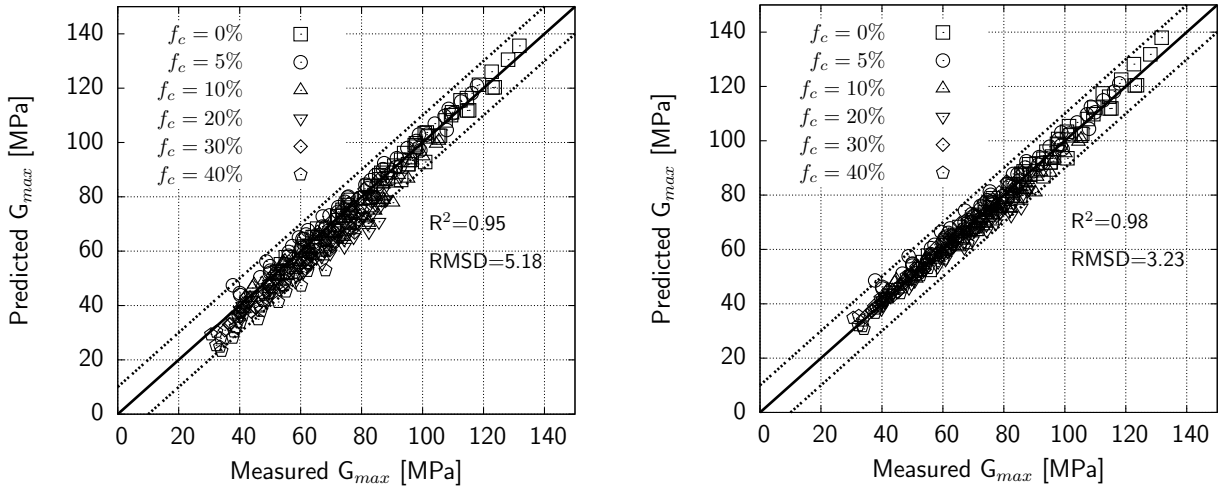

(a) (b)

Figure 4.26: Measured G_{max} versus predicted G_{max} for calibration IV: (a) Hardin's $f(e)$; (b) Jamiolkowski's $f(e)$

Figure 4.25a and Figure 4.25b show G_{max} vs e^* only for $p' = 55$ and 200 kPa. Although it may not be visually recognizable, the data points for $f_c > f_{thr}$ are closer to fitting curves in comparison to calibration II.
The plot for predicted vs measured G_{max} for all data points are shown in Figure 4.26a and Figure 4.26b. Again, Jamiolkowski's $f(e)$ gave a better prediction than Hardin's $f(e)$. The reduction of RMSD for Jamiolkowski's $f(e)$ is only about 10% of 3.58, although a fraction of data used in the back analysis to obtaine m.

- **Calibration V**

In calibration V, λ in Equation 4.3 was determined by back analysis of the test data where $f_c < f_{thr}$. For $f_c > f_{thr}$, m value was determined by back analysis of test data (m_{30} and m_{40}). Figure 4.27 shows G_{max} vs e^* for all of the applied confining pressures. As can be seen in Figure 4.27, the effect of f_c can be captured by e^* for all of the confining pressures. The scatter of the data points are lowest compared to all other calibrations. The same as other calibrations, Jamiolkowski's $f(e)$ gives better prediction than Hardin's $f(e)$. A good agreement between the predicted and measured G_{max} was confirmed as shown in Figure 4.28a and Figure 4.28b. The values of R^2 and RMSD are presented in Appendix A (Table A.3 and Table A.4). The reduction of RMSD for Jamiolkowski's $f(e)$ is about 24% of 3.58 confirming the best prediction among all calibrations. Figure 4.32 shows the effect of e^* and p' on the maximum shear modulus for all of the mixtures.

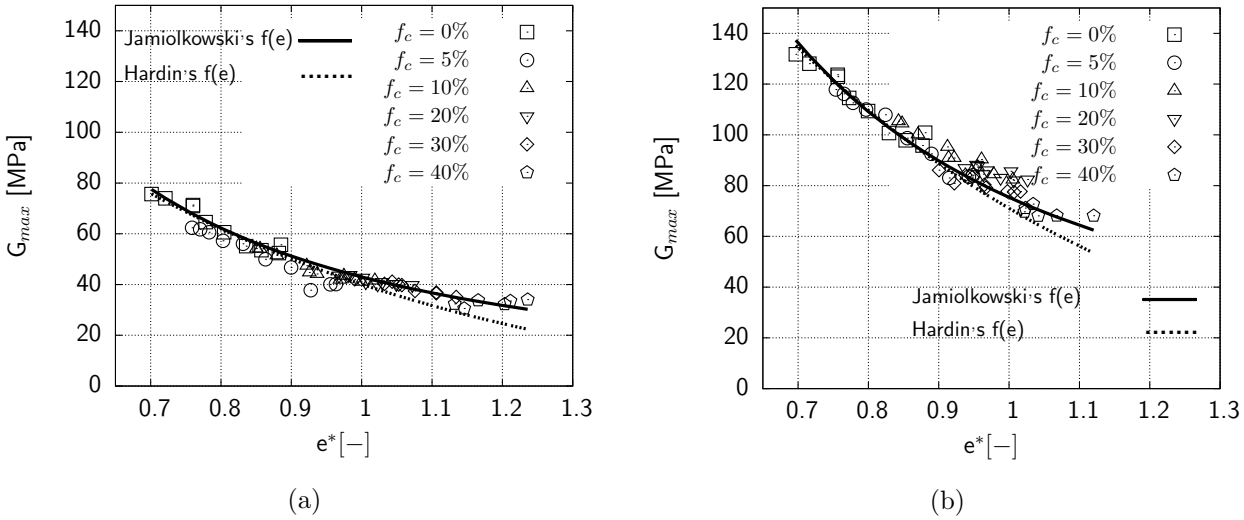

Figure 4.27: G_{max} versus e^* for calibration V at (a) p'=55 kPa and (b) p'=200 kPa

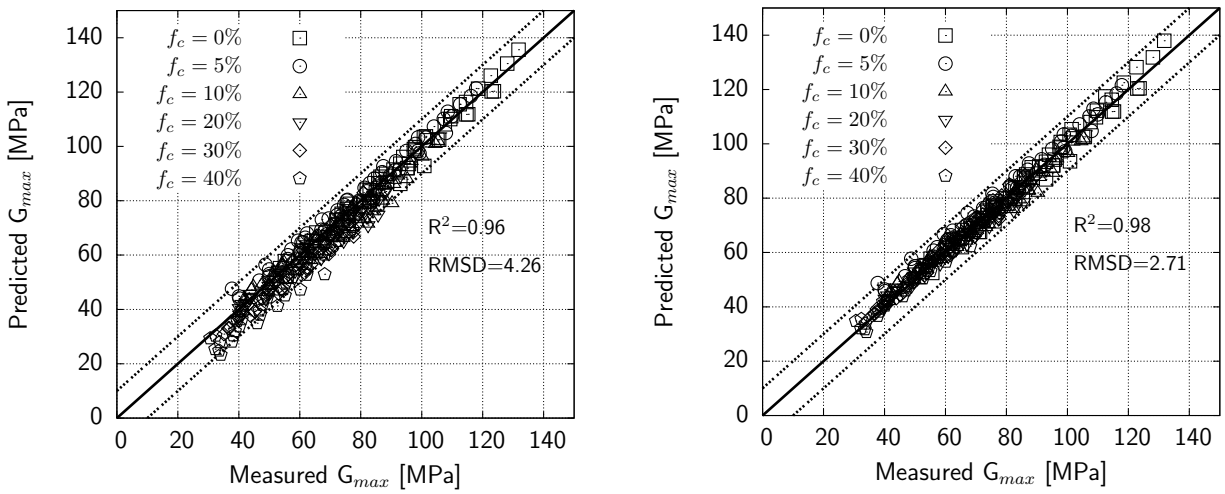

(a) (b)

Figure 4.28: Measured G_{max} versus predicted G_{max} at calibration V: (a) Hardin's $f(e)$; (b) Jamiolkowski's $f(e)$

4.7 Empirical relationships for glass bead mixtures

4.7.1 Hardin's relation

In this section the fitting parameter of Hardin's relation will be determined for coarse glass beads. Jamiolkowski's void ratio function (Equation 4.7) has been used to discuss the results of glass bead mixtures at a macro level.

As a first step, the fitting parameter of Jamiolkowski's void ratio function, y, must be determined accurately. The value of y was determined by fitting the curve $kf(e)$ to the test data in Figure 4.29a. The trend lines are plotted in this figure as a form of $kf(e)$; where $f(e)$ is the void ratio function and k is the remaining part of Equation 4.5 which depends on the value of p'. The constant value of y was determined after performing a regression analysis. The dashed lines in Figure 4.29a are related to the Jamiolkowski's void ratio function. Afterwards, G_{max} was normalized with respect to the void ratio function (Figure 4.29b). The normalized G_{max} was drawn versus p'/p_a. This curve was useful to find the value of parameter A and the exponent of stress (n) in Hardin's relation (Equation 4.5) for coarse glass beads. The same analysis were conducted to find the constant fitting parameters of Hardin's relation to estimate the values of M_{max} and E_{max}. Table 4.3 presents the values of the fitting parameters in Hardin's relation for coarse glass beads from the performed analyses.

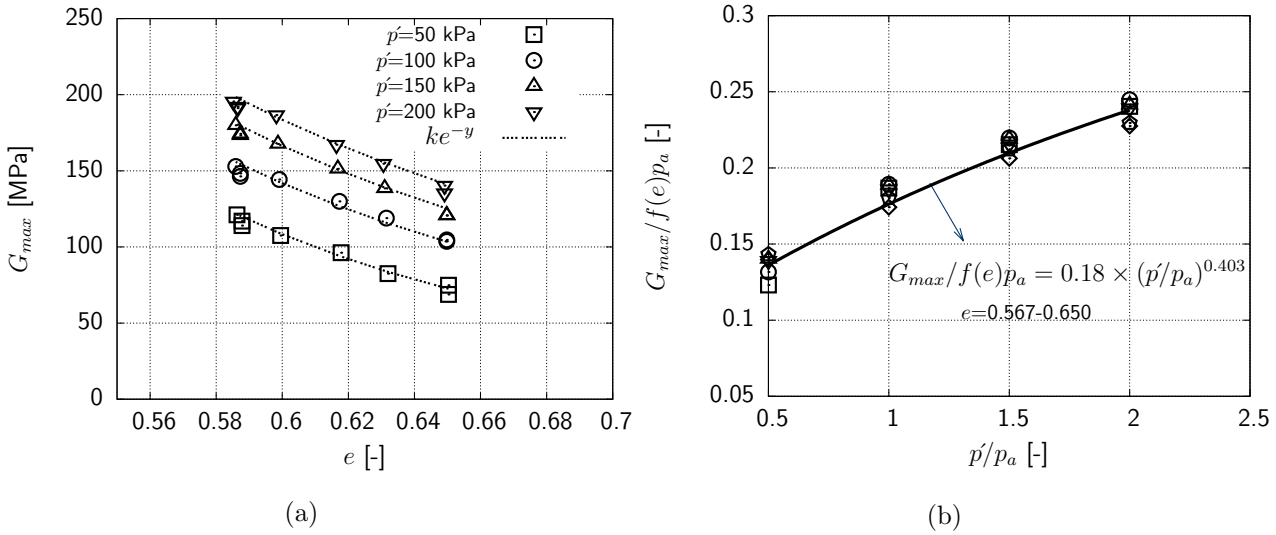

(a) (b)

Figure 4.29: Determination of fitting parameters of Hardin's relation for coarse glass beads: (a) G_{max} vs e and (b) $G_{max}/f(e)$ vs p'/p_a

Table 4.3: Summary of the parameters of Hardin's relationship

Modulus	Dr [%]	y	A	n	R^2
G_{max}	40-80	3.98	0.180	0.403	0.98
M_{max}	40-80	1.869	2.002	0.301	0.97
E_{max}	40-80	3.99	0.479	0.385	0.97

4.7.2 e^* in Hardin's relation

The concept of equivalent void ratio will be used to predict the maximum muduli of granular packing containing fine particles without performing test on mixtures at a macroscopic level. This is one of the advantages of this approach compared to previous methods to predict the stiffness of materials. In this approach, the fitting parameters of Hardin's relation will be the same as those determined for coarse glass beads. The impact of fines can be expressed through their influence on the equivalent void ratio function (Equation 4.2 and Equation 4.4). Accuracy of the equivalent void ratio concept depends on the parameter b (f_c less than f_{thr}) and m (f_c more than f_{thr}) in the e^* relation. Equation 4.3 was used to predict parameter b and also parameter m in the equivalent void ratio was determined by the back analysis of test data for G_{max} from the resonant column test.

Table 4.4: Summary of fitting parameters for the equivalent void ratio

p' [kPa]	m_{30}	m_{40}	m_{50}	R^2	RMSD
50	0.62	0.63	0.63	0.95	5.19
100	0.59	0.59	0.59	0.96	6.16
150	0.55	0.56	0.55	0.96	6.68
200	0.53	0.56	0.56	0.95	8.66
Ave.	0.573	0.585	0.583	0.96	8.63

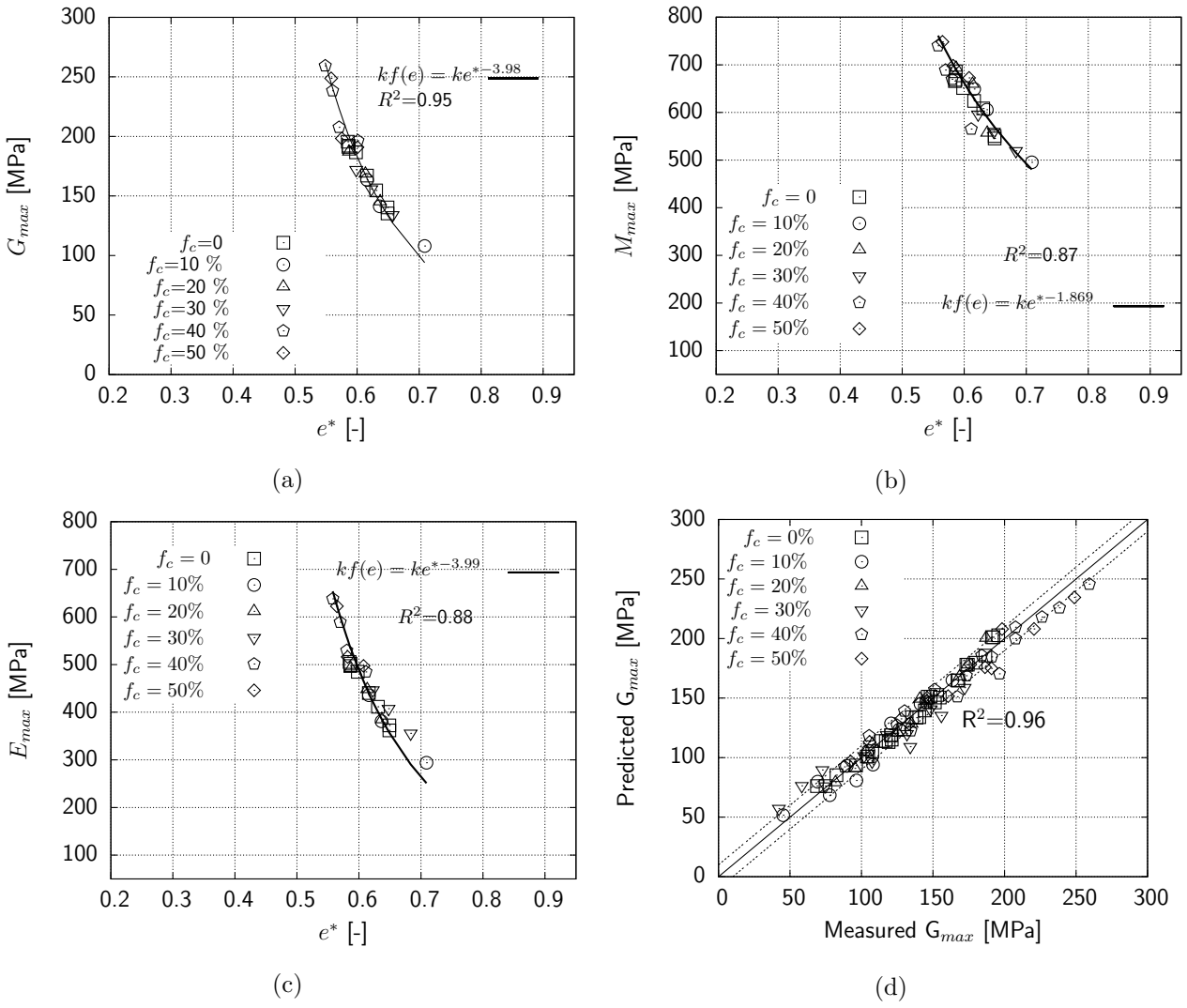

Figure 4.30: (a) G_{max} vs e^* for the mixtures at p'=200 kPa; (b) M_{max} vs e^* for the mixtures at p'=200 kPa; (c) E_{max} vs e^* for the mixtures at p'=200 kPa; (d) predicted G_{max} vs measured G_{max} for all of the mixtures

Table 4.4 shows the summary of determined values for parameter m in the samples containing 30%, 40% and 50% fines content. The average value of m (Table 4.4) was used to determine the equivalent void ratio (e^*) when f_c is more than f_{thr}.
Figure 4.30a shows G_{max} vs e^* only for 200 kPa. The solid line in Figure 4.30a is $kf(e)$ curves obtained for coarse glass beads at the same confining pressure as Table 4.3.
As can be seen in Figure 4.30a, the data points for all of the mixtures are close to the test data for coarse glass beads. This means the effect of f_c can be captured through the concept of equivalent void ratio for "fines-in-coarse" and "coarse-in-fines" mixtures. Figure 4.30b and Figure 4.30c show M_{max} vs e^* and E_{max} vs e^* only for 200 kPa. The solid lines in these figures are $kf(e)$ curves obtained from M_{max}-e and E_{max}-e of coarse glass beads at the same confining pressure. Figure 4.30d shows the predicted G_{max} using the Equation 4.5 and by replacing e by e^*, versus measured G_{max} using the resonant column device. The results show a good agreement between the predicted and measured results.

4.8 Discussion

The micro-mechanic considerations for sand with fines revealed that the concept of equivalent void ratio, e^*, is valid for Hardin's relation to predict G_{max} of granular materials for a wide range of f_c. However, the accuracy of the predicted results depends on the parameters b and m in Equation 4.2 and Equation 4.4 respectively.

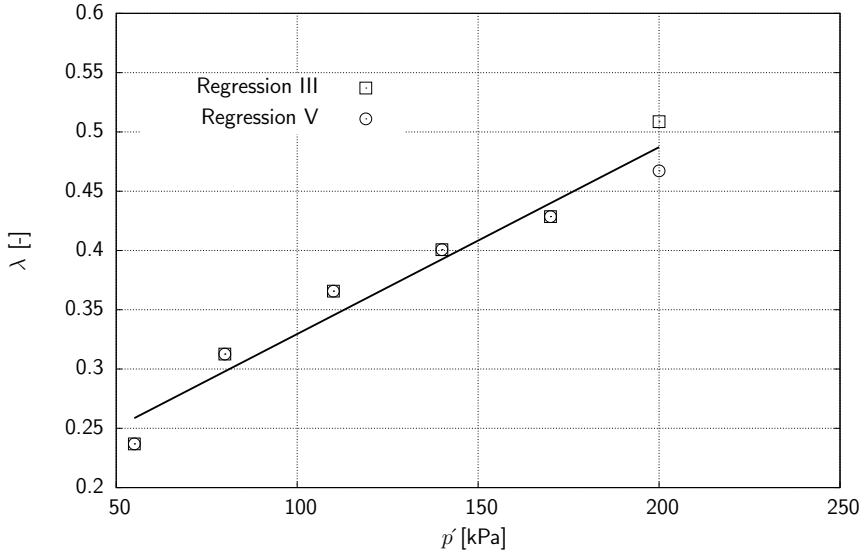

Figure 4.31: The effect of p' on λ from calibrations III and V for Jamiolkowski's $f(e)$

The calibration V was the best approach with the lowest RMSD, however λ and m were obtained by back analysis. This model would be preferable if some data for different f_c, at least three set of data, were available and so back analysis would be affordable. Calibrations III and IV also require back analysis to a lesser extent. However, the value of λ back analyzed for calibration III showed a good correlation with p' as shown in Figure 4.31, which can be used for the material used in this study. Calibration II, in comparison to other approaches, does not need back analysis and seems to be sufficient to predict G_{max} irrespective of f_c. The values of b and m in e^* were determined from the grading properties of sand and fines or from the back analysis of test data. Figure 4.32 shows that e^* in comparison with e provides a unique relationship between G_{max}, $f(p')$ and $f(e^*)$ in space, where the fitting parameters of Hardin´s relationship are the same as clean sand. The main advantage of such a single relationship is that if Hardin's relationship is established for clean sand or sand with any f_c, then the relation can be transformed to e^* space where e for clean sand is equal to e^* for sand with fines. This allows us to predict unknown G_{max} for different f_c.

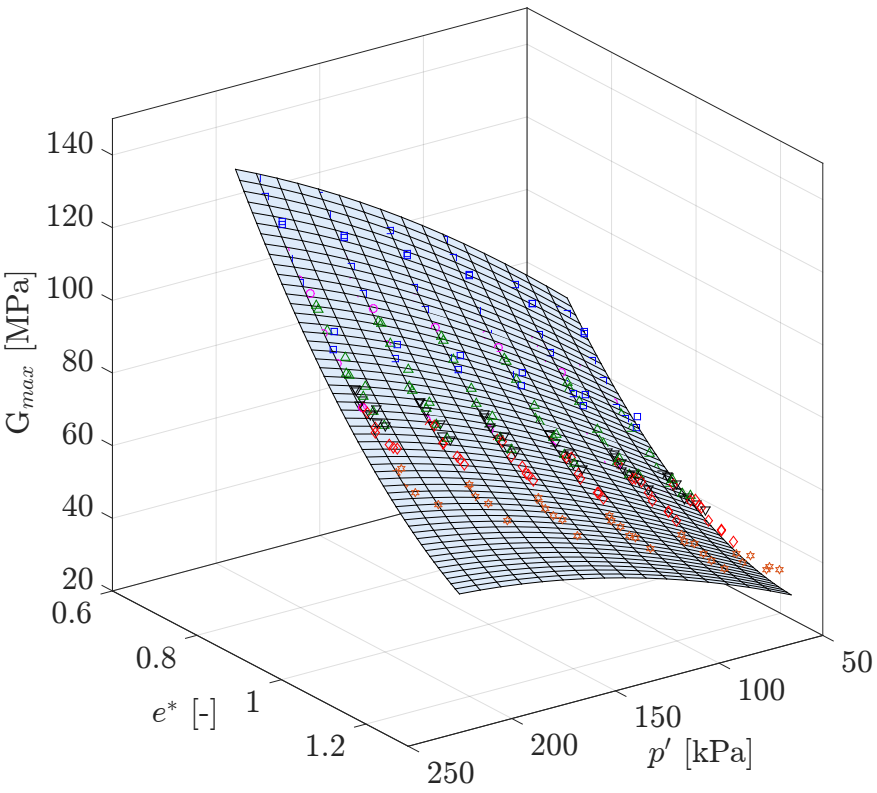

Figure 4.32: Maximum shear modulus versus equivalent void ratio and mean effective stress, the meshed surface is: $G_{max} = Af(e^*)f(p')$ for clean Hostun Sand

A detailed description of such a prediction approach for steady state data can be found in Rahman & Lo (2014). This prediction approach is also applicable for $f_c > f_{thr}$ but with the "sand-in-fines" model.

4.9 Published data sets

Calibration II for $f_c < f_{thr}$ is evaluated for four collected data sets from the literature as shown in Table 4.5. All the parameters for e^* were obtained from soil grading properties.

Table 4.5: Summary of published datasets in Figure 4.33

Sands	Fines	D_{10}	d_{50}	f_c	References
Iruma Z1	Iruma X1	0.13	0.050	0-14	Iwasaki & Tatsuoka (1977)
Iruma W	Iruma X1	0.65	0.050	0-11	Iwasaki & Tatsuoka (1977)
Foundary	Sil-co-Sil	0.17	0.01	0-30	Thevanayagam & Liang (2001)
Volcanic Coarse	same	2.05	0.05	3.2-17.3	Sahaphol & Miura (2005)

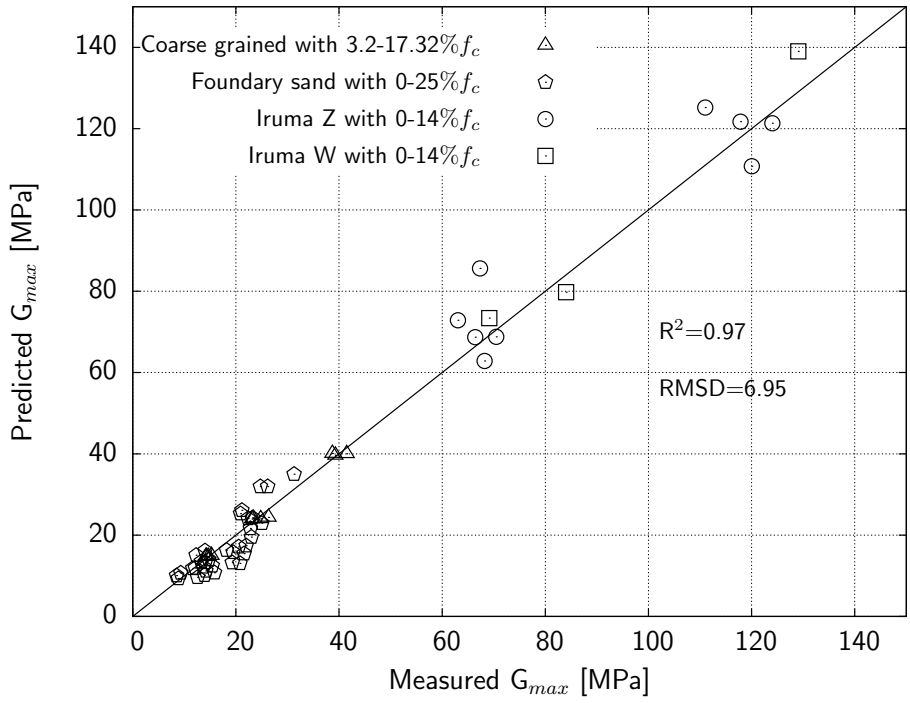

Figure 4.33: Measured G_{max} versus predicted G_{max} for published datasets with Jamiolkowski's void ratio function

A good agreement between predicted and measured G_{max}, with Jamiolkowski's $f(e)$, was confirmed as shown in Figure 4.33 with R^2 of 0.97 and RMSD of 6.95.

4.10 Application and limitations

There are soils with almost the same sand grading but different fines along the geological profile, e.g. Christchurch, New Zealand (Green & Cubrinovski 2010) and Ahmedabad, India (Ravishankar et al. 2005), where both sites severely liquefied during earthquakes. In these cases, RC tests on the original material (which may or may not have fines) would be performed to establish Hardin's relation. This relationship can be transformed to e^* space to predict G_{max} irrespective of f_c. This has a significant advantage when a slight variation in f_c considerably changes G_{max}, an average of 20% change in G_{max} was observed for a variation in f_c from 0 to 5% as shown in Figure 4.3. This is particularly helpful when a bore log has almost the same host sand but different fc along the depth profile.
This study has a number of limitations - the concept of e^* was developed based on binary packing which requires sand and fines particle´s disparity ratio to be greater than 6.5. This was achieved in this study for gap graded Huston Sand and quartz powder. The outcomes of this study are not directly transferable to well graded sands. The concept of threshold fines content, f_{thr}, is important for separating "fines-in-sand" and "sand-in-fines" models. However, f_{thr} is an idealization of a flat transition zone and can not be determined precisely. The e^* at f_{thr} for "fines-in-sand" and "sand-in-fines" models are close but not exactly the same for the entire range of e used in this study. This is due to the lack of a continuing equation for e^* for f_c before and after f_{thr}. This may have contributed to the scatter of the data points and has already been reflected in the reported RMSDs. The e^* was mostly validated with non-plastic to low plastic fines and thus one may not expect a single Hardin's relationship for sand with plastic fines. Despite the limitations, the above approach offers a simple and unified methodology to predict G_{max} irrespective of f_c which has a practical engineering application and may trigger significant research interest in this challenging problem.

4.11 Summary

Resonant column tests were conducted on clean Hostun Sand to evaluate the influence of mean effective stress, p', and void ratio, e, on the maximum shear modulus, G_{max}. Then, the effect of fines on G_{max} was investigated with a systematic increase in fines content, f_c, up to 40%. The major outcomes of the study are:

- A decrease in G_{max} with an increase in e and an increase in G_{max} with an increase in p' was observed for clean Hostun Sand. Hardin's relation was adequate to predict G_{max} with both Hardin's and Jamiolkowski's void ratio function, $f(e)$. A systematic increase in fines content, f_c, up to 40% in RC tests showed that G_{max} decreased with an increase in the f_c.

- A micro-CT scan revealed that sand with fines develops two different micro-structures: "fines-in-sand" and "sand-in-fines". For "fines-in-sand", fine particles are partially active in sand force structure and for "sand-in fines", sand particles are floating in fine particles. The void ratio, e, for sand with fines does not represent the same force structure as clean sand and is not suitable for a consistent comparison. The equivalent granular void ratio, e^* appears to be a consistent state parameter for density.

- The conversion of e to e^* requires two parameters, b and m. b can be obtained from soil grading properties with a fitting parameter λ=0.30 as in Rahman et al. (2008) and m can be obtained from correlation as in Figure 4.19. However, the parameters, λ and m can be further optimized by back analysis. Therefore, five calibration were conducted, including Rahman's method which does not require back analysis. The best calibration model was obtained when λ and m were back analyzed (calibration V). The second best model was obtained when only λ was determined by a back analysis of test data (calibration III). The back analyzed λ was linearly related to p' which can be used to predict λ for Hostun Sand.

- Jamiolkowski's $f(e)$ provides a better fit than Hardin's $f(e)$ for a large number of data points with f_c. An inverse power function of e appeared to be a better function than a function with a limiting void ratio constant, x.

- The unique relationship in space in G_{max}, $\frac{p'}{p_a}$ and e^* cloud be defined for clean sand or sand with fines. The main advantage of such a single relationship is that if Hardin's relationship is established for clean sand or sand with any $f_c < f_{thr}$, then

the relationship can be transformed to e^* space where e for clean sand is equal to e^* for sand with fines. This allows us to predict unknown G_{max} for different f_c. This prediction approach is also applicable for $f_c > f_{thr}$ but only with the "sand-in-fines" model.

- From the microscopic point of view, the results for glass bead mixtures showed that some fine glass beads were placed in between the gaps in coarse glass beads. They reduced overall e, i.e. increased density, but did not contribute to a coarse skeleton. This caused a leftward shift in the trends. However, other fine glass beads may be placed in between the coarse glass beads and may contribute to the coarse skeleton. This reduced the rate of the leftward shift with a higher f_c. Therefore, one can observe a decrease in the stiffness of the packing with f_c less than f_{thr}. However, for f_c more than f_{thr}, fine glass beads dominant in coarse glass beads and, therefore, coarse particles acted like reinforced elements inside fine materials.

5 Stress induced anisotropy

5.1 Introduction

Settlement of soils is one of the challenging problems in the soil-structure interaction during vibration, e.g. earthquake phenomena. Differential settlement may cause distress in the structures founded in the soil mass during earthquake. Maximum shear modulus and modulus degradation curves can be used to estimate the magnitude of ground settlements during earthquake (e.g. Tokimatsu & Seed 1987). The effect of isotropic confining pressure and soil properties on modulus degradation of soils have been studied in the previous works, as referred in Chapter 2. However, soil elements may be subjected to more complicated stress conditions in comparison with the stress conditions applied in the existing studies on intermediate strain properties up to now. Furthermore, the effect of density on maximum shear modulus of sample subjected to stress induced anisotropy at different stress paths must be discussed. Therefore, the objective of this chapter is to find the effect of stress induced anisotropy for different stress paths on the small and especially intermediate strain properties of sand.

This chapter is divided into two main parts. The main goal of part one is to find the effect of stress induced anisotropy on small strain properties of glass bead packing from the microscopic point of view. Therefore, for approaching to this objective, DEM simulation, by means TRUBAL code (Magnanimo et al. 2008), and modified resonant column device were adopted for this study. Since TRUBAL code is restricted to modeling of the spherical particles, the resonant column test were also conducted on spherical glass particles. The outcome of this part is to discuss the effect of stress induced anisotropy for different stress paths on micro and macro mechanical properties of granular packings. In part two, the resonant column test was conducted on Hostun Sand sample and experimental results are presented. The main goal of this section is to find the effect of stress induced anisotropy on small and intermediate strain properties of sand samples. Furthermore, the experimental results on intermediate strain stiffness will be used to modify the empirical

relations for prediction of modulus degradation curves in the samples subjected to stress induced anisotropy.

5.2 Glass beads: Numerical and experimental results

5.2.1 Overview

In this section, a combined experimental and numerical approach is used to study the shear stiffness at small and intermediate strain in granular materials. A set of experiments is performed on glass beads samples by using a resonant column device under different stress paths, namely isotropic compression, triaxial compression (GB-I) and constant stress ratio K deformation (GB-II). The results revealed that the maximum shear modulus is a function of the stress induced anisotropy, as determined by the specific stress paths. Existing analytical relations fail in describing this extra dependence, either when Equation 2.8 is used or the contribution of (induced) deviatoric stress is included through Equation 2.9. Along with laboratory tests, DEM simulations were performed to propose a micro-mechanical interpretation of the observed behavior. Starting from the numerical observations a modified version of Hardin's relation is proposed, that includes a dependence of the maximum shear modulus on the coordination number.

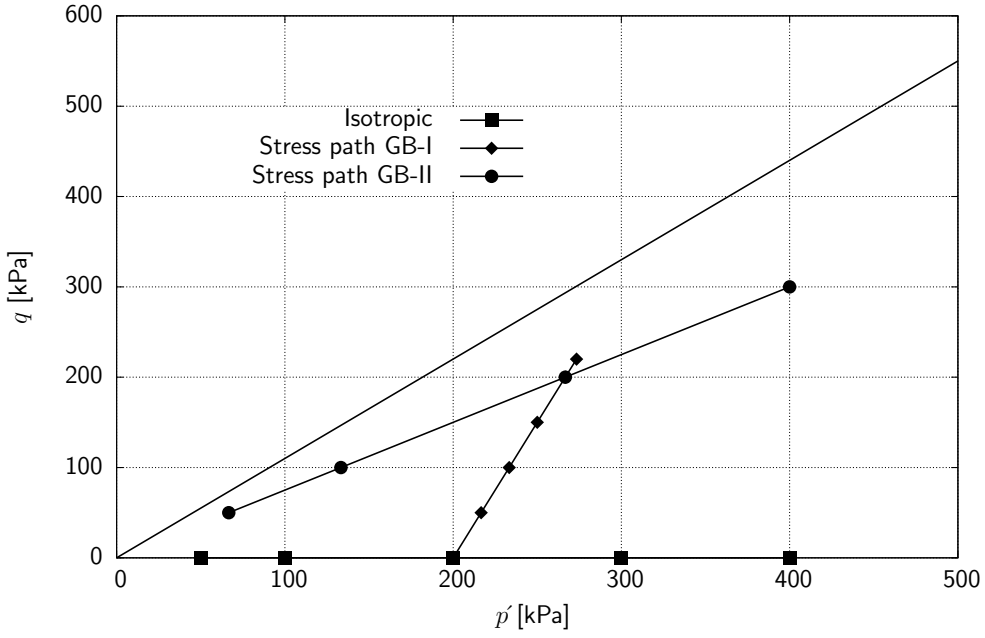

Figure 5.1: Adopted stress paths for performing tests on spherical glass beads

The section has been divided into the three parts. In part one, experimental results for samples subjected to isotropic and anisotropic loading will be presented. Afterwards, the experimental results will be presented in comparison with numerical results for calibration and validation of the DEM model. Finally, in part three, the effect of stress induced anisotropy is studied from the micro-mechanical point of view along different stress paths.

5.2.2 Experimental procedure

A series of Resonant column tests were conducted on glass bead samples subjected to stress paths GB-I and GB-II (Figure 5.1). The experimental procedure is the same as presented procedure in Section 3.6. It must be noted that initial void ratio in all of the samples, in experimental and numerical procedure, was equal to 0.57.

5.2.2.1 Experimental results on G_{max}

The experimental results on G_{max} for isotropic loading were presented in Section 4.3. Figure 4.9a in Section 4.3 showed the increasing of G_{max} with an increase in the isotropic confining pressure.

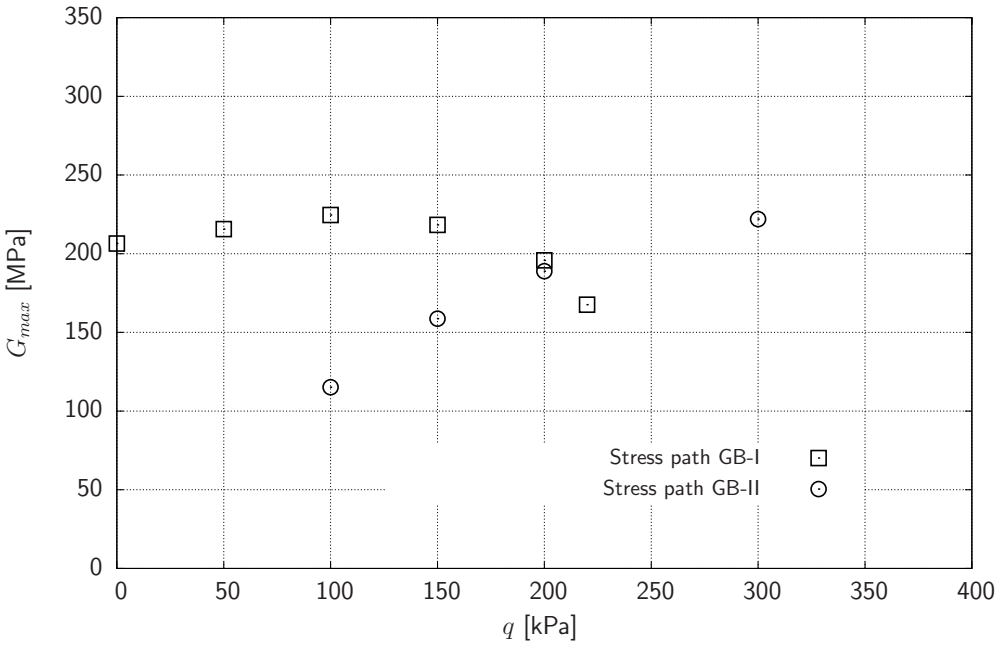

Figure 5.2: The effect of stress induced anisotropy on maximum shear modulus of glass bead packing

Figure 5.2 shows the effect of stress induced anisotropy for stress path GB-I and GB-II on maximum shear modulus, G_{max}. As it is apparent from this figure, G_{max} increases slightly with an increase in the shear stress and it then decreases with further increasing of shear stress for stress path GB-I which is due to increasing of shear contact forces at contact points and decreasing of coordination number, CN. This Figure shows that G_{max} for stress path GB-II increases with an increase in the shear stress which is due to the increasing of CN and normal contact forces for this stress path. The observed results will be discussed in comparison with numerical results with more details in Section 5.2.4.

5.2.2.2 Experimental results on $G(\gamma)$ and $\eta(\gamma)$

The results of the resonant column test on the dense glass bead samples, subjected to stress induced anisotropy for stress paths GB-I and GB-II, are presented in this section. This section is divided into two main parts: in the first part, the results of isotropic loading are presented and in the second part, the results of stress induced anisotropy are presented.

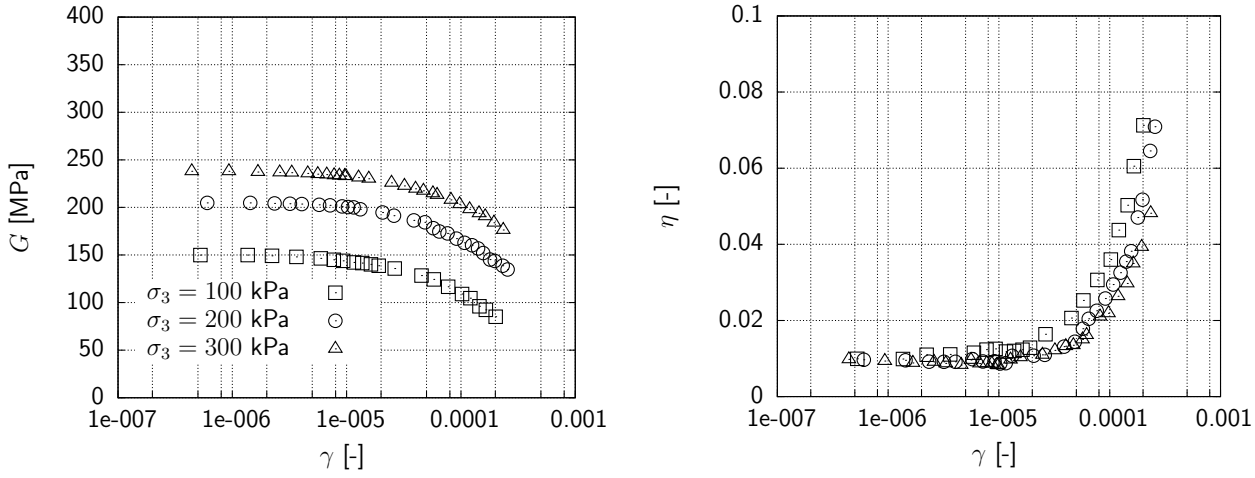

(a) (b)

Figure 5.3: G and η versus shear strain for dense glass bead packing with Dr=88% – 91% and subjected to isotropic loading: (a) $G-\gamma$; (b) $\eta-\gamma$

Isotropic loading

It is well-known that at a given strain amplitude, the shear modulus (G) and modulus ratio (G/G_{max}) increase with an increase in the confining pressure, and damping ratio decreases with an increase in the confining pressure. The observed experimental results (Figure 5.3a and Figure 5.3b) also show the dependency of modulus degradation and damping ratio on the isotropic confining pressure and amplitude of shear strain which is in line with the observed results from DEM simulation and the results from the literature. Figure 5.3a shows that the shear modulus is constant and equal to the maximum shear modulus up to shear strain of 8E-6 which decreases with an decrease in the confining pressure. Figure 5.3b shows that damping ratio has the minimum value up to shear strain of 8E-6 which decreases with an increase in the confining pressure. The results show that shear stiffness increases with an increase in the confining pressure and damping ratio decreases with an increase in the confining pressure.

Anisotropic loading

Figure 5.4 show the effect of shear strain on the modulus ratio and damping ratio of the glass bead sample with a relative density of 90% and subjected to anisotropic stress conditions at stress paths GB-I and GB-II respectively. Figure 5.4a and Figure 5.4c show that the shear stiffness is constant and equal to the maximum shear modulus up to the shear strain of 6E-6. Figure 5.4b and Figure 5.4d show the effect of stress induced anisotropy on the damping ratio versus the shear strain for stress paths GB-I and GB-II respectively. For stress path GB-I, the experimental test data show that damping ratio decreases slightly with an increase in the vertical stress up to vertical stress of 300 kPa and it then increases at a vertical stress of 350 kPa (Figure 5.4b).

However, the damping ratio decreases with an increase in the confining and vertical stress for stress path GB-II (Figure 5.4d). Figure 5.4 shows the effect of stress induced anisotropy on damping ratio for stress path GB-II is more obvious than stress path GB-I. The effect of stress induced anisotropy on shear modulus (G) is presented in Figure 5.4a and Figure 5.4c for stress paths GB-I and GB-II respectively.

For stress path GB-I, Figure 5.4a reveals that the modulus ratio increases slightly with an increase in the vertical stress up to vertical stress of 300 kPa and it then decreases at a vertical stress of 350 kPa. Figure 5.4c shows modulus ratio increases significantly with an increase in the confining pressure and the vertical stress. Figure 5.4 reveals that the effect of stress induced anisotropy on G for stress path GB-II is more significant than stress path GB-I. The results confirm that G is affected by stress induced anisotropy but the impact of stress induced anisotropy strongly depends on the adopted stress path and history of loading.

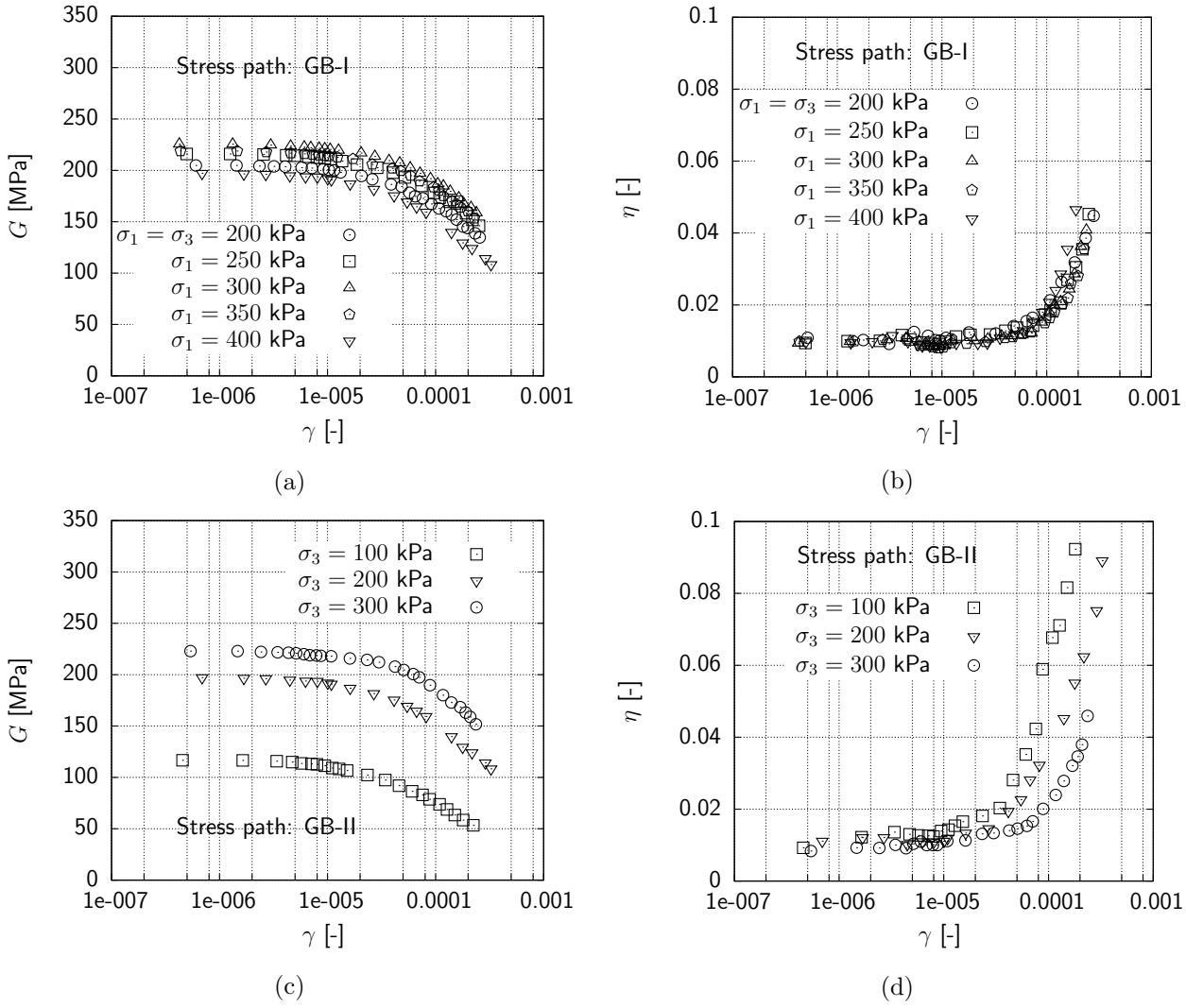

Figure 5.4: G and η versus shear strain for dense Glass bead packing, Dr=88% − 91%: (a) $G-\gamma$ curve at stress path GB-I; (b) $\eta-\gamma$ curve at stress path GB-I; (c) $G-\gamma$ curve at stress path GB-II; (d) $\eta-\gamma$ curve at stress path GB-II

5.2.3 Numerical procedure

5.2.3.1 Adopted DEM code

Distinct element method originated from Cundall & Strack (1979) was used to prepare random assemblies of identical, frictional, elastic spheres. 10,000 particles with diameter d=1.25mm were randomly generated in a periodic cubic cell. The elastic material properties typical for glass spheres with shear modulus G_p=29GPa and Poisson's ratio, $\nu = 0.2$ were assigned to the particles. The interaction between particles is represented by a non-

central contact force in which the normal component follows the non-linear Hertz's law and for the tangential component a bilinear relationship with elastic displacement and frictional Coulomb sliding with friction coefficient μ_f were incorporated (details are given in Makse et al. 1999). For the sake of simplicity gravity was neglected in the numerical experiments. The following definition of the stress tensor was applied to quantify the macroscopic response of a DEM assembly (Cundall & Strack 1979 and Magnanimo et al. 2008):

$$\sigma_{ij} = \frac{1}{V} \sum_{N_c}^{c} f_i^c l_j^c, \tag{5.1}$$

where, V is the total volume of the assembly, N_c is the total number of contacts, f^c denotes the contact force at a contact, and l^c defines the branch vector joining the centers of two contacted particles. The mean effective stress and deviatoric stress can then be determined by $p' = 1/3\sigma_{ii}$ and $q = \sqrt{3 s_{ij} s_{ij}/2}$, where $s_{ij} = \sigma_{ij} - \delta_{ij} p'$ (δ_{ij} is the Kronecker delta). Coordination number was used to characterize the average number of contacts in the sample, that is the particle arrangement. The simple definition of the coordination number is $CN = 2N_c/N_B$, with N_B number of particles in the sample. However, numerical simulation have revealed that at any time during compression, there are some particles with no contacts and some particles with only one contact. None of these particles are contributing to the stable state of stress (Thornton & Antony 1998). Hence a corrected coordination number is introduced:

$$CN = \frac{2N_c - N_1}{(N_B - N_0 - N_1)}, \tag{5.2}$$

where, N_1 and N_0 are the number of particles with only one or no contacts, respectively. It is worthwhile to notice that the focus is on a unique scalar quantity CN and the orientation of the contact network is neglected.

5.2.3.2 Sample preparation

The density of the generated sample in DEM must be close to the experimental value $e \sim 0.57$. It is well-known experimentally that different packing structures are realizable according to the preparation protocol (Figure 5.5). The adopted approach is to generate numerically packings of different structure and determine the relevant variables needed to characterize the elastic response (for details see Magnanimo et al. 2008). Independent on the preparation used, the final structure of the packings which in turn determines the moduli is interest. Here a protocol was employed as suggested by Magnanimo et al. (2008) and Makse et al. (1999), where μ and p' are set in two different phases during

the compression of the sample, as depicted in Figure 5.5. After random generation in a periodic box, frictionless particles are isotropically compressed from an initial gas to the target density. The compression is stopped just before this density to obtain a dense but non-equilibrated packing. Then, the sample is relaxed, reaching zero-pressure and zero-coordination number. It follows a second isotropic compression with friction to reach the target pressure, $p' = 100$KPa, as in the experiments. This stress-controlled deformation is carried out using a servo-mechanism that constantly adjusts the applied strain rate according to the difference between the target stress state σ^*_{ij} and the measured stress state σ_{ij}. At each time step, the strain rates $\dot{\epsilon}_{ij}$ are adjusted to the value:

$$\dot{\epsilon}^s_{ij} = \dot{\epsilon}_{ij} + g(\sigma_{ij} - \sigma^*_{ij}), \tag{5.3}$$

where g is a gain factor that is tuned to achieve equilibrium in an optimal way. In this stage, for a fixed pressure, four different coefficients of friction, $\mu_i = 0.01, 0.04, 0.06$ and 0.1 were used to create four different packings, respectively. When the coordination number becomes constant with variation of number of cycles the same final friction coefficient $\mu_f = 0.3$ was imposed for all packings and, with further servo-control adjustment, we create an equilibrated condition for the system, until the system is fully equilibrated. All packings are now characterized by the same friction coefficient. However their structure depends on different preparations during the compaction loading. The result is that, for a given pressure and density, packings with different coordination number, ranging from $CN_0 = 5.239$ to $CN_0 = 5.943$ at the highest, have been generated (see Table 5.1). All packings are generated to have the same density $e \simeq 0.57$ and friction coefficient $\mu_f = 0.3$, when they reach the final reference state.

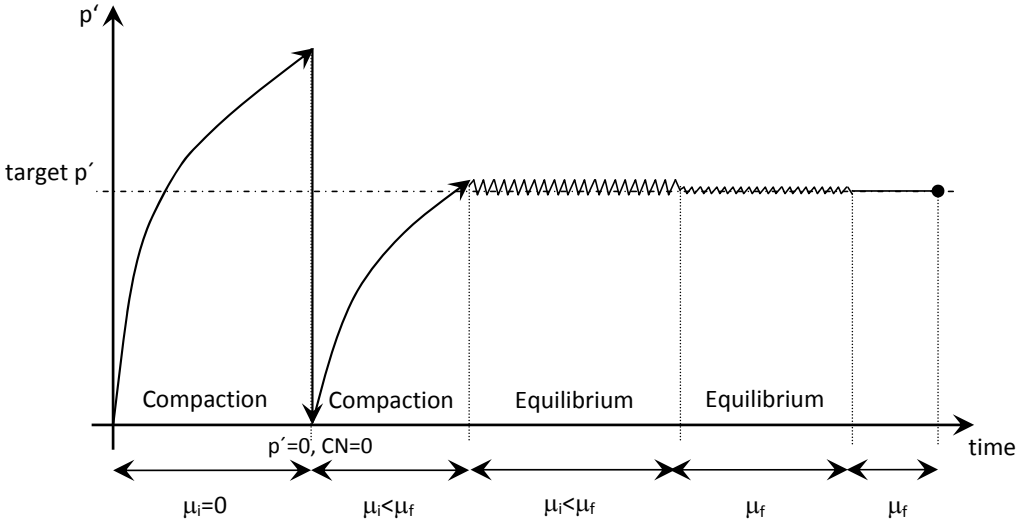

Figure 5.5: Specimen preparation stages in this study

Table 5.1: The effect of μ_i on coordination number, CN, and shear stiffness at isotropic pressure of 200 kPa

p'	μ_i	e	CN	F_N	$G_{max}[MPa]$
200	0.01	0.57	6.04	0.280	249.4
200	0.04	0.58	5.81	0.294	226.6
200	0.06	0.58	5.64	0.307	208
200	0.1	0.58	5.47	0.321	193.7

5.2.3.3 Isotropic compression, triaxial compression and constant K deformation

The four samples described above are subjected to further isotropic compression in order to reproduce the isotropic samples at $50, 100, 200$ and 300 kPa as performed in the experiments. During each loading step, the target pressure is maintained with the servo mechanism in Equation 5.3. Starting from the sample at 200kPa a triaxial compression (stress path GB-I) is performed, by applying strain along the axial direction ($e_{11} = e1$) and keeping the lateral stress, $\sigma_{22} = \sigma_{33} = \sigma_3$, constant through the servo mechanism. Numerical samples with identical (p', q) value as applied the experiments (Figure 5.1) are then created. Similarly to the procedure used in experiments, every sample in the triaxial loading path is prepared starting from the initial isotropic state at 200kPa. The goal is to reproduce triaxial loading, so the sample is compressed very slowly ($\gamma_{\partial t}/\Delta_0$ is lower than 5×10^{-3}, where $\gamma_{\partial t}$ is the accumulated strain in the time step ∂t, and Δ_0 the average volumetric compression in the isotropic state). After each increment the system is relaxed until a new equilibrium state is reached. The procedure is repeated for the full set of packings obtained with the different μ_i preparations, that is for each point on the triaxial path in Figure 5.1, four numerical data are created. Finally, a similar procedure by means of the servo-control mechanism is adopted to deform the samples along a constant stress ratio $K_0 = \sigma_3/\sigma_1$. Configurations that reproduce the stress states in the stress path GB-II are reproduced. Values for the characteristics of the samples are reported in Tables 5.2, 5.3, and 5.4 for isotropic compression, triaxial compression and constant K respectively.

5.2.3.4 Elastic moduli

At each step along the different loading paths (for all four samples) in Figure 5.1 (isotropic, GB-I and GB-II), the maximum shear modulus of the aggregate is calculated by applying an incremental strain to the sample and then allowing it to relax. The corresponding incremental stress response is then measured and modulus is calculated as Magnanimo et al. (2008):

$$G_{12} = \frac{(\sigma_{12})_f - (\sigma_{12})_i}{\epsilon_{12}}, \tag{5.4}$$

where, $(\sigma_{12})_i$ is he shear stress before applying the incremental strain, while $(\sigma_{12})_f$ is the final value after relaxation. The experimental results from the Bochum resonant column device show that the shear stiffness is constant and equal to maximum shear modulus up to the shear strain of less than 5×10^{-6}. That is, a similar behavior is expected in simulations. For each sample, the procedure is repeated several time by applying increasing amplitudes of the shear strain and the G_{max} is extracted in the small amplitude range. Figure 5.6 shows the variation of G_{12} with ϵ_{12} etc.

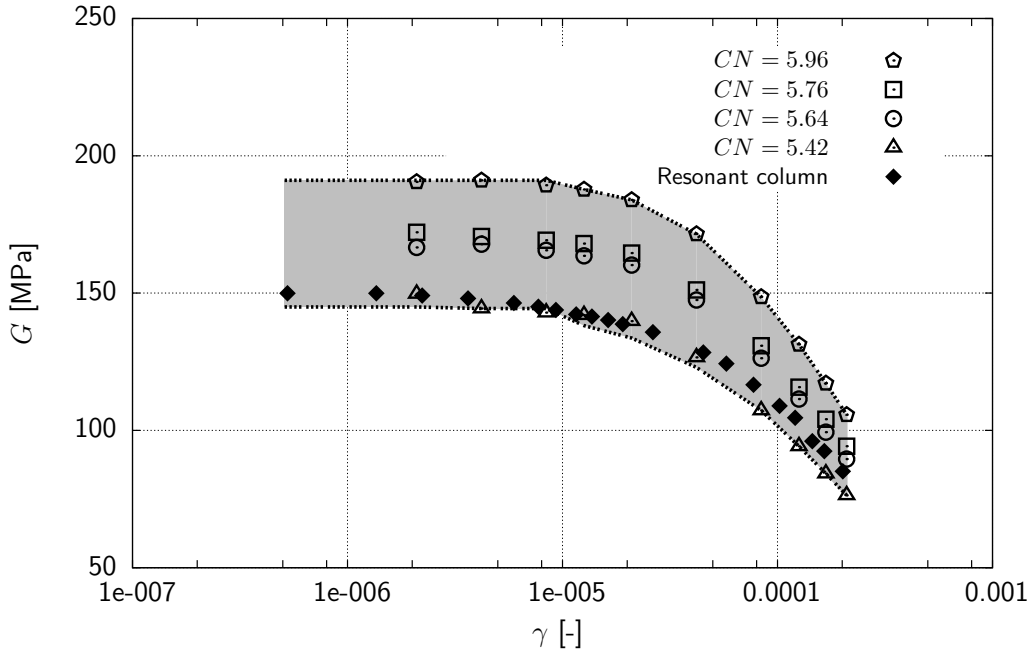

Figure 5.6: Shear modulus versus shear strain from experimental and numerical procedure for $p' = 100$ kPa

5.2.4 Numerical results on G_{max}

5.2.4.1 Isotropic loading and calibration of the numerical model

The maximum shear modulus obtained with the four numerical preparations (different μ_i) in the isotropic configurations are reported in Figure 5.7, along with the experimental data. The results show that the maximum shear modulus increases with an increase in the confining pressure. The results from DEM simulations show the significant effect of coordination number on maximum shear modulus in the specimens with the same density (e=0.57). The figure shows that, for packings with same pressure and density, a difference in the coordination number due to the preparation, leads to different shear modulus. Three variables (pressure, density and coordination number) are needed to fully characterize the stiffness of an isotropically consolidated sample, in agreement with findings in Magnanimo et al. (2008). Moreover, comparison with experiments shows that samples with less coordinated packings better reproduce our physical samples. The comparison of the macroscopic shear modulus allows for a back analysis. From the back analysis, the internal coordination number of the experimental sample is a value between the values characterized by $CN_0 = 5.09$ and $CN_0 = 5.38$ (created with μ_i =0.01 and 0.04). Even if these two packings could be used to proceed further in the analysis, in the following the whole set of prepared packings will be used in order to define the boundaries of the physical samples.

5.2.4.2 Anisotropic loading

Results of analyses for stress path GB-I and GB-II are presented in Figure 5.8. Figure 5.8a shows the effect of shear stress, q, and coordination number on maximum shear modulus of sample subjected to stress path GB-I. The results show that the maximum shear modulus increases with an increase in the q up to q of 100 kPa and it then decreases significantly with further increase of q. The measured results for specimens subjected to stress path GB-II, using DEM simulation, are presented in Figure 5.8b. As can be seen in this figure, the value of G_{max} increases significantly with an increase in the value of q. The experimental results showed that maximum shear modulus was affected by stress induced anisotropy for stress paths GB-I and GB-II.
Figure 5.9 shows G_{max}-q curves obtained from experimental method in comparison with the DEM results for the sample with (μ_i, μ_f)=(0.04, 0.3). This figure shows the effect of q on maximum shear modulus for stress paths GB-I and GB-II. Figure 5.10 shows the

effect of q on CN for the sample with (μ_i, μ_f)=(0.04, 0.3). The results show that CN increases with increasing q for the stress path GB-II. However, for the stress path GB-I, CN increases slightly up to q of 100 kPa and it then decreases with further increasing of q.

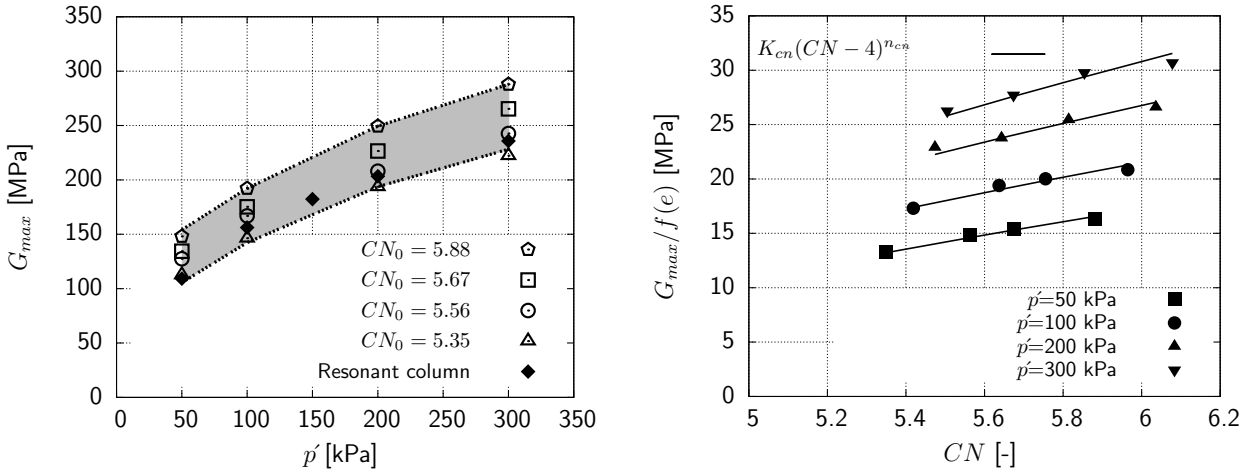

(a) (b)

Figure 5.7: The effect of p' and CN on G_{max} of dense specimen $e = 0.57$: (a) G_{max}-p'; (b) $G_{max}/f(e)$-CN (isotropic loading)

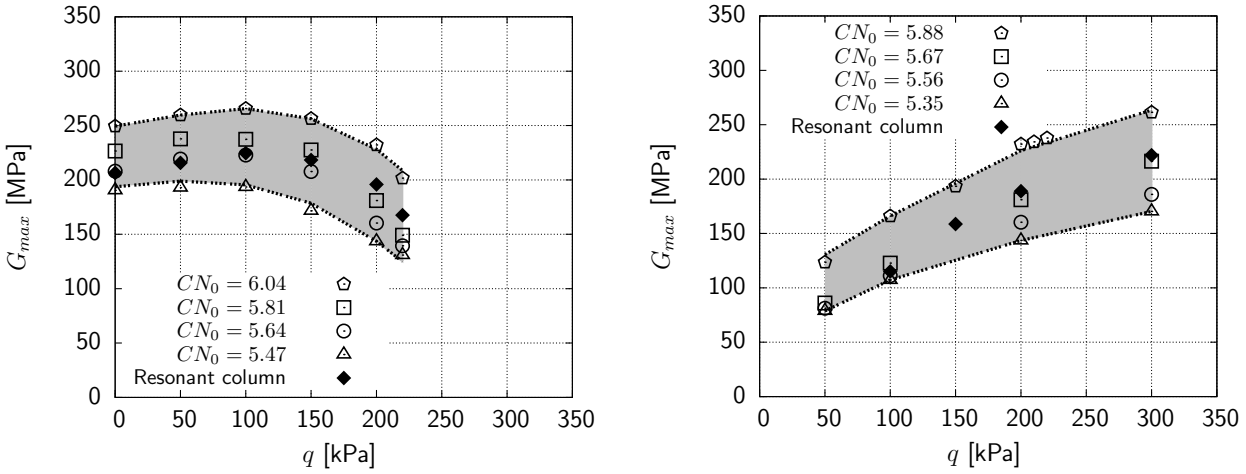

(a) (b)

Figure 5.8: The effect of shear stress, q, on maximum shear modulus of dense packing: (a) stress path GB-I; (b) stress path GB-II

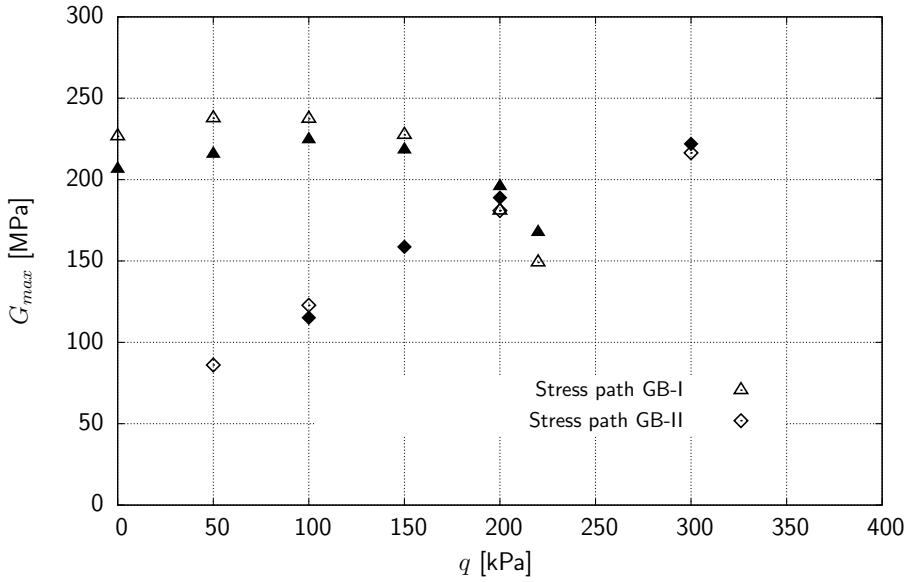

Figure 5.9: G_{max} versus q from experimental, filled points, and DEM simulation with μ_i=0.04 and μ_f=0.3, unfilled points

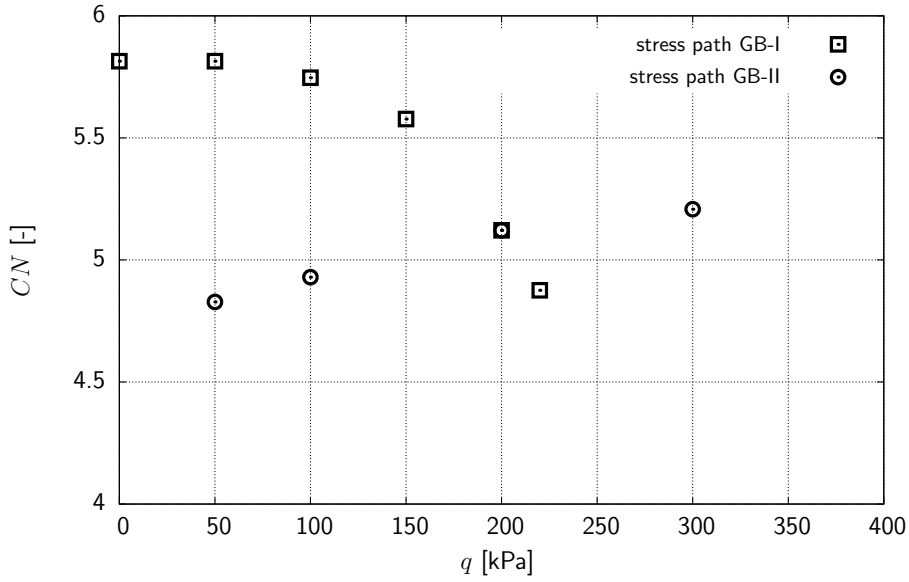

Figure 5.10: CN versus q from DEM simulation with μ_i=0.04 and μ_f=0.3, unfilled points

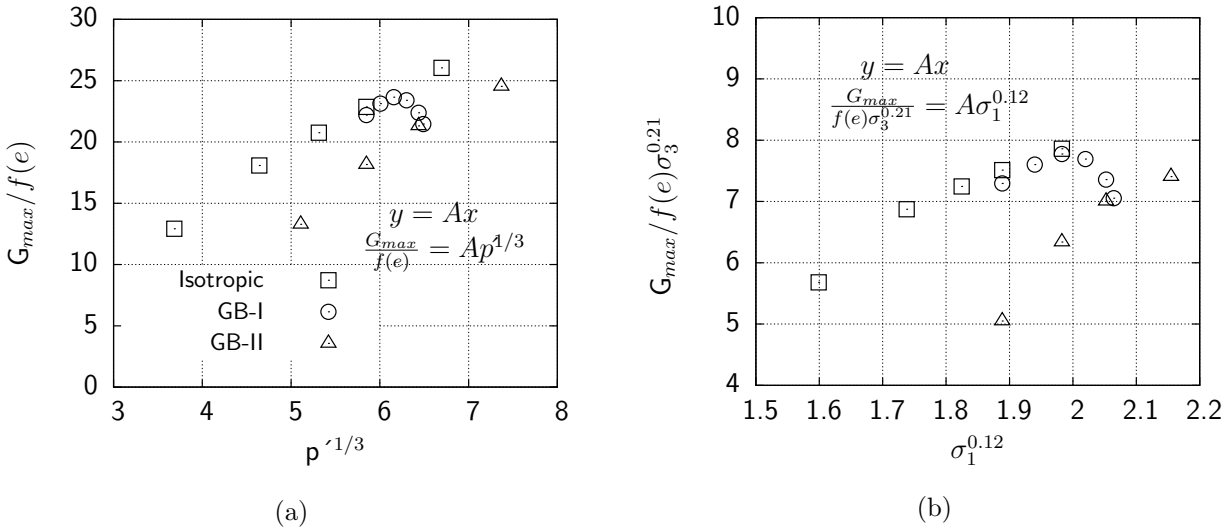

(a) (b)

Figure 5.11: Normalized shear modulus versus pressure function: (a) Hardin's relation; (b) Roesler's relation

Hardin's and Roesler's relations (Equations 2.8 and 2.9) are two common empirical relations which are applicable to predict G_{max} in the samples subjected to stress induced anisotropy. Firstly, G_{max} from the experimental results was normalized with respect to the void ratio (void ratio at the time of RC test). Normalized shear modulus was drawn versus pressure function, $p'^{1/3}$, (Figure 5.11a). Figure 5.11a shows a significant deviation between the results from stress paths GB-I and GB-II in comparison with isotropic loading. As is apparent from this figure, for stress path GB-I, the results up to vertical stress of 300 kPa are in line with the results from isotropic loading but, the scatter of results increases with further increasing of σ_1. Also, this figure shows that the results for stress path GB-II are not in the line with the results from isotropic loading. Therefore, there is not a unique curve (e.g. Equation 2.8 in Figure 5.11a or Equation 2.9 in Figure 5.11b) to predict the value of G_{max} in the samples subjected to stress induced anisotropy which will be assessed in the next section from a microscopical point of view.

5.2.4.3 Modified Hardin's relationship

Hardin & Drnevich (1972*a*) developed a well known relationship to predict the maximum shear modulus which was a function of void ratio and pressure. Presented results from DEM simulation show that maximum shear modulus of the specimens with the same density not only depends on the void ratio and confining pressure but also depends on the coordination number, therefore, Hardin's relation can be rewritten as a function of

coordination number, void ratio and pressure (Equation 5.5).

$$G_{max} = Bf(e)f(CN)(p')^n \tag{5.5}$$

where, B is a constant parameter, $f(e)$ is void ratio function which is equal to $e^{-3.98}$ for glass particles with diameter of 1.25 mm (Goudarzy et al. 2014), $f(CN)$ is the coordination number function, p' is the isotropic pressure and n is the pressure exponent. The value of n was assumed to be $n = 1/3$, as can be derived when interaction between particles is the Hertzian contact (Walton 1987, Rothenburg & Bathurst 1989). Coordination number was assumed to be a power function. Equation 5.6 was used to capture the effect of coordination number in Equation 5.5:

$$f(CN) = (CN - 4)^{n_{cn}} \tag{5.6}$$

where, CN is the coordination number and n_{cn} is its exponent. In Figure 5.12, the normalized shear modulus, G_{max}, with respect to the void ratio and pressure ($G_{max}/f(e)p^{1/3}$), was drawn versus the coordination number for all collected packings, created with different procedures and deformed along the three loading paths considered (isotropic, GB-I and GB-II). Surprisingly, all data results were located in a unique curve, irrespective of induced anisotropy or (deviatoric) stress state. The results clearly demonstrate the influence of the micro-structure characterized just by CN. Shear stiffness can be associated with a unique coordination number, that acts as a state variable and able to completely characterize the granular sample, when associated with pressure and volume fraction.
It is worthwhile to notice that the constant parameters of B and n_{cn} were also determined by fitting the power function of $B(CN-4)^{n_{cn}}$ to the data (Figure 5.12). From the performed regressions the value of B and n_{cn} were equal to 2.96 and 0.63 respectively. Therefore, Hardin's relationship, Equation 5.5, can be used to predict the value of G_{max} in samples subjected to anisotropic loading with sufficient accuracy (Figure 5.13a). The accuracy of predicted results can be improved by using the Roesler's relationship, where, $f(cn) = (CN - 4)^{0.63}$, $B = 2.96$, $m_1 = 0.12$ and $m_3 = 0.21$ (Figure 5.13b).

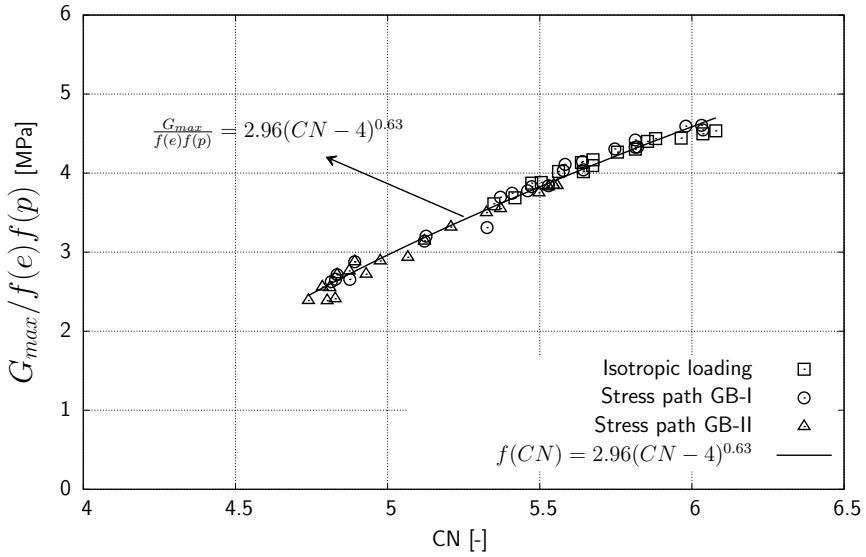

Figure 5.12: Normalized results: $G_{max}/f(e)f(p)$ versus CN for all of the stress paths

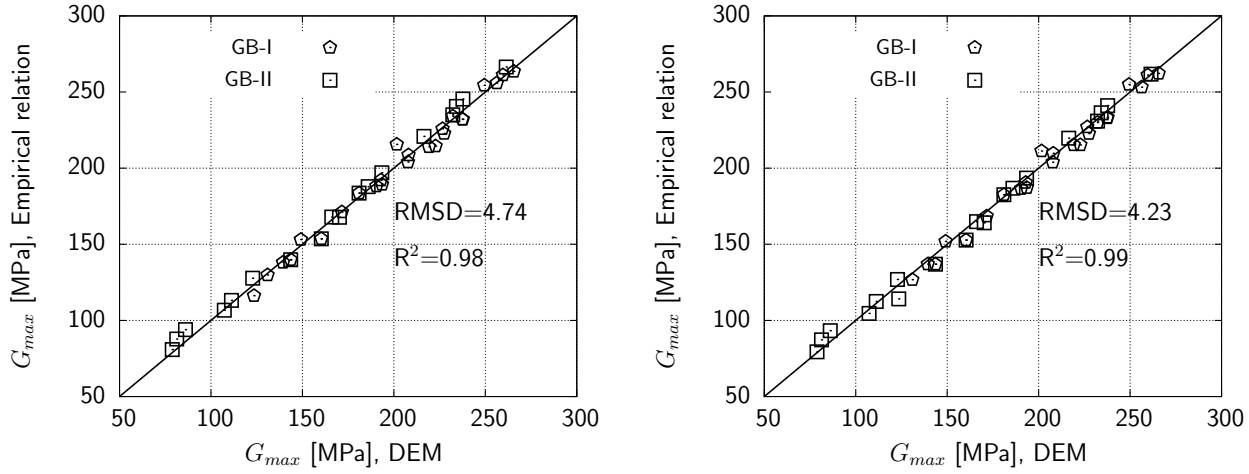

Figure 5.13: Comparing the obtained value of G_{max} from DEM simulation and empirical relation: (a) Hardin's relation; (b) Roesler's relation

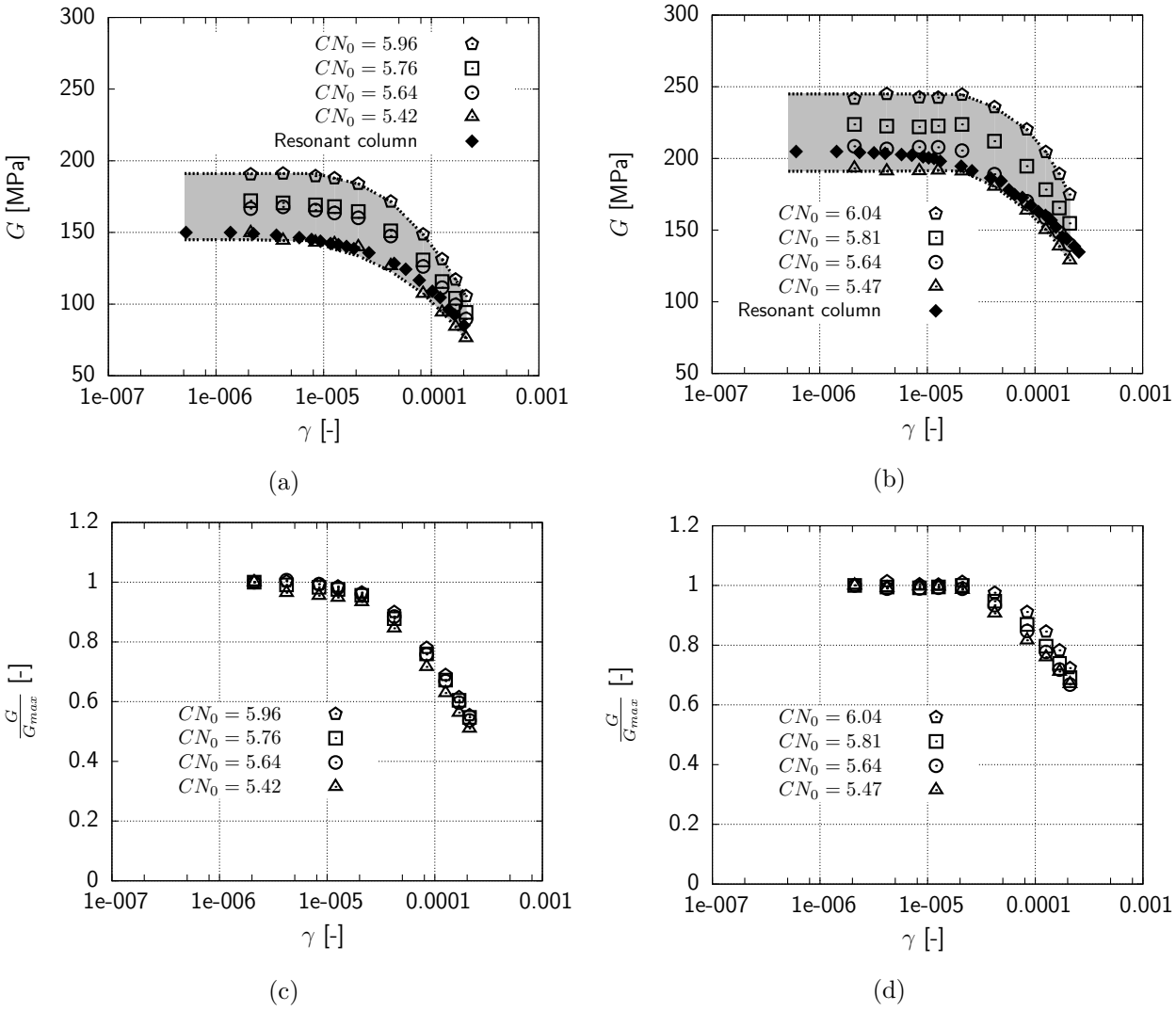

Figure 5.14: DEM simulation and experimental results: (a) $G-\gamma$, p'=100 kPa; (b) $G-\gamma$, p'=200 kPa; (c) $\frac{G}{G_{max}}-\gamma$, p'=100 kPa; (d) $\frac{G}{G_{max}}-\gamma$, p'=200 kPa

5.2.5 Numerical results on $G(\gamma)$

The prepared specimens in section 5.2.3.2 were used to find the effect of shear strain on shear modulus, G. To preform the simulations the boundary movement were applied to the specimens slowly. Then, the specimen were relaxed without servo control under the applied shear strain. Afterward, the value of shear stress was extracted from the stress tensor of specimen and the values of shear strain and shear modulus were calculated. For higher amplitude of shear strain the value of boundary movement was increased slowly step by step up to desired shear strain. Figure 5.14 shows the $G-\gamma$ curves from the numerical simulation in comparison with the experimental results for isotropic loading.

The maximum value of G (so-called G_{max}) in these figures are consistent with the obtained values for G_{max} in Section 5.2.3.2. Figure 5.14 shows that the experimental results are located in the grey band obtained from numerical simulation for the specimens with the same density but with different coordination number. These figures show a good agreement between the results from DEM simulation and the obtained results from RC tests although the method of applying shear strain is different.
Figure 5.14c and Figure 5.14d show the effect of coordination number on G/G_{max}. As can be seen in these figures, G/G_{max} increases slightly with an increase in the coordination number.

5.2.6 Interpretation from microscopic point of view

5.2.6.1 Links between macro properties and micro information

Hertz (1882) developed expressions to describe the contact between the smooth elastic surfaces. Hertzian theory has been used as a basic to explain the relationship between shear modulus and confining pressure. According to the Hertz-Mindlin's theory, the normal and tangential stiffness are function of contact forces and elastic properties of particles (Yimsiri & Soga 2002 and Johnson 1985). The normal contact stiffness (K_N) between to identical smooth spheres, is given by:

$$K_N = \frac{2G_p}{1-\nu_p}\alpha \tag{5.7}$$

$$\alpha = \left[\frac{3R(1-\nu_p)}{8G_p}\right]^{1/3} F_N^{1/3} \tag{5.8}$$

where, G_p is the shear modulus of particles, ν_p is Poisson's ratio of particles, a is the radius of contact area, R is the radius of particles and F_N is the normal contact forces. Deresiewicz (1953) described the tangential contact stiffness (K_T) between smooth spheres using Hertzian theory.

$$K_T = \frac{4G_p}{2-\nu_p}\alpha\left[1-\frac{F_T}{\mu F_N}\right]^{1/3} \tag{5.9}$$

where, μ is the coefficient of friction between particles and F_T is the shear contact force. Chang & Liao (1994) used a micro-mechanic based model to relate the shear modulus, G_{max}, of an assembly of the randomly packed identical spheres to normal, K_N, and tangential, K_T, stiffness at contact points. Using the static hypothesis which assumes uniform strain and uniform stress respectively, expression for estimate of the elastic modulus was

proposed (Otsubo et al. 2015):

$$G_{max} = \frac{2NR^2K_N}{3V}\left[\frac{5(K_T/K_N)}{3+2(K_T/K_N)}\right] \tag{5.10}$$

where, N is the number of particles and V is the volume of the sample and K_T/K_N is equal to $f(\nu_p)\left[1-\frac{F_T}{\mu F_N}\right]^{1/3}$. Based on Equation 5.10 maximum shear modulus increases with an increase in the coordination number, CN, and normal contact force, F_N, from microscopic level.

Equation 5.10 is helpful for discussion of the observed results at the macroscopic level using the microscopic or contact observations.

5.2.6.2 Polar presentation of contact properties

The outputs of TRUBAL code are a text files including the particles and contact properties. For ease of discussing the results, some analyses were done to present the effect of loading on contact and particle properties graphically. MATHEMATICA programming was used to visualize the results of TRUBAL code. The programming codes were written for 3D presentation. The details of written code for presentation of contact forces and contact distributions are briefly discussed in this section.

If the contact points are drawn, using the output text files, the spherical distribution achieves for normal contact forces (Figure 5.15b). In the next step, the contact force vectors were surrounded by a sphere with unit radius. The unit sphere was divided into the pyramids with the same slopes, θ. One pyramid was chosen for performing the analyses. The pyramid was defined with a given slope angle (θ), then, the boundary surfaces (slant faces) of the pyramid were determined (Figure 5.15a). In the next step, the normal vectors of contacts that were located in this pyramid were determined and the average of them was calculated (Figure 5.15b). In a given pyramid, the average of normal contact forces (K) was the length of the desired pyramid (Figure 5.15a). Then, the analysis were extended for all of the data to find the length of the other pyramids.

Figure 5.15c shows an example of polar distribution of normal contact forces using discussed procedure for 10000 particles subjected to anisotropic pressure. The same procedure was used for polar presentation of shear contact forces (Figure 5.15d). The unit normal vectors of contacts were used to present the polar distribution of contacts at different time steps. In this case, the length of pyramid (K) was the number of contacts which were located in the one pyramid.

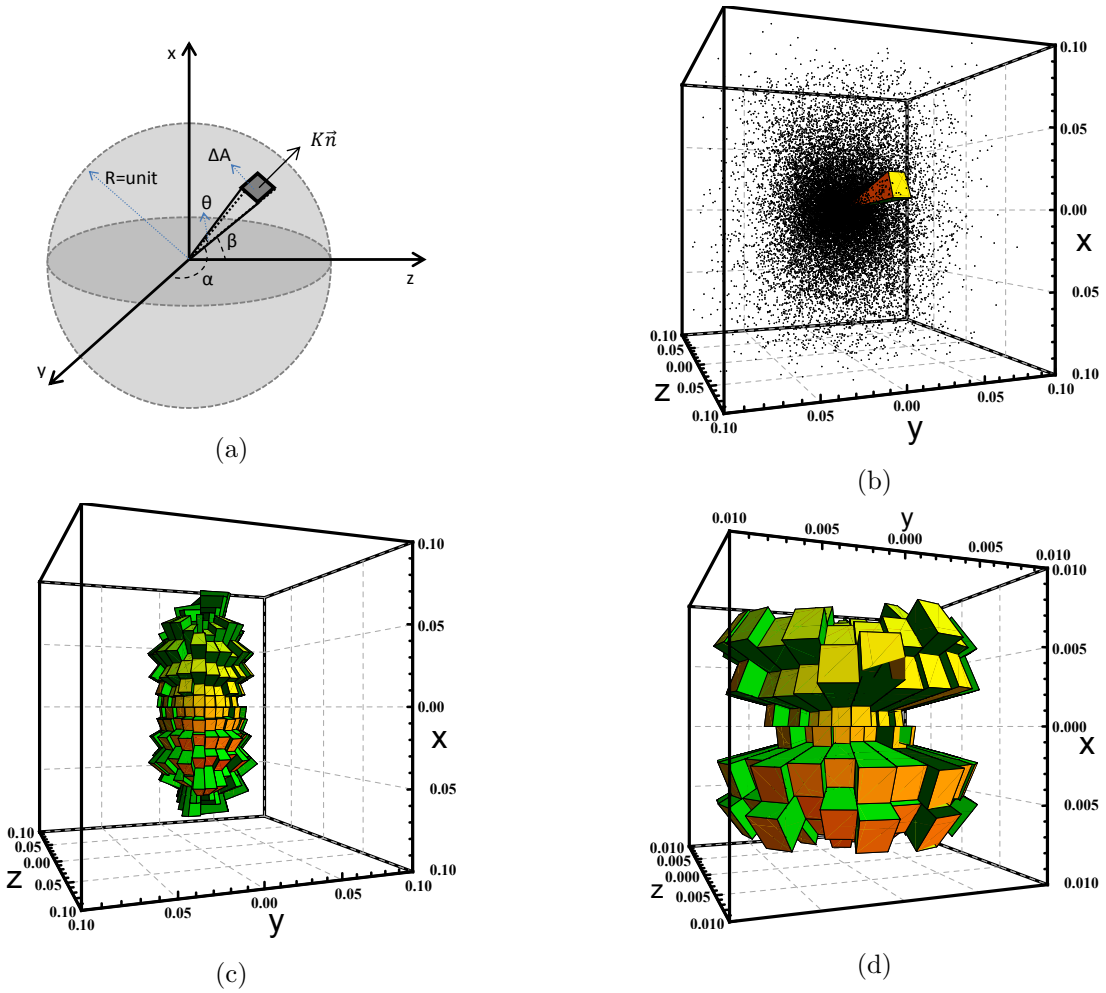

Figure 5.15: 3D polar presentation of contact forces at σ_3=200 kPa and σ_1=300 kPa: (a) spherical coordination system; (b) normal contact forces distribution; (c) 3D polar presentation of normal contact forces; (d) 3D polar presentation of shear contact forces

5.2.6.3 Contact properties

The value of contact properties in respect to the isotropic pressures for dense sample, e=0.58, with the initial and final friction of 0.01 and 0.3 have been summarized in Table 5.2. As can be seen in Table 5.2, the value of coordination number, CN, increases slightly with an increase in the confining pressure although the increasing of CN with p' is not so significant in comparison with the other contact parameters. The normal contact force increases significantly with an increase in the isotropic pressure, p'. However, the effect of isotropic pressure on shear contact force and contact distribution is not significant during isotropic loading. As it is apparent from Table 5.2, shear contact force increases with an increase in the isotropic pressure which can be discussed through the friction resistance

and sliding of particles with an increase in the isotropic pressure. Polar distribution of contact properties for isotropic loading are presented in Figure 5.16. As it is apparent from this figure, the normal contact forces increase isotropically with an increase in the confining pressure. Also, this figure shows that contact distribution is isotropic and it remains isotropic with an increase in the confining pressure.

Table 5.2: The effect of isotropic loading on contact properties in the sample with μ_i=0.01 and μ_f=0.3

p' $[kPa]$	e $[-]$	CN $[-]$	F_N $[-]$	F_T $[-]$	$\frac{F_T}{F_N}$ $[-]$	G_{max} $[MPa]$
50	0.58	5.88	0.0726	0.0046	0.0629	148.1
100	0.58	5.97	0.1424	0.0042	0.0292	192.2
200	0.58	6.04	0.2806	0.0051	0.0181	249.4
300	0.58	6.08	0.4168	0.0059	0.0143	287.9

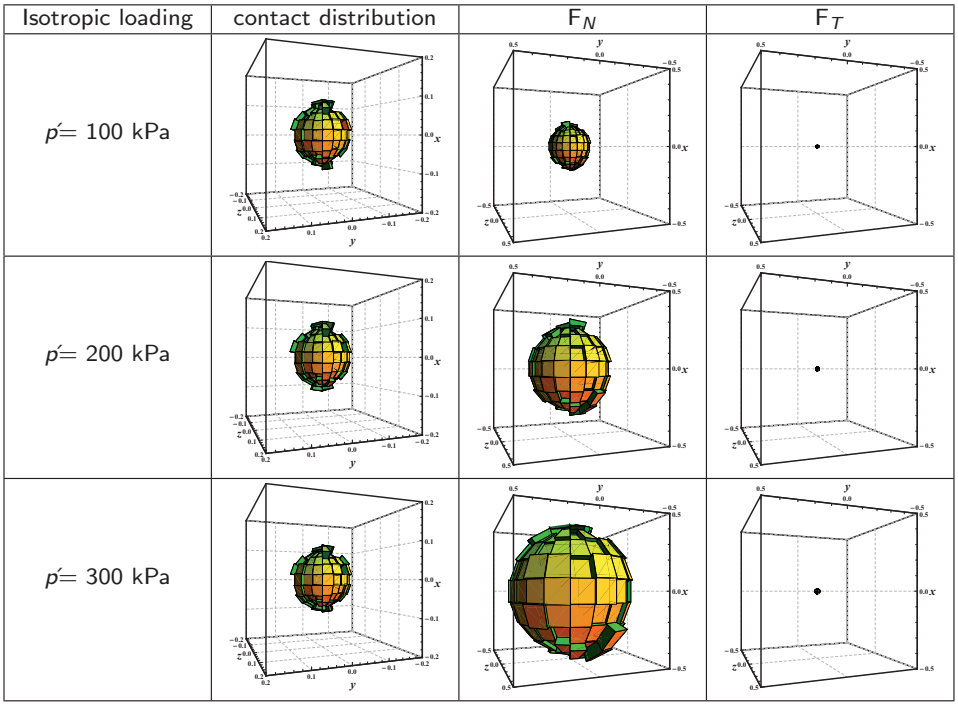

Figure 5.16: The effect of isotropic pressure on contact properties of dense glass bead packing, $\mu_i = 0.01$ and $\mu_f = 0.3$

Table 5.3: The effect of stress induced anisotropy on contact parameters in the sample with μ_i=0.01 and μ_f=0.3, stress path GB-I

σ_3 $[kPa]$	σ_1 $[kPa]$	q $[kPa]$	e $[-]$	CN $[-]$	F_N $[-]$	F_T $[-]$	$\frac{F_T}{F_N}$ $[-]$	G_{max} $[MPa]$
200	200	0	0.58	6.04	0.2951	0.0123	0.0417	249.4
200	250	50	0.58	6.03	0.3042	0.0224	0.0735	259.6
200	300	100	0.58	5.98	0.3297	0.0402	0.1219	265.6
200	350	150	0.58	5.82	0.3635	0.0549	0.1511	256.3
200	400	200	0.58	5.53	0.4116	0.0698	0.1695	232.2
200	420	220	0.58	5.33	0.4407	0.0775	0.1759	201.6

Table 5.4: The effect of stress induced anisotropy on contact parameters in the sample with μ_i=0.01 and μ_f=0.3, stress path GB-II

σ_3 $[kPa]$	σ_1 $[kPa]$	q $[kPa]$	e $[-]$	CN $[-]$	F_N $[-]$	F_T $[-]$	$\frac{F_T}{F_N}$ $[-]$	G_{max} $[MPa]$
50	100	50	0.58	5.07	0.1156	0.0191	0.1651	110.49
100	200	100	0.58	5.32	0.2157	0.0360	0.1670	166.07
150	300	150	0.58	5.37	0.3206	0.0538	0.1678	193.40
200	400	200	0.58	5.53	0.4115	0.0698	0.1695	232.20
220	440	220	0.58	5.56	0.4509	0.0766	0.1698	240.73
300	600	300	0.58	5.50	0.6214	0.1047	0.1686	261.44

The obtained values for CN, F_N and F_T for stress path GB-I are summarized in Table 5.3. As can be seen in Table 5.3, coordination number and F_T/F_N are significantly affected by stress induced anisotropy at stress path GB-I. The results show the decreasing of coordination number and increasing of F_T/F_N with an increase in the vertical stress which have the negative effect on the shear stiffness of packing.

The results of DEM analysis for stress path GB-II are summarized in Table 5.4. As can be seen in Table 5.4, coordination number increases with an increase in the value of q at this stress path. Furthermore, the results show that the effect of stress induced anisotropy on the value of F_T/F_N is not significant in comparison with the stress path GB-I.

The effect of stress induced anisotropy on maximum shear modulus can be explained

through the effect of stress state on contact properties which are presented for stress paths GB-I and GB-II in Figure 5.17 and Figure 5.18 respectively.
Figure 5.17 reveals that the normal contact forces in the vertical direction increases significantly with an increase in the vertical stress, σ_1. However, the value of normal contact forces in horizontal direction was constant and equal to the obtained normal contact forces for specimen subjected to isotropic loading. Also, this figure shows the increasing of shear contact forces (F_T) with an increase in the vertical stress. The other micro-mechanical parameter, contact distribution, is also affected with vertical stress. The results show that the contact distribution is oriented to the vertical direction at this stress path.
Figure 5.18 shows the effect of stress induced anisotropy on contact parameters at stress path GB-II. As can be seen in this figure, the normal contact forces increases significantly in all of the directions with an increase in the shear stress, q.
Also, Figure 5.18 shows that the shear contact forces (F_T) increases with an increase in the vertical stress. The contact distributions are oriented to the vertical direction and has the same orientation for all of the stress states at this stress path.
The experimental and numerical results on glass bead packing revealed that the maximum shear modulus was affected by stress induced anisotropy which was strongly depended on the applied stress paths. For explaining the $G_{max} - q$ curves, Figure 5.9, the effect of stress induced anisotropy on contact properties are compared in some given stress states, e.g. at q equal to: 50, 100, 150 and 220kPa.

Table 5.5: The effect of stress induced anisotropy on contact parameters

q $[kPa]$	stress path $[-]$	CN $[-]$	F_N $[-]$	F_T $[-]$	$\frac{F_T}{F_N}$ $[-]$	G_{max} $[MPa]$
50	GB-I	6.032	0.3042	0.0224	0.0735	259.6
	GB-II	5.0672	0.1156	0.01908	0.1650	110.491
100	GB-I	5.979	0.329	0.04018	0.12186	265.6
	GB-II	5.324	0.2157	0.03588	0.1663	166.0691
150	GB-I	5.821	0.3635	0.0549	0.1511	256.3
	GB-II	5.529	0.3208	0.05378	0.1676	193.4
220	GB-I	5.327	0.4407	0.0775	0.1759	201.06
	GB-II	5.557	0.4511	0.07656	0.1697	240.73

At q=50 kPa, in Figure 5.9, the value of G_{max} at stress path GB-II is less than the obtained value for G_{max} at the same shear stress for stress path GB-I. The results of DEM simulation for this stress state are summarized in Table 5.5. As can be seen in this table, at the shear stress of 50 kPa the value of coordination number, CN, and normal contact force at stress path GB-II are less than stress path GB-I and shear contact force is also more than stress path GB-I, therefore, the stiffness is less than the stress path GB-I at this stress stat. As can be seen in Figure 5.9, for shear stress of 100 and 150 kPa, the value of G_{max} at stress path GB-II is less than the obtained values for G_{max} at the same shear stress for stress path GB-I.

$q[kPa]$	contact distribution	F_N	F_T
q=50	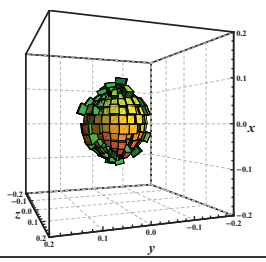	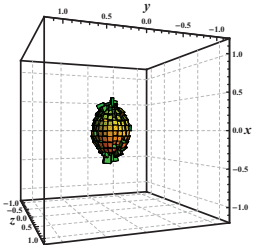	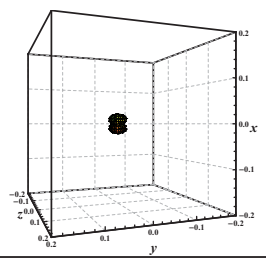
q=100	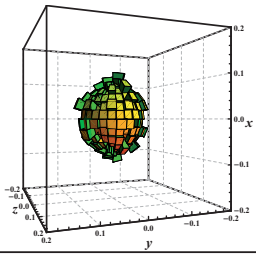	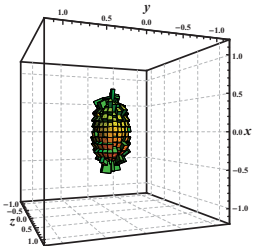	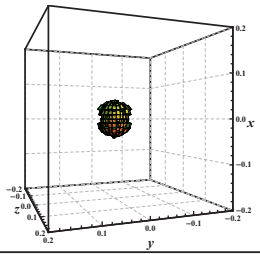
q=150	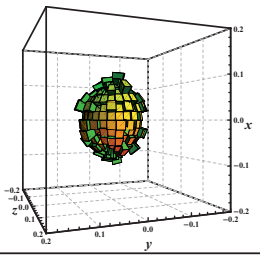	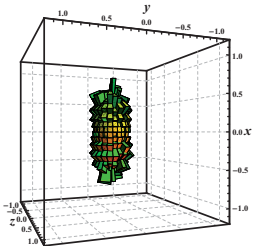	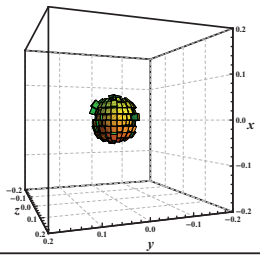
q=220	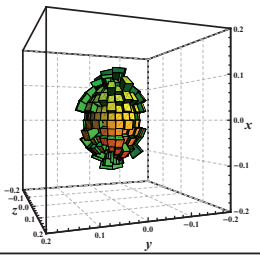	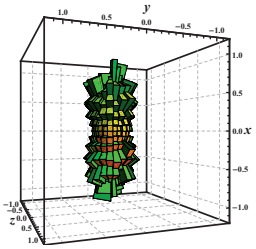	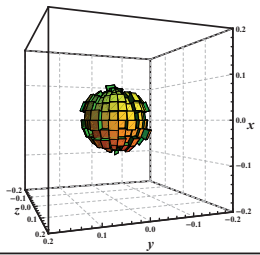

Figure 5.17: Polar presentation of contact properties in specimen subjected to stress path GB-I

At the shear stress of 100 and 150 kPa, the value of CN at stress path GB-I is more than stress path GB-II and also the value of F_T/F_N for the stress path GB-I is less than GB-II, therefore, the value of G_{max} at stress path GB-I is more than obtained value at stress path GB-II.

As can be seen in Figure 5.9, at shear stress of 220 kPa, the value of G_{max} at stress path GB-I is less than the obtained values for G_{max} at the same shear stress at stress path GB-II. At the shear stress of 220 kPa, as can be seen in Table 5.5, the value of CN at stress path GB-II is more than stress path GB-I and also the value of F_T/F_N for the stress path GB-II is less than GB-I, therefore, G_{max} at stress path GB-I is less than G_{max} at stress path GB-II.

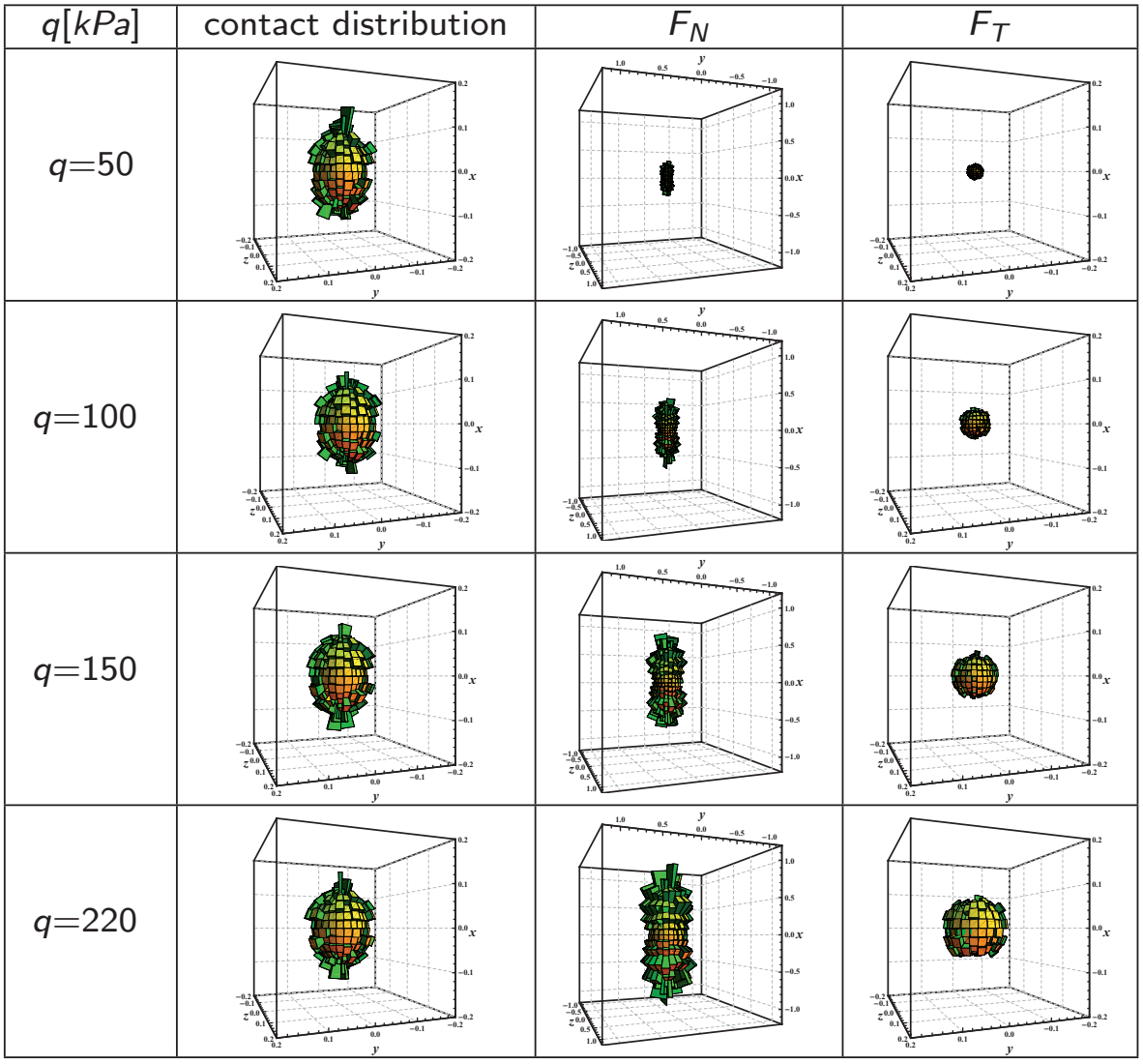

Figure 5.18: Polar presentation of contact properties in specimen subjected to stress path GB-II

5.2.7 Summary

A set of experiments was performed on glass beads samples by using a resonant column device under different stress paths, namely isotropic compression, triaxial compression (GB-I) and constant stress ratio K deformation (GB-II). The results revealed:

- The maximum shear modulus was a function of the stress induced anisotropy, as determined for the specific stress paths. That was the variation of G_{max} with isotropic/deviatoric stress was not unique but depends on the previous history. Existing analytical relations fail in describing this extra dependence, either when Hardin's relationship is used or the contribution of (induced) deviatoric stress is included through Roesler's relation. Along with laboratory tests, DEM simulations were performed and proposed a micro-mechanical interpretation of the peculiar behavior observed.

- It is apparent from experimental results that the maximum shear modulus was significantly affected with stress induced anisotropy at different stress paths. Therefore, DEM analysis were conducted on a granular packing to find the effect of stress induced anisotropy on contact properties for various stress paths. From macroscopic point of view, the maximum shear stiffness of granular packing increased with an increase in the mean effective stress which was due to the increasing of the normal contact forces at contact points from the microscopic point of view.

- DEM results revealed that Coordination Number, CN, is affected significantly by sample preparation. Starting from the numerical observations a modified version of Hardin's relationship is proposed, that included a dependence of the maximum shear modulus on the coordination number.

- The results show that the effect of stress induced anisotropy on maximum shear modulus strongly depends on the applied stress path. The experimental and numerical results revealed that at the same q, maximum shear modulus is different in the specimens which are consolidated at stress paths GB-I, GB-II. Micro-mechanical observations show that the increasing of F_T/F_N and decreasing of coordination number in stress path GB-I is faster than the other stress path. Therefore, with reference to Equation 5.10, the stiffness decreases with an increase in the vertical stress in this stress path. Furthermore, the DEM results show that the coordination number, CN, and normal contact forces, F_N, increase with an increase in the value of σ_1 at

stress path GB-II and isotropic stress path. Therefore, stiffness increases with an increase in the σ_1 at these stress paths in comparison with stress path GB-I.

- The results at macroscopic level reveal that Roesler's relationship with coordination number function can be used with sufficient accuracy to predict the maximum shear modulus in the specimens subjected to anisotropic loading.

5.3 Hostun sand: Experimental results and empirical relationships

5.3.1 overview

A series of stress induced anisotropic tests were conducted on dry Hostun sand with a relative density of 35%-90% to evaluate the effect of the stress path on small and intermediate strain properties (G_{max}, $G(\gamma)$ and $\eta(\gamma)$). From the experimental study using true triaxial device, Sadek (2006) concluded that the effect of the direction of sand pluviation on maximum shear modulus of Hostun sand is not significant. This means that the effect of pluviation of Hostun sand on the fabric of sample is not significant. Therefore, in this section, all of the samples were prepared by a dry air pluviation method (Section 3.4). Stress induced anisotropy was applied to the samples by different stress paths (Figure 3.14a). The experimental procedure was explained in section 3.6. The main results of this experimental program are presented in this Section. For ease of discussion, this section is divided into three main parts. In part one, the effect of stress induced anisotropy on the small strain properties (G_{max}) of dry Hostun Sand is presented. The effect of stress induced anisotropy on intermediate strain properties ($G(\gamma)$ and $\eta(\gamma)$) of dry Hostun Sand for different stress paths will be discussed in part two. In part three, the effect of stress induced anisotropy on the reference shear strain, γ_r, (Equation 2.10) will be presented. These results are used to develop an empirical relationship to predict the value of G/G_{max} of samples subjected to stress induced anisotropy.

5.3.2 Test results on G_{max}

The effects of void ratio and stress induced anisotropy on the maximum shear modulus (G_{max}) of dry Hostun Sand are explained in this section. Adopted stress paths are the same as Figure 3.14a.

- **Stress path I**

The experimental results for this stress path are presented in Figure 5.19. The test data in Figure 5.19a reveal that the value of G_{max} increases with an increase in the shear stress, q, for this stress path. Also, the significant effect of confining pressure on the maximum shear modulus can be concluded from Figure 5.19a.
Figure 5.19b reveals that G_{max} decreases with an increase in the void ratio, e. The experimental test data for stress path I show that the density of sample not only changes

the value of G_{max} but can also have an effect on the trend of the $G_{max} - q$ curve in comparison with the dense sample. As can be seen in Figure 5.19b, the maximum shear modulus, G_{max}, increases with an increase in q up to q of 300 kPa, but the slope of the $G_{max} - q$ curve of the loose sample (e=0.91) is different to the dense sample (e=0.71) for q of more than 300 kPa. G_{max} was normalized with respect to the G_{max} obtained for isotropic loading. This normalization is helpful to show the effect of density on the trend of the observed results.

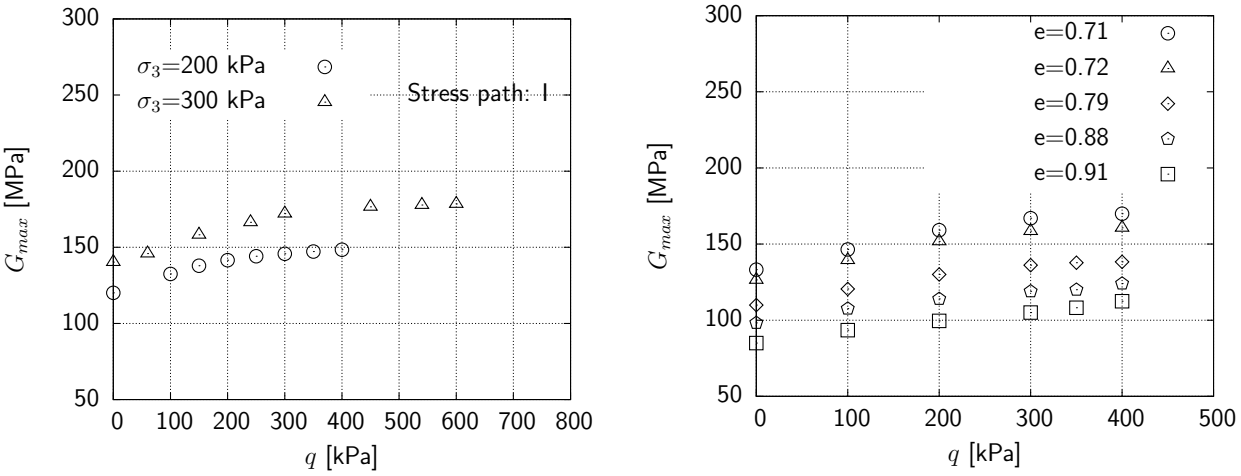

(a) (b)

Figure 5.19: $G_{max} - q$ curves for stress path I: (a) the effect of σ_3, $e = 0.73$; (b) the effect of the void ratio

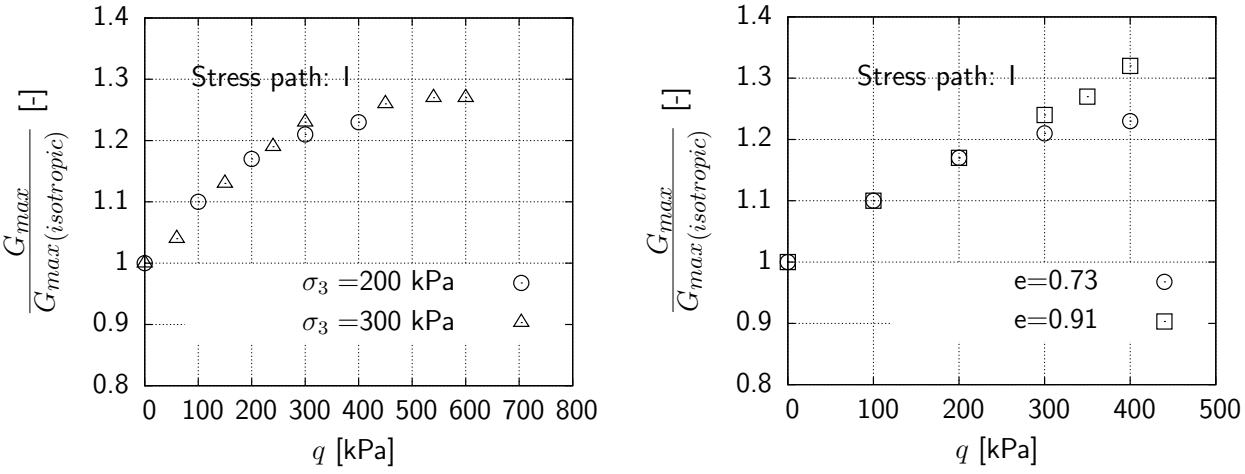

(a) (b)

Figure 5.20: $\frac{G_{max}}{G_{max(isotropic)}} - q$ curves for stress path I: (a) the effect of σ_3, $e = 0.73$; (b) the effect of the void ratio

Figure 5.20a shows normalized G_{max} versus q in the samples with a void ratio of 0.73. This figure shows that the effect of isotropic confining pressure on the trend of normalized G_{max} versus q is not significant. However, Figure 5.20b shows the significant effect of density on results which is due to the effect of anisotropic loading on the fabric of the samples. For instance, during anisotropic loading, due to the compaction of loose sample, the value of the coordination number increases faster and, consequently, the maximum shear stiffness increases faster than the dense sample.

- **Stress path II**

The experimental test results for stress path II are presented in Figure 5.21. As it is apparent from Figure 5.21a, the value of G_{max} increases slightly with an increase in the q and it then decreases significantly with a further increase in q ($q > 0.7p'$). This figure also shows that the value of G_{max} is significantly affected by p'. The test data show that the value of G_{max} increases with an increase in the value of p' (Figure 5.21a). Furthermore, the test results show that the value of G_{max} decreases with an increase in the void ratio (Figure 5.21b) although the trend of results for the loose and dense samples is obviously different, especially for $q > 0.7p'$ for this stress path. This difference is due to the change of coordination number and void ratio, during the compaction of the sample, which has a direct effect on the value of G_{max}.

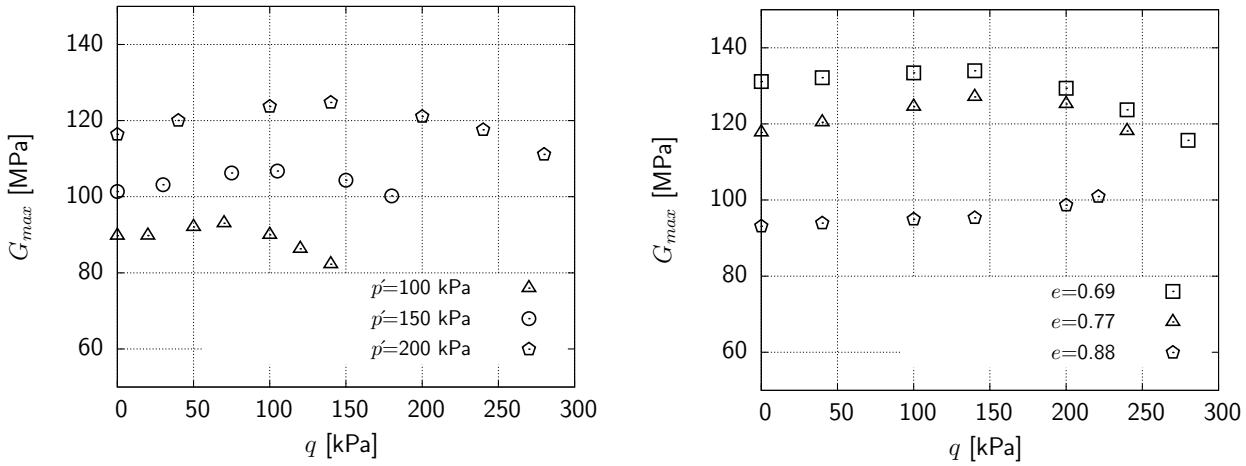

Figure 5.21: $G_{max} - q$ curves for stress path II: (a) the effect of p' , $e = 0.73$; (b) the effect of the void ratio (K=0.5)

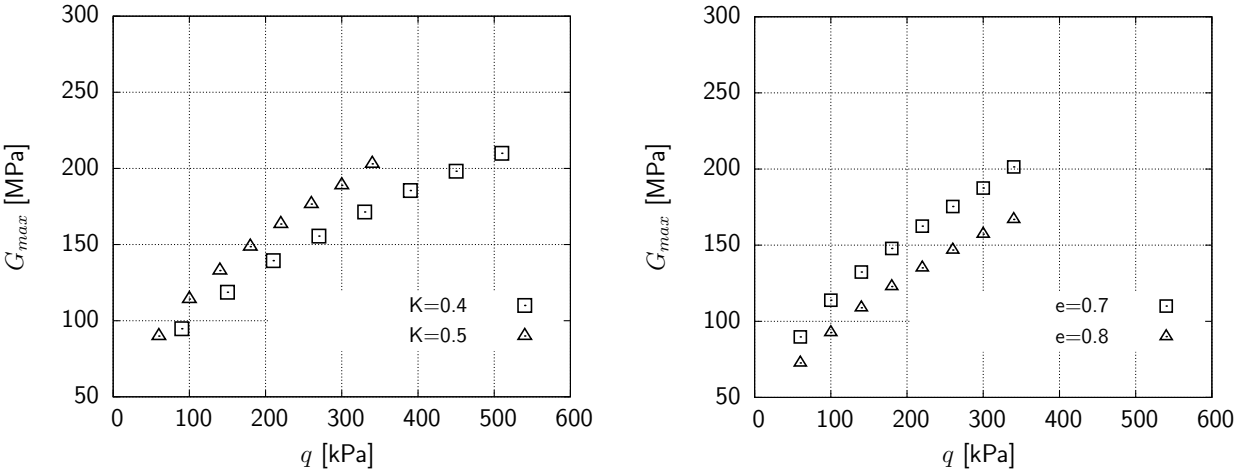

(a) (b)

Figure 5.22: $G_{max} - q$ curves for stress path III: (a) the effect of $K = \sigma_h/\sigma_v$, $e = 0.71$; (b) the effect of the void ratio

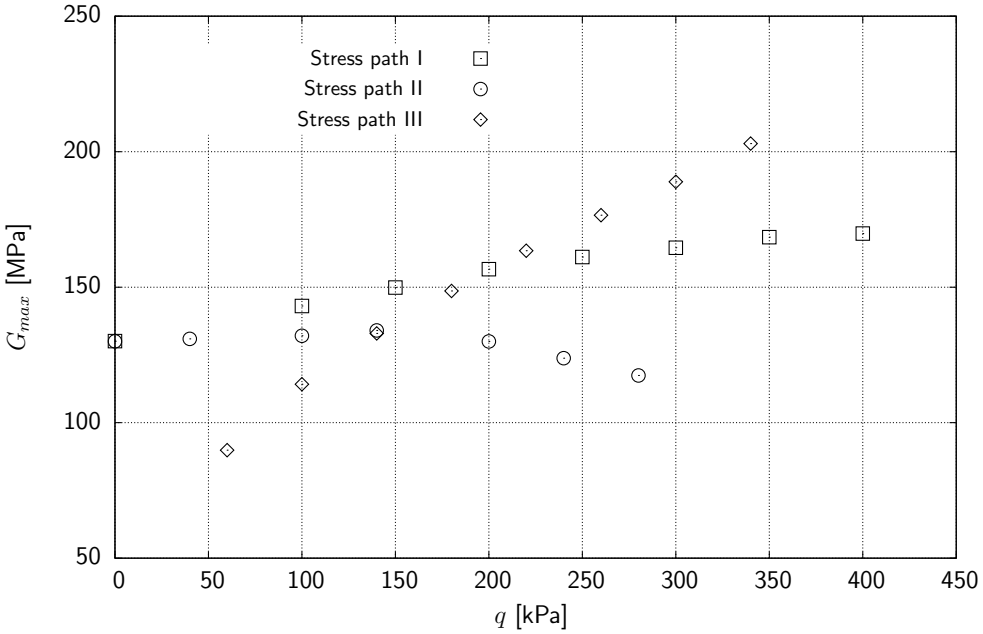

Figure 5.23: G_{max} versus q for Hostun Sand with $e_0 = 0.72$ and stress paths I, II and III

- **Stress path III**

Figure 5.22 presents the effect of stress induced anisotropy on the maximum shear modulus for stress path III. As is apparent from Figure 5.24a, the value of G_{max} increases significantly with an increase in the value of q for this stress path. This figure shows that

the value of G_{max} increases with an increase in the stress ratio, $K = \sigma_h/\sigma_v$. Furthermore, the experimental results at stress path III show that the value of G_{max} decreases with an increase in the void ratio (Figure 5.22b).
For example, Figure 5.23 shows the effect of stress induced anisotropy at different stress paths on the maximum shear modulus of Hostun Sand with a relative density of 86%. For stress path I, this figure shows that the maximum shear modulus, G_{max}, increases with an increase in the value of q but the rate of increase in G_{max} decreases significantly with q of more than 200 kPa. For stress path II, G_{max} increases slightly with an increase in the value of q, but G_{max} decreases significantly with q of more than 150 kPa ($q > 0.7p'$) (Figure 5.23). For stress path III, experimental results reveal that G_{max} increases as long as q increases (Figure 5.23).

5.3.2.1 Empirical relationship for G_{max}

Hardin's relation (Equation 2.8) and Roesler's relation (Equation 2.9) were used to predict the maximum shear modulus in the soil samples subjected to stress induced anisotropy. Hardin's void ratio function (Equation 4.6) was also used to capture the effect of the void ratio in these relationships. As discussed in Chapter 2, Hardin believed that G_{max} is independent of shear stress. Thus, Equation 2.8 with sufficient accuracy can be used to predict the value of G_{max} but the average of stresses ($\frac{\sigma_1+\sigma_3}{2}$) must be used instead of p'. According to the performed regressions, constant parameters A and n in Hardin's relation (Equation 2.8) were equal to 0.83 and 0.44 respectively (Chapter 4). Roesler's relation (Equation 2.9) includes four constant parameters: x in void ratio function, A constant parameters of Equation 2.9 and stress exponents (n_1 and n_3). Parameters x and A in Roesler's relation were assumed to be the same as the values obtained for Hardin's relation. However, the unknown values of n_v and n_h were determined by regression of the test results for stress path I to get the best value for R^2 (Figure 5.24). Then, the average of the obtained values for the stress exponents, n_3 and n_1, were used to predict the value of G_{max} for stress paths II and III.
The test data for stress path I were used for determining the value of stress exponents in Roesler's relation. G_{max} was normalized with respect to the $Af(e)(\sigma_3^{n_3})$, where A and f(e) were the same as the determined values for Hardin's relation and n_3 was assumed to be a value less than 0.5. Normalized shear modulus were drawn versus vertical stress, σ_1. Figure 5.24a shows an example of normalized shear modulus versus σ_1 for a sample with $e_0 = 0.72$. The value of n_h was changed to get a value close to 1 for K factor in Figure 5.24a.

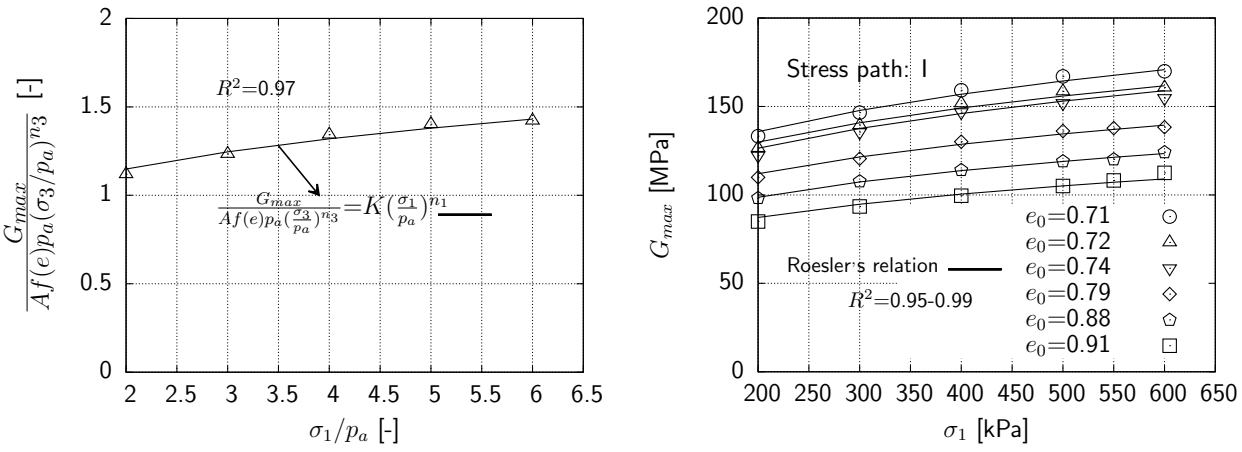

(a) (b)

Figure 5.24: Fitted curves to the experimental data for stress paths I: (a) normalized $G_{max} - \sigma_v$ curve; (b) $G_{max} - \sigma_v$ curves for samples with various densities

This procedure was performed for all of the samples subjected to stress induced anisotropy at stress path I. Figure 5.24b shows the test data for samples with various densities, the solid lines fitted are curves predicted with Roesler's relation. The average value of n_1 and n_3 were used as stress exponents in Roesler's relation. The average value of the stress exponents, n_3 and n_1, in Roesler's relationship (Equation 2.9), were equal to 0.23 and 0.21 respectively which confirms that the effect of confining pressure on the maximum shear modulus is more than the effect of vertical stress.

Figure 5.25a and Figure 5.25b show the value of G_{max}, predicted with Equation 2.8 and Equation 2.9, in comparison with the measured values for stress paths I, II and III. Figure 5.25a shows that both of the relations (Equation 2.8 and Equation 2.9) predict the value of G_{max} with the same accuracy up to the vertical stress of 400 kPa for stress path I and 300 kPa for stress path II. However, at a vertical stress of more than 400 kPa, in a dense sample volumetric changes in the sample was not significant during RC tests, therefore, the rate of increase in the maximum shear modulus was affected by contact forces at a microscopic level (contact force ratio). The impact of shear force can be observed through Equation 2.8 in comparison with Equation 2.9. As can be seen in Figure 5.25a, the accuracy of the predicted G_{max} using Equation 2.9 is more than Equation 2.8, whereas Equation 2.8 is independent of shear stress. In the loose sample due to the compaction of the sample, the coordination number increases which has a direct effect on G_{max}. Therefore, in the loose sample the value of G_{max} increases with an increase in the value of q at stress path I (Figure 5.25a). The same behaviour was observed for samples subjected to stress path II. Figure 5.25b shows an example of measured maximum shear modulus for stress path

III. The results for stress path III (Figure 5.25b) show that Equation 2.8 and Equation 2.9 can be used to predict the value of G_{max} with the same accuracy. Figure 5.26 shows the accuracy of the predicted G_{max} using Equation 2.8 and Equation 2.9 in comparison with the measured values for stress paths I, II and III. Figure 5.26a shows the predicted G_{max} using Equation 2.8 versus measured G_{max} for dry Hostun Sand with a different void ratio.

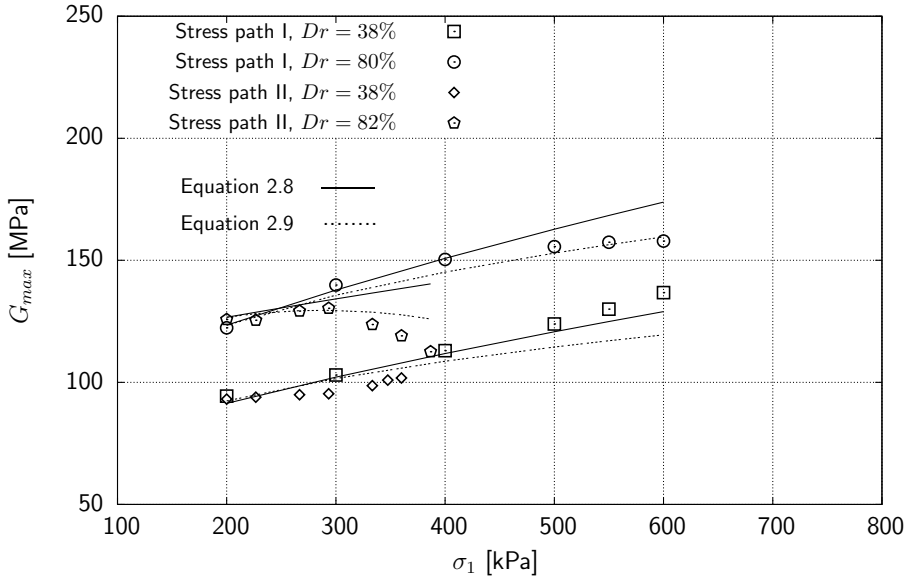

(a)

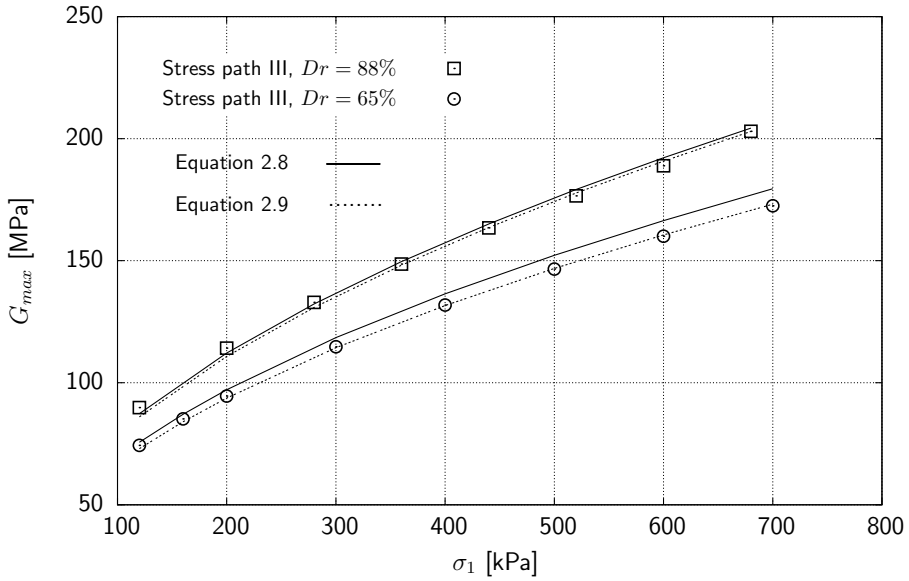

(b)

Figure 5.25: The predicted and measured G_{max} for dry Hostun Sand subjected to: (a) stress paths I and II; (b) stress path III

Figure 5.26b shows the predicted results using Equation 2.9 versus the experimental results. A comparison of Figure 5.26a and Figure 5.26b reveals that the predicted results using Equation 2.9 have a higher accuracy in comparison with the predicted results using Equation 2.8 for stress path I. The same conclusion can be extracted for the other stress paths. However, as can be seen in Figure 5.26e and Figure 5.26f, both of the relationships, Equation 2.8 and Equation 2.9, predict the maximum shear modulus with the same accuracy for stress path III.

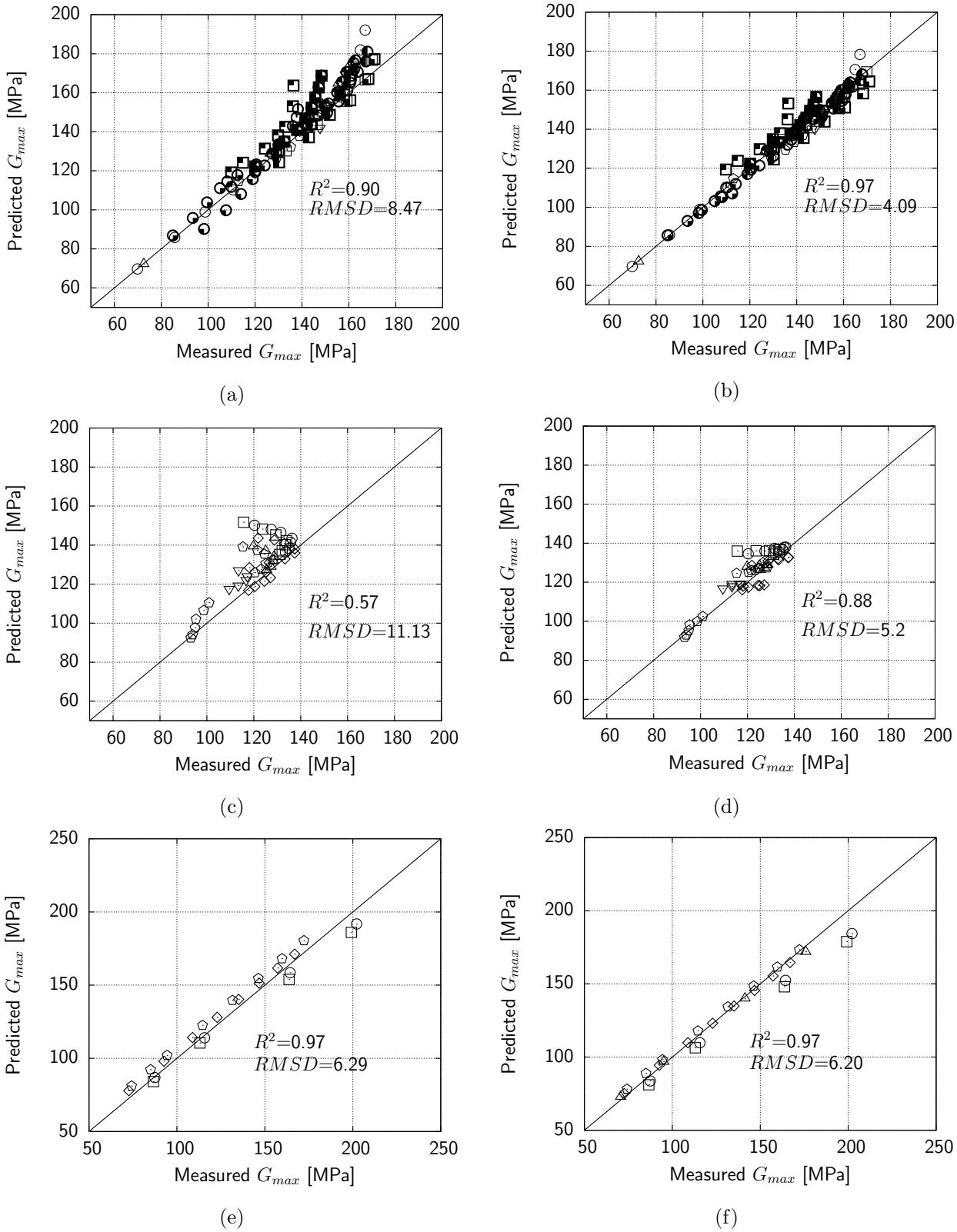

Figure 5.26: The accuracy of predicted G_{max} with empirical relationships and determined fitting parameters based on the test data for stress path I: (a) Hardin's relationship for stress path I; (b) Roesler's relation for stress path I; (c) Hardin's relation for stress path II; (d) Roesler's relation for stress path II; (e) Hardin's relation at stress path III; (f) Roesler's relation for stress path III

5.3.3 Published data sets on G_{max}

The experimental results for G_{max} obtained from the resonant column device have been compared with previous studies in Figure 5.27. It must be noted that the published results for stress path I are presented in this Figure. As can be seen in this figure, the effect of stress induced anisotropy on dense samples for stress path I depends on the stress ratio. Stiffness increases with an increase in vertical stress up to stress ratio 2 and it then decreases with a further increase in vertical stress for this stress path which is in agreement with the observed experimental results in this study.

5.3.4 Test results on $G(\gamma)$

The resonant column tests were conducted on the samples which were consolidated at stress paths I, II and III to assess the effects of stress path and stress induced anisotropy on the curves of damping ratio and modulus ratio.
Figure 5.28 shows the effect of shear strain on the shear modulus of clean Hostun sand with a relative density of $86\% - 90\%$ which were subjected to isotropic and anisotropic stress conditions at stress paths I, II and III respectively.

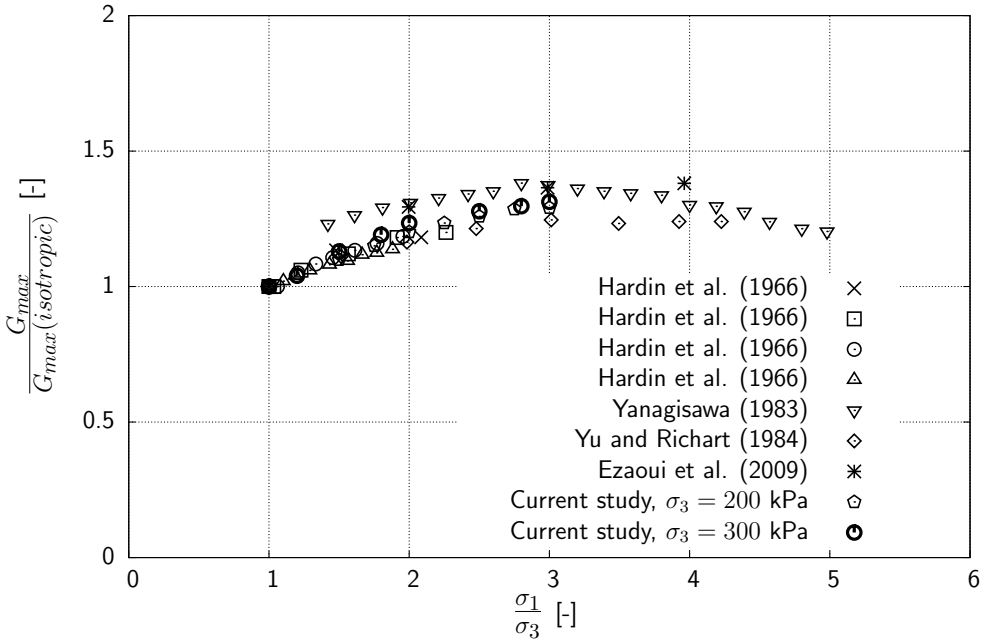

Figure 5.27: Normalized G_{max} versus σ_v/σ_h from the literatures for stress path I in comparison with this study for the same stress path

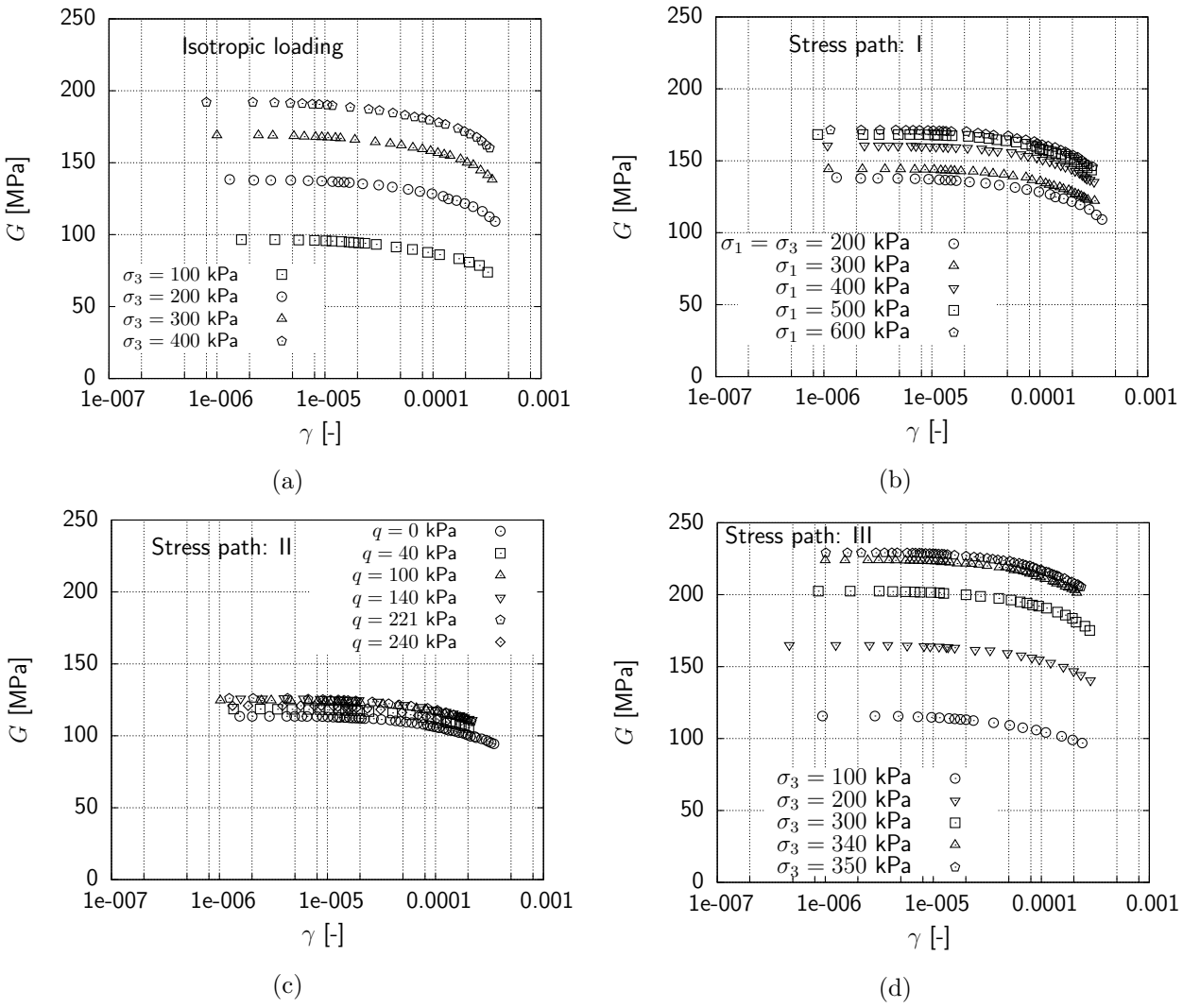

Figure 5.28: G versus shear strain for clean Hostun Sand, Dr=72% − 75%: (a) isotropic loading; (b) anisotropic loading at stress path I; (c) anisotropic loading at stress path II; (d) anisotropic loading at stress path III

Figure 5.28 shows that the shear stiffness is constant and equal to the maximum shear modulus up to the shear strain of 1E-5. Figure 5.28b shows that the shear stiffness increases with an increase in the vertical stress (σ_1) up to the vertical stress of 600 kPa. However, for stress path II (Figure 5.28c), the shear stiffness increases slightly with an increase in the shear stress, up to the shear stress of less than $0.7p'$, and it then decreases with further increases in the shear stress. The results for stress path III (Figure 5.28d) show the shear stiffness increases with an increase in the confining pressure at this stress path. Additionally, the presented results show the dependency of shear stiffness on the shear strain in the samples subjected to the anisotropic loading for stress paths I, II and

III.

Figure 5.29 shows the effect of stress induced anisotropy on the damping ratio versus the shear strain for isotropic and anisotropic loading at stress paths I, II and III respectively. For isotropic loading, the experimental test data show that damping ratio decreases significantly with an increase in the confining pressure (Figure 5.29a). Figure 5.29b shows the effect of stress induced anisotropy on damping ratio for stress path I. The results show that damping ratio decreases slightly with an increase in the vertical stress. Figure 5.29c shows that the effect of shear stress on damping ratio for stress path II.

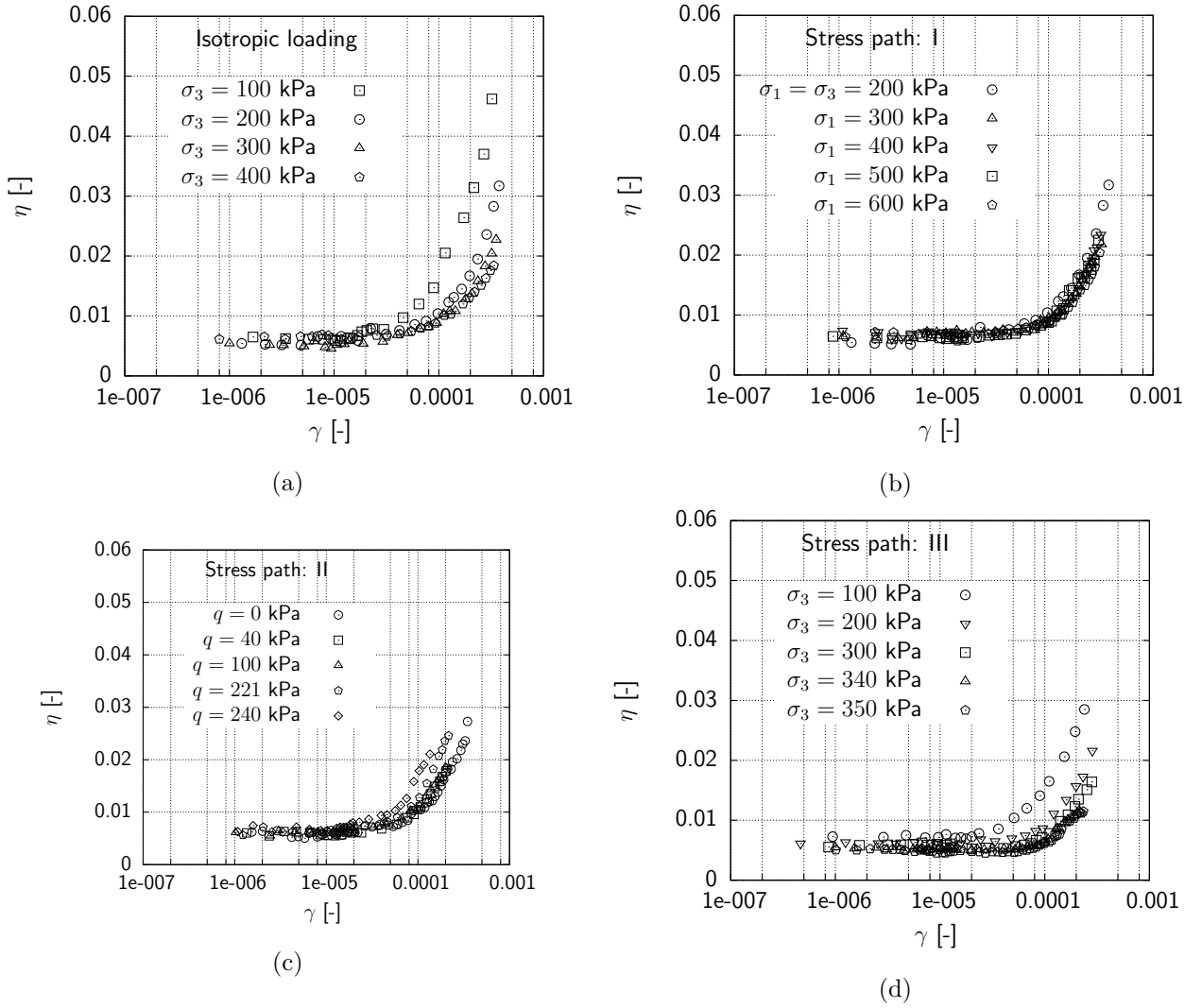

Figure 5.29: Damping ratio, η, versus shear strain for clean Hostun Sand, Dr=72% – 75%: (a) isotropic loading; (b) anisotropic loading at stress path I; (c) anisotropic loading at stress path II; (d) anisotropic loading at stress path III

The results reveal that damping ratio decreases slightly with an increase in the shear stress up to shear stress of 40 kPa and it then increases with further increase in the shear stress (Figure 5.29c). For stress path III, however, the damping ratio decreases with an increase in the confining and vertical stress (Figure 5.29d). As it is apparent from Figure 5.29, the effect of stress induced anisotropy on damping ratio for isotropic loading and stress path III are more obvious than stress paths I and II. The relationship between $G/G_{max} - log\gamma$ curves for dry Hostun sand subjected to isotropy and stress induced anisotropy are presented in Figure 5.30. For isotropic loading, the experimental test data show that G/G_{max} increases significantly with an increase in the confining pressure (Figure 5.29a).

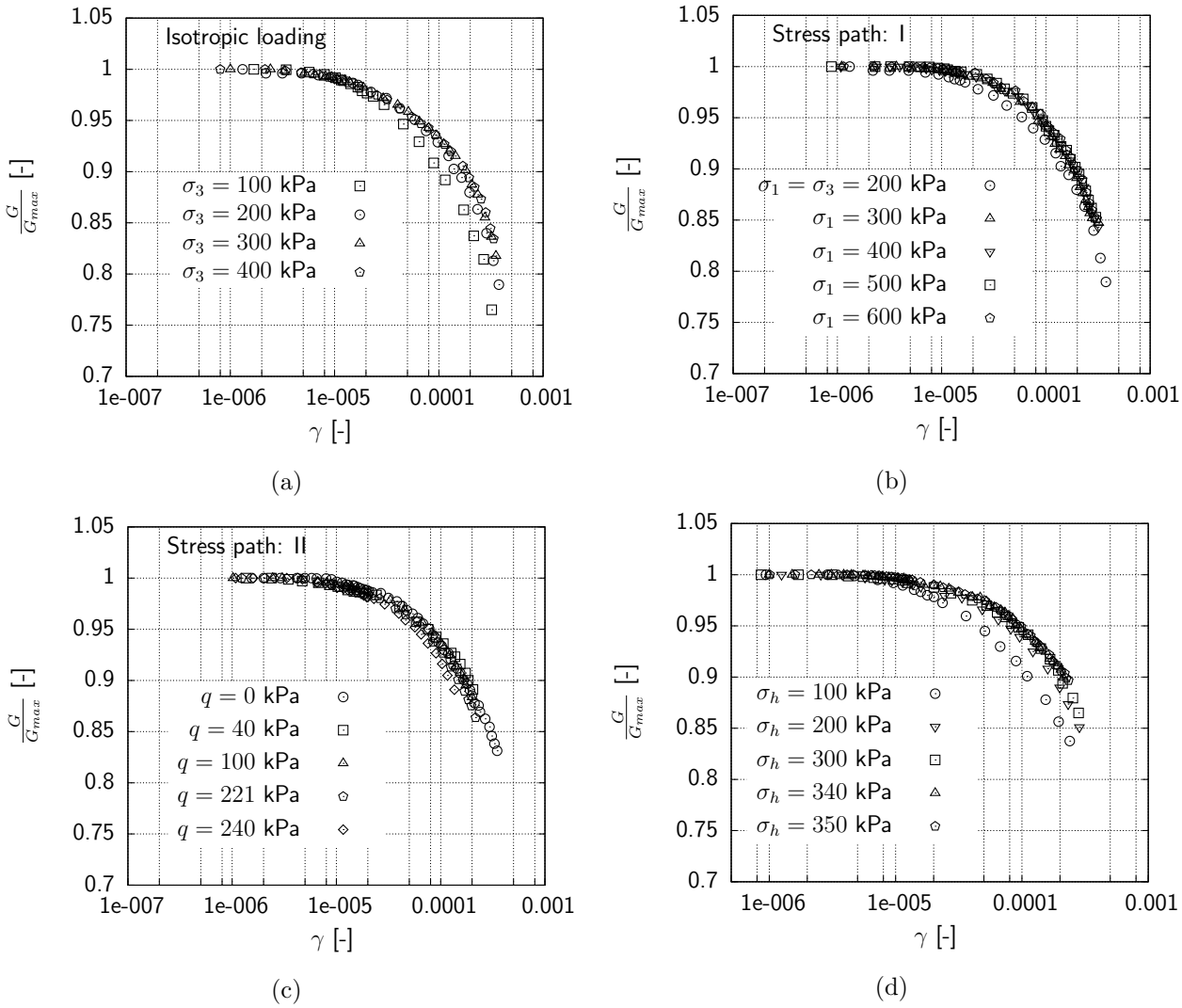

Figure 5.30: G/G_{max} versus shear strain for clean Hostun Sand with Dr=72% – 75% subjected to: (a) isotropic loading; (b) anisotropic loading at stress path I; (c) anisotropic loading at stress path II; (d) anisotropic loading at stress path III

For stress path I, the experimental test data show that $G/G_{max} - log\gamma$ curve was slightly shifted to higher values in comparison with the results for isotropic loading at the confining pressure of 200 kPa (Figure 5.30b). Since the test data are close to each other the effect of stress induced anisotropy on $G/G_{max} - log\gamma$ curves is not so obvious in Figure 5.30b. Figure 5.30c shows the effect of stress induced anisotropy on $G/G_{max} - log\gamma$ curve for stress path II. The results reveal that G/G_{max} increases slightly with an increase in the shear stress up to shear stress of 40 kPa and it then decreases with further increase in the shear stress (Figure 5.30c). For stress path III, however, the G/G_{max} increases with an increase in the confining and vertical stress (Figure 5.30d). Figure 5.30 also shows the

effect of stress induced anisotropy on G/G_{max} for isotropic loading and stress path III are more obvious than stress paths I and II. Figure 5.31 shows the variation of γ_r in respect to σ_1 for all of the applied stress paths.

Figure 5.31 shows that the value of γ_r increases significantly with an increase in the confining pressure. This figure shows that the value of γ_r increases slightly with an increase in the vertical stress in the samples subjected to anisotropic loading at stress path I. As can be seen in Figure 5.31, at stress path II, the value of γ_r increases slightly with an increase in the shear stress up to shear stress of less than 40 kPa and it then decreases significantly with an increase in the shear stress. The value of γ_r increases with an increase in the confining pressure for the sample subjected to stress path III (Figure 5.31).

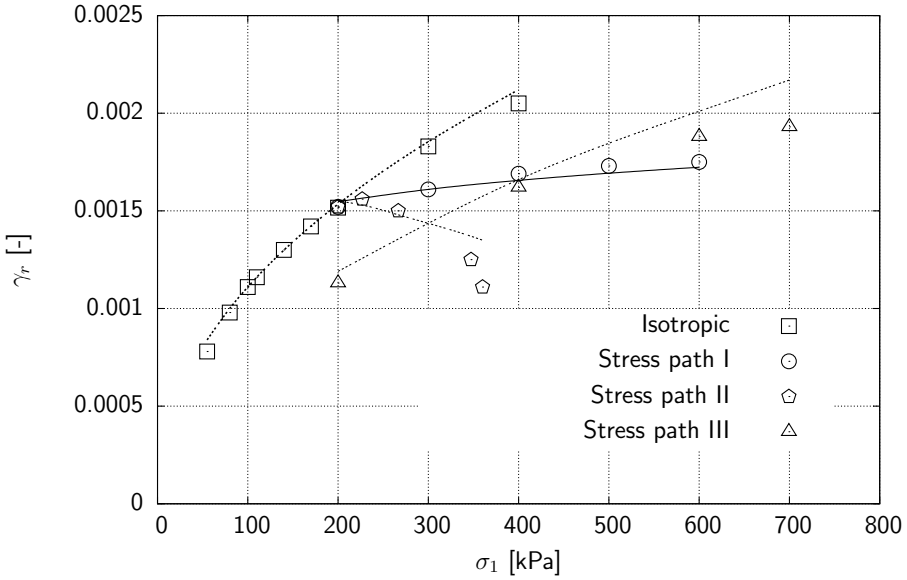

Figure 5.31: The effect of stress induced anisotropy on reference shear strain

5.3.4.1 Empirical relationship

Equation 2.13 and Equation 2.14 are not valid to determine the value of γ_r for samples subjected to the anisotropic loading at stress path I (Tatsuoka et al. 1979). Therefore, the back analysis of the test data, using Equation 2.10, was used to determine the value of γ_r from the experimental test data for sample subjected to the isotropic and anisotropic loading.

Equation 2.15 was used to predict the value of γ_r in the samples subjected to anisotropic loading. This relation is based on the mean effective stress (p'). However, the experimental

test data show that the value of γ_r is affected by shear stress at various stress paths (Figure 5.31). Therefore, in this study, Equation 2.15 was modified as a function of principle stress components instead of mean effective stress (Equation 5.11):

$$\gamma_r = \gamma_{r1} \left[\frac{\sigma_1^{'}}{p_a}\right]^{m_1} \left[\frac{\sigma_3^{'}}{p_a}\right]^{m_3} \tag{5.11}$$

where, γ_r is the reference shear strain, γ_{r1} is the reference shear strain for isotropic loading at p'= 100 kPa, σ_1 and σ_3 are the maximum and minimum principle stress components respectively, and m_1 and m_3 are exponents of vertical and horizontal stresses respectively. Equation 5.11 was used to predict the value of γ_r for samples subjected to isotropic and anisotropic loading at different stress paths. γ_{r1} is the value of γ_r for a certain isotropic pressure (p'=100 kPa). Afterwards, Equation 5.11 was fitted to the data for stress path I in Figure 5.31 to find the parameters m_1 and m_h (solid line in Figure 5.31). By performing this regression, the values of 0.08 and 0.31 were obtained for m_1 and m_3 respectively. Determined fitting parameters (m_1 and m_3) for stress path I were used in Equation 5.11 to predict the value of γ_r for a sample subjected to the other stress paths (dashed lines, in Figure 5.31). As can be seen in Figure 5.31, the results show a good agreement between the predicted and measured values.

5.3.4.2 Prediction of G/G_{max}

The normalized shear strain, γ/γ_r, is the key parameter to predict the G/G_{max} using Equation 2.10 and Equation 2.12. To predict the G/G_{max} for the sample subjected to anisotropic loading, the shear strain was normalized with respect to the γ_r which was obtained from Equation 5.11.

Figure 5.32 shows the G/G_{max} curves versus the normalized shear strain for the samples subjected to the isotropic (Figure 5.32a) and anisotropic loading (Figure 5.32b, Figure 5.32c and Figure 5.32d). In Figure 5.32, the solid lines are the predicted results using Equation 2.12, where the fitting parameters a and b were equal to 0.05 and 1, and γ_r was determined with Equation 5.11. Figure 5.33 shows the damping ratio versus the normalized shear strain for all of the stress paths (Isotropic (Figure 5.33a), anisotropic loading (Figure 5.33b, Figure 5.33c and Figure 5.33d)). The predicted curves, using Equation 2.16, have been added as a solid lines in these figures. The values of η_{min}, c_1 and c_2 in Equation 2.16 were equal to 0.0102, 0.393 and 0.808 respectively. The results show a good agreement between predicted and measured results.

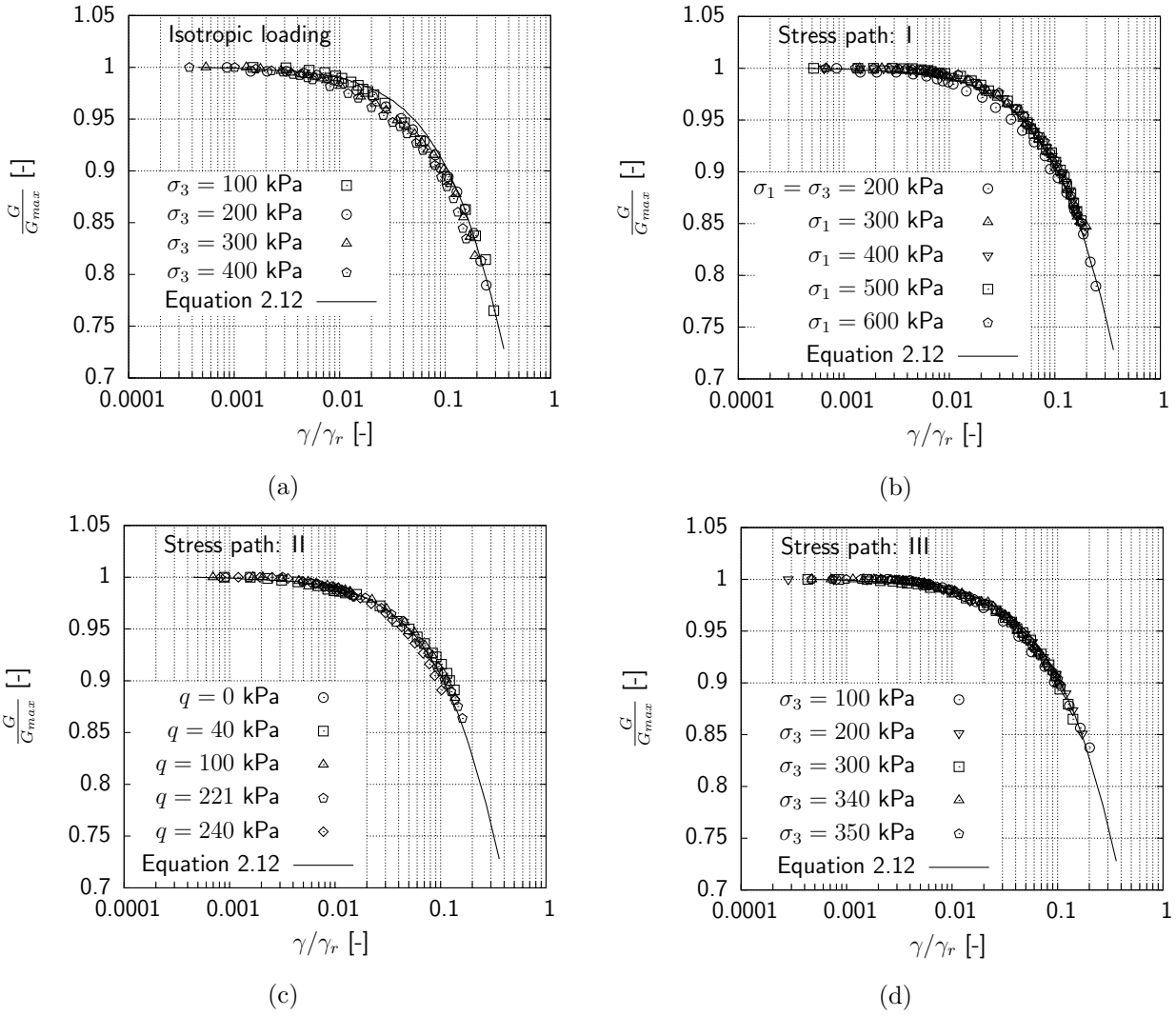

Figure 5.32: G/G_{max} versus normalized shear strain of clean Hostun Sand with Dr=72% − 75% and subjected to: (a) isotropic loading; (b) anisotropic loading at stress path I; (c) anisotropic loading at stress path II; (d) anisotropic loading at stress path III

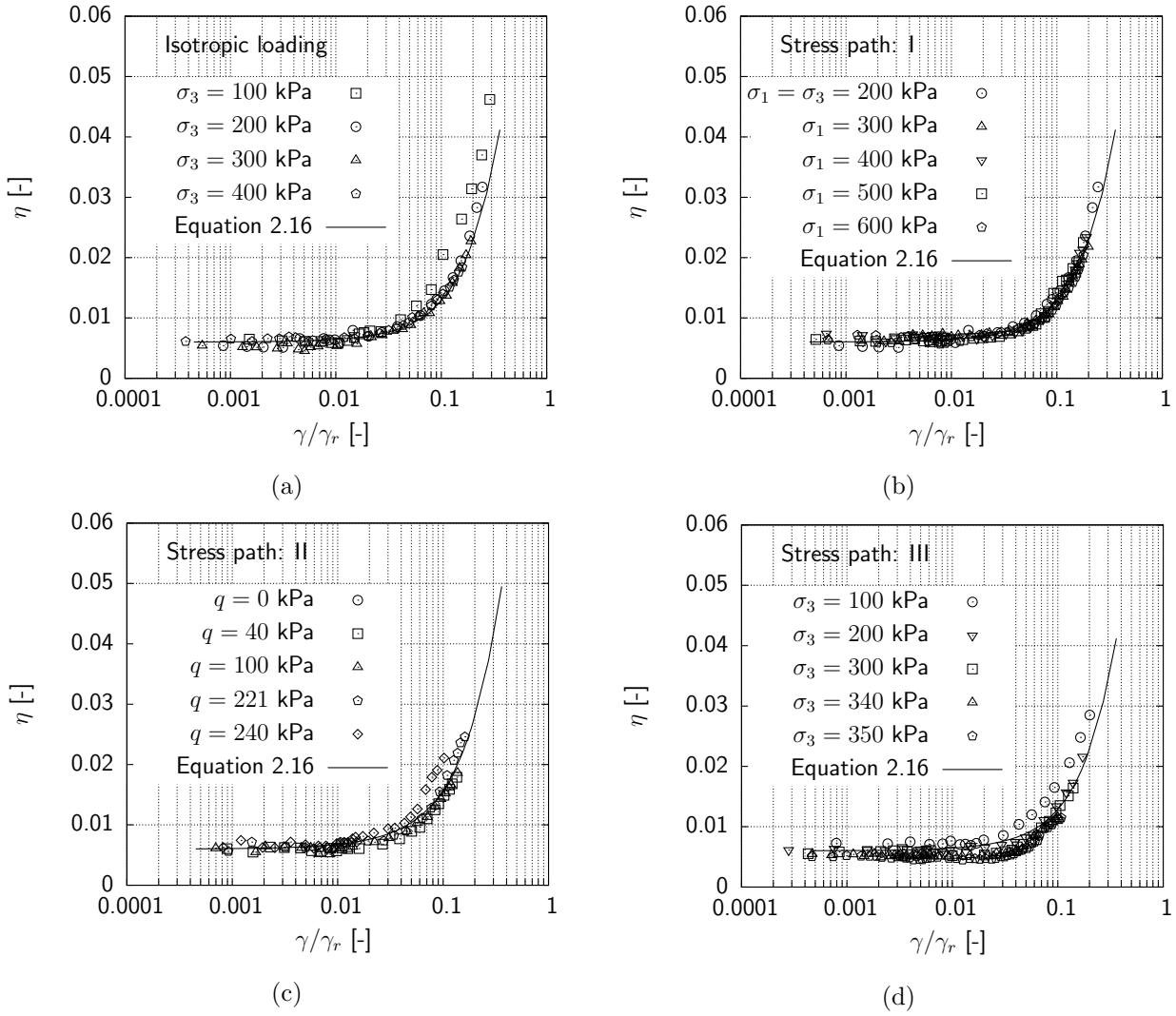

Figure 5.33: Damping ratio, η, versus normalized shear strain for clean Hostun Sand with Dr=72% − 75% and subjected to: (a) isotropic loading; (b) anisotropic loading at stress path I; (c) anisotropic loading at stress path II; (d) anisotropic loading at stress path III

5.3.5 Summary

The stress induced anisotropic tests were conducted on Hostun sand specimens. In this experimental study, Hostun Sand was subjected to four main stress paths: isotropic, stress path I, stress path II and stress path III. For isotropic loading confining pressure was increased from 55 kPa to 200 kPa. For stress path I, confining pressure (σ_3) was kept constant at 200 kPa and vertical stress was increased. For stress path II, p' was kept constant at 200 kPa and q was increased and finally, for stress path III, confining pressure was increased to 100, 200 and 300 kPa then, the vertical stress was increased up to $\sigma_1 = 2\sigma_3$. After that, the resonant column tests were conducted on the samples.
Measured results for induced anisotropy tests on dry Hostun sand under three different stress paths were presented in this work. Experimental results showed that the impact of stress induced anisotropic on small and intermediate strain properties of dry Hostun sand (G_{max}, $G(\gamma)$ and $\eta(\gamma)$) depends on the adopted stress path. In stress path I, the effect of stress ratio was significant on G_{max} but the influence of stress ratio on G/G_{max} and damping ratio was not significant. At stress path II and III, G_{max}, $G(\gamma)$ and $\eta(\gamma)$ were significantly affected by stress induced anisotropy. The experimental results on Hostun sand samples showed the significant effect of density on maximum shear modulus of sample subjected to stress induced anisotropy although the effect of density on G/G_{max} and η was not significant.

6 Conclusions and recommendations

6.1 The effect of fines content

Resonant column tests were conducted on clean Hostun Sand to evaluate the influence of confining stress, p', and void ratio, e, on G_{max}, $G(\gamma)$ and $\eta(\gamma)$. Then the effect of fines on G_{max}, $G(\gamma)$ and $\eta(\gamma)$ was investigated with a systematic increase in fines content, f_c up to 40%. The major outcomes of the study are:

- A decrease in G_{max} with an increase in e and an increase in G_{max} with an increase in p' was observed for clean Hostun Sand. Hardin's relation is adequate to predict G_{max} with both Hardin's and Jamiolkowski's void ratio function, $f(e)$. A systematic increase in fines content, f_c up to 40% in RC tests showed that G_{max} decreased with an increase in f_c which is consistent with earlier studies for sand with non-plastic fines.

- A micro-structural study with a micro CT scan revealed that sand with fines develops two different micro-structures: "fines-in-sand" and "sand-in-fines". For "fines-in-sand", fine particles were partially active in the sand force structure and for "sand-in-fines", sand particles were floating in fines particles. The void ratio, e did not represent the same force structure as clean sand and is not suitable for a consistent comparison. The equivalent granular void ratio, e^*, appears to be a consistent state parameter for density.

- The conversion of e to e^* requires two parameters, b and m. b can be obtained from soil grading properties with a fitting parameter λ=0.30 as in Rahman et al. (2008) and m can be obtained from correlation as in Figure 4.19. However, the parameters, λ and m can be further optimized by back analysis. Therefore, five regression analyses were conducted, including Rahman's method that does not require back analysis. The best regression model was obtained when λ and m were back analyzed (regression V). The second best model was obtained when only λ was determined by back analysis of test data (regression III). The back analyzed λ was linearly related

to p' which can be used to predict λ for Hostun sand.
To predict G_{max} as a function of e^* and p', Rahman's relation with the same proposed fitting parameters (regression I) can be used when f_c is less than f_{thr} and the m value is used for f_c greater than f_{thr} (regression II and regression III).

- Jamiolkowski's $f(e)$ gives a better fit than Hardin's $f(e)$ for a large number of data points with f_c. An inverse power function of e appeared to be a better function than a function with a limiting void ratio constant, x.

These conclusions are derived from the test data for gap graded sand with non-plastic fines and may not be applicable to sand with plastic fines.
Furthermore, a series of tests was conducted on glass bead mixtures containing 0, 10, 20, 30, 40 and 50 percentage fine glass beads using the resonant column test and piezoelectric elements. The outcomes of the study are:

- G_{max}, M_{max} and E_{max} in glass bead mixtures decrease with an increase in fines content up to 30% f_c and then decrease with further increase in f_c.
- The conversion of e to e^* requires two parameters, b and m. b was obtained from particle size properties with a fitting parameter λ=0.30 as in Rahman et al. (2008) and m was optimized by back analysis of test data for G_{max}. The results confirmed the applicability of e^* in Hardin's relation to predict the value of G_{max}, M_{max} and E_{max}.
- Micro-CT imaging shows that the number of contacts between coarse particles decreases with an increase in the fines content and therefore, stiffness decreases with fines content.

6.2 Stress induced anisotropy

The small and intermediate strain properties of dry Hostun Sand subjected to three different stress paths were presented in this paper. Experimental results show that the impact of stress induced anisotropic on the small and intermediate strain properties of dry Hostun sand (G_{max}, $G(\gamma)$ and $\eta(\gamma)$) depends on the adopted stress path. In stress path I, the effect of the stress ratio on G_{max} was significant but the influence of the stress ratio on G/G_{max} and damping ratio was not significant. At stress paths II and III, G_{max}, $G(\gamma)$ and $\eta(\gamma)$ were significantly affected by stress induced anisotropy. The experimental

results on Hostun Sand samples show a significant effect of density on the maximum shear modulus of the sample subjected to stress induced anisotropy although the effect of density on G/G_{max} and η was not significant.
The results show that the Stokoe relationship, Equation 2.15, can be used in terms of stress components, Equation 5.11, to predict the value of γ_r in the soil samples subjected to stress induced anisotropy.

6.3 DEM simulations

It is apparent from the experimental and numerical results that the maximum shear modulus was significantly affected by stress induced anisotropy at different stress paths. Therefore, DEM analyses were conducted on granular packings to find the effect of stress induced anisotropy on contact properties at various stress paths. From a macroscopic point of view, the maximum shear stiffness of granular packing increased with an increase in the confining pressure which was due to the increase in the normal contact forces at contact points from the microscopic point of view. Furthermore, the DEM results reveal that Coordination Number, CN, was affected significantly by sample preparation. From the performed regressions, the effect of the coordination number on the maximum shear modulus was captured through the coordination number function in Hardin's relation.
The results show that the effect of stress induced anisotropy on the maximum shear modulus strongly depends on the applied stress path. The experimental and numerical results reveal that for constant q, the maximum shear modulus was different in the specimens which were consolidated at isotropic and anisotropic loading at stress paths GB-I and GB-II. Micro-mechanical observations show that the increase in F_T/F_N and decrease in the coordination number for stress path GB-I was faster than the other stress paths. Therefore, with reference to Equation 5.10, stiffness decreases with an increase in the shear stress in this stress path. Furthermore, the DEM results show that the coordination number, CN, and normal contact forces (F_N) increase with an increase in the value of q at stress path GB-II and the isotropic stress path. Therefore, stiffness increases with an increase in the σ_v at these stress paths in comparison with stress path GB-I. Additionally, the results at the macroscopic level reveal that Roesler's relation with the coordination number function can be used with sufficient accuracy to predict the maximum shear modulus in the specimens subjected to anisotropic loading.

6.4 Suggested future works

This thesis could be developed further in the future. Based on the findings of this study further research is suggested as follows:

- Most of the previous studies have been conducted on the fine in sand mixtures. However, the studies on sand in fine mixtures are rare and additional studies are essential to determine the effects of particle characteristics, e.g. size and shape of fine particles, on the small and intermediate strain properties of granular materials.
- There is no relationship to predict the value of m in e^* for the sand in fine mixture. Therefore, additional systematic studies on the mixtures containing fines content beyond the f_{thr} must be conducted to determine the empirical relation between the parameter m and the particle characteristics of fine and coarse particles.

Bibliography

Afifi, S. S. & Richart, F. E. (1973), 'Stress history effects on shear modulus of soils', *Soils and Foundations* **13**, 77–95.

Amat, A. S. (2007), Elastic stiffness moduli of hostun sand, Master's thesis, Department of Civil Engineering, University of Bristol.

Ashmawy, A. K. & Drnevich, V. P. (1994), 'A general dynamic model for the resonant column/quasi-static torsional shear apparatus', *American Society for Testing and Materials* **17**, 337–348.

Avramidis, A. S. & Saxena, S. K. (1990), 'The modified stiffned drnevich resonant column apparatus', *Soils and Foundations* **30**, 53–68.

Azéma, E., Radjai, F. & Saussine, G. (2009), 'Quasistatic rheology, force transmission and fabric properties of a packing of irregular polyhedral particles', *Mechanics of Materials* **41**, 729–741.

Bai, L. (2011), Preloading Effects on Dynamic Sand Behavior by Resonant Column Tests, PhD thesis, von der Fakultät VI - Planen Bauen Umwelt der Technischen Universität Berlin.

Barrett, P. (1980), 'The shape of rock particles, a critical review', *Sedimentology* **27**, 291–303.

Bartake, P. P. & Singh, D. N. (2007), 'Studies on the determination of shear wave velocity in sands', *Geomech. Geoengng* **2**, 41–49.

Bellotti, R., Jamiolkowski, M., Lo Presti, D. C. & O'Neill, D. A. (1996), 'Anisotropy of small strain stiffness in ticino sand', *Géotechnique* **46**, 115–131.

Benz, T. (2007), Small-strain stiffness of soils and its numerical consequences, PhD thesis, Üniversität Stuttgart.

Birch, F. (1961), 'The velocity of compression waves in rocks to 10 kilobars, part 2.', *Journal of Geophysical Research* **66**, 2199–2224.

Bowden, F. & Tabor, D. (1950), *The friction and lubrication of solids*, Clarendon Press, Oxford.

Brandt (1955), 'A study of the speed of sound in porous media', *Journal of Applied Mechanics* **22**, 479–486.

Bui, M. T. (2009), Influence of some particle characteristics on the small strain response of granular material, PhD thesis, University of Southampton , School of Civil Engineering and the Environment.

Carraro, J. A. H., Prezzi, M. & Salgado, R. (2009), 'Shear strength and stiffness of sands containing plastic of nonplastic fines', *Journals of Geotechnical and Geoenviromental Engineering* **135**, 1167–1178.

Cascante, G. & Santamarina, C. (1996), 'Interparticle contact behavior and wave propagation', *Journal of Geotechnical Engineering* **122**, 831–839.

Cascante, G., Santamarina, C. & Yassir, N. (1998), 'Flexural excitation in a standard torsinal-resonant column device', *Canadian Geotechnical Journal* **35**, 478–490.

Cascante, G., Vanderkooy, J. & Chung, W. (2005), 'A new mathematical model for resonant-column measurements including eddy-current effects', *Canadian Geotechnical Journal* **42**, 121–135.

Chang, C. & Liao, C. (1994), 'Estimates of elastic shear modulus for randomly packed granule', *Applied Mechanics Reviews* **47**, 197–206.

Chang, H., Cho, G. C., Lee, J. G. & Kim, L. H. (2006), 'Characterization of clay sedimentation using piezoelectric bender elements', *Engineering Materials* **321**, 1415–1420.

Chien, L. K. & Oh, Y. N. (1998), 'Influence on the shear modulus and damping ratio of hydraulic reclaimed soil in west taiwan', *Journal of Offshore and Polar Engineering* **8**, 228–235.

Chien, L. K. & Oh, Y. N. (2002), 'Influence of fines content and initial shear stress on dynamic properties of hydraulic reclaimed soil', *Canadian Geotechnical Journal* **39**, 242–253.

Cho, G. C., Dodds, J. & Santamarina, C. (2006), 'Particle shape effects on packing density, stiffness, and strength: Natural and crushed sands', *Journal of Geotechnical and Geoenviromental Engineering* **132**, 591–602.

Choo, J., Jung, Y. H., Cho, W. & Chung, C. K. (2013), 'Effect of pre-shear stress path on nonlinear shear stiffness degradation of cohesive soils', *Geotechnical Testing Journal* **36**, No.2.

Clayton, C. R. I. (2011), 'Stiffness at small strain: research and practice', *Géotechnique* **61**, 5–37.

Clayton, C. R. I., Priest, J. A., Zervos, A. & Kim, S. G. (2009), 'The stokoe resonant column apparatus: effects of stiffness, mass and specimen fixity', *Géotechnique* **59**, 429–437.

Cundall, P. A. & Strack, O. D. L. (1979), 'A discrete numerical model for granular assemblies', *Géotechnique* **29**, 47–65.

Darendeli, M. B. (2001), Development of a new family of normalized modulus reduction and material damping curves, PhD thesis, University of Texas at Austin.

Das, B. M. (1993), *Principles of soil dynamics*, PWS-KENT Publishing Company Boston.

Deresiewicz, H. (1953), Effects of an oscillating torsional couple on the contact surfaces of elastic spheres, Technical report, Office of Naval Research Project NR-064-388.

Drnevich, V. P. (1978), 'Resonant-column testing: Problems and solutions', *Dynamic Geotechnical Testing* **.**, 384–398.

Duffy, J. (1959), 'A different stress-strain relation for the hexagonal close-packed array of elastic spheres', *Journal of Applied Mechanics* **26**, 88–94.

Duffy, J. & Mindlin, R. D. (1957), 'stress strain relations andvibrations of a granular medium', *Journal of applied mechanics* **24**, 585–593.

Ezaoui, A. & Di Benedetto, H. (2009), 'Experimental measurements of the global anisotropic elastic behaviour of dry hostun sand during triaxial tests, and effect of sample preparation', *Géotechnique* **59**, 621–635.

Field, W. (1963), Towards the statistical definition of a granular mass, *in* 'Proceeding of the 4th Australia-New Zeland Conference on Soil Mechanics'.

Fioravante, V. (2000), 'Anisotropy of small strain stiffness of ticino and kenya sands from seismic wave propagation measured in triaxial testing', *Soils and Foundations* **40**, 129–142.

Flavigny, E., Dersuse, J. & Palayer, B. (1990), 'Le sable d'hostun rf.', *Géotechnique* **53**, 67–70.

Gassmann, F. (1951), 'Elastic waves through a packing of spheres', *Geophysics,* **16**, 673–685.

Ghayoomi, M., Khosravi, A., McCartney, J. & Ko, H. (2010), Challenges in prediction earthquake-induced settlements of partially saturated sands, *in* 'GeoFlorida 2010: pp. 3052-3061'.

Goudarzy, M., Viefhaus, H., König, D. & Schanz, T. (2014), Micro and macro mechanical response of granular packing containing fine materials, *in* 'Geomechanics from Micro to Macro-IS Cambridge'.

Green, R. A. & Cubrinovski, M. (2010), Geotechnical reconnaissance of the 2010 darfield (new zealand), Technical report.

Gu, X. Q. & Yang, J. (2013), 'A discrete element analysis of elastic properties of granular materials', *Granular Matter* **15**, 139–148.

Hardin, B. O. & Black, W. L. (1966), 'Sand stiffness under various triaxial stresses', *Soils Mechanics and Foundations Division* **.**, 27–42.

Hardin, B. O. & Drnevich, V. P. (1972*a*), 'Shear modulus and damping in soils: Design equations and curves', *Soil Mechanics and Foundation Division* **98**, 667–692.

Hardin, B. O. & Drnevich, V. P. (1972*b*), 'Shear modulus and damping in soils measurment and parameter effects', *Soils Mechanics and Foundations Division* **98**, 603–624.

Hardin, B. O. & Kalinski, M. E. (2005), 'Estimating the shear modulus of gravelly soils', *Journal of Geotechnical and Geoenvironmental Engineering* **131**, 867–875.

Hardin, B. O. & Richart, F. E. (1963), 'Elastic wave velocities in granular soils', *Journal of Soil Mechanics and Foundation Engineering Division* **89**, 39–56.

Hertz, H. R. (1882), 'Über die Beruhrüng fester elastischer Köper.', *Journal für Die Reine Und Angewandte Mathematik* **92**, 156–171.

Hosseininia, E. S. (2012), 'Discrete element modeling of inherently anisotropic granular assemblies with polygonal particles', *Particuology* **10**, 542–552.

Idriss, I. & Sun, J. I. (1992), A computer program for conducting equivalent linear seismic response anayses of horizentally layered soil deposits, Technical report, Center for geotechnical modelling, University of California.

Iida, K. (1937), 'The velocity of elastic wave in sands', *Earthquake research institute* **.**, 132–145.

Isenhower, W. M., Stokoe, K. H. & Allen, J. C. (1987), 'Instrumentation for torsional shear resonant column measurments under anisotropic stresses', *Geotechnical Testing Journal* **10**, 183–191.

Ishibashi, I., Chen, Y. C. & Chen, M. T. (1991), 'anisotropic behavior of ottawa sand in comparison with glass spheres', *Soils and Foundations* **31**, 145–155.

Ishibashi, I. & Zhang, X. (1993), 'Unified dynamic shear moduli and damping of sand and clay', *Soils and foundations* **33**, 182–191.

Ishihara, K. (1993), 'Liquifaction and flow failure during earthquakes', *Géotechnique* **43**, 351–415.

Ishihara, K. (1996), *Soil behavior in earthquake geotechnics*, Oxford Engineering Science.

Iwasaki, T. & Tatsuoka, F. (1977), 'Effects of grain size and grading on dynamic shear moduli of sands', *Soils and Foundations* **17**, 19–35.

Iwasaki, T., Tatsuoka, F. & Takagi, Y. (1978), 'Shear moduli of sands under cyclic torsional shear loading', *Soils and Foundations* **18**, 39–56.

Jamiolkowski, M., Lancellotta, R. & Lo Presti, D. (1995), 'Remarks on the stiffness at small strains of six italian clays', *Pre-failure Deformation of Geomaterials* **1**, 817–836.

Johnson, K. L. (1985), *Contact Mechanics*, Cambridge university press.

Jovicic, V. & Coop, M. R. (1988), 'The measurement of stiffness anisotropy in clays with bender element tests in the triaxial apparatus', *Geotechnical Testing Journal* **21**, 3–10.

Juneja, A. & Raghunandan, M. (2011), Effect of sample preparation on strength of sands, *in* 'Indian Geotechnical Conference'.

Karl, L., Haegeman, W., Degrande, G. & Dooms, D. (2008), 'Determination of the material damping ratio with the bender element test', *Journal of Geotechnical and Geoenvironmental Engineering* **134**, 1743–1756.

Koerner, R. M. (1970), 'Effects of particle characteristics on soil strength', *Journal of the Soil Mechanics and Foundation Division* **96**, 1221–1234.

Kokusho, T. (1980), 'Cyclic triaxial test of dynamic soil properties for wide strain range', *Soils and Foundations* **20**, 45–60.

Kokusho, T., Yoshida, Y. & Esashi, Y. (1982), 'Dynamic properties of soft clay for wide strain range', *Soils and Foundations* **22**, 1–18.

Kuwano, R., Connolly, T. M. & Jardine, R. J. (2000), 'Anisotropic stiffness measurements in a stress-path triaxial cell', *Geotechnical Testing Journal* **23**, 141–157.

Kuwano, R. & Jardine, R. J. (2004), 'On the applicability of cross-anisotropic elasticity to granular materials at very small strains', *Géotechnique* **52**, 727–749.

Lade, P. V. & Yamamuro, J. A. (1997), 'Effects of nonplastic fines on static liquifaction of sands', *Canadian Geotechnical Journal* **34**, 918–928.

Liao, C. L., Chan, T. C., Suiker, A. S. J. & Chang, C. S. (2000), 'Pressure-dependent elastic moduli of granular assemblies', *International Journal for Numerical and Analitical Methods in Geomechanics* **24**, 265–279.

Lins, Y. (2009), Hydro-Mechanical Properties of Partially Saturated Sand, PhD thesis, at the Faculty of Civil Egineering Ruhr-Universität Bochum.

Lo Presti, D. C. F., Pallara, O., Lancellotta, R. & Armandi, M. R. M. (1993), 'Monotonic and cyclic loading behavior of two sands at small strains', *Geotechnical Testing Journal* **16**, 409–424.

Lo Presti, D., Jamiolkowski, M., Pallara, O., Cavallaro, A. & Pedroni, S. (1997), 'Shear modulus and damping of soils', *Geotechnique* **47**, 603–617.

Lo Presti, D. & O'Neill, D. A. (1991), 'Laboratory investigation of small strain modulus anisotropic in sand', *Calibration chamber testing, Elsevier Science Publishing* pp. 213–224.

Magnanimo, V., La Ragione, L., Jenkins, J. T., Wang, P. & Makse, H. A. (2008), 'Characterizing the shear and bulk moduli of an idealized granular material', *Europhysics Letters* **81**, No.34006.

Mahmood, A. & Mitchell, J. K. (1974), 'Fabric-property relationships in fine granular materials', *Clays and Clay Minerals* **22**, 397–408.

Makse, H., Gland, N., Johnson, D. & Schwartz, L. (1999), 'Why eective medium theory fails in granular materials', *Physics Review Letter* **83**, 5070–5073.

Marcuson, W. E. & Whals, H. E. (1972), 'Time effects on dynamic shear modulus of clays', *Journal of the Soil Mechanics and Foundations Division* **98**, 1359–1373.

Mavok, G., Mukerji, T. & Dvorkin, J. (2009), *The Rock Physics Handbook*, Cambridge University Press.

Menq, F. Y. (2003), Dynamic Properties of Sandy and Gravelly Soils, PhD thesis, The University of Texas at Austin.

Mitchell, J. K. (1976), *Fundamental of soil behavior*, Taylor & Francis, London.

Mitchell, J. & Soga, K. (2005), *Fundamental of soil behavior*, John wiley & sons.

Miura, K., Maeda, K., Furukawa, M. & Toki, S. (1997), 'Physical characteristics of sand with different primary properties', *Soils and Foundations* **37**, 53–64.

Monkul, M. M. & Yamamuro, J. A. (2011), 'Influence of silt size and content on liquefaction behavior of sands', *Canadian Geotechnical Journal* **48**, 931–942.

Naeini, S. A. & Baziar, M. H. (2004), 'Effect of fines content on steady-state strength of mixed and layered samples of a sand', *Soil Dynamics and Earthquake Engineering* **24**, 181–187.

Ng, T. T. (2004), 'Macro- and micro-behaviors of granular materials under different sample preparation methods and stress paths', *International Journal of Solids and Structures* **41**, 5871–5884.

Ng, T. T. & Petrakis, E. (1996), 'small-strain response of random arrays of spheres using discrete element method', *Journal of Engineering Mechanics* **122**, 239–244.

Ni, Q. Tan, T. S., Dasari, G. R. & Hight, D. W. (2005), 'Contribution of fines to the compressive strength of mixed soils', *Géotechnique* **55**, 627–628.

Oda, M. (1972), 'Initial fabric and their relations to mechanical properties of granular material', *Soils and Foundations* **12**, 17–36.

Oda, M. (1977), 'Coordination number and its relation to shear strength of granular material', *Soils and Foundations* **17**, 29–42.

Otsubo, M., O´Sullivan, C., Sim, W. W. & Ibraim, E. (2015), 'Quantitative assessment of the influence of surface roughness on soil stiffness', *Géotechnique* **65**, 694–700.

Patel, A., Bartake, P. P. & Singh, D. N. (2008), 'An empirical relationship for determining shear wave velocity in granular materials accounting for grain morphology', *Geotechnical Testing Journal* **32**, 1–10.

Petrakis, E. & Dobry, R. (1987), Micromechanics modeling of granular soil at small strain by arrays of elastic spheres, Technical report, Department of civil engineering Rensselaer Polytechnic Institute.

Petrakis, E., Dobry, R. & Ng, T. T. (1988), Small strain response of random arrays of elastic spheres using a nonlinear distinct element procedure, Technical report, Department of civil engineering Rensselaer Polytechnic Institute.

Procter, D. & Barton, R. (1974), 'Measurements of the angle of interparticle friction', *Géotechnique* **24**, 581–604.

Rahman, M., Cubrinovski, M. & Lo, S. (2012), 'Initial shear modulus of sandy soils and equivalent granular void ratio', *Geomechanics and Geoengineering: An International Journal* **7**, 219–226.

Rahman, M. M. & Lo, S. R. (2008), 'The prediction of equivalent granular steady state line of loose sand with fines', *Geomechanics and Geoengineering: An International Journal* **3**, 179–190.

Rahman, M. M. & Lo, S. R. (2012), 'Predicting the onset of static liquefaction of loose sand with fines', *Journal of Geotechnical and Geoenvironmental Engineering* **138**, 1037–1041.

Rahman, M. M. & Lo, S. R. (2014), 'Undrained behaviour of sand-fines mixtures and their state parameters', *Journal of Geotechnical and Geoenvironmental Engineering* **140**.

Rahman, M. M., Lo, S. R. & Gnanendran, C. T. (2008), 'On equivalent granular void ratio and steady state behaviour of loose sand with fines', *Canadian Geotechnical Journal* **45**, 1439–14561.

Raju, L. G., Ramana, G. V., Rao, C. H. & Sitharam, T. G. (2004), 'Site specific ground response analysis', *Geotechnics and Earthquake Hazards* **87**, 1354–1362.

Ravishankar, B. V., Sitharam, T. G. & Raju, G. L. (2005), Dynamic properties of ahmedabad sands at large strain, *in* 'Indian Geotechnical Conference (IGC 2005)'.

Reddy, A. (2008), Particle Form and its Impact on Packing and Shear Behaviour of Particulate Materials, PhD thesis, School of Civil Engineering and the Environment, University of Southampton.

Richart, F. E., Hall, J. R. & Woods, R. D. (1970), *Vibration of Soils and Foundations*, Prentice-Hall, Englewood Cliffs, N J.

Roesler, S. (1979), 'Anisotropic shear modulus due to stress anisotropy', *Journal of the Geotechnical Engineering Division* **105**, 871–880.

Rothenburg, L. & Bathurst, R. J. (1989), 'Analytical study of induced anisotropy in idealized granular materials', *Géotechnique* **39**, 601–614.

Sadek, T. (2006), The multiaxial behavior and elastic stiffness of Hostun sand, PhD thesis, University of Bristol.

Sadek, T., Lings, M., Dihoru, L. & Wood, D. M. (2007), 'Anisotropic stiffness of hostun sand', *Book Chapter: Numerical models in geomechancis NUMOG X, London* pp. 147–152.

Sahaphol, T. & Miura, S. (2005), 'Shear moduli of volcanic soils', *Soil Dynamics and Earthquake Engineering* **25**, 157–165.

Salgado, R., Bandini, P. & Karim, A. (2000), 'Shear strength and stiffness of silty sand', *Journal of Geotechnical and Geoenviromental Engineering* **126**, 451–462.

Santamarina, C. & Cascante, G. (1996), 'Stress anisotropy and wave propagation: a micromechanical view', *Canadian Geotechnical Journal* **33**, 770–782.

Santamarina, J. C. & Aloufi, M. (1999), Small strain stiffness: A micromechanical experimental study, *in* 'Proceeding of pre-failure deformation characteristics of geomaterials, 451-459'.

Saxena, S. & Reddy, K. (1989), 'Dynamic moduli and damping ratios for monterey no.0 sand by resonant column tests', *Soils and Foundations* **29**, 37–51.

Schanz, T. & Vermeer, P. (1996), 'Angles of friction and dilatancy of sand', *Géotechnique* **46**, 145–151.

Schnable, P. B., Lysmer, J. & Seed, H. B. (1972), Shaker: A computer program for earthquake response analysis of horizentally layerd sites, Technical report, Earthquake engineering research center, University of California.

Schneider, J. A. & Mayne, P. W. (1999), Soil liquefaction response in mid-america evaluated by seismic piezocone tests, Technical report, Mid-America Earthquake Center Report MAE-GT-3A Atlanta.

Seed, B., Wong, R., Idriss, I. & Tokimatsu, K. (1984), Moduli and damping factors for dynamic analyses of cohesionless soils, Technical report, National science foundation.

Seed, B., Wong, R., Idriss, I. & Tokimatsu, K. (1986), 'Moduli and damping factors for dynamic analyses of cohesionless soils', *Journal of Geotechnical and Geoenviromental Engineering* **112**, 1016–1032.

Shibuya, S., Hwang, S. C. & Mitachi, T. (1997), 'Elastic shear modulus of soft clays from shear wave velocity measurement', *Géotechnique* **47**, 593–601.

Shin, H. & Santamarina, C. (2013), 'Role of particle angularity on the mechanical behavior of granular mixtures', *Journal of Geotechnical and Geoenvironmental Engineering,* **139**, 353–355.

Shire, T., O'Sullivan, C. & Hanley, K. (2014), The influence of finner fraction and size-ratio on the micro-scale properties of dense bimodal material, *in* 'International Symposium on Geomechanics from Micro to Macro'.

Skinner, A. (1969), 'A note on the influence of interparticle friction on the shearing strength of a random assembly of spherical particles', *Géotechnique* **19**, 150–157.

Smith, W. O., Foote, P. D. & Busang, P. (1929), 'Packing of homogeneous spheres', *Phys. Rev.* **34**, 1271–1274.

Stokoe, II, K., Darendeli, M. B., Andrus, R. D. & Brown, L. T. (1999*a*), 'Dynamic soil properties: Laboratory, field and correlation studies', *Earthquake Geotechnical Engineering* pp. 811–845.

Stokoe, K. H., Darendeli, M. B., Andrus, R. D. & Brown, L. T. (1999*b*), Dynamic soil properties: Laboratory, field and correlation studies, *in* 'In Proc. 2nd Int. Conf. on earthquake Geotech. Eng.'.

Tao, M., Figueroa, J. & Saada, A. (2004), Influence of nonplastic fines content on the liquefaction resistence of soils in terms of the unit energy, *in* 'Cyclic behavior of soils and liquifaction phenomena'.

Tatsuoka, F., Iwasaki, T., Fukushima, S. & Sudo, H. (1979), 'Stress conditions and stress histories affecting shear modulus and damping of sand under cyclic loading', *Soils and Foundations* **19**, 30–43.

Tatsuoka, F., Iwasaki, T. & Takagi, Y. (1978), 'Hysteretic damping of sands under cyclic loading and its relation to shear modulus', *Soils and Foundations* **18**, 26–39.

Tatsuoka, F., Ochi, K., Fujii, S. & Okamoto, M. (1986), 'Cyclic undrained triaxial and torsional shear strength of sands for different sample preparation methods', *Soils and Foundations* **26**, 23–41.

Tatsuoka, F. & Silver, M. L. (1980), 'New method for the calibration of the inertia of resonant column device', *Geotechnical Testing Journal* **3**, 30–34.

Terzaghi, K., Peck, B. R. & Mersi, G. (1996), *Soil mechanics in engineering practice*, John Wiley & Sons.

Thevanayagam, S. (1998), 'Effect of fines and confining stress on undrained shear strength of silty sands', *Journal of Geotechnical and Geoenviromental Engineering* **124**, 479–491.

Thevanayagam, S. (1999), Intergranular contact and shear modulus of non-plastic granular mixes, *in* '13th ASCE Conference on Engineering Mechanics. John Hopkins University'.

Thevanayagam, S. (2007), 'Intergrain contact density indices for granular mixes-i: framework', *Earthquake Enginnering and Engineering Vibration* **6**, 123–134.

Thevanayagam, S. & Liang, J. (2001), Shear wave velocity relations for silty and gravel soils, *in* 'Proc. 4th international conferences on soil dynamics and earthquake engineering'.

Thevanayagam, S., Shenthan, T., Mohan, S. & Liang, J. (2002), 'Undrained fragility of clean sands, silty sands, and sandy silts', *Journal of Geotechnical and Geoenviromental Engineering* **128**, 849–859.

Thornton, C. & Antony, S. J. (1998), 'Quasi-static deformation of particulate media', *Phil. Trans. R. Soc. Lond.* **356**, 2763–2782.

Tokimatsu, K. & Seed, B. (1987), 'Evaluation of settlements in sands due to earthquake shaking', *Journal of Geotechnical Engineering* **113**, 861–878.

Vaid, Y. P., Sivathayalan, S. & Stedman, D. (1999), 'Influence of specimen-reconstituting method on the undrained response of sand', *American Society for Testing and Materials* **22**, 187–195.

Walton, K. (1987), 'The effective elastic moduli of a random packing of spheres', *Journal of the Mechanics and Physics of Solids* **35**, 213–226.

Wang, Y. & Mok, C. (2008), 'Mechanisms of small strain shear modulus anisotropy in soils', *Journal of Geotechnical and Geoenviromental Engineering* **134**, 1516–1530.

Wang, Y. & Santamarina, C. (2007), 'Attenuation in sand: an exploratory study on the small-strain behavior and the influence of moisture condensation', *Granular Matter* **9**, 365–376.

White, J. E. & Sengbush, R. L. (1953), 'Velocity measurments in near surface formation', *Geophysics* **18**, 54–69.

Wichtmann, T., Hernández, M. A. N. & Triantafyllidis, T. (2015), 'On the influence of a non-cohesive fines content on small strain stiffness, modulus degradation and damping of quartz sand', *Soil Dynamics and Earthquake Engineering* **69**, 103–114.

Wichtmann, T., Sonntag, T. & Triantafyllidis, T. (2001), 'Über das Erinnerungsvermögen von Sand unter zyklischer Belastung', *Bautechnik* **78**, 852–865.

Wichtmann, T. & Triantafyllidis, T. (2009), 'On the influence of the grain size distribution curve of quartz sand on the small strain shear modulus', *Journal of Geotechnical and Geoenviromental Engineering* **135**, 1404–1418.

Wichtmann, T. & Triantafyllidis, T. (2013), 'Effect of uniformity coefficiensands g/g_{max} and damping ratio of uniform to well graded quartz sands', *Journal of Geotechnical and Geoenviromental Engineering* **139**, 59–72.

Wichtmann, T. & Triantafyllidis, T. (2014), 'Stiffness and damping of clean quartz sand with various grain size distribution curves', *Journal of Geotechnical an Geoenviromental Engineering* **ASCE,**, ISSN 1090–0241/06013003(4).

Yamamuro, J. A. & Lade, P. V. (1997), 'Static liquifaction of very loose sands', *Canadian Geotechnical Journal* **34**, 905–917.

Yamashita, S., Fujiwara, T., Kawaguchi, T., Mikami, T., Nakata, Y. & Shibuya, S. (2005), International parallel test on the measurement of gmax using bender elements organized by tc-29, Technical report, Japanese Domestic Committee for TC-29.

Yanagisawa, E. (1983), 'Influence of void ratio and stress condition on the dynamic shear modulus of granular media', *Adv. in the mechanics and the flow of Granular Materials* **2**, 947–960.

Yang, J. & Wei, L. M. (2012), 'Collapse of loose sand with addition of fines: the role of particle shape', *Geotechnique* **62**, 1111–1125.

Yimsiri, S. & Soga, K. (2002), 'Application of micromechanics model to study anisotropy of soils at small strains', *Soils and Foundations* **42**, 15–26.

Yu, P. & Richart, F. (1984), 'Stress ratio effects on shear modulus of dry sands', *Journal of Geotechnical Engineering* **110**, 331–345.

Zemanek, J. & Rudnick, I. (1961), 'Attenuation and dispersion of elastic waves in a cylindrical bar', *The Journal of the Acoustical Society of America* **33**, 1283–1288.

Zhang, J., Andrus, R. D. & Juang, C. H. (2005), 'Normalized shear modulus and material damping ratio relationships', *Journal of Geotechnical and Geoenvironmental Engineering* **131**, 453–464.

Zuo, L. & Baudet, B. A. (2015), 'Determination of the transitional fines content of sand-non plastic fines mixtures', *Soils and Foundations* **55**, 213–219.

Appendix A

Table A.1: Summary of calibrations I, II and III, Hardin's void ratio function

	Calibration I				Calibration II					Calibration III				
	Eq. 4.3	$k_H f(e^*)$	Eq.4.8		Eq.4.3, Eq.4.4		$k_H f(e^*)$	Eq.4.8		Eq.4.3, Eq.4.4		$k_H.f(e^*)$	Eq.4.8	
p [kPa]	λ	R^2	R^2	RMSD	λ	m	R^2	R^2	RMSD	λ	m	R^2	R^2	RMSD
55	0.3	0.90	0.95	6,40	0.3	0.12	0.92	0.98	3.59	0.24	0.12	0.92	0.98	3.89
80	0.3	0.76	0.96	7.54	0.3	0.12	0.89	0.97	3.88	0.31	0.12	0.89	0.97	3.81
110	0.3	0.72	0.97	8.86	0.3	0.12	0.87	0.93	4.44	0.37	0.12	0.90	0.95	3.92
140	0.3	0.66	0.88	10.25	0.3	0.12	0.84	0.91	5.27	0.40	0.12	0.90	0.94	4.30
170	0.3	0.45	0.77	11.35	0.3	0.12	0.85	0.92	5.93	0.43	0.12	0.91	0.95	4.52
200	0.3	0.34	0.77	12.81	0.3	0.12	0.79	0.92	7.08	0.51	0.12	0.89	0.96	5.12
Overall R^2 & RMSD			0.86	8.92	Overall R^2 & RMSD			0.94	5.18	Overall R^2 & RMSD			0.96	4.29

Table A.2: Summary of calibrations I, II and III, Jamiolkowski's void ratio function

	Calibration I				Calibration II					Calibration III				
	Eq.4.3	$k_J f(e^*)$	Eq.4.8		Eq.4.3, Eq.4.4		$k_J f(e^*)$	Eq.4.8		Eq.4.3, Eq.4.4		$k_J.f(e^*)$	Eq.4.8	
p [kPa]	λ	R^2	R^2	RMSD	λ	m	R^2	R^2	RMSD	λ	m	R^2	R^2	RMSD
55	0.3	0.9	0.98	3.61	0.3	0.12	0.92	0.99	3.12	0.24	0.12	0.92	0.99	3.05
80	0.3	0.92	0.98	3.73	0.3	0.12	0.96	0.98	2.73	0.31	0.12	0.96	0.98	2.76
110	0.3	0.89	0.97	4.45	0.3	0.12	0.96	0.96	2.83	0.37	0.12	0.96	0.96	2.74
140	0.3	0.86	0.88	5.48	0.3	0.12	0.95	0.96	3.34	0.40	0.12	0.96	0.97	2.94
170	0.3	0.82	0.90	6.46	0.3	0.12	0.93	0.96	3.97	0.43	0.12	0.96	0.98	3.26
200	0.3	0.74	0.92	7.83	0.3	0.12	0.90	0.97	4.97	0.51	0.12	0.94	0.98	3.99
Overall R^2 & RMSD			0.94	5.16	Overall R^2 & RMSD			0.97	3.58	Overall R^2 & RMSD			0.98	3.15

Table A.3: Summary of calibrations IV and V, Hardin's void ratio function, m is a function of f_c

	Calibration IV						Calibration V					
	Eq.4.3, Eq.4.4			$k_H f(e^*)$	Eq.4.8		Eq.4.3, Eq.4.4			$k_H f(e^*)$	Eq.4.8	
p [kPa]	λ	m_{30}	m_{40}	R^2	R^2	RMSD	λ	m_{30}	m_{40}	R^2	R^2	RMSD
55	0.3	0.12	0.14	0.93	0.98	4.15	0.24	0.12	0.14	0.93	0.98	4.40
80	0.3	0.11	0.14	0.91	0.97	3.99	0.31	0.11	0.13	0.92	0.97	3.91
110	0.3	0.11	0.14	0.89	0.93	4.52	0.37	0.11	0.14	0.93	0.95	4.01
140	0.3	0.11	0.14	0.87	0.92	5.19	0.40	0.11	0.14	0.93	0.94	4.20
170	0.3	0.11	0.14	0.86	0.92	5.80	0.43	0.11	0.14	0.92	0.96	4.30
200	0.3	0.11	0.14	0.81	0.93	6.72	0.47	0.11	0.14	0.91	0.97	4.68
Overall R^2 & RMSD					0.95	5.18	Overall R^2 & RMSD				0.96	4.26

Table A.4: Summary of calibrations IV, V, Jamiolkowski's void ratio function, m is a function of f_c

	Calibration IV						Calibration V					
	Eq.4.3, Eq.4.4			$k_J f(e^*)$	Eq.4.8		Eq.4.3, Eq.4.4			$k_J f(e^*)$	Eq.4.8	
p [kPa]	λ	m_{30}	m_{40}	R^2	R^2	RMSD	λ	m_{30}	m_{40}	R^2	R^2	RMSD
55	0.3	0.12	0.14	0.93	0.99	2.98	0.24	0.12	0.14	0.93	0.99	2.90
80	0.3	0.11	0.14	0.96	0.98	2.46	0.31	0.11	0.13	0.96	0.98	2.46
110	0.3	0.11	0.14	0.97	0.97	2.50	0.37	0.11	0.14	0.97	0.97	2.40
140	0.3	0.11	0.14	0.96	0.97	2.95	0.40	0.11	0.14	0.97	0.98	2.49
170	0.3	0.11	0.14	0.94	0.97	3.52	0.43	0.11	0.14	0.97	0.98	2.70
200	0.3	0.11	0.14	0.91	0.97	4.50	0.47	0.11	0.14	0.96	0.99	3.21
Overall R^2 & RMSD					0.98	3.23	Overall R^2 & RMSD				0.98	2.71

Schriftenreihe des Lehrstuhls für Grundbau, Boden- und Felsmechanik der Ruhr-Universität Bochum

Herausgeber: H.L. Jessberger

1 (1979) **Hans Ludwig Jessberger**
Grundbau und Bodenmechanik an der Ruhr-Universität Bochum

2 (1978) **Joachim Klein**
Nichtlineares Kriechen von künstlich gefrorenem Emschermergel

3 (1979) **Heinz-Joachim Gödecke**
Die Dynamische Intensivverdichtung wenig wasserdurchlässiger Böden

4 (1979) **Poul V. Lade**
Three Dimensional Stress-Strain Behaviour and Modeling of Soils

5 (1979) **Roland Pusch**
Creep of soils

6 (1979) **Norbert Diekmann**
Zeitabhängiges, nichtlineares Spannungs-Verformungsverhalten von gefrorenem Schluff unter triaxialer Belastung

7 (1979) **Rudolf Dörr**
Zeitabhängiges Setzungsverhalten von Gründungen in Schnee, Firn und Eis der Antarktis am Beispiel der deutschen Georg-von-Neumayer- und Filchner-Station

8 (1984) **Ulrich Güttler**
Beurteilung des Steifigkeits- und Nachverdichtungsverhaltens von ungebundenen Mineralstoffen

9 (1986) **Peter Jordan**
Einfluss der Belastungsfrequenz und der partiellen Entwässerungs-möglichkeiten auf die Verflüssigung von Feinsand

10 (1986) **Eugen Makowski**
Modellierung der künstlichen Bodenvereisung im grundwasserdurchströmten Untergrund mit der Methode der finiten Elemente

11 (1986) **Reinhard A. Beine**
Verdichtungswirkung der Fallmasse auf Lastausbreitung in nichtbindigem Boden bei der Dynamischen Intensivverdichtung

12 (1986) **Wolfgang Ebel**
Einfluss des Spannungspfades auf das Spannungs-Verformungsverhalten von gefrorenem Schluff im Hinblick auf die Berechnung von Gefrierschächten

13 (1987) **Uwe Stoffers**
Berechnungen und Zentrifugen-Modellversuche zur Verformungsabhängigkeit der Ausbaubeanspruchung von Tunnelausbauten in Lockergestein

14 (1988) **Gerhard Thiel**
Steifigkeit und Dämpfung von wassergesättigtem Feinsand unter Erdbebenbelastung

15 (1991) **Mahmud Thaher**
Tragverhalten von Pfahl-Platten-Gründungen im bindigen Baugrund,
Berechnungsmodelle und Zentrifugen-Modellversuche

16 (1992) **Rainer Scherbeck**
Geotechnisches Verhalten mineralischer Deponieabdichtungsschichten
bei ungleichförmiger Verformungswirkung

17 (1992) **Martin M. Bizialiele**
Torsional Cyclic Loading Response of a Single Pile in Sand

18 (1993) **Michael Kotthaus**
Zum Tragverhalten von horizontal belasteten Pfahlreihen aus langen Pfählen in Sand

19 (1993) **Ulrich Mann**
Stofftransport durch mineralische Deponieabdichtungen:
Versuchsmethodik und Berechnungsverfahren

20 (1992) **Festschrift anlässlich des 60. Geburtstages von**
Prof. Dr.-Ing. H. L. Jessberger
20 Jahre Grundbau und Bodenmechanik an der Ruhr-Universität Bochum

21 (1993) **Stephan Demmert**
Analyse des Emissionsverhaltens einer Kombinationsabdichtung im Rahmen der
Risikobetrachtung von Abfalldeponien

22 (1994) **Diethard König**
Beanspruchung von Tunnel- und Schachtausbauten in kohäsionslosem Lockergestein
unter Berücksichtigung der Verformung im Boden

23 (1995) **Thomas Neteler**
Bewertungsmodell für die nutzungsbezogene Auswahl von Verfahren zur Altlastensanierung

24 (1995) **Ralph Kockel**
Scherfestigkeit von Mischabfall im Hinblick auf die Standsicherheit von Deponien

25 (1996) **Jan Laue**
Zur Setzung von Flachfundamenten auf Sand unter wiederholten Lastereignissen

26 (1996) **Gunnar Heibrock**
Zur Rissbildung durch Austrocknung in mineralischen Abdichtungsschichten
an der Basis von Deponien

27 (1996) **Thomas Siemer**
Zentrifugen-Modellversuche zur dynamischen Wechselwirkung zwischen Bauwerken
und Baugrund infolge stoßartiger Belastung

28 (1996) **Viswanadham V. S. Bhamidipati**
Geosynthetic Reinforced Mineral Sealing Layers of Landfills

29 (1997) **Frank Trappmann**
Abschätzung von technischem Risiko und Energiebedarf bei Sanierungsmaßnahmen
für Altlasten

30 (1997) **André Schürmann**
Zum Erddruck auf unverankerte flexible Verbauwände

31 (1997) **Jessberger, H. L. (Herausgeber)**
Environment Geotechnics, Report of ISSMGE Technical Committee TC 5
on Environmental Geotechnics

Herausgeber: Th. Triantafyllidis

32 (2000) **Triantafyllidis, Th. (Herausgeber)**
Boden unter fast zyklischer Belastung: Erfahrung und Forschungsergebnisse (Workshop)

33 (2002) **Christof Gehle**
Bruch- und Scherverhalten von Gesteinstrennflächen mit dazwischenliegenden Materialbrücken

34 (2003) **Andrzej Niemunis**
Extended hypoplastic models for soils

35 (2004) **Christiane Hof**
Über das Verpressankertragverhalten unter kalklösendem Kohlensäureangriff

36 (2004) **René Schäfer**
Einfluss der Herstellungsmethode auf das Verformungsverhalten von Schlitzwänden in weichen bindigen Böden

37 (2005) **Henning Wolf**
Zur Scherfugenbänderung granularer Materialien unter Extensionsbeanspruchung

38 (2005) **Torsten Wichtmann**
Explicit accumulation model for non-cohesive soils under cyclic loading

39 (2008) **Christoph M. Loreck**
Die Entwicklung des Frischbetondruckes bei der Herstellung von Schlitzwänden

40 (2008) **Igor Arsic**
Über die Bettung von Rohrleitungen in Flüssigböden

41 (2009) **Anna Arwanitaki**
Über das Kontaktverhalten zwischen einer Zweiphasenschlitzwand und nichtbindigen Böden

Herausgeber: T. Schanz

42 (2009) **Yvonne Lins**
Hydro-Mechanical Properties of Partially Saturated Sand

43 (2010) **Tom Schanz (Herausgeber)**
Geotechnische Herausforderungen beim Umbau des Emscher-Systems
Beiträge zum RuhrGeo Tag 2010

44 (2010) **Jamal Alabdullah**
Testing Unsaturated Soil for Plane Strain Conditions: A New Double-Wall Biaxial Device

45 (2011) **Lars Röchter**
Systeme paralleler Scherbänder unter Extension im ebenen Verformungszustand

46 (2011) **Yasir Al-Badran**
Volumetric Yielding Behavior of Unsaturated Fine-Grained Soils

47 (2011) **Usque ad finem**
Selected research papers

48 (2012) **Muhammad Ibrar Khan**
Hydraulic Conductivity of Moderate and Highly Dense Expansive Clays

49 (2014) **Long Nguyen-Tuan**
Coupled Thermo-Hydro-Mechanical Analysis: Experimental and Back Analysis

50 (2014) **Tom Schanz (Herausgeber)**
Ende des Steinkohlenbergbaus im Ruhrrevier: Realität und Perspektiven für die Geotechnik
Beiträge zum RuhrGeo Tag 2014

51 (2014) **Usque ad finem**
Selected research papers

52 (2014) **Houman Soleimani Fard**
Study on the Hydro-Mechanical Behavior of Fiber Reinforced Fine Grained Soils,
with Application to the Preservation of Historical Monuments

53 (2014) **Wiebke Baille**
Hydro-Mechanical Behaviour of Clays - Significance of Mineralogy

54 (2014) **Qasim Abdulkarem Jassim Al-Obaidi**
Hydro-Mechanical Behavior of Collapsible Soils

55 (2015) **Veselin Zarev**
Model Identification for the Adaption of Numerical Simulation Models -
Application to Mechanized Shield Tunneling

56 (2015) **Meisam Goudarzy**
Micro and Macro Mechanical Assessment of Small and Intermediate Strain
Properties of Granular Material